STRUCTURE AND PROPERTIES

OF COMPOSITE POLYOLEFIN MATERIALS

Dissertation zur Erlangung des Grades
“Doctor der Naturwissenschaften“
am Fachbereich Chemie, Pharmazie und Geowissenschaften
der Johannes Gutenberg-Universität Mainz

vorgelegt von

Olga Pryadilova
geboren in Nizhnii Novgorod

Mainz 2006

List of Abbreviations

AFM	Atomic Force Microscopy
BS	Brillouin Spectroscopy
DMA	Dynamic Mechanical Analysis
DSC	Differential Scanning Calorimetry
iPP	Isotactic Poly(Propylene)
iPPMA	Isotactic Poly(Propylene)-*graft*-Maleic Anhydride
iPP/iPPMA	Isotactic Poly(propylene)/Isotactic Poly(Propylene)-*graft*-Maleic Anhydride blend
PDMS	Poly(dimethylsiloxane)
PI	Polyisoprene
IR	Infrared spectroscopy
LDPE	Low Density Poly(Ethylene)
LDPE	Low Density Poly(Ethylene)/isotactic Poly(Propylene) binary blend
LDPE/iPP/Dutral054	Low Density Poly(Ethylene)/isotactic Poly(Propylene)/ Dutral054 ternary blend
LDPE/iPP/Keltan13	Low Density Poly(Ethylene)/isotactic Poly(Propylene)/ Keltan13 ternary blend
LDPE/iPP/Keltan740	Low Density Poly(Ethylene)/isotactic Poly(Propylene)/ Keltan740 ternary blend
Mw	Molecular weight
q	Scattered vector
c_L	Longitudinal velocity
λ	Wavelength
ρ	Density
PE	Poly(Ethylene)
POM	Polarized Optical Microscopy
SALS	Small angle Light Scattering
SAXS	Small angle X-ray Scattering
SEM	Scanning Electron Microscopy
TEM	Transmission Electron Microscopy
WAXS	Wide angle X-ray Scattering

T-FPI	Tandem-Fabry-Perot Interferometer
FSR	Free Spectral Range

Table of Content

Chapter 1 - Introduction

1.1. Background

Development of composites materials was continuously performed to address the technical barriers hindering their penetration into commercial market. The outstanding properties of composites make them potential candidates for the preparation of new products with superior and well defined properties that may be very competitive with respect to traditional materials.[1,2] There are plenty of industries as diverse as transportation, construction, marine, medical devices, sporting goods that may significantly benefit of the high competitiveness of these materials.[3,4] In the context of industrial application, competitive materials do no refer only to properties but also to cost. A first idea to take into account all these requirements was to blend polymers. Because the synthetic tools enabling the design of macromolecules with perfectly controlled macromolecular architecture (that is the topology, chemical composition and distribution of the elements along the polymer chain) generally impose drastic synthetic conditions difficult to transfer in a large scale production. Moreover, blending technology opens new possibilities to address the problem of materials recycling.[5] However, it is obvious that the behaviour of multiphase systems may become very complex, depending primarily on the compatibility of the combined components (miscible versus immiscible systems) and on their respective nature; amorphous or semicrystalline. The case of an immiscible semicrystalline/ semicrystalline blend can be at first be considered as a four phases systems, where each semicrystalline polymer is composed of amorphous and crystalline domains assuming the typical layer-like structure. However, the advantages of semicrystalline polymers, compared to amorphous ones, are that their maximum temperature of application is directed by the melting temperature instead of the glassy temperature. The main disadvantage is that impact toughness of most of polymeric materials is low. Nevertheless, pathways exist to overcome this weakness as for example adding a rubber component.[6] But various parameters, such as chemical nature of the rubbery additive as well as blend composition and processing conditions have to be perfectly chosen in order to create materials with improved properties, essentially mechanical properties with respect to the primary components. For example, addition of rubber material in uncontrolled way may lead to a decrease in stiffness.

The control of macroscopic properties is primarily determined by the size scale at which the dispersion of the minor phase within the major one occurs. In the case of immiscible binary polymer blends, the size scale is in the micrometer range. Even, if the level of dispersion can be reduced by adding a third component, usually referred as to compatibilizer, the microscopic dimensions of the heterogeneous structure is the major limitation to the properties improvement. In search for ultimate properties, it was admitted that addition of rigid particles to semicrystalline polymers leads to an enhancement of both stiffness as impact toughness. This is notably the case when the particles, as for example layered silicate, are dispersed in the state of single platelet. The achievement of nanoscopic dispersion is the key way to prepare materials with optimum properties.[7,8]

1.2. Overview of the Thesis

This thesis is based on three main studies, all dealing with structure-property investigation of semicrystalline polyolefin-based composites. Low density poly(ethylene) (LDPE) and isotactic poly(propylene) (iPP) were chosen as parts of the composites materials and they were investigated either separately (as homoploymers), either in blend systems with the composition LDPE/iPP 80/20 or as filled matrix with layered silicate (montmorillonite).

In **Chapter 2** the effect of three ethylene-co-propylene copolymers, namely Keltan13, Keltan740 and Dutral054, on morphologies and physical-mechanical properties of thermodynamically immiscible low density poly(ethylene)/isotactic poly(propylene) blend with weight ratio (80/20) are discussed on the basis of data obtained by means of ten experimental complementary methods. The three ethylene-co-propylene copolymers were used as compatibilizers at weight content of 5, 10 and 15%. Characterization of ethylene-co-propylene copolymers is initially presented by means of DSC, IR and DMA. In the next section, it is shown that not only the content of compatibilizer but also its chemical nature (composition, molecular weight) are the key parameters controlling the structure and related properties of ternary blends. Selected results from this study will be published as a chapter of a book on *Polymer Blending*.

The **Chapter 3** introduces a very promising technique for mechanical analysis of at least two component heterogeneous films. This study relies on the application of Brillouin scattering as a powerful non-destructive method for evaluating the sound velocity within semicrystalline materials. Brillouin scattering is a powerful non-destructive method for evaluating the sound velocity within materials. Films of LDPE, iPP and LDPE/iPP (80/20) blend have been investigated. The crystalline superstructure of the samples has been controlled through various thermal treatments from the melt. This study is to our knowledge, the first report on application of Brillouin spectroscopy to reveal the effect of sizeable spherulites on the high frequency mechanical properties of semicrystalline polymers and the part of this chapter dealing with the investigation of poly(ethylene) and poly(propylene) homopolymers has been published in *Macromolecules*.[9]

The **Chapter 4** presents a comprehensive investigation of structure and physical properties of isotactic poly(propylene)/montmorillonite nanocomposites. Isotactic poly(propylene)-*graft*-maleic anhydride was used at a fixed weight content of 4% as compatibilizer of the polymer-clay systems. The clay loading was varied from 2%, through 5% and to 7%. Various experimental methods were applied to get information on the structural elements on various size scales; ranging from the micrometer level (where spherulites were observed by POM) down to the nanometer level (where WAXS and TEM revealed the state of dispersion of the nanoclay). A key structural element is the interaction strength between filler-nanoclay and polymer matrix. For our systems this interaction was found to decrease as the clay loading increased revealing the importance of the weight ratio between compatibilizer and clay. The nanocomposite containing 2% of clay behaves as a one phase system and exhibits the largest improvement in mechanical properties. Furthermore, this chapter demonstrates a correlation between micro- and macro-mechanical properties for isotactic poly(propylene)/montmorillonite hybrid materials.

Finally, **Chapter 5** describes the methods and techniques used in this study as well as some information about the preparation of the samples.

We present general conclusion about this work in **Chapter 6**.

Chapter 2 - Structure and properties of ternary blends.

This chapter covers different aspects of the science of polymer blends ranging from the practical aspects (preparation and properties) to more fundamental ones (thermodynamics and morphology-properties relationship). A polymer blend can be simply defined as a mixture of at least two polymers or copolymers. Polymer blending is a well established and economical strategy to design new materials from existing polymers. After the great progress recorded in monomer synthesis and new polymer or copolymer design, innovation was slowed down by cost criteria. Designing new random, block or graft copolymers is more expensive than developing novel polymer mixtures. Indeed, driven by a tough competition, the development of new materials via blending of existing homopolymers and copolymers has been initiated during the seventies. The major advantages of blending can be summarized as follows:

i) opportunity to develop new properties or improve the existing ones to meet specific customer needs

ii) significant material cost reduction without substantial loss in properties

iii) improvement of the processability of some interesting polymers that are difficult to shape as neat

iv) ability of recycling two, three or more polymers of different nature.

However, a fundamental question which should be addressed when dealing with any blend system of particular interest is whether the components are miscible or not since the thermodynamic of the blend is a key parameter influencing the micro and macroscopic properties of the resulting material. After a short description of preparation methods, the first part of this chapter is devoted to a brief recall about the thermodynamics of miscibility and a discussion about the case of polymer based systems is presented. Polymer blends are first introduced based their miscible or immiscible nature. The advantages and disadvantages of one class over the other are briefly highlighted. The two main strategies of compatibilization, i.e., physical blending which consist of adding a pre-formed copolymer to compatibilize the blend and reactive blending which is based on the in-situ generation of the compatibilizing agent, are compared and some methods usually used to study the compatibilization effect are presented. In the last section of this chapter, a general discussion about polyolefin blends is given. The case of polyethylene/polypropylene blends is

presented with more details and the effect of adding a third component (ethylene-propylene copolymer) on the morphology, thermal and mechanical properties of the resulting blends is illustrated through various examples.

1. Preparation of polymer blend

Polyblends are prepared by mixing polymers. This blending process is performed at high temperature or with the help of diluents or suspending mediums. Melt mixing, solution mixing and latex mixing are the more widely used methods for preparing commercial blends. Chemical reactions occurring during mixing may lead to the formation of polymer-polymer covalent bonding with the polyblend. Depending on the chemical structure of the components used to prepare the blend as well as the desired properties for the final material, with proper control these reactions can be either avoided or limited to a low extent.

1.1. Melt Mixing.

The melt mixing method presents various advantages. It avoids the contamination of the blend by diluents and consequently the removal problems of the diluents. It assures a system that will not change in further molding operation. Because of the amount of heat necessary to maintain low viscosity and the shearing rates needed for thorough mixing, a degradation of either or both polymers can occur. Crosslinking, block and graft formation and chain-scission reactions can result because of the degradative conditions so that polyblends are often different from what might be expected. Melt mixing is used for systems in which degradation does not ordinarily occur.

1.2. Solution mixing

In a solution melting process, a diluent is added to lower the temperature and shear-force requirements for satisfactory mixing, without degradation. However, as the solvent is removed from a one-phase mixed polymer solution during the removal step, changes in the domain sizes of the blend may occur and in extreme cases it can result in complete polymer phase separation. This is because polymers exhibit different affinity for the solvent and the polymer with the lowest affinity will selectively precipitate. The resulting gradient will favour the macroscopic phase separation of the polymers as would be observed upon addition of a poor solvent.

1.3. Latex mixing

Latex mixing is one of the most important techniques for the preparation of commercial polyblends. In a latex, polymer are suspended as microspheres and the interactions between neighbouring microspheres are prevented by the suspending medium. Upon thorough blending, a mixture of two latexes made of a random suspension of dissimilar polymeric particles is obtained. Melt mixing is often employed for compounding and pelletizing the latex-blended materials, and necessary precaution in this stage must be taken to avoid degradation. Acrylonitrile-butadiene-styrene, for instances, are prepared by this pathway.

2. Miscibility versus immiscibility in polymer mixtures as a function of the chemical structure.

A major concern is the relationship between polymer structure and blend thermodynamics since this is a crucial parameter for the prediction and design of polymer blends with advanced properties. When looking at the chemical structure of poly(ethylene terephthalate) and poly(butylene terephthalate) or poly(styrene) and poly(phenylene oxide) it is quiet easily understandable that these two polymer systems will form homogeneous mixtures, independently on their macromolecular characteristics (**Figure 2.1**). Effectively, in the latter case the miscibility can be explained by the presence of aromatic rings in the chemical structure of both poly(styrene) and poly(phenylene oxide) backbones. The strong interactions between the conjugated moieties make these two polymers to like to associate with each others. But most of the time, polymers are not miscible so that the desired properties of the final materials are not easy to control. A way the make two polymers miscible is to use copolymers. Referring to the examples of miscible polymers mentioned above, poly(styrene) can not be mixed with many polymers and this limitation has been for example overcame by using copolymers made of styrene and (hexafluoro-2-hydroxyisopropyl)styrene.

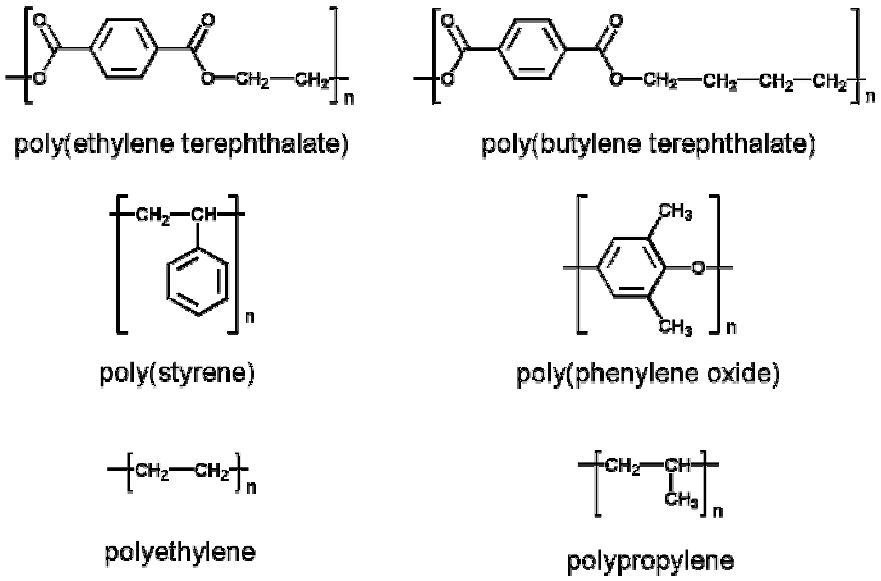

Figure 2.1 - Chemical structures of some polymers forming miscible or immiscible blends.

On the other hand, when considering the chemical structures of polyethylene and polypropylene it is not so evident why these two polymers do not mix. This finding seems inconsistent with the old "like dissolves like" rule that is one of the first principle taught in high school chemistry. Both polyethylene and polypropylene are highly non-polar hydrocarbon polymers. This non-miscibility between polyethylene and polypropylene is to be related to entropy of mixing.

3. Thermodynamics of miscibility.

The concept of miscibility is necessarily connected with the study of multi-component systems and the question of miscibility can be treated only in terms of thermodynamics. The basis of thermodynamics as taught in high school chemistry says that the necessary conditions for miscibility of a binary system at a defined composition are

$$\Delta G_m < 0 \qquad (2.1)$$

$$\left(\frac{\partial^2 \Delta G_m}{\partial \Phi_2^2}\right)_{T,P} > 0 \qquad (2.2)$$

Where ΔG_m represents the free energy of mixing per unit volume and Φ_2 is the volume fraction of the component 2. The value of ΔG_m is known to vary with the blend composition and three cases can be encountered (**Figure 2.2**).

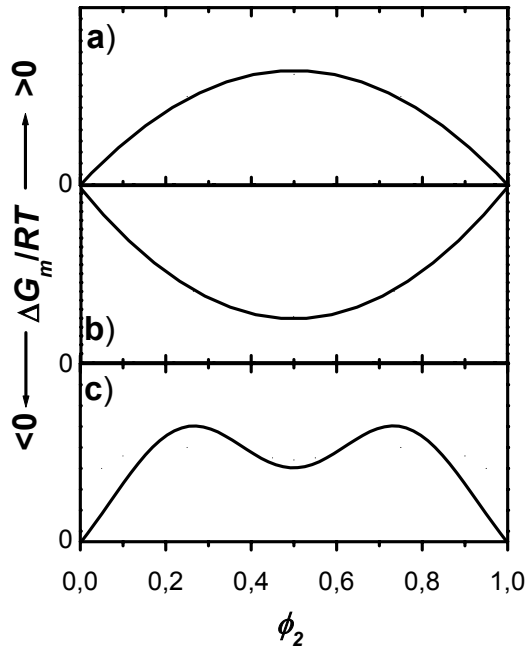

Figure 2.2 - Dependences of the free energy of mixing ΔG_m for binary systems which are a) completely immiscible, b) completely miscible and c) partially miscible.

The **part a** of **Figure 2.2** shows the case for a completely immiscible blend system, i.e. ΔG_m >0, over the entire composition range. The opposite behaviour is described by the curve in the **part b** of the **Figure 2.2** where ΔG_m *a*ssumes negative values at all compositions. The system representative of the curve c exhibits a miscibility gap for ~ 0.3<Φ_2<0.7 since in this composition range the miscibility conditions defined in equation (2) is not satisfied. This miscibility gap behaviour is rather general for polymer blends as will be discuss later which are only miscible when one of the polymers is used as a major component as schematically illustrated in **Figure 2.3**.

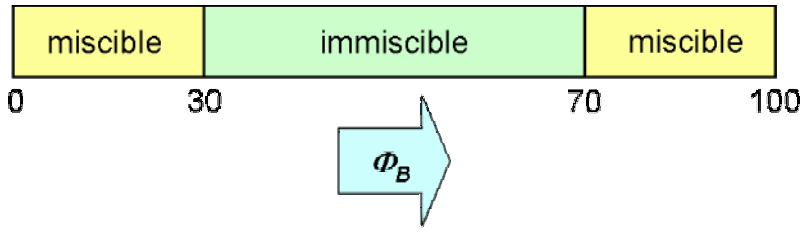

Figure 2.3 - Schematic representation of the composition-dependence miscibility of binary systems.

Another important parameter that has to be taken into account when dealing with miscibility problems is temperature. Returning to equation (2) it is seen that the value of the free energy of mixing as a function of composition is dependent on the temperature. The change in temperature may lead to a change in the shape of the curve presenting the variation of ΔG_m versus Φ_2. As extreme situations, liquid-liquid equilibrium phase boundaries can be observed as displayed in **Figure 2.4**. When the system remains completely miscible upon temperature variation, the free energy must behave as in **Figure 2.2b** (ΔG_m <0). In contrast, if for well defined temperature and composition ranges, coexistence of two phases is observed, the free energy of mixing will show a miscibility gap as in **Figure 2.2c**.

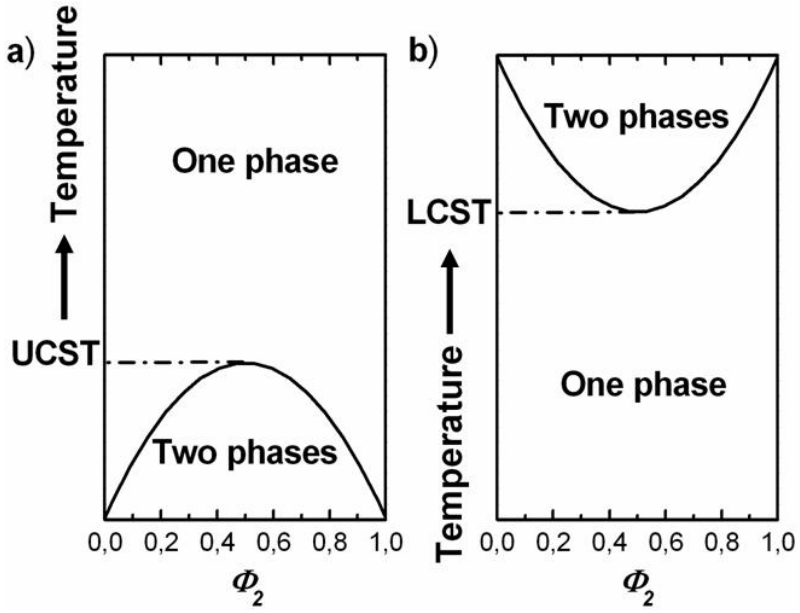

Figure 2.4 - Liquid-liquid phase behaviour for binary mixtures illustrating a) a system with an upper critical solution temperature (UCST) and b) a system with a lower critical solution temperature (LCST). The temperature increases from the In the diagrams

The free energy of mixing can be written as the sum of three contributions of enthalpic and entropic natures as :

$$\Delta G_m = \Delta H_m - T\Delta S_m^{(c)} - T\Delta S_m^{(e)} \qquad (2.3)$$

Where ΔH_m, $\Delta S_m^{(c)}$ and $\Delta S_m^{(e)}$ are the heat of mixing, combinatorial entropy of mixing and excess entropy of mixing, respectively. Possible behaviours for binary systems are presented in **Figure 2.4**. The magnitude of these parameters, as functions of the blend composition, will govern the miscible or immiscible nature of the blend. The

objective of the developed thermodynamic theory of mixing was to give some information about the both enthalpic and entropic terms in equation (3). Discussions about polymer miscibility usually start with the simplest statistical thermodynamics model of polymer blends developed initially by Flory and Huggins (FH theory).[10] In the Flory's book, *Principles of Polymer Chemistry*, the entropy of mixing, ΔS_m, is assumed to be purely combinatorial and is calculated by enumerating the number of arrangements of the molecules on a lattice. This result is expressed by the well know expression :

$$\Delta S_m^{(c)} = -R\left(\frac{\varphi_1}{V_1} ln\varphi_1 + \frac{\varphi_2}{V_2} ln\varphi_2\right) \qquad (2.4)$$

Where V_i that is the molar volume of species *i* is proportional to the molecular weight of *i*. A direct and obvious conclusion drawn from this expression about thermodynamics of polymer blends is that for high molecular weight compounds, the combinatorial entropy of mixing is small and very close to zero. As the combinatorial entropy of mixing is often the most important driving parameter for miscibility, it is clear that most of commercial polymers, having high molecular weight, are not miscible with each other. The major limitation of the Flory model, is that it does not take into account the change in volume occurring upon polymer blending as in many cases dilatation or contraction are observed. The entropy of a system is volume dependent and thus an additional entropic term has to be considered, namely the excess entropy of mixing. This latter parameter also accounts for other contributions.
The heat of mixing is given by a van Laar type equation as follows:

$$\Delta H_m = B\varphi_1\varphi_2 \qquad (2.5)$$

Where *B* is an empirical parameter that determines the sign and the magnitude of heat of mixing. B can be predicted through the Hildebrand solubility parameter theory.

$$B = (\delta_1 - \delta_2)^2 \qquad (2.6)$$

Where δ_i is the solubility parameter of each component.[11] It is related to the Flory–Huggins interaction parameter, χ_{12} which varies linearly with the inverse of the temperature so long as the interaction energy itself is temperature independent. The enthalpy of mixing can be simply describe as the van der Waals energy of contact, and the difference between like and unlike pairs is summarized into a single term χ_{12}. Expression (5) is by far too simple to account of real systems since i) it assumes a parabolic dependence of the heat of mixing versus composition, ii) it does not include

temperature dependence of the interaction between component, iii) it implies the treatment of the interaction parameter as a free energy quantity rather than as a term of purely enthalpic origin and iv) in most cases the magnitude of the interaction can not be evaluated on the basis of the developed models and χ_{12} must be deduced experimentally.

Thus, in general, ***complete miscibility in polymer-polymer systems results from an exothermic heat of mixing***, in other words, ***miscibility in polymer-polymer systems results from a negative interaction parameter***.

4. Theory of compatibilization

Beyond the economical aspects (lower prices, recycling…) that play a very predominant role in the choice of new strategies whatever the type of industry considered, the development of blending technology in the field of polymer science has been strongly motivated by the desire to produce new competitive materials with specific properties such as barrier, electric and mechanical properties. We will discuss mainly this latter aspect, since it has represented a central part of our focus while investigating polyolefinic blends. Usually the mechanical properties of the primarily mixed blends are poor. However, a lot of researchers from both academic and industrial origins have shown that these mechanical properties can be brought back to their original level and even greatly improved by adding a third component. This added component will form, through specific interactions with the blend making polymers a new phase, namely the interphase. This overall process is referred as compatibilization. It is of course, restricted to the cases of immiscible polymeric systems that may give a broad range of heterogeneous bulk morphologies, for instances droplets or fibers in a matrix, and stratified or cocontinuous structures (**Figure 2.5**). In peculiar cases ordered morphologies can be obtained.

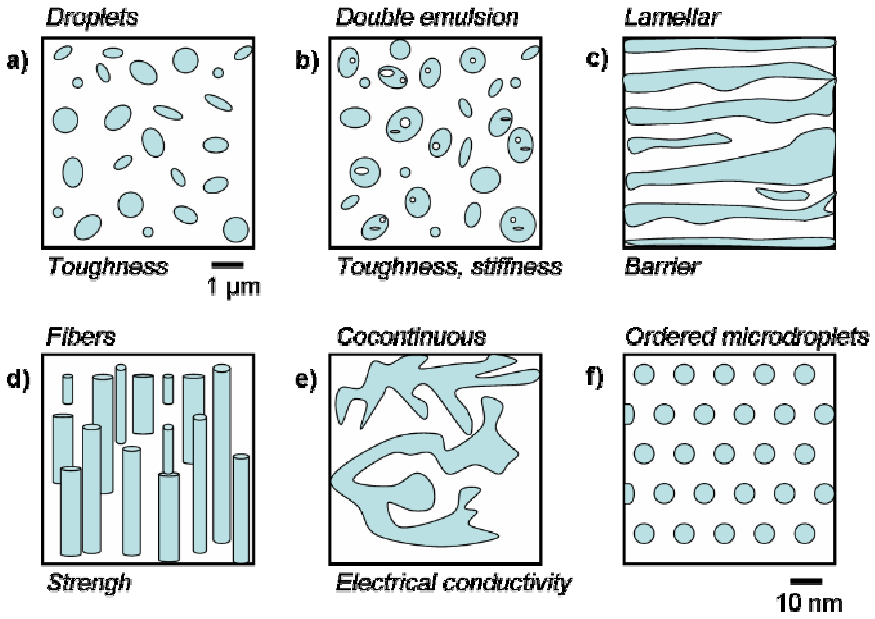

Figure 2.5 - Schematic representations of morphologies obtainable by polymer-polymer melt mixing. of binary polymer blends

The type of developed morphology depends on various parameters related to the processing conditions and blend composition. A well-known example of morphology transition in binary immiscible polymer blend A B from droplets-dispersed (B in A), through co-continuous to droplets-dispersed (A in B) versus the change in the relative volume fractions of polymers is illustrated in **Figure 2.6**. The left and right schemes represent the cases where one of the component is added in a large excess (polymer A and B in the left and right cases, respectively). It constitutes the matrix of the morphology in which the minor component is dispersed under the shape of nearly spherical droplets. The intermediate regime, the co-continuous morphology results from coalescence of the growing dispersed droplets upon increasing the relative amount of the minor component.

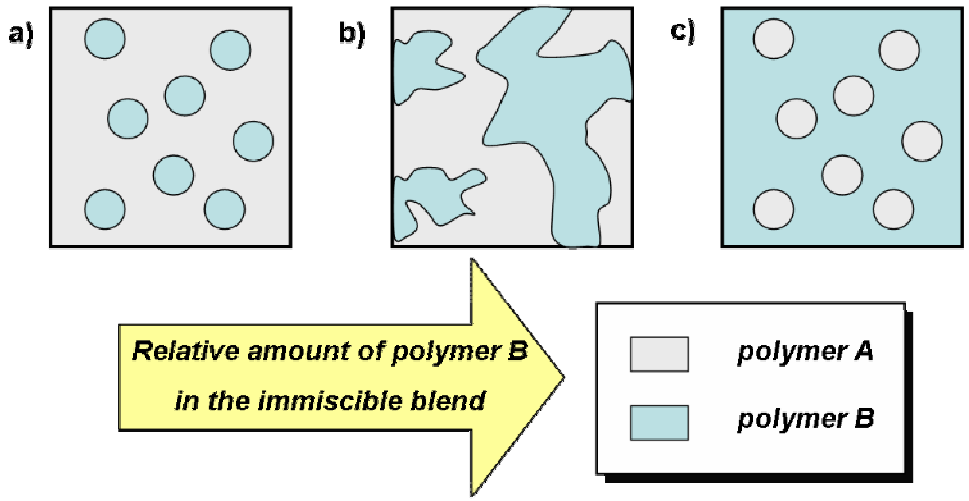

Figure 2.6 - Schematic representations of biphasic morphologies developed in immiscible binary blend depending on the blend composition.

The 1 dimension composition profile (as a function of *l*) for biphasic polymer blend is shown in the bottom part of **Figure 2.7**. Going through the bulk material and starting from the matrix phase, one meets a phase domain of intermediate composition between the pure phase before to enter the dispersed phase B. This intermediate domain is called the interfacial layer and exhibits a thickness Δl that can be as large as few nanometers. It constitutes a real interphase, i.e. a third phase within the bulk material having its own properties.[12] If the basic thermodynamics concepts presented in the former paragraph determines the conditions of phase separation they do not permit to predict neither the size of the dispersed domains, nor the composition of the interphase usually expressed by the concentration gradient$\left(\frac{\partial \Phi}{\partial l}\right)$. The interphase consists of an interdiffusion zone of the two types of macromolecules making the matrix and dispersed phases. The thickness of the interphase domain depends on the thermodynamic interactions, macromolecular size segment and concentration of the compatibilizer.

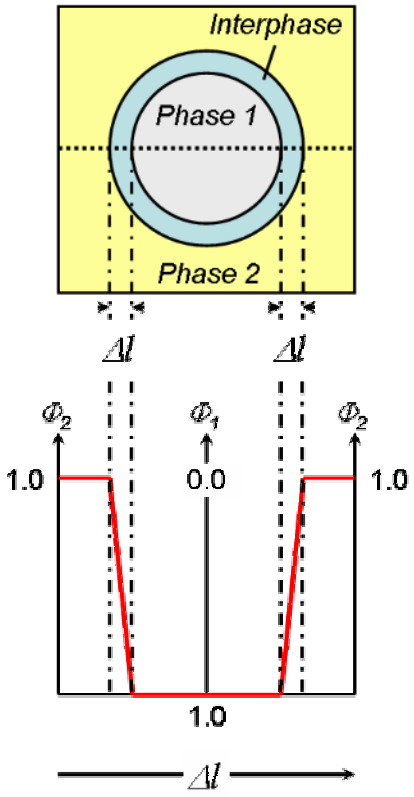

Figure 2.7 - Schematic representations of (top) a phase dispersed morphology showing the existence of an intermediate phase (interphase) between the matrix (phase 2) and the dispersed (phase 1) phases and (bottom) concentration profile as observed along the horizontal dotted line.

5. Compatibilization methods

From a practical viewpoint to produce heterogeneous systems is very advantageous; the dispersed phase may improve the toughness of brittle polymers, provide reinforcing properties. However, to produce manufactured articles with reproducible and stable properties is a prerequisite before to envision any commercial application. In short, the aim of compatibilization is to obtain materials behaving in a way similar as homopolymers.

5.1. Physical compatibilization

In physical blending the compatibilizing agent is chemically synthesized prior to the blending operation, and subsequently added to the blend components as a non-reactive component.

The basic concepts that classic colloid science[13] teaches about mixtures of oil and water can be easily transposed to the case of dispersing one polymer in another.

Addition of surfactant molecules which migrate to the oil-water interface lowers the interfacial tension and improves the stability of the dispersion, or emulsion. Block and graft copolymers, which self-assemble into microdomains because of the immiscibility of the different segments, are the polymeric equivalents of surfactants. If properly chosen, they can migrate to the interface in a blend of two immiscible polymers as shown in **part a** of **Figure 2.8**.

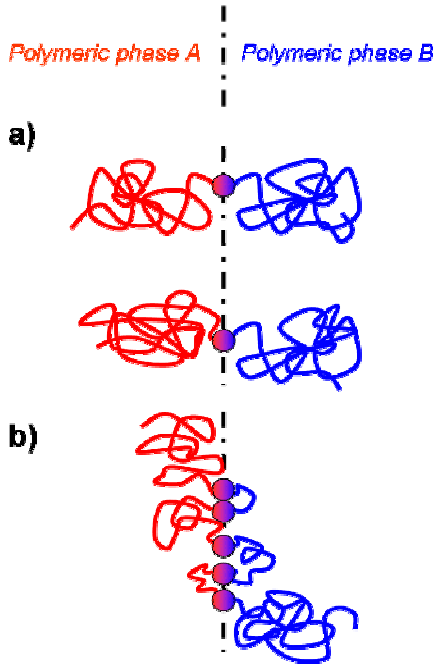

Figure 2.8 - Schematic illustrations of how a) block and b) random (with rather long homogeneous sequences) copolymers locate at the interface between immiscible polymeric phases A and B.

To design such interphase morphology, the copolymer segments must be chemically identical or at least miscible with the macromolecules making the phases A and B on either side of the interface.[14] Just as surfactants do, such copolymers can reduce the interfacial tension which makes break-up easier. It follows that addition of copolymer compatibilizers may lead to a great reduction of the size of the dispersed phase domains by slightly reducing the resistance to break-up while strongly decreasing the probability of coalescence. In the case of an uncompatibilized blend, the size of the dispersed phase depends on the blend composition; it increases with the volume fraction of the dispersed phase.[15] Compatibilization can reduce particle size for all volume fraction but especially at

higher values because of the increased stability against coalescence. Unlike surfactants at oil-water interfaces, block and graft copolymers can provide tremendous increases in the interfacial strength in the solid state owing to the chemical bonds traversing the interface. The extent of improvement in interfacial strength or toughness is a strong function of the number of chains traversing a unit area of the interface.[16] The efficiency of block copolymer in decreasing the interfacial tension is enhanced when high molecular weight materials are used. Because the individual segments in block or graft copolymers are joined by valence bonds and because these segments can extend themselves into similar or the same type homopolymers, a strong bond between free polymer and block or graft copolymer interface is formed. Block and graft copolymers, therefore, are used almost exclusively in blends that require strong interaction adhesion. It is important, for example, in acrylonitrile-butadiene-styrene resins to have a strong bond between rubber particle and the plastic phase. Because of this block copolymer are preferred for making ABS materials. The maximum efficiency is reached near the critical-micelle-concentration (CMC), at which the interface is saturated by copolymer macromolecules. Further addition of block copolymer will not permit to modify the nature of the interphase and micelle will be formed within the homopolymer phases. The use of random copolymer as compatibilizer has been much less illustrated but some examples of using ethylene-co-propylene polymer to compatibilize polyolefine blends are presented later on in this chapter.

5.2. Chemical compatibilization

In chemical compatibilzation process, also referred as reactive blending, the compatibilization of immiscible polymers is ensured by a chemical reaction achieved during the melt-mixing process. Similarly to physical compatibilization, the *in situ* synthesized compatibilizer reduces the interfacial tension between the immiscible phases, improves the adhesion between the components, so that materials with new mechanical properties are obtained.[17]

For reactive compatibilization to be proceeded, both types of macromolecules forming the biphasic system should carry functional groups that may, when meet together on the interface, give rise to the formation of covalent link. Depending on the specific location of the reactive groups along the macromolecules various types of

topology can be formed (see **Figure 2.9**, where A and B represent the functional groups).

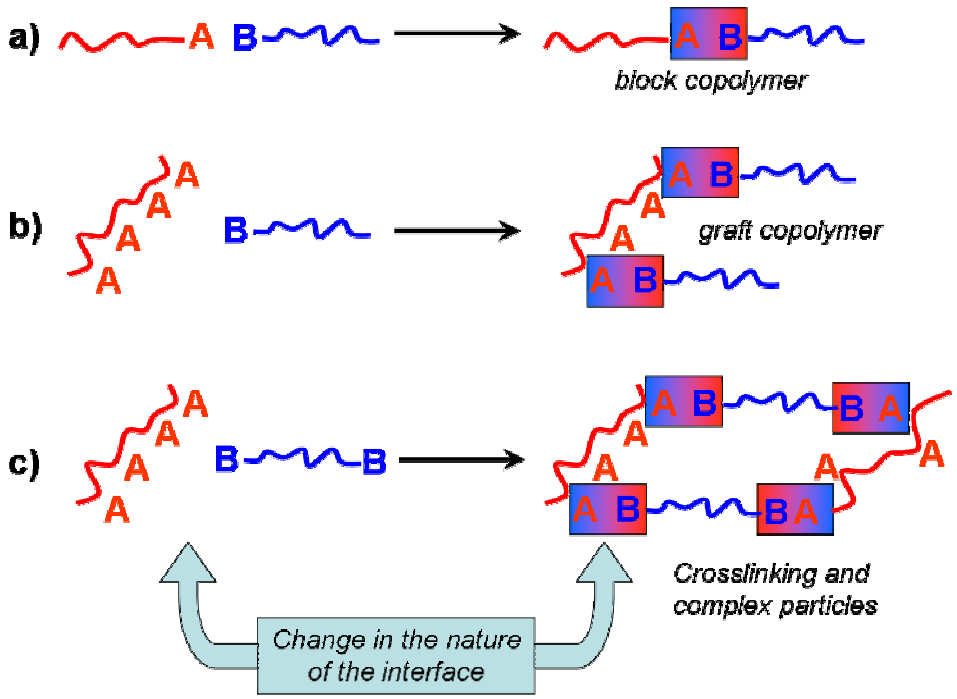

Figure 2.9 - Schematic representations of various reaction topologies possible in chemical compatibilization

A broad diversity of functional groups has been used to performed *in situ* chemical compatibilization depending on the nature of the polymeric phases and the chemistry by which they were produced. Reactive compatibilization of polyamides generally relies on the reactivity of the amino groups located at the chain ends towards carboxyl groups [18] or anhydrides. [19] This latter reactive scheme was notably applied for the improvement of toughness of engineering thermoplastic like nylon 6 upon addition of rubbery materials. When the rubbery materials include a chemically modified rubber fraction (maleic anhydride grafted ethylene-propylene copolymer and maleated styrene-butadiene-styrene, with hydrogenated midblock) compatibilization effect was observed as expressed by the decrease of the size of the rubber particles.[20] Functionality within the polymer chains is usually incorporated through copolymerization or grafting.[21]

Another important issue is the “topology” of the reaction possibilities. The reaction in **part (a)** of **Figure 2.9** leads to a block copolymer which is an efficient compatibilizer. However, it requires the prior synthesis of polymer chains bearing

functional groups on only one end of polymer chains that may be difficult to achieve. A more common situation is shown in **part (b)** of **Figure 2.9**. Here, there is only one reactive group B per chain; however, there may be multiple A groups on the other functional polymer. This leads to a graft topology. Finally, we may consider the case shown in **part (c)** of **Figure 2.9**. In addition to multiple A units on the chains in the phase on the left, some of the chains in the phase on the right contain two or more B groups. This leads to a cross-linked morphology.

6. Evaluation of Polymer/Polymer miscibility

As discussed in the above paragraph, thermodynamically speaking, the term miscible should be assigned to systems showing homogeneity down to the molecular level. However, in a more pragmatic sense, a system can be designed as miscible when it appears homogeneous in the type of testing method apply to investigate any kind of bulk properties. Taking account this principle, a new definition in terms of degree of dispersion has been admitted for miscibility. This definition is not very objective and this is why many contradictory reports dealing with miscibility of given polymeric pairs can be found in the literature. One may differentiate between three types of methods often used to examine the miscible character of polyblends; **Phase equilibria methods,** measurement of the interaction parameter χ_{ij} and indirect testing of the miscibility. The choice of the employed method can be guided according to the nature, amorphous versus semi-crystalline, of the polymeric components, and thus the properties examined. Although an exhaustive discussion about these three methods is by far beyond the objective of this part, some few examples of experimental, some of them were used during the experiment investigation of this thesis, will be shortly presented in the next lines.

6.1. Phase equilibria methods:

Due to the reasons mentioned above, i.e. combinatorial entropy of mixing is nearly negligible and the free volume contribution increases the free energy of mixing, the miscibility is strongly related to either specific interactions or intramolecular repulsions. As examples, hydrogen bonding, dipolar interactions, phenyl group coupling, lewis acid base interactions may act as driving interactions to compatibilize complex polymeric mixtures. Phase equilibria of a given binary polymer blend can be determined by various techniques. Turbidity measurement is the oldest

method used to determine the phase relationship in complex mixtures. It was applied to study liquid/liquid or liquid/solid phase transitions in polymer solutions [22] as well as in film forming systems. [23] Extension of the turbidity method, has led to the application of light scattering methods to the study of the dynamics of phase separation process. [24] Other radiation sources, such as X-rays and neutrons, have been applied to study density fluctuations in the sub-micrometer size scale. [25]

6.2. Methods based on the determination of polymer$_i$/polymer$_j$ interaction parameter χ_{ij}

The interaction parameter χ_{ij} of a *ij* polymeric pair can be investigated through the determination of various experimentally accessible parameters. The melting point depression as observed for a semi-crystalline polymer *j* upon addition of a diluent acting component *i*, i.e. *i* is an amorphous polymer, has often been considered as an evidence of miscibility according to [26]

$$\frac{1}{T_m} - \frac{1}{T_m^{\,0}} = -\frac{RV_{ju}}{\Delta H_{ju} V_{iu}} \chi_{ij} \left(1 - V_j\right)^2 \qquad (2.7)$$

Where T_m and $T_m^{\,0}$ are the meting and equilibrium melting temperatures, respectively, ΔH_u is the enthalpy of fusion per repeat unit, V_u is the molar volume of the repeating unit, and *V* represents the volume fraction of a polymeric component. Many reports using the Nishi et Wang expression (equation 2.7) can be found in the literature.[27] Although the measurement of melting temperature is very easy in practise, to measure it in conditions allowing to determine χ_{ij} might be more complicated, so that care should be taken for the interpretation of the experimental results. It is worth recalling here that χ_{ij} or *B* (eq 5 and 6) are functions of the independent variables *T*, *P* and Φ. The interaction parameter of polymer mixtures can also be determined through *PVT* measurements.[28]

6.3. Methods based on an indirect evaluation of the miscibility.

Here, we present briefly methods which do not provide information about the binodal/spinodal composition relationship and do not require numerical calculation of the interaction parameter. Undoubtedly, the most widely used thermal characteristic in determination of polymer/polymer miscibility if the glass transition temperature, T_g.

Theoretically, when two polymers are ‘‘totally’’ miscible, the T_g of the blend can be estimated empirically from the individual components T_g and their weight percentage in the blend, applying different theories, such as the Fox equation as follows:[29]

$$\frac{1}{T_g} = \frac{w_i}{T_{g_i}} + \frac{w_j}{T_{g_j}} \qquad (2.8)$$

where w_i and w_j are the weight percentages of polymers 1 and 2, respectively; and $T_{g(i,j)}$ the glass transition temperatures of each pure component. T_g stands for the glass transition of the blend. However, the glass transition is related to a variation of the density fluctuation leading to a discontinuous jump in the first derivatives $\left(\frac{dX}{dT}\right)$ and $\left(\frac{dX}{dp}\right)$ of any thermodynamic quantity relative to temperature or pressure. The thermodynamic quantity X can be either G, S or H (V). T_g can be determined by physical methods; dilatometry, calorimetry,[30] rheology. Thermodynamically speaking, the recording of a single glass transition for a binary polymer blend is not a measure of miscibility. Effectivelly, in polymeric materials, T_g is a cooperative segmental motion. This means that at the T_g about 50 to 100 atoms constitutive of the polymeric backbone may be involved. This chain portion represents an approximate domain size of about 2 to 3 nanometer in diameter. Thus, detection of a single T_g in a two-component system only evidences a state of dispersion. [31] In the field of polymer blends, initial application of microscopic techniques has been mainly directed to the study of the developed morphological forms. However, due to its simplicity, speed and range of accessible magnification allowing to investigate morphological elements with dimensions typical of polyblends, scanning electron microscopy has been largely used to study miscibility. It was shown that in the cases of two phases blend morphology, the size of the dispersed phases is greatly reduced upon limited addition of a third component. This change in the state of dispersion can be considered as an evidence of enhanced interaction between the two blend components. The Last category of techniques that we may mention are the spectroscopic ones such as infrared spectroscopy (see for example the study of interaction in polymer blends through hydrogen bond[32]), nuclear magnetic resonance and dynamic mechanical

analysis (see for example the study of the glass transition temperature-related variations in molecular mobility[33]).

7. Discussion about selected studies on poly(ethylene)/poly(propylene) blends

The objective of this paragraph is not to give an exhaustive review on poly(propylene)/poly(ethylene)-based blends but to illustrate clearly some of the effects and related references that will allow us a better understanding of our experimental results. Here, we will present the main motivation for mixing either poly(ethylene) or poly(propylene), we will report on the miscibility conditions for PE/PP blends depending on the blend composition, macromolecular parameters of the homopolymers. Thus, the discussion is structured around effect of compatibilizer on thermal properties, morphologies and mechanical properties of the resulting blend.

For the majority of the reports on blending polymers the main motivation was to obtain a combination of properties of the mixed polymers. Various changes in the physical properties of parent polymeric materials have been observed upon mixing. Depending on the fine structure of the macromolecular chains, polymers may exist either as amorphous or semicrystalline polymeric substances. Namely, a semicrystalline polymer has an amorphous and a crystalline part. The latter one has a more or less ordered structure in which the polymer chains are often folded in a random way. Amorphous macromolecules are either very brittle (polystyrene) or very tough (polycarbonate). Mechanical properties of semicrystalline polymers are strongly controlled by the crystal entities which usually enhance the stiffness of the sample (for example in poly(propylene)). Moreover, due to their biphasic structure, mechanical properties of semicrystalline materials are hardly predictable. Effectively parameters such as degree of crystallinity, size and size distribution of crystallites are essential in determining the response of the materials under external loading. Thus theoretical as well as practical investigations of crystallization behaviour and morphology are important in particular the non isothermal crystallization process from the melt that is of increasing technological importance, since very close to the actually employed industrial conditions. Addition of small amounts of one polymer to another may lead to a better structural homogeneity and enhancement of the strength.[34] The polymer added in low amount plays the role of a damper in

redistribution of the internal stress or fills the defects of the solid state microstructure of the polymer.

Among polyolefin polymers, polypropylene is one of the most widely used although its practical application has been restricted in a number of cases due to its low fracture toughness at low temperature and high notch sensitivity at ambient temperature. To overcome these poor properties, incorporation of dispersed elastomeric phases has been successfully tested.[35] At first thinking, a straightforward pathway to modify properties of polypropylene was to copolymerize propylene with ethylene.[36] Propylene-based elastomeric materials are produced by incorporating individual ethylene units, through copolymerization within propylene polymer chain. This incorporation hinders the crystallization ability of propylene sequences and thus decreases the overall crystallinity of the macromolecules. This is accompanied by a decrease in the rigidity and melting point of poly(propylene). The mixing of propylene and elastomeric material in appropriate amounts permits to double the impact strength of PP while maintaining the tensile strength to a level similar as the one of pure PP.[37] Influence of rubbery polymers on crystallization behaviour, morphology and mechanical properties of polypropylene has been well documented.[38]

Probably because of the small technological need to toughen polyethylene matrices, mixtures of ethylene-co-propylene polymers and polyethylene have received less attention. Greco et al have studied the effect of the composition and structure of the ethylene-co-propylene polymer on the structure, morphology and mechanical properties of blends prepared from high-density polyethylene.[39] The main results of this study were (i) the copolymer exhibits a nucleating effect, (ii) the compatibility between the copolymer and the polyethylene matrix increases as the ethylene content in the copolymer increases, (iii) the crystallinity is lowered upon blending, (iv) mechanical properties of the blends are decreased when copolymers of low ethylene content are used and (v) less the blend is compatible better are the impact properties. Nearly similar behaviour was observed when studying isotactic polypropylene/ethylene-propylene copolymer blends.[40]

For simplicity purpose original studies on semicrystalline/semicrystalline pairs have been largely directed toward investigation of pair-like polymeric blends, where the effect of unlike intermolecular interactions is avoided. Blends made of high-density polyethylene (HDPE) and low-density polyethylene (LDPE) have thus been considered as “ideal model systems”.[41] Poly(ethylene) and poly(propylene) have

been mixed in various proportions and the phase behaviour of the resulting blends has been largely discussed. Miscibility or immiscibility has been assessed on the basis of experimental observation by means of microscopic or scattering techniques. However these experimental results have brought many debates. For instance, blends of poly(propylene) and high-density poly(ethylene), i.e. linear poly(ethylene), have been observed to phase segregate by many authors,[42] although it was reported that HDPE may penetrate the PP phase at low HDPE contents as deduced from the delayed nucleation and crystallization of the PP phase.[43] Many studies dealing with polyethylene/polypropylene blends have been published in which poly(ethylene) served as matrix similarly to the systems studied in this thesis (PE/PP 80/20). Shanks at al. have discussed in details the effect of thermal history on morphology and mechanical properties of polypropylene/polyethylene 20/80 blends, including high density polyethylene, low density polyethylene, linear low density polyethylene and very low density polyethylene.[44] The thermal treatment was performed in a temperature range between the crystallization temperatures of PP and PE to allow PP to crystallize first from the blend. From the results obtained by complementary experimental techniques such as DSC, POM, SEM and tensile testing the authors could correlate the crystallinity and morphology of the PP dispersed phase to the mechanical behaviour. In all cases, the thermally treated samples exhibited larger crystallinity and correspondingly improved tensile properties. For instance, in the case of linear low density polyethylene/polypropylene blends, the PP diffuse spherulitic morphology embedded within a PE matrix was assumed to increase the interfacial adhesion between the phases and thus to improve the tensile properties.

Unfortunately for many combinations of polymers, the mechanical properties of blends are usually worse than the ones of the parent components instead of better. The dispersion of a phase within another one usually generates stress concentration and weak interfaces due to a poor mechanical coupling between the chemically different phases. The strong influence of the macromolecular architecture of the copolymer that is the topology, the composition and the distribution of the comonomer units along the backbone has been clearly evidenced. Ethylene-co-propylene polymers of various compositions were used as compatibiliser for polypropylene/low-density polyethylene blends.[45] For high-density poly(ethylene)/poly(propylene) systems, a linear relationship between tensile strength and composition is obtained if 5% of EPR is added.

Numerous other semicrystalline polymeric pairs have been investigated among which poly(ethylene terephthalate)/poly(butylene terephthalate)[46] (PET/PBT), poly(butylene terephthalate/polyarylates[47] (PBT/PAr), (PC/PCL), poly(vinylidene fluoride)/poly(butylene adipate)[48] (PVDF/PBA), poly(3-hydroxybutyrate)/poly(ethylene oxide)[49] (PHB/PEO) may be mentioned. At last, it should be mentioned that the literature is rich of examples where blends made of the same types of polymers show different mechanical behaviour. This is not very surprising in the light of the strong dependence of the mechanical characteristics on changes in the preparation method, temperature, composition and related morphology of the blend, etc.

8. Bulk characterization of ethylene-co-propylene polymers

Ethylene-co-propylene polymers (EPR) were added as compatibilizater to the bulk low density poly(ethylene)/isotactic poly(propylene) (LDPE/iPP) blend of composition 80/20 (w/w) in the weight fraction range up to 15%. EPR copolymers differ in chemical composition, rheological behaviour and chain microstructure that are key parameters controlling their ability to compatibilize immiscible PE/PP blends.

8.1. Infra-Red spectroscopy

Chemical and physical characteristics of the three random ethylene/propylene copolymers Keltan740, Keltan13 and Dutral054 are presented in **Table 2.1**. The thermal behaviour of the three EPRs was initially investigated by means of DSC (not shown here). Crystallization and melting processes were not detected in the temperature range characteristic for the parent components but the rubbery behaviour of EPR was evidenced by the glass transitions detected in all cases at temperatures comprised between -66 and -59 °C that is between the typical glass transition temperatures of the PE (-100°C) and PP (-10°C) homopolymers. These findings indicate that all three copolymers are amorphous in nature due mainly to their random nature. Keltan740 has the highest ethylene content (65%) while Keltan13 (55%) and Dutral054 (54%) exhibit a nearly similar chemical composition.

Table 2.1 - Chemical and physical characteristics of ethylene-propylene copolymers

EPR	Ethylene (wt.-%)	Insoluble gel fraction (wt.-%)	Viscosity at T=125°C by Mooney	Mw Kg/mole	Tg by DSC (°C)	Tg by DMA (°C)
Keltan-13	55	6	29	100	-66	-64
Keltan-740	64	20	63	200	-56	-53
Dutral-054	54	13	46	160	-59	-58

However, synthesis processes based on different catalytic systems may lead to polymeric materials with different chemical composition and different chain microstructure such as the branching ratio, degree of polymerisation and distribution of comonomers along the macromolecule.[50,51] The chain microstructure of copolymers can differ from a tendency to form short versus long monomer sequences and can be evaluated by means of IR-spectroscopy.[52,53] Exact correlation between IR-spectroscopy data and chemical composition is very complex making difficult truly quantitative analysis of ethylene propylene rubber composition as well as identification of monomer sequences.[54,55] Absorption bands of polymeric systems can be divided into three groups; (1) oscillation of functional groups, (2) oscillation of backbone and (3) bands related to crystalline structure. The local structural details of the three EPR macromolecules have been estimated using the integrated intensities of the absorption bands characteristic of the second group observed in the IR spectra. Regular ethylene chains are characterised by peaks at positions 722, 733, 753 and 812 cm^{-1} corresponding to methylene $(-CH_2-)_n$ sequences with a number of units $n \geq 5$, n=3, n=2 and n=1, respectively. In the case of propylene segments $(-CH_2-CH-(CH)_3-)_m$ the detection of bands at positions 936, 973 and 1155 cm^{-1} is indicative of sequences consisting of a number of units m=1, $m \geq 4$ and $m \geq 10$, respectively. To exclude the effect of the film thickness, optical densities of characteristic bands were normalized to the reference peak at 1470 cm^{-1}. As can be seen from Diagrams presented in **Figure 2.10**, with increasing content of ethylene units in EPR, the relative absorbance at 722 cm^{-1} is larger so that the existence of long methylene blocks is evident. From this, we assume that general regularity of the ethylene component in Keltan740 is greater than for Dutral054 and Keltan13. As the ethylene comonomer increases, the amount of propylene $(-CH_2-CH-(CH)_3-)_4$ blocks decreases.

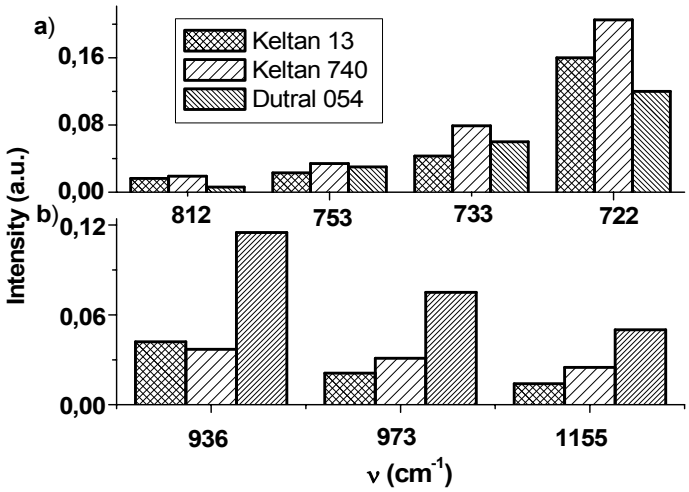

Figure 2.10 - Diagrams showing the relative intensities of absorbance IR bands characteristic for a) ethylene and b) propylene units within EPR macromolecules.

According to the data on the equilibrium swelling in toluene, EPR copolymers form different physical network (**Table 2.1**). Keltan740 is characterized by the largest insoluble volume fraction in toluene as expected for ethylene rich and high molecular weight copolymer. We assumed that Keltan740 has a dense structure made of larger domains that are not crystalline but packed more closely leading to more ordered and dense network.

Keltan13 and Dutral054 have similar chemical composition; however the difference in the amount of insoluble gel-fraction in toluene at room temperature suggests a different microstructure. In the case of Dutral054, the insoluble fraction was still observed at a temperature of 110°C suggesting that long propylene sequences are present (PP T_m=160°C).

8.2. Dynamic mechanical analysis

Differences in molecular mobility within EPR materials were evaluated by means of dynamic mechanical measurements. **Figure 2.11** shows the temperature dependences of the storage (*G'*) and loss (*G''*) shear moduli measured at constant deformation frequency (1Hz) on heating with a temperature rate of 2°C.min^{-1}. Both copolymers exhibit similar features in their dynamic mechanical properties and the different regions characteristic for the viscoelastic behaviour of amorphous polymers can be distinguished. In the low temperature regime, EPR exhibit moduli with typical glassy-state values. The second region corresponds to the interval of temperature

where an abrupt decrease in shear moduli is observed. In the third region, namely the rubbery-plateau zone, the modulus remains nearly constant for Keltan13 while variation with much lower slope is observed for Dutral054 and Keltan740. In the terminal zone, the polymeric material remain rubbery but with a pronounced flow component. Although an exact discussion on the molecular origin of the EPR dynamics is beyond the scope of this work we may notice that the occurrence of the rubbery-plateau zone may be attributed to mechanical entanglement between long enough macromolecules and from a dynamics aspects, it reflects the slower cooperative motion of macromolecular fragments between the non permanent cross linking. The width of the plateau may be as a first approximation related to the nature and spacing of the entanglements along the chain. In **Figure 2.11**, it is seen that the width of the rubbery plateau is increased from Keltan13, through Dutral054 and to Keltan740 mainly because the temperature at which the crossover between *G'* and *G''* occurs for these copolymers increased from 100°C through 150°C and to 200°C, respectively. The well-pronounced transition zone in the temperature range between -70 and 0°C is assigned to the glass-rubber relaxation also referred as the α- or segmental-relaxation. It indicates that segments of the polymer chain or side chains undergo short-range diffusional motion. Correspondingly to this transition from glassy state toward rubbery state as observed from the logarithmic plots of the moduli, the temperature dependences of the loss tangent (tan δ) show a broad peak in the same temperature range. For the experimental conditions we used, the maximum in the tan δ can be associated with *Tg* and the obtained values are in good agreement with data obtained by DSC analysis (**Table 2.1**). This good concordance is also illustrated in **Figure 2.12** where both temperature dependences of the heat flow and mechanical loss factor are shown for the case of LDPE/iPP/Keltan740-*15* as a representative example.

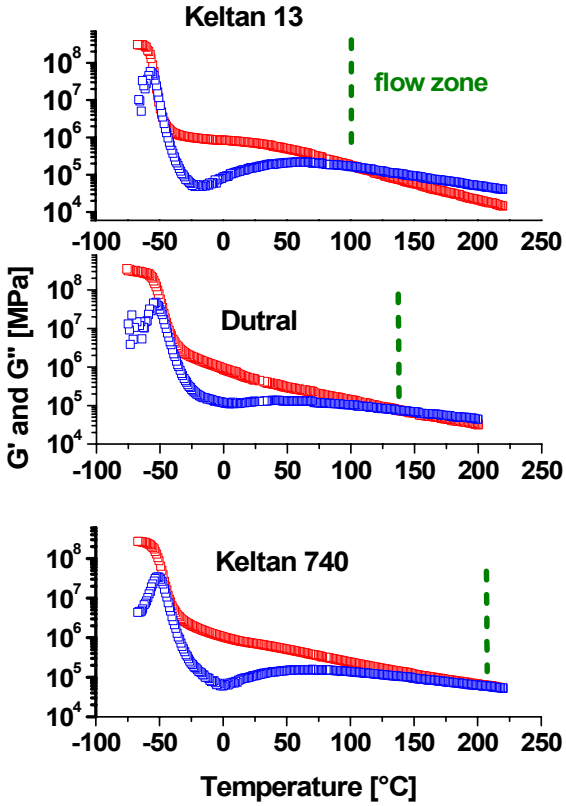

Figure 2.11 - Temperature dependencies of the storage (*G´*) and loss (*G´´*) shear moduli as measured for the three EPR copolymers; Keltan13, Dutral054 and Keltan740 upon cooling from the melt with the temperature rate of 2°C.min^{-1}

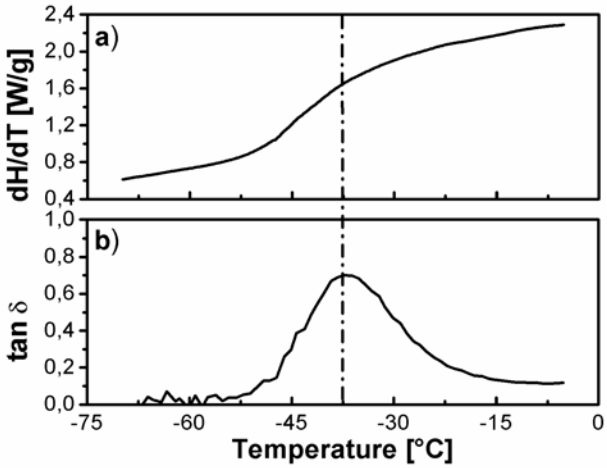

Figure 2.12 - Temperature dependences of a) the heat flow recorded during heating with the rate 10°C/min and b) the mechanical loss factor (tan δ) recorded during heating with the rate 2°C/min showing the rubbery character of the ethylene-propylene copolymer Keltan740.

The flow region is strongly depending on the spacing between entanglements together with the molecular weight and molecular weight distribution. The specific flow behaviour observed for EPR, where *G'* is not observed to vanish, was in good agreement with the data viscosity (Mw~η). In **Figure 2.13** the plots of log $|\eta^*|$ versus log *w* are presented for the three EPR at room temperature (i.e. 80°C above *Tg*) where η^* is the complex viscosity defined as $|\eta^*| = \left[\left(\frac{G'}{w}\right)^2 + \left(\frac{G''}{w}\right)^2\right]^{\frac{1}{2}}$ All three copolymers exhibit lower complex viscosity at high angular frequencies. For Keltan13 deviation from newtonian-like flow behaviour is observed only at high frequency, while for Dutral054 and Ketan740 pseudo-plastic behaviour is observed over nearly the entire range of angular frequencies tested. In the high frequency regime, the values of η^* increase of nearly one order of magnitude from Keltan13 (~10^8) through Dutral054 (~10^9) to Keltan740 (~10^{10}), reflecting an increase of molecular weight. This finding is in agreement with the molecular weight values of 100 000, 160 000 and 200 000 g.mol^{-1} given by the supplier for Keltan13, Dutral054 and Keltan740, respectively.

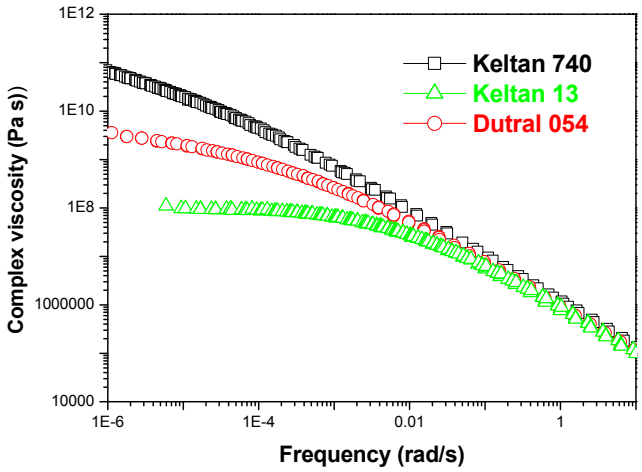

Figure 2.13 - Frequency dependences of the complex viscosity measured for the three EPR copolymers; Keltan13, Dutral054 and Keltan740 at room temperature.

9. Structure and properties of LDPE/iPP/EPR ternary blends

The blend investigated here is a low density polyethylene/isotactic polypropylene 80/20 (w/w). The choice of this blend composition has been motivated by the following reason. The chemical resistance of binary blends of LDPE-PP and of the parent homopolymers has been analyzed under the effect of aggressive

reagent such as ozone (O_3). It is known that polyolefins react with O_3 through the mechanism of radical oxidation reaction[56,57]. In the presence O_3 peroxyl radicals are formed in both polyethylene and polypropylene. The peroxyl radicals may evaluate towards hydroperoxide and subsequently react to produce alkoxyl and hydroxyl radicals or peroxyl groups. Analysis of the degree of oxidation in blends was performed by means of IR-spectroscopy. The level of oxidation was determined from absorbance ratio of the two characteristic bands located at 1720cm^{-1} which is a characteristic of the carbonyl groups (resulting from reaction of ozone with polyolefin chain[58]) with respect to common band of polyethylene and polypropylene for methylene groups (–CH_2–) situated at 1460 cm^{-1}. An example of such measurement is presented in Figure as a function of the composition of LDPE/iPP.

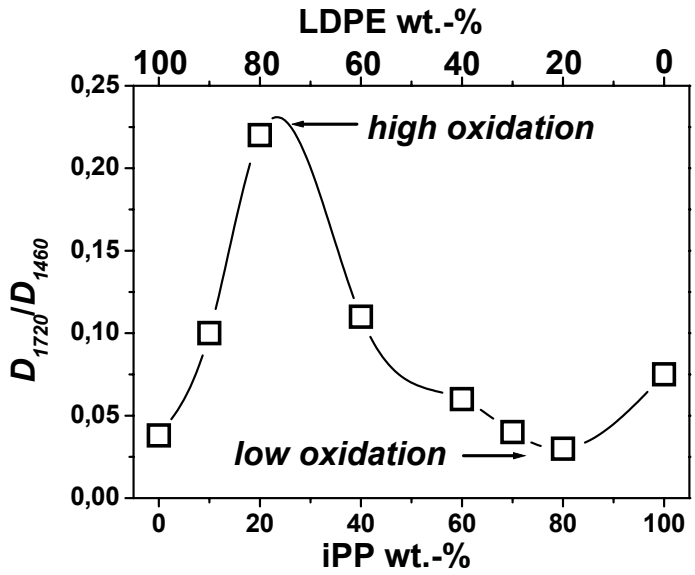

Figure 2.14 - Example of oxidation sensitivity of low-density polyethylene/isotactic polypropylene (LDPE/iPP) blends of various compositions as estimated from infra-red spectroscopy measurements.

The blend with the composition LDPE/PP 80/20 (w/w) exhibits the strongest oxidation in comparison to homopolymers and other blend compositions. As seen in the **Figure 2.14** the degree of oxidation does not follow rule of additivity relatively to the composition. A small addition of LDPE to a matrix of PP makes the system more stable and resistant toward ozone attack. This is due to the fact that LDPE and PP are immiscible giving rise to phase separation. Consequently a third phase, i.e. *interfacial layer,* is formed between the two components. This third phase plays a significant role in the control of properties in the bulk. In contrast, the blend with the

composition LDPE/iPP 80/20 has poor properties compared to the original components and blends where the LDPE is the minor component. This is primarily due to the lack of stress transfer across the sharp interface. This incompatibility and the resulting sharp interface may be improved upon addition of a third component. One of the most efficient methods is based on the insertion of a ethylene-propylene copolymer that will reside at the interface. In the case of a phase separated blend, the copolymer acts as a coupling agent between the two phases, leading to improved morphology, as express in terms of finer dispersion, mechanical properties, and interfacial adhesion in the blend. In our study we were concerned on testing the ability of three different ethylene-co-propylene polymers to modify the nature of the interfacial layer in blend made of 80% of LDPE and 20% iPP. In the text, ternary blends are referred to as LDPE/iPP/compatibilizer-x, where x is the compatibilizer content (5, 10 or 15%).

9.1. Differential scanning calorimetry and polarized optical microscopy.

The typical semicrystalline phase behaviors of LDPE and iPP are presented **Figure 2.15**. Semi-crystalline polymers do not have sharp melting transition. The small or imperfect crystallites melt at a temperature below the transition peak temperature.

It is usually admitted that for polymers with a broad molecular mass distribution, the longest macromolecules crystallize first upon cooling at highest temperature. Upon further cooling, at lowest temperature the shorter macromolecules are expected to crystallize. This is expected from the following prediction.[59]

$$\frac{1}{T_m} - \frac{1}{T_m^0} = \frac{2RM_0}{\Delta H_u \bar{M}_n} \qquad (2.9)$$

where T_m is the melting temperature expressed in degrees Kelvin of the polymer having a given molecular weight M_n, T_m^0 is the melting temperature of the polymer having an infinite molecular weight. M_0 represents the molecular weight of the repeating unit, R is the gas constant and ΔH_u is the heat of fusion per mole of crystalline polymer repeating unit.

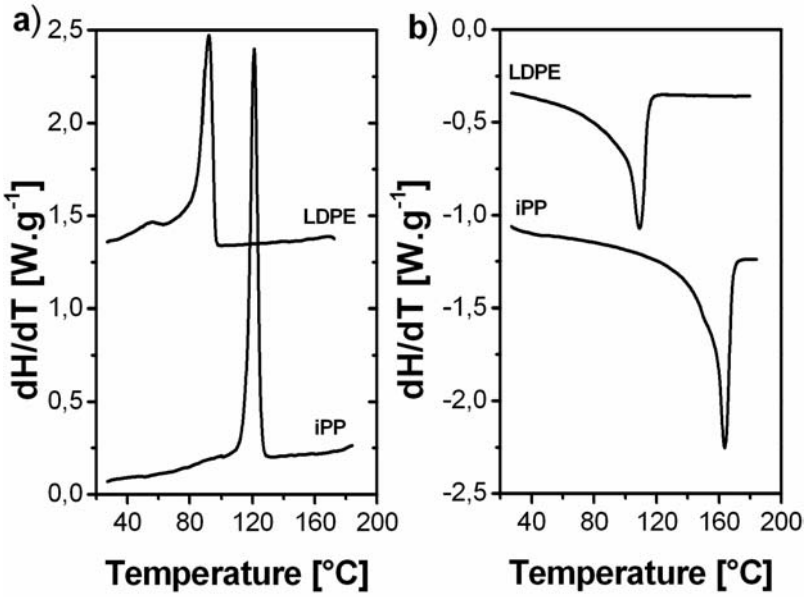

Figure 2.15 - DSC thermograms recorded with the temperature rate of 10°C/min upon (a) first cooling and (b) second heating cycles for the homopolymers LDPE and iPP.

On the basis of complementary polarized optical microscopic observations, the exothermic and endothermic processes recorded for the homopolymers are assigned to primary crystallization, that is the radial growth of spherulites [60] (**Figure 2.16**) and subsequent melting, respectively. Upon cooling iPP film, growth of spherulites was clearly observed in a range of temperature correlating well with the exothermic peak detected by DSC. The spherulites grow until they impinge with each other and reach size in the range 30-80 μm in diameter. For LDPE, formation of birefringent superstructures was also observed by POM, but the size of the morphological elements was greatly reduced (about 10 μm in diameter) in comparison to iPP owing to higher nucleation rate.

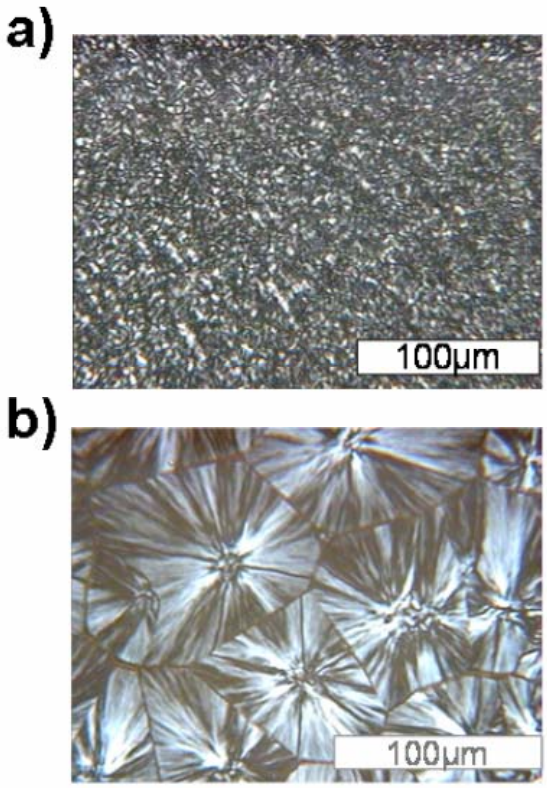

Figure 2.16 - Polarized optical microscope images showing the melt crystallized morphology of a) LDPE and b) iPP.

It is well-established that structural details of ordered materials (semi-crystalline, liquid crystalline) are strongly dependent on the conditions chosen for the structure formation. As a clear example of this dependence, **Figure 2.17** exhibits the heating DSC trace recorded for iPP samples that were submitted to different thermal treatment during cooling from the melt. The cases of slowly cooled and quenched samples are shown.

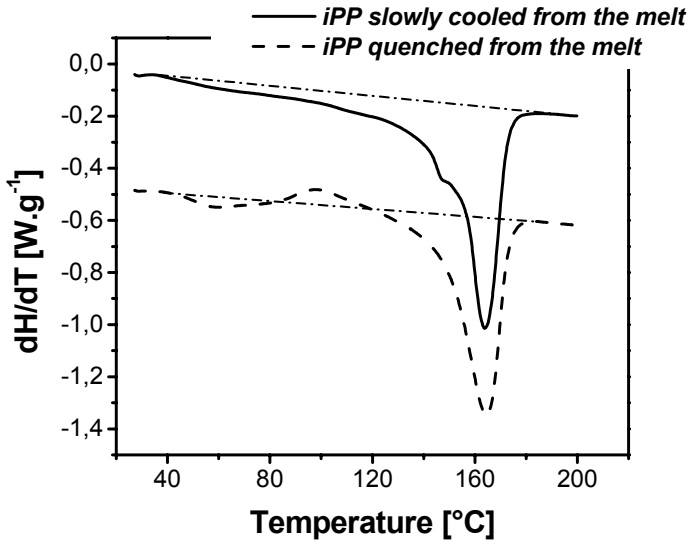

Figure 2.17 - DSC thermograms recorded with the temperature rate of 10°C/min upon heating cycles for iPP (solid line) slowly cooled and (solid line) quenched from the melt.

Beyond the main melting processed observed in both cases in the temperature range between 120 and 180°C, the heat flow trace observed in the low temperature regime reveals different thermal behaviour. For the slowly cooled iPP sample, the endothermic transition peak is highly asymmetric and considerably broadened on the low temperature side. The negative deviation of the heat flow signal starts from a temperature of about 35°C, that is much below the main melting peak maximum $\Delta T \sim 130$°C. This kind of behavior is characteristic for systems which show a partial melting consisting of dismounting or rearranging structures of various thermal stability. The quenched sample exhibits a more complex behaviour, where subsequently to the pre-melting, a cold crystallization phenomenon is observed between 83 and 120°C. These finding indicate that iPP cannot completely crystallize under the relatively fast cooling (10°C/min) so that upon subsequent heating, annealing of the quenched structure is observed. It is thus obvious from these very simple experiments, that many of the published results may contain an uncertainty related to the specific thermal history used. Through our experimental work, special care has been taken to apply similar thermal treatments to the different samples investigated so that comparisons of effects of blends composition, nature of compatibiliser remains possible and reliable.

Figure 2-18, **2.19** and **2.20** show the DSC traces of binary blend LDPE/iPP (80/20) and compatibilized ternary blends with EPR compositions 5, 10 and 15 wt.-%, respectively. The thermograms were recorded during the first cooling (left hand side of the figures) and second heating (left hand side of the figures) scans.

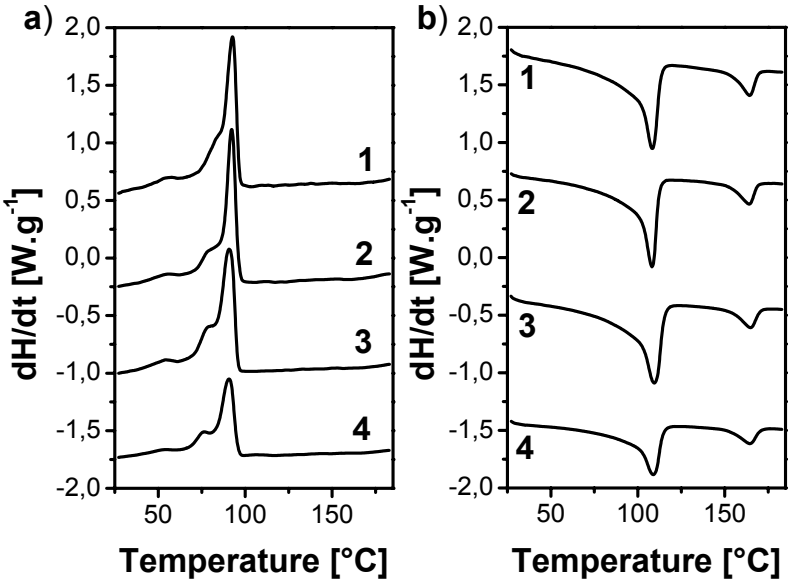

Figure 2.18 - DSC thermograms recorded with the temperature rate of 10°C/min upon (left) first cooling and (right) second heating cycles. The DSC traces correspond to the blends assigned as (1) LDPE/iPP, (2) LDPE/iPP/Keltan13-5, (3) LDPE/iPP/Dutral054-5 and (4) LDPE/iPP/Keltan740-5.

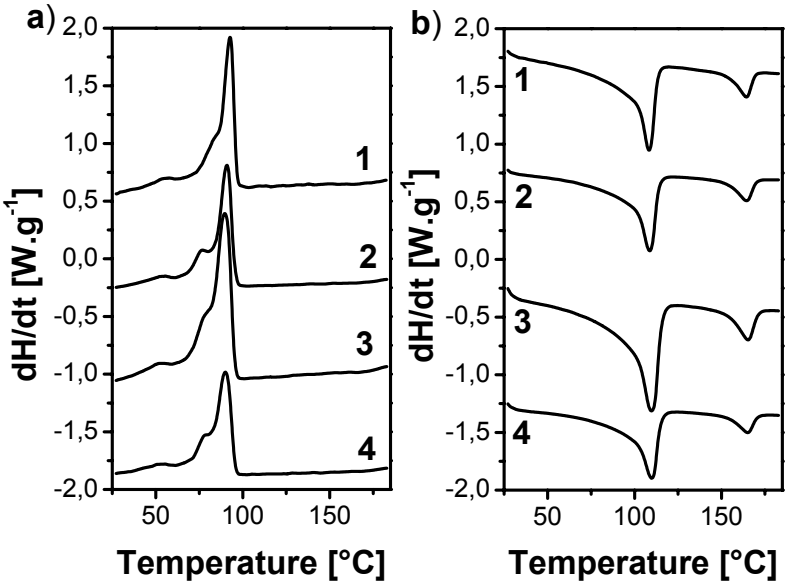

Figure 2.19 - DSC thermograms recorded with the temperature rate of 10°C/min upon (a) first cooling and (b) second heating cycles. The DSC traces correspond to the blends assigned as (1) LDPE/iPP, (2) LDPE/iPP/Keltan13-10, (3) LDPE/iPP/Dutral054-10 and (4) LDPE/iPP/Keltan740-10.

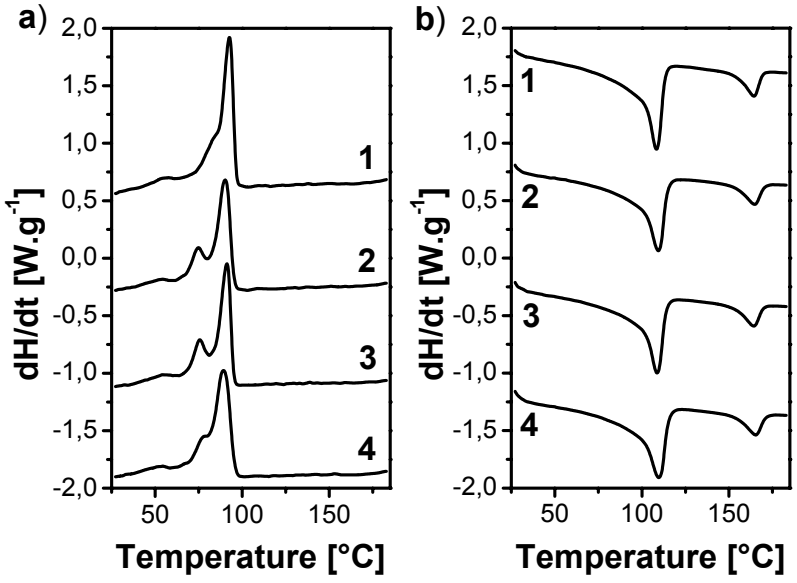

Figure 2.20 - DSC thermograms recorded with the temperature rate of 10°C/min upon (a) first cooling and (b) second heating cycles. The DSC traces correspond to the blends assigned as (1) LDPE/iPP, (2) LDPE/iPP/Keltan13-15, (3) LDPE/iPP/Dutral054-15 and (4) LDPE/iPP/Keltan740-15.

A first comparison of the DSC traces recorded for the homopolymers and for binary as well as ternary blends indicates that LDPE/iPP composite materials in the mass ratio 80/20 form immiscible crystalline/crystalline blends. This can be easily recognized from the DSC data recorded upon cooling where melting curves of both binary and ternary blends, regardless the nature and amount of the EPR used, indicate two well decoupled melting peaks assigned to the individual homopolymers. This melting behaviour gives evidence of formation of separated LDPE and PP crystals during the crystallization process where the faster crystallizing component expulses the other component during crystallization. Under the relatively fast cooling from the melt (10°C/min), binary LDPE/iPP blend revealed a complex solidification process with exothermic peaks at temperatures of about 92 and 77 °C (**Figure 2.21**). For all blends a shoulder was recorded on the low temperature side of the main endothermic peaks. This effect was more pronounced for the compatibilized blends based on the polypropylene rich EPR, i.e. Dutral 054 and Keltan 13, and was EPR content dependent. It is worth noting that in the cases of the blends the crystallization of iPP occurs with a considerable undercooling with respect to the case of the pure homopolymer. From these results, we assume that the nucleation for crystallization of iPP is considerably delayed for composite materials consisting of iPP dispersed phase surrounded by a LDPE matrix so that the crystallization process is significantly shifted towards lower temperature in this case.

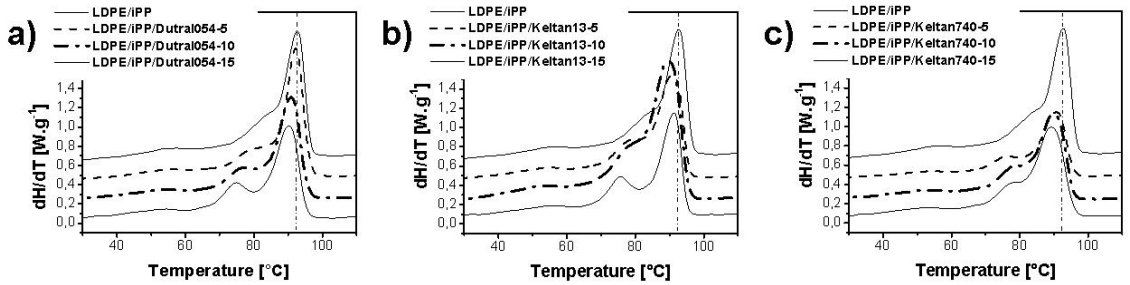

Figure 2.21 - Fragments of DSC cooling traces (10°C/min) indicating the crystallization in a) LDPE/iPP/Dutral054-*x,* b) LDPE/iPP/Keltan13-*x* and c) LDPE/iPP/Keltan740-*x* blends taking place in the temperature range corresponding to the crystallization temperature of bulk LDPE.

Space filling spherulitic patterns was observed for all ternary blends and the crystalline morphology was largely influenced by the major component (LDPE) since

no large spherulites can be observed. The details of the crystalline superstructures could not be clearly revealed by optical microscopy (**Figure 2.22**).

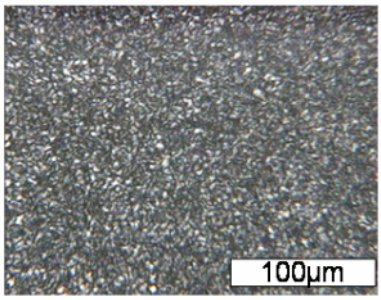

Figure 2.22 - Polarized optical microscope images showing the melt crystallized morphology of a) LDPE-PP (80/20) blend.

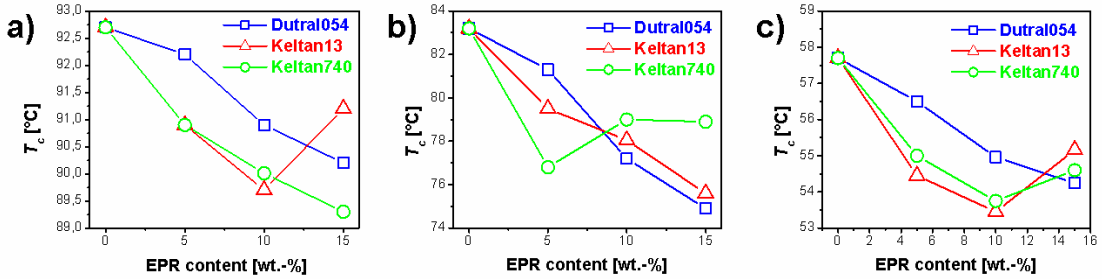

Figure 2.23 - Influence of the nature and content of the ethylene-co-propylene polymer on the temperatures of the exothermic peaks observed from the first DSC cooling runs at the rate of 10°C/min. The temperatures correspond to the a) main crystallization process, b) exothermic shoulder and c) low temperature crystallization process.

This type of cooling DSC trace, where a main but complex crystallization peak is detected at a temperature characteristic for the major component crystallization process, suggests that the LDPE and iPP crystal species are either co-crystallizing or crystallizing separately but over a similar temperature range. The peak crystallization temperatures as a function on the nature of the compatibilizer and composition on blend are shown in **Figure 2.23**. Despite the variation in the crystallization temperatures when changing, the melting temperature remained constant (**Figure 2.24**).

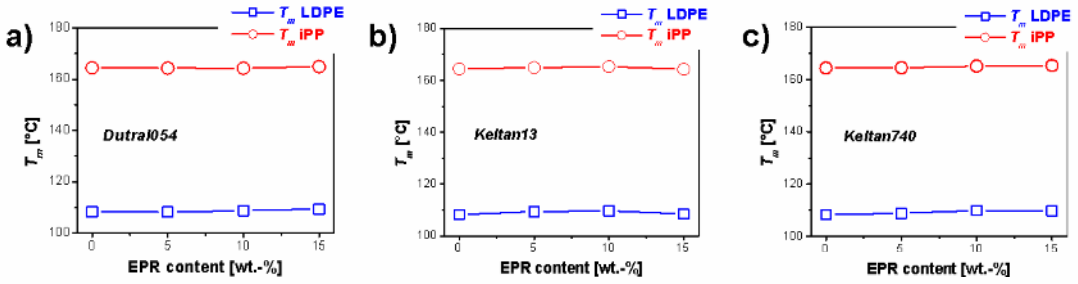

Figure 2.24 - Influence of the content of a) Dutral054, b) Keltan13 and c) Keltan740 on the endothermic peak temperatures corresponding to the melting processes of LDPE and iPP components observed from the second DSC heating runs at the rate of 10°C/min.

9.2. 2D small angle light scattering

The birefringent superstructures observed to develop on cooling have size of the order of a few micrometers that corresponds to the limit of sensitivity of classical optical microscopy techniques. Thus, the structural details (shape, size) of the morphological elements could not be clearly assessed from simple optical microscopic observations. The morphology formation during crystallization was thus further elucidated by carrying out small-angle light scattering experiments using a 2 dimension position sensitive detector. The variety of patterns and the structural informations that can be obtained under either *Vv* or *Hv* mode makes the SALS method very powerful for the investigation of heterophasic systems. In our case the measurements were performed under crossed (*Hv*) polarization conditions. Thin polymer films were placed between two glass slides and were submitted to the same thermal conditions as the ones used for the DSC measurements (cooling from the melt with the rate 10°C/min). Binary LDPE/iPP blend was initially investigated and the left panel of **Figure 2.25** displays an experimental 2D pattern representative for at least 5 independent LDPE/iPP film samples. The measurement was performed at room temperature. For each film, the scattering features were recorded on various positions of the films were found to be homogeneous.

Employing these experimental conditions, similar anisotropic patterns with azimuthal distribution of the scattered intensity characteristic for spherulitic superstructures were obtained for all the ternary blends containing either Dutral054, or Keltan13 or Keltan740 in the composition range up to 15 wt.%. This shows that similarly to the cases of pure homopolymers, structure formation from the melt in

blends also proceeds via nucleation and growth and leads to the formation of superstructure with spherical geometries. Temperature dependent SALS analyses performed under non-isothermal conditions (10°C/min) did not allow for investigating the kinetic of crystallization. Qualitative analysis of the developed patterns reveals that upon continuous cooling, the position of the maximum scattering intensity was shifted to smaller scattering angle. This reflects an increase in the size of the scattering elements, i.e. growth of spherulites.

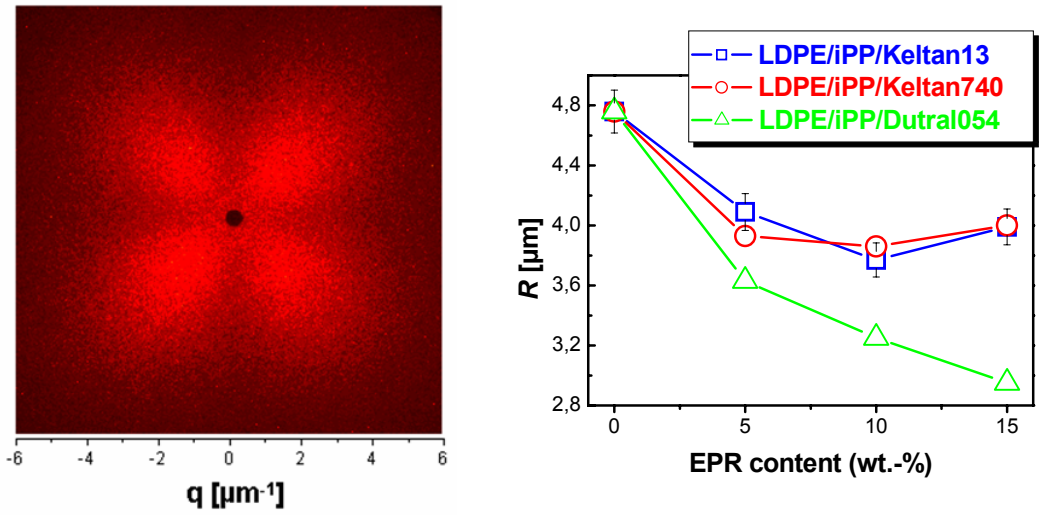

Figure 2.25 - (Left panel) an example of 2D small-angle light scattering pattern recorded for a melt crystallized thin film of uncompatibilized LDPE/iPP blend at room temperature (cooling from the melt with the temperature rate of 10°C/min). (Right panel) Influence of the nature and content of the compatibiliser on the radius of the spherulitic superstructures measured for thin films of LDPE/iPP/EPR-x crystallized from the melt with the cooling temperature rate of 10°C/min. The radius of spherulites was calculated from the position of the scattering intensity maximum observed in the intensity distributions recorded at 45° with respect to polarization directions in the *Hv* pattern.

Although similar morphology was obtained for all investigated blends, the dimensions of the crystalline superstructures changed with EPR content. The **Figure 2.25** (right panel) shows the average size of spherulite in radius for all EPR blends with varied composition. The sizes of spherulites were observed to decrease upon addition of compatibilizater and this effect is dependent on the type and amount of

the ethylene-co-propylene polymer added to LDPE/iPP. This observation indicates that in presence of elastomeric copolymer the nucleation rate is increased. This strongly suggests that the amorphous ethylene-co-propylene polymers act as nucleating agent.

9.3. Dynamic mechanical analysis.

Visco-elastic properties of blends were evaluated through dynamic mechanical analysis. This technique is very sensitive to the crystallization/melting process and was mainly used as a complementary method of the DSC analysis to confirm transition temperatures. Herein we will limit ourselves to the presentation of fragmentary results which are representative for the observed behaviour. A typical thermo-mechanical behaviour of the uncompatibilized LDPE/iPP blend is shown in **Figure 2.26** as the temperature dependencies of the real (*G'*) and imaginary (*G''*) components of the complex shear modulus. The measurement was performed in isochronal conditions (at ω= 1 rad.s^{-1}) over a broad range of temperature during cooling from the molten state with a temperature rate of 2°C/min. Accordingly the mechanical data indicate an abrupt variation in both real and imaginary components of the complex shear modulus by three orders of magnitude. On the basis of the DSC data coupled to the POM observations, the observed moduli increase when decreasing temperature was attributed to the nearly simultaneous crystallization of both LDPE and iPP.

A good concordance was obtained for the transition temperatures detected by the three techniques. In the high and low temperature regimes, soft and hard responses of the materials are obtained characterized by modulus values in the range of 10^4 and 10^7 Pa, respectively. Independent of the nature of the compatibiliser and of the blend composition, similar crystallization-related thermo-mechanical effects were observed for all blends (see **Figure 2.27** where the result of the isochronal temperature scans for the case of the LDPE/iPP/Keltan13-15 blend is shown).

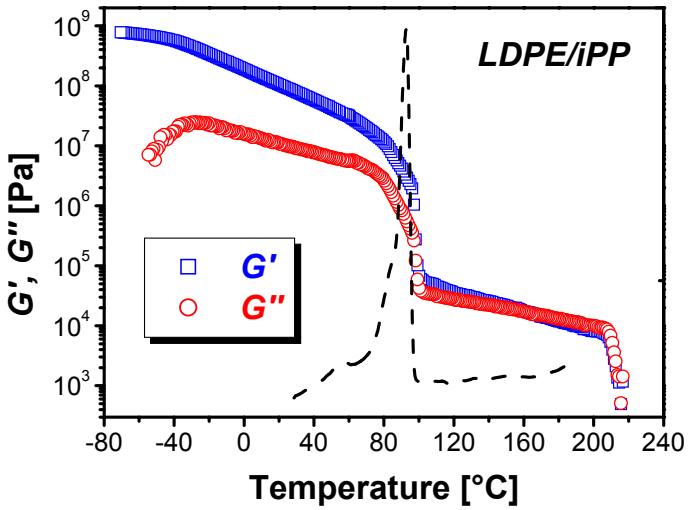

Figure 2.26 - Temperature dependencies of the storage (*G´*) and loss (*G´´*) shear moduli as measured for the LDPE/iPP upon cooling from the melt with the temperature rate of 2°C/min. The dotted line corresponds to the DSC trace recorded on cooling with the temperature rate of 10°C/min. A good agreement is obtained for the transition temperature by the two techniques despite differences in the heating rates.

Similarly to the cooling run, both moduli showed discontinuities upon heating from the crystalline state (**Figure 2.28**). However, while the cooling scan reveals unique change in mechanical properties, two changes were observed during the heating cycle. These latter effects indicate the melting of two phase segregated crystal entities. The relaxations recorded upon cooling are assigned to the melting of the polyethylene crystalline phase and to the subsequent melting of the polypropylene phase in the order to the higher temperature. The cross over between *G'* and *G''* observed in the temperature located above the melting of the polypropylene component indicates a flow behaviour of the material in the high temperature regime

A good agreement was also observed between the values of transition temperatures determined from the DSC analysis (**Figures 2.27** and **2.28)** and these dynamic mechanical spectra showing one and two relaxation processes during cooling and heating runs, respectively for ternary at all compostions. These three processes are uniquely assigned to the relaxations of the crystalline phase.

The main softening transition is observed at the melting of the LDPE component as expected from the blend composition since LDPE is the major component.

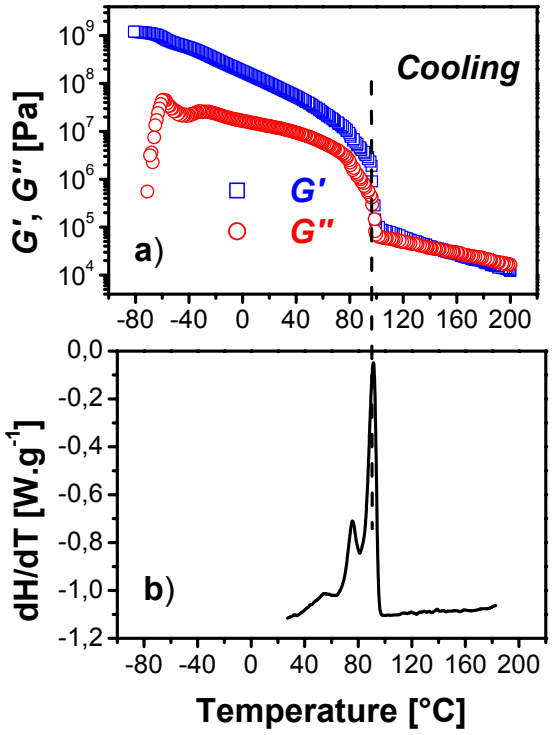

Figure 2.27 - a) Temperature dependencies of the storage (*G´*) and loss (*G´´*) shear moduli as measured for LDPE/iPP/Keltan13-15 upon cooling from the melt with the temperature rate of 2°C/min b) DSC thermograms recorded during cooling scan measured with the temperature rate of 10°C/min for LDPE/iPP/Keltan13-15. A good agreement is obtained for the transition temperature by the two techniques despite differences in the heating rates.

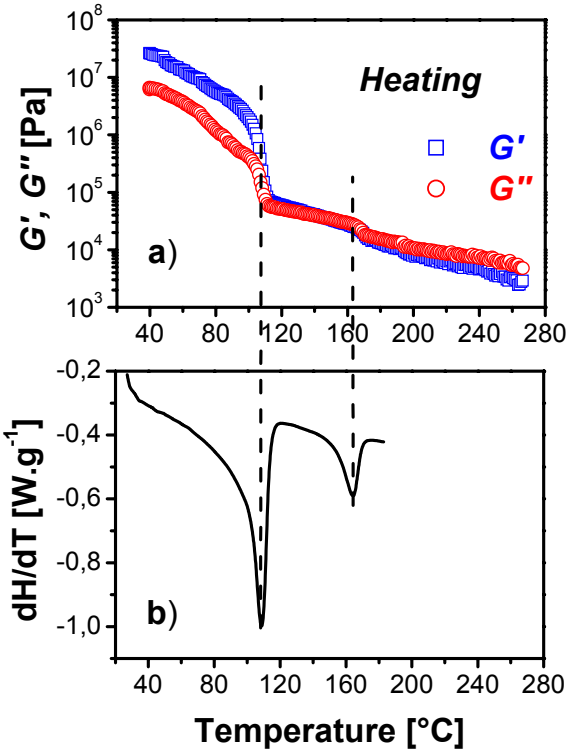

Figure 2.28 - a) Temperature dependencies of the storage (*G´*) and loss (*G´´*) shear moduli as measured for LDPE/iPP/Keltan13-15 upon heating from the crystalline state with the temperature rate of 2°C.min b) DSC thermograms recorded during heating scan measured with the temperature rate of 10°C/min for the bulk LDPE/iPP/Keltan13-15. A good agreement is obtained for the transition temperature by the two techniques despite differences in the temperature rates.

9.4. Atomic force microscopy

To gain more insight into the crystal morphology, the fine details of the spherulitic patterns developed in binary and ternary blends was examined using atomic force microscopy. Polymer blends samples were prepared on glass slides by flowing films of a 10 μm thickness from the melt. The conversion of the melt material into ordered superstructures was performed through non-isothermal crystallization to resemble the conditions used in DSC, POM and DMA. The type of spherulitic pattern is a very important parameter in the control of the properties of the semicrystalline materials since for example, interspherulitic boundaries, which are rather weak structural parts, affect not only the mechanical properties but also others characteristics of polymeric systems such as gas sorption problems.[61] It is precisely the type of spherulites as well as the nature of the interspherulitic boundaries that

were found to show major differences. Both parts of **Figure 2.29** display the crystalline morphology of the binary LDPE/iPP as observed at different magnification. The existence of spherulite-like aggregates is evidenced by both phase and height images showing clearly lamellae-based nanoscale organization. Rather similar morphology was observed for LDPE/iPP/Keltan13-15 (**Figure 2.30**). The center of the spherulites is well-seen but the presence of 15% of Keltan13 makes the borders between adjacent spherulites less sharp. This indicates that the copolymer actually affect the interfacial characteristics.

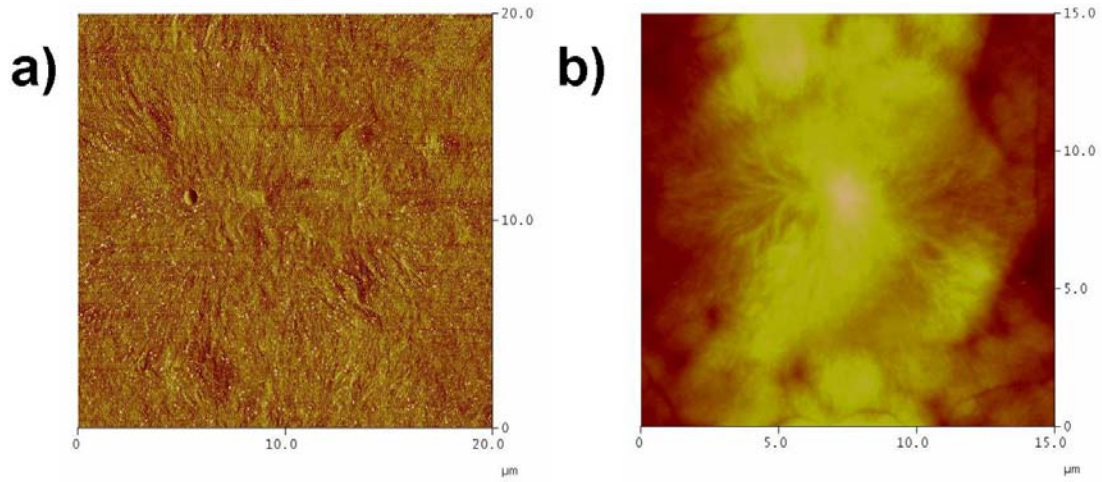

Figure 2.29 - AFM images recorded in a) phase and b) height modes showing the surface morphology for the LDPE/iPP binary blend.

Very peculiar surface morphology was obtained for the ternary blends compatibilized by the two EPR, Dutral054 and Keltan740. These systems formed well-defined dendritic structures (**Figures 2.31** and **2.32**). For LDPE/iPP/Keltan740-15 highly branched dendritic morphologies merged into long branched two-dimensional structures to form superstructures where the length of the backbones (10-15 µm) is about ten time larger than the length of branches (1-2 µm). The nucleating centers are also clearly distinguishable. For LDPE/iPP/Dutral054-15 the dendritic structure is denser. The AFM images also reveal the difference in internal domain structures of the dendrites formed in LDPE/iPP/Keltan740-15 and LDPE/iPP/Dutral054-15. In the latter case, the dendrites are assembled by the aggregation of cylindrical domains merging into larger aggregates. However due to the high density of the structure, it is difficult to estimate the length of the backbones and branches, but their size are lower than in LDPE/iPP/Keltan740-15.

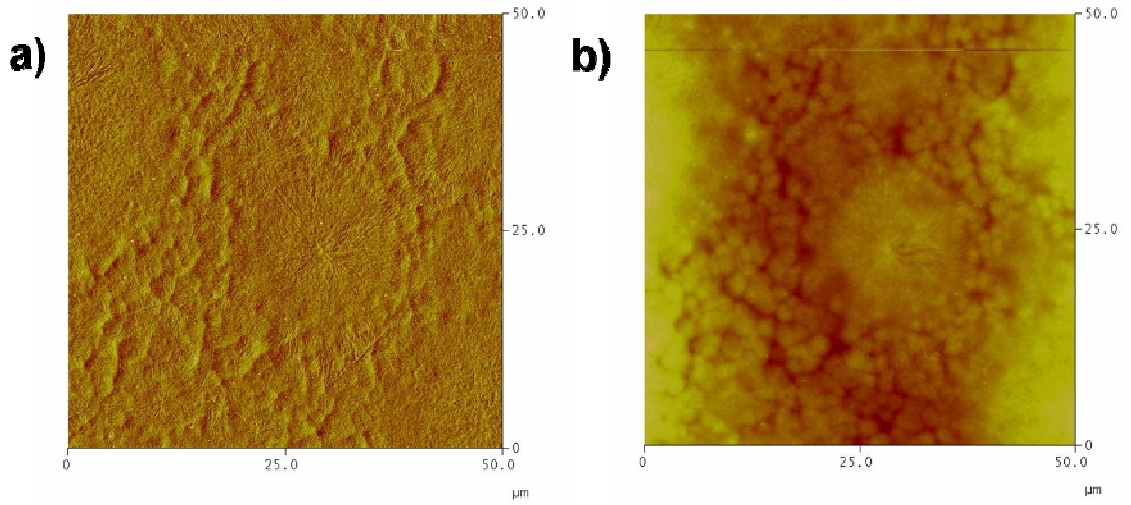

Figure 2.30 - AFM images recorded in a) phase and b) height modes showing the surface morphology for the LDPE/iPP/Keltan13-15 ternary blend.

Although it is difficult from a limited number of AFM images to quantify precisely the size of the crystalline domains, the apparent dimensions determined by AFM (3-10µm) are in rather good agreement with the SALS data (3-4µm). The difference in size may be assign to the fact that AFM data provide only information about surface morphology that may be slightly different as compared to the morphology developed in the bulk. Upon cooling the film in the oven, a temperature gradient may occur within the bulk material where the temperature at the surface in contact with air may be lower than the temperature at the surface in contact with the glass. Moreover, films of different thickness were used; 10 and 1 µm for the AFM and SALS measurements, respectively.

Another feature is the clear contrast seen in the AFM images of LDPE/iPP/Keltan740-*15* and LDPE/iPP/Dutral054-*15*. The regions between adjacent spherulites have darker appearance in contrast to the central region of the sphrehulite. This indicates that these two regions are different in nature and that the change in modulus is due to the presence of the ethylene-co-propylene polymer with higher concentration at the outer region of the dendrites.

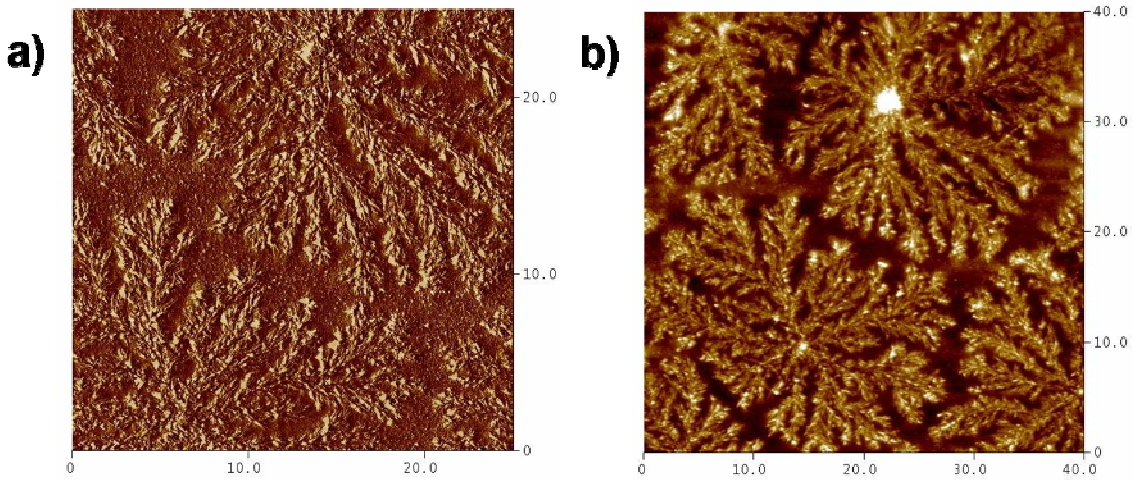

Figure 2.31 - AFM images recorded in a) phase and b) height modes showing the surface morphology for the LDPE/iPP/Keltan740-15 ternary blend.

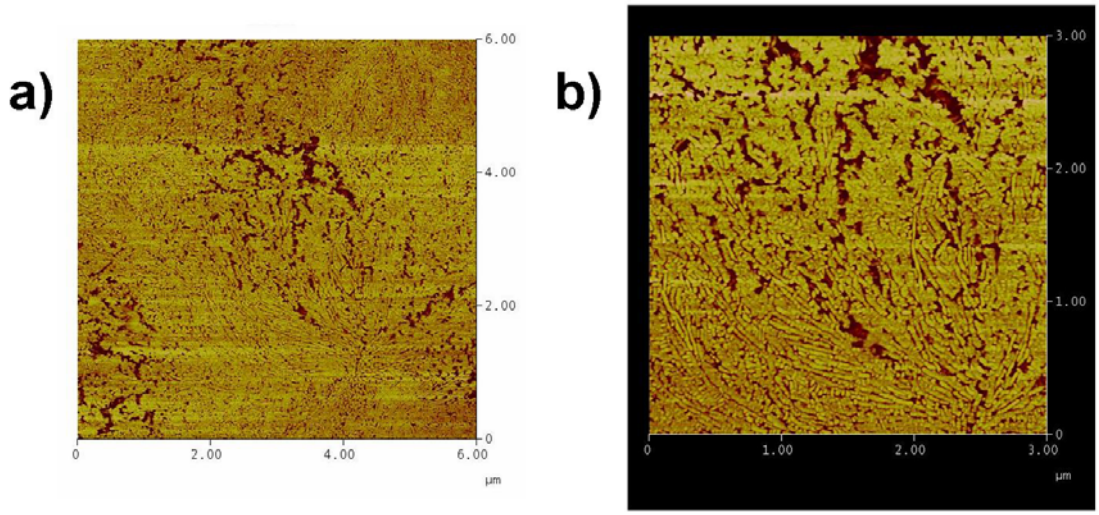

Figure 2.32 - AFM images recorded in height mode showing the surface morphology for the LDPE/iPP/Dutral054-15 ternary blend.

This AFM study reveals that Keltan740 and Dutral054 may induce a morphological transition in contrast to Keltan13. It also suggests that for the three ternary blends, the homopolymers crystallize and the amorphous copolymer is expelled out of the crystalline structure.

9.5. Scanning electron microscopy

The morphology of the cryogenically fractured surface of LDPE/PP blend is shown in **Figure 2.33a**. For the ratio 80/20, heterogenous morphology is clearly observed where LDPE constitutes a continuous matrix in which the PP phase is

dispersed with clearly visible phase boundaries. The shape of PP domains is nearly spherical with an average size of about 2.4μm in diameter, although a broad size distribution of PP domains is noticed. For example, in **Figure 2.33b** domains in the size range between less than 1μm to more than 3 μm in diameter can be seen.

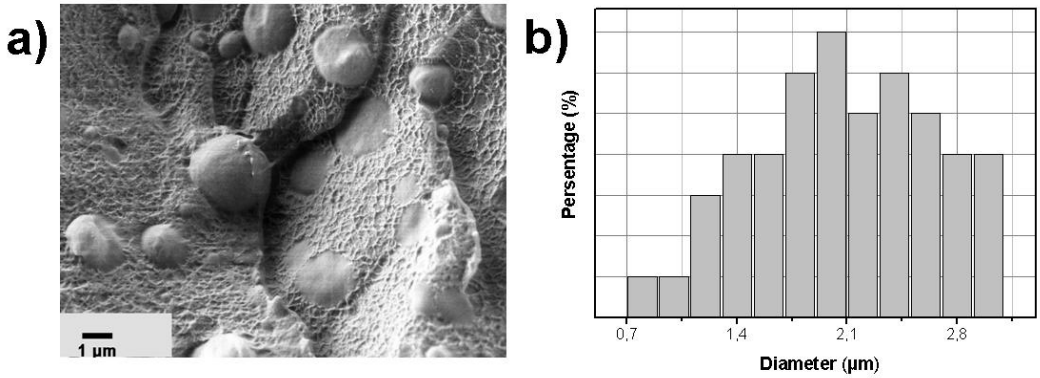

Figure 2.33 - a) SEM picture of fractured sample showing the phase dispersed morphology for LDPE/iPP. b) Diagram of the size distribution of iPP phase separated domains for LDPE/iPP binary blend.

The distributions of domains size for the ternary blends are in range between 0.8 and 2.2 μm. The SEM micrographs shown in **parts a-c** of **Figure 2.34** confirm that LDPE and PP components remain phase separated in the 15wt.-% Keltan13, Dutral-054 and Keltan 740 compatibilized ternary blends.

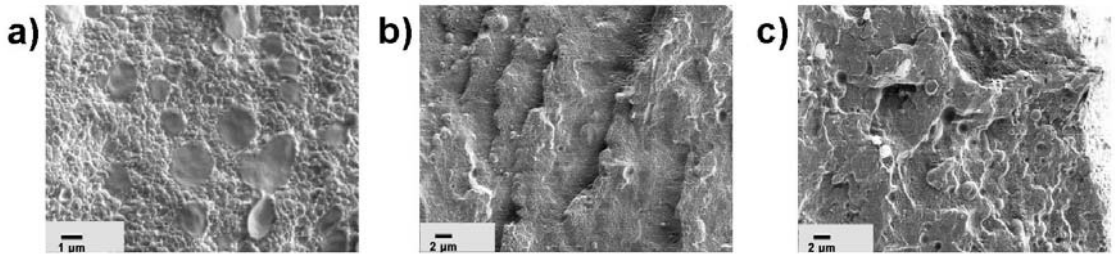

Figure 2.34 - SEM pictures of fractured samples showing the phase dispersed morphology for a) LDPE/iPP/Keltan740-*15*, b) LDPE/iPP/Dutral054-15 and c) LDPE/iPP/Keltan13-*15* blends.

The same observation was made for lower EPR content blends. Moreover, the size of the phase segregated domains was found to be significantly dependent on the content of EPR. The domains size decrease in the presence of EPR. This effect is clearly illustrated in **Figures 2.35** and **2.36** for LDPE/iPP/Keltan740 and LDPE/iPP/Keltan13, respectively. Qualitative analysis of SEM images indicates that

as the content in Keltan740 is increased from 5 through 10 to 15%, the iPP domains remain nearly spherical in shape but there is decreased proportionally.

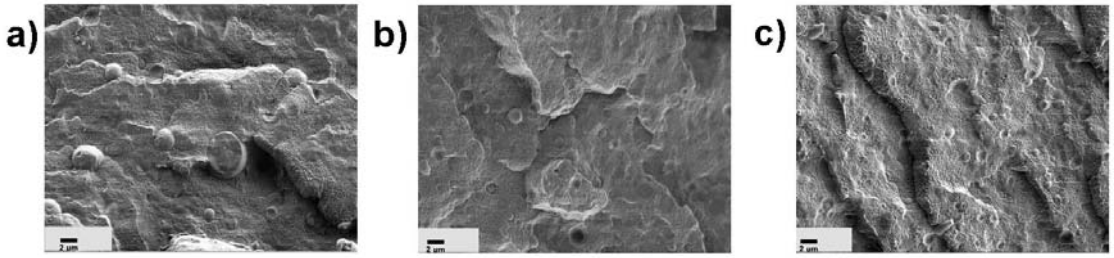

Figure 2.35 - SEM pictures of fractured samples showing the phase dispersed morphology for a) LDPE/iPP/Keltan740-*5*, b) LDPE/iPP/Keltan740-10 and c) LDPE/iPP/Keltan740-15 blends.

For the Keltan13 containing blends, an example of quantitative analysis of the size distribution of iPP phase separated domains is presented based on the investigation of greater numbers of SEM images. The same tendency is also observed, i.e. decrease of the size domains when increasing the Keltan13 content. In summary, **Figure 2.37** presents the plots of the sizes of the dispersed phase domains as a function of the blends composition for the three type of EPR. It is clear in all cases, that addition of EPR leads to a decrease of the size of the phase separated domains. For Keltan740 and Keltan13 the decrease in size was observed to be proportional to the EPR content, while for Dutral054 the domain size of about 1.4 μm in diameter obtained for a composition of 5wt.-% was not influenced by further addition of compatibilizer.

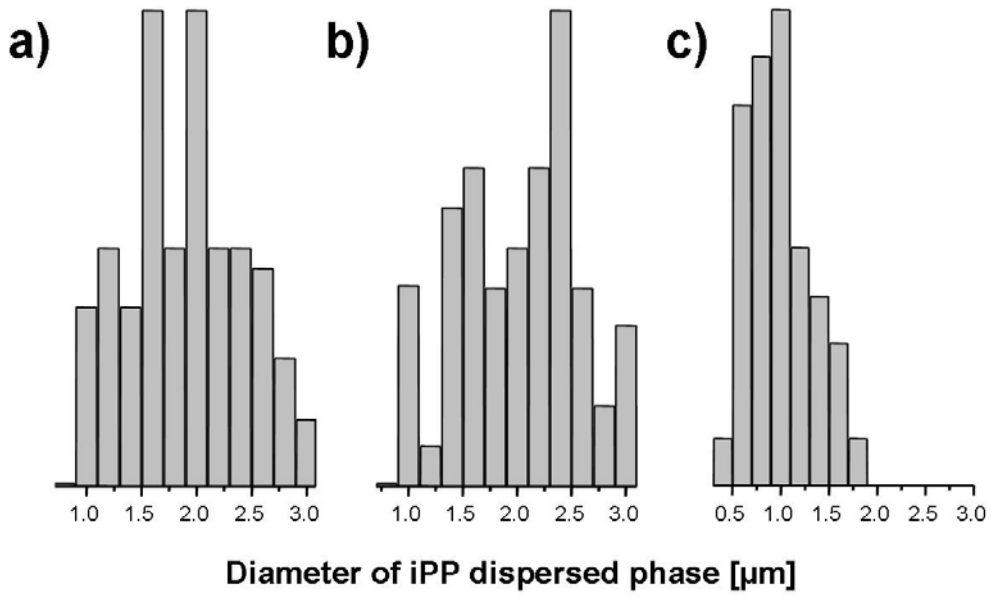

Figure 2.36 - Diagrams of the size distribution of iPP phase separated domains for a) LDPE/iPP/Keltan13-*5*, b) LDPE/iPP/Keltan13-*10* and c) LDPE/iPP/Keltan13-*15* blends.

The reduction of the size of the PP dispersion, leading to an increase of the contact surface/volume ratio, indicates that interfacial tension is lowered upon EPR addition. This should lead to a significant improvement of mechanical properties as will be discussed later. Additional information about fracture behaviour of composite materials can be obtained. Major differences in the microstructures of ternary blends concern the fracture features of the dispersed phase. For the 15wt.-% Keltan-13 containing blend, either globules or cavities are observed with average size in diameter in the same order of dimensions. The spherically shaped imprints embedded within the continuous phase (i.e. cavities) are presumed to be initially filled by the dispersed PP phase that was pulled out from the matrix during breaking leading to the formation of PP globules on the opposite side of the fractured sample. Keltan740 containing blends exhibit very different microstructure. The surfaces as observed after ruptures are much smoother are more homogeneous in terms of chemical composition. Both continuous and dispersed phases are fractured so that only PP rich phase separated domains are seen while PP free cavities are not formed.

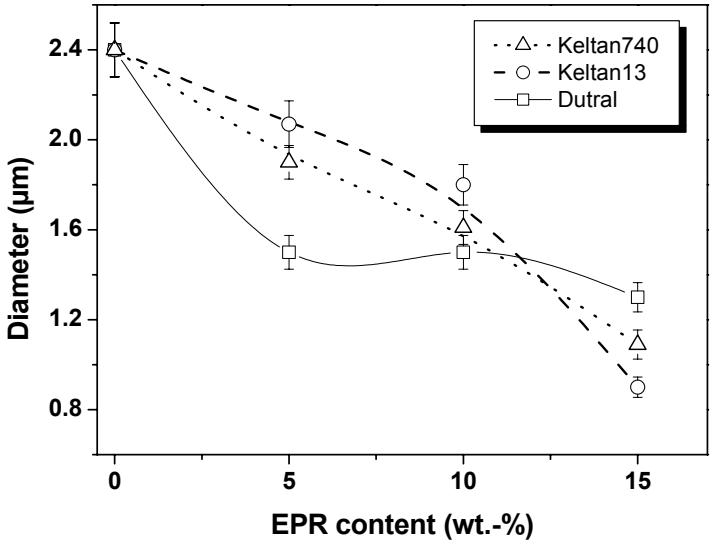

Figure 2.37 - Dependences of the diameter of the phase separated iPP domains versus the content in EPR for LDPE/iPP/keltan13, LDPE/iPP/keltan740 and LDPE/iPP/Dutral054 blends.

9.6. Wide angle X-ray scattering

Polyethylene usually shows an orthorhombic crystal structure with corresponding reflections at scattering angle values of 21 and 24°.[62]

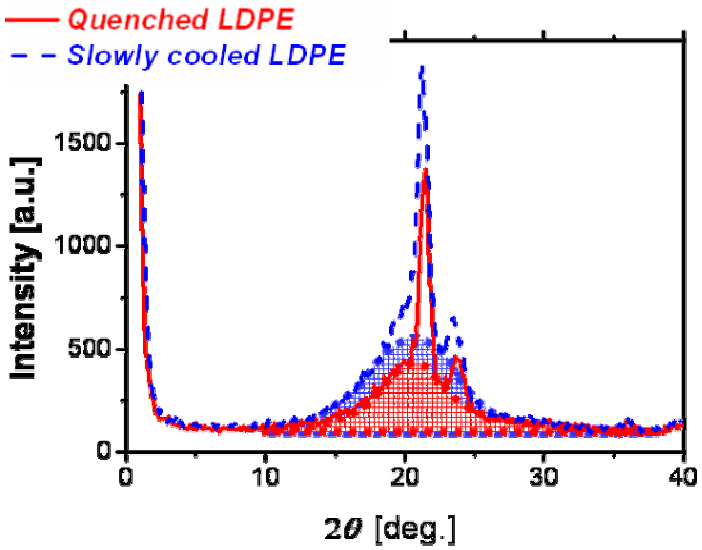

Figure 2.38 - Wide-angle X-ray diffractograms recorded at room temperature for LDPE submitted to different thermal treatments while cooling from the molten state. The sample was melt-crystallized through (dashed line) slow cooling or (solid line) quenching thermal treatment.

When the crystallization is carried out under isothermal conditions, the degree of ordering within the bulk material is strongly dependent on the crystallization temperature. An equilibrium theory relating the degree of crystallinity to the temperature has been developed by Flory for crystallisable copolymers. [63] Another model based on non equilibrium theory applicable to quenched polymers has been proposed by Wunderlich.[64]

Two wide-angle X-ray scattering profiles recorded for LDPE sample are shown in **Figure 2.38** Here again, the effect of thermal history on the fine details of the two phases structure is clearly evidenced. From a qualitative aspect, it is seen that the diffuse halo typical for the amorphous part of the semicrystalline polymer is increased when the sample is quickly cooled. The quantitative determination of the weight fraction of crystallinity (X_c) can be estimated from the area under the amorphous halo (I_a) and crystalline reflections (I_c) as:

$$X_c^{WAXS} = \left(\frac{I_c}{I_c + I_a} \right) \qquad (2.10)$$

However the observed change was of the order of only a few percent. The structure of the isotactic polypropylene sample we studied is shown in the **figure 2.39**. Polypropylene is known to crystallize in different forms, namely α, β and γ crystal modifications.[65] In the same lamella, polypropylene chains may be organized in different crystal forms as reported for the α and β cases.[66] The polymorphism observed in polymeric substance if of primary importance since each phase may exhibit different physical and mechanical properties. So it is a crucial parameter enabling to determine structure-property relationship.

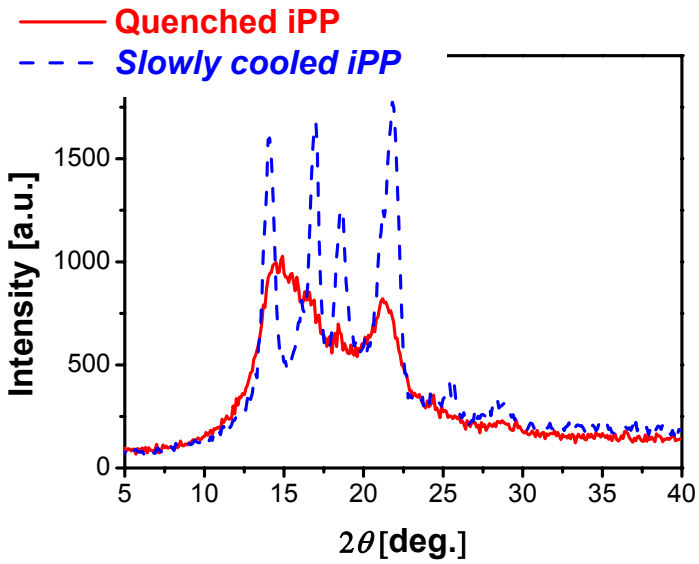

Figure 2.39 - Wide-angle X-ray diffractograms recorded at room temperature for iPP submitted to different thermal treatments while cooling from the molten state. The sample was melt-crystallized through (dashed line) slow cooling or (solid line) quenching thermal treatment.

In **Figure 2.40** the WAXS intensity distributions recorded at room temperature for the ternary blends made with the three ethylene-propylene copolymer at a weight content of 15% are shown in comparison to the uncompatibilized binary blend. The fours presented diffractograms are typical for two-phase systems. The presence of scattering peak superimposed to an amorphous halo indicates that dense domains of crystalline nature co-exist with less ordered domains where the polymer chains assume a liquid-like organization. The more intense reflection is observed at the scattering angle value of 21° in all cases. This peak together with the well resolved reflection at a 2θ value of 24° is assigned to the orthorhombic modification of the polyethylene making the matrix of the blend. Beyond these two clearly seen reflections a series of three scattering maxima is seen in the scattering angle range between 14 and 20°. These peaks are related to the crystallization the polypropylene dispersed phase. From a qualitative aspect the intensity ratio, between the peaks characteristic of the polyethylene and polypropylene are in a good agreement with the composition of the blend. It was clear that the peak positions from the WAXS profiles of the various blends were almost identical. This indicates that the unit-cell dimensions of both LDPE and iPP are not disturbed by blending and by further addition of ethylene-propylene based compatibilizers.

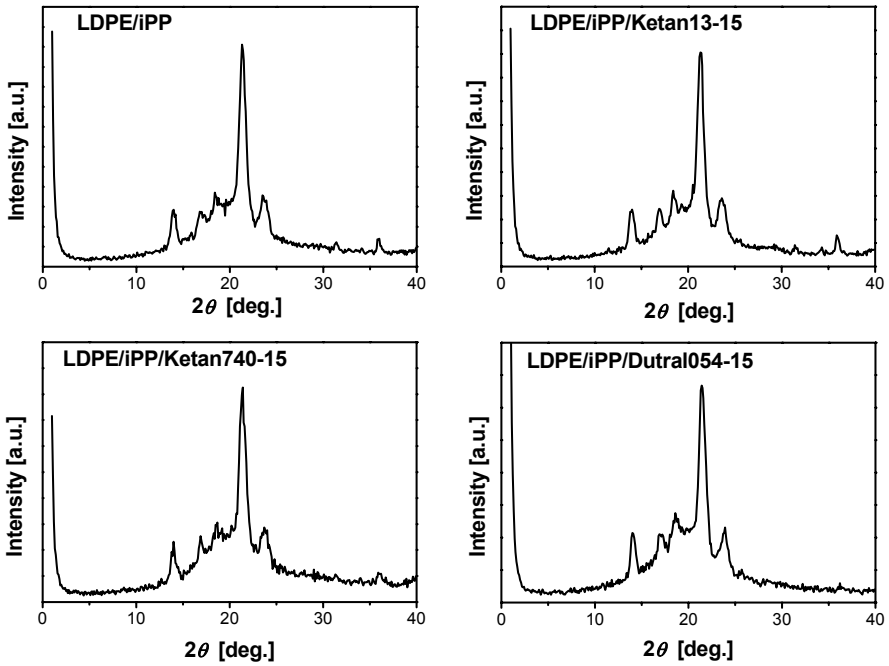

Figure 2.40 - Wide-angle X-ray diffractograms recorded at room temperature for the binary LDPE/iPP and ternary LDPE/iPP/EPR-15 Blends.

Furthermore, temperature-dependent wide-angle X-ray scattering data were collected for all the blend systems. The temperatures at which data were collected upon heating/cooling cycles were purposely chosen to express the various morphological combinations possible for the matrix/dispersed (LDPE/iPP) phases. Upon heating, three different combinations are possible. In the low temperature regime defined from the DSC analysis as the temperature range extending below the melting process of LDPE, semicrystalline/semicrystalline morphology is expected. In contrast, in the high temperature regime that corresponds to the temperature range above the melting transition of iPP, the X-ray scattering features should be characteristic for a completely disordered morphology (amorphous/amorphous). Finally, in the intermediate temperature regime, comprised between the melting temperatures of LDPE and iPP, an amorphous/semicrystalline morphology should develop where iPP domains with crystalline ordering should be dispersed within a disordered matrix since LDPE has the lowest temperature of melting. Due to the fact that LDPE and iPP crystallize in the same range of temperature only two regimes, amorphous/amorphous at high temperature and semicrystalline/semicrystalline at low temperature, are expected while cooling the system from the melt. All these findings were confirmed to a large extend by the experimental data. No significant differences

were observed when comparing binary to ternary blends and when the nature and content of the ethylene-co-propylene polymer were changed. Thus, only the WAXS intensity distributions acquired during a heating scan followed by a cooling run is shown in **Figure 2.41** for the LDPE/iPP/Keltan740-15 blend as a representative example. In the top Figure, the patterns of both LDPE and iPP are clearly observed in the room temperature profile. From a temperature of 140°C, the two major diffraction peaks of the LDPE at 21 and 24° are not detected. This indicates that the melting of the matrix has occurred contributing to the enhancement of the amorphous scattering as expressed by the diffuse halo. Above 140°C, the iPP phase started to melt and at a temperature of 200°C only a broad halo is obtained. This type of scattering effect originates from liquid-like intermolecular correlation and expresses a broad distribution of intermolecular distances, i.e. both crystallizable olefinic polymers are in amorphous state. The melt-crystallization process was further investigated by cooling the sample down to room temperature and the results obtained at 100, 75 and 25°C are shown in the bottom figure. It is worth noting that over the whole 2θ axis, the diffraction peaks representative of the room temperature scattering profile show up concomitantly while the temperature was maintained constant in the cooling steps. The peaks are assigned to both LDPE and iPP. Thus the wide-angle X-ray scattering experiments confirmed that LDPE and iPP crystallize in the same range of temperature in full concordance with the DSC data but they crystallize in phase separated domains.

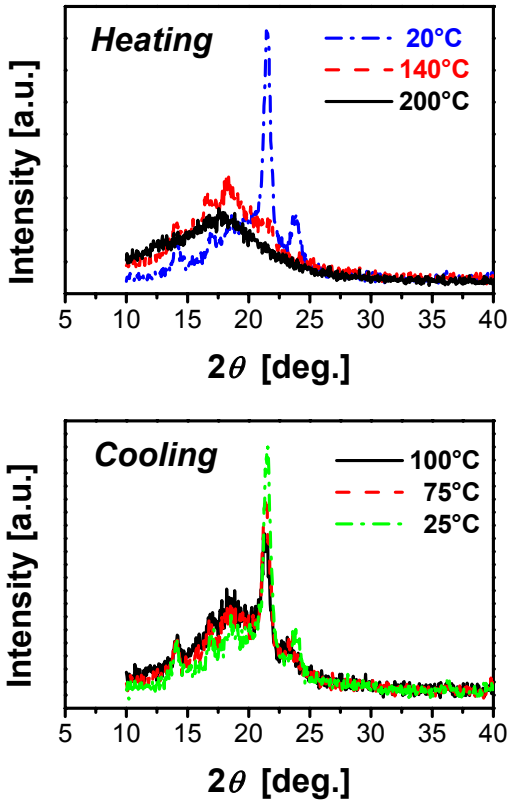

Figure 2.41 - Wide-angle X-ray scattering intensity distributions recorded at various temperature for the ternary blend LDPE/iPP/Keltan740-15. The data were collected at selected temperatures during (top) heating and (bottom) cooling runs.

9.7. Small angle X-ray scattering

As demonstrated by X-ray data collected at wide angles, incorporation of ethylene-co-propylene polymers does not affect the crystal structures of both LDPE and iPP. Thus we have performed small angle X-ray scattering experiments to probes the influence of EPR on larger size scale structural elements. Under the assumption of the two-phase model consisting of the alternately stacked structure of the crystalline and amorphous layers, the detection of scattering maximum, i.e. long period, in the SAXS pattern reflects the changes in densities between ordered and disordered regions. For all the blend systems investigated here, i.e. binary and ternary, unique scattering maximum was observed in the small angle X-ray scattering patterns and the results are shown in **Figure 2.42** as dependences of the long period as functions of the nature of the EPR and blend composition. In other words, the SAXS intensity distributions did not evidence two types of long period attributable to LDPE and iPP. This might be related to the LDPE-rich composition of the blends for

which the contribution of iPP is not observable. The measurement preformed on melt-crystallized and annealed LDPE/iPP samples indicated long period of 16.6 nm and 18 nm, respectively. This evidences a very little sensitivity of the system towards thermal treatment. It is expected that addition of a third amorphous component, as EPR, will first change the phase distribution within the long period and second lead to a more pronounced sensitivity of the systems with respect to annealing. This assumption was largely confirmed when Dutral054 and Keltan740 were used as compatibilizer, while addition of Keltan13 did not induce remarkable changes.

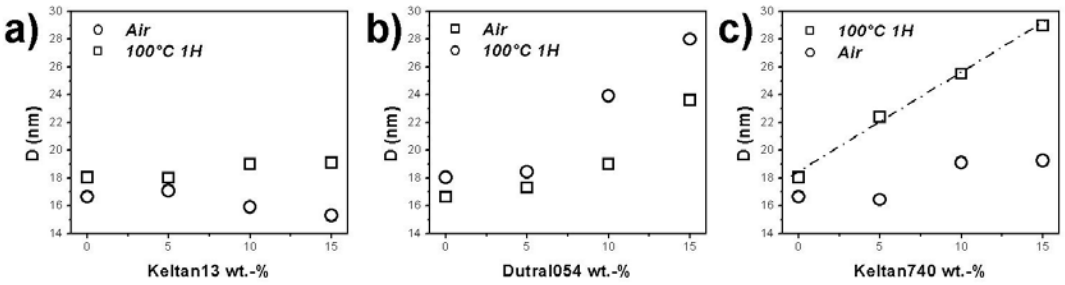

Figure 2.42 - Dependences of the long period as functions of EPR content for a) LDPE/iPP/Keltan13, b) LDPE/iPP/Dutral054 and c) LDPE/iPP/Keltan740 blends. The measurements were performed at room temperature for sample films as obtained directly after cooling by contact with air from the melt and after annealing for 1h at 100°C.

For the two sets of measurements, increasing the content of both Dutral054 and Keltan740 leads to an increase of the long period and a direct relationship, linear dependence, is seen for the annealed LDPE/iPP/Keltan740 samples over the whole composition range (including the LDPE/iPP sample). Similar behaviour is observed for LDPE/iPP/Dutral054 from the 5% composition. Therefore, only a qualitative interpretation of these results is possible in terms of better compatibility between on the amorphous copolymers Dutral054 or Keltan740 and the amorphous domains of the LDPE/iPP blend.

9.8. Mechanical properties

The main motivation of the widespread use of plastic materials is probably because they exhibit very interesting mechanical properties. For this reasons, mechanical properties has long been considered as the most important of all physical and chemical characteristics of high commodity polymers and many efforts have

been dedicated to the understanding of the structure-property relationship. The effect of compatibilzing LDPE/iPP blend was evaluated through stress-strain testing. In this type of measurement the build-up of force (or stress) is measured while the specimen is submitted to a deformation at a constant rate. Stress-strain tests have been for long the most universally used of all mechanical methods. **Figure 2.43** gives a schematic illustration of the behaviour of long chain molecules as measured at constant rate. The terminology commonly used for stress-strain test is indicated. It should be noted that the scales on this graph is not exact but is intended to give an order-of-magnitude of typical values. The slope of the initial stress-strain variation showing a linear dependence represents the elastic modulus *E*. In a tensile test, this modulus is the Young's modulus defined as:

$$E = \frac{d\sigma}{d\varepsilon} \qquad (2.11)$$

The elastic modulus is a measure of the resistance of the material under test to a given deformation. The maximum in the plot, referred as yield point in the figure, indicates the stress at yield σ_y and the elongation at yield ε_y. The last portion of the figure is representative of the characteristics at break of the polymer with the tensile strength σ_B and the ultimate strain or elongation at break ε_B. The stress-strain curve is obtained from the load-deformation curve measured experimentally by the following expressions;

$$\text{Stress } \sigma = \frac{F}{A} \qquad (2.12)$$

where *F* is the force or load and *A* is the cross sectional area,

$$\text{Strain } \varepsilon = \frac{L - L_0}{L_0} \qquad (13)$$

where L_0 is the original length of the sample and *L* is the stretched length of the sample after deformation.

As shown above, highly crystalline polymers such as polyolefin have a complex morphological structure. The macromolecules generally fold within lamellae structural elements with the size of the order of tenth of nanometer in thickness. Between the layers, chains are in a disordered arrangement and the fact that some chains may connect together crystalline domains by going through the amorphous phase gives the mechanical strength of the whole structure.

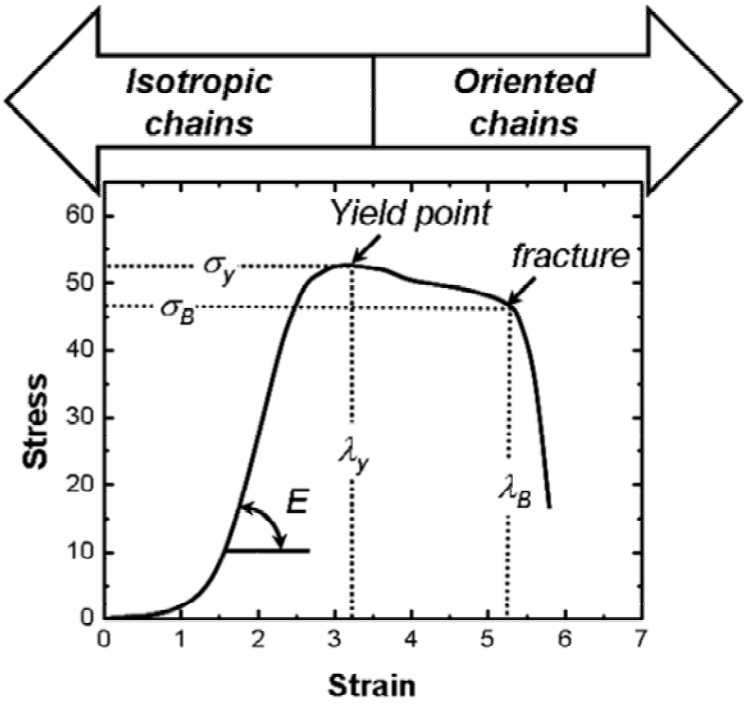

Figure 2.43 - Schematic stress-strain dependence with the indication of the parameters characterizing the elasticity at small deformation as well as the yield and the break points[67].

Interfacial interactions are one of the key parameters controlling the mechanical behaviour of multicomponent heterogeneous systems such as polymer blends. Interfacial adhesion can be experimentally evaluated through SEM observations as discussed above or by determination of the maximum tensile strain at break by mechanical tensile-test measurements. From the stress-strain curves (not shown here) the typical mechanical parameters; Young modulus (*E*), yield point (λ_y, σ_y), tensile (σ_B) as well as elongation (λ_B) at break were determined and the results are shown in the **Figure 2.44**. It may be nevertheless mentioned that rather similar shape of stress-strain curves, showing yield points and plateau of strain hardening region, was obtained for the compatibilized blends and the effect of the nature of the polymeric compatibilizater is clearly seen in the plateau region observed after the yield point.

It is seen that the Young modulus (*E*) decreases with increasing the EPR content. and this effect is more pronounced for Dutral054. In general, Young modulus is closely related to hard domains within materials. Similarly, addition of Dutral054 leads to a significant decrease of the yield stress whose value is divided by two for

LDPE/iPP/Dutral054-15 as compared to LDPE/iPP. Only a slight decreased is observed upon addition of 10% of Keltan740 and Keltan13. Further addition gives Yield stress values nearly similar to the ones obtained in the absence or compatibilizer. In the EPR wt.% investigated, a linear increase of the tensile at break was obtained upon addition of the Keltan740. This indicates that the use of the high molecular weight and ethylene-rich Keltan740 as compatibilizater enhances the resistance of the materials probably due to a stronger adhesion between immiscible homopolymer phases through interaction with the copolymer. It is assumed that longer polymer chains make the system more resistant to the stress. In contrast, addition of Keltan13 or Dutral054 having almost similar ethylene content (54-55%) reduces the tensile strength. The observed variation is sharper in these cases and the tensile at break attain plateau values of about 10 and 7 MPa for ternary blends containing 5wt.-% of Keltan13 and 15wt.-% of Dutral054. Reduction in the strain at break for Dutral-054 and Keltan 13 containing blends is assumed to result from a lack of specific interactions between homopolymers, thereby giving low interfacial adhesion. Addition of EPR significantly increases elongation at break and for EPR content above 5wt.% the values for the Keltan740 based system are much greater in comparison to the cases of the Dutral054 and Keltan13 containing blends. The increased elasticity is assigned to the plasticizer effect of the EPR that is able to incorporate amorphous domains of both homopolymers. Copolymer with the higher molecular weight is assumed to go through a greater number of domains and consequently acting as a more efficient linker. Generally speaking, the more significant improvement of macroscopic mechanical properties, such as elongation at break, observed for ternary blends containing Keltan740 as third component is in a perfect agreement with the SEM observations, from which we concluded that a better adhesion occurs between the two homopolymers upon addition of Keltan740.

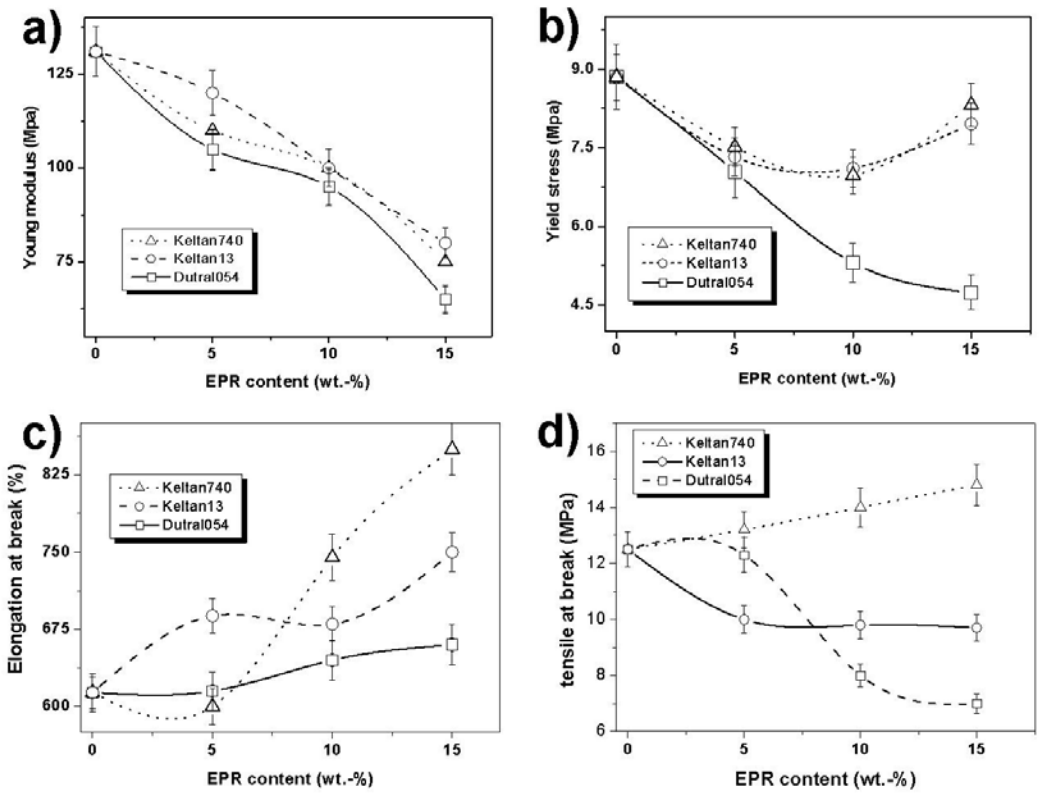

Figure 2.44 - Dependences of a) Young modulus, b) Yield stress, c) elongation at break and d) tensile at break for ternary LDPE/iPP/Keltan13, LDPE/iPP/Dutral054 and LDPE/iPP/Keltan740 blends as functions of EPR content. Meaning of the determined parameters is illustrated in **Figure 2.43**.

9.9. Two-dimension wide and small angle X-ray scattering

The objectives of performing wide and small angle X-ray scattering experiments using a 2D position sensitive detector were to investigate the morphological structures that have undergone deformation after tensile tests.

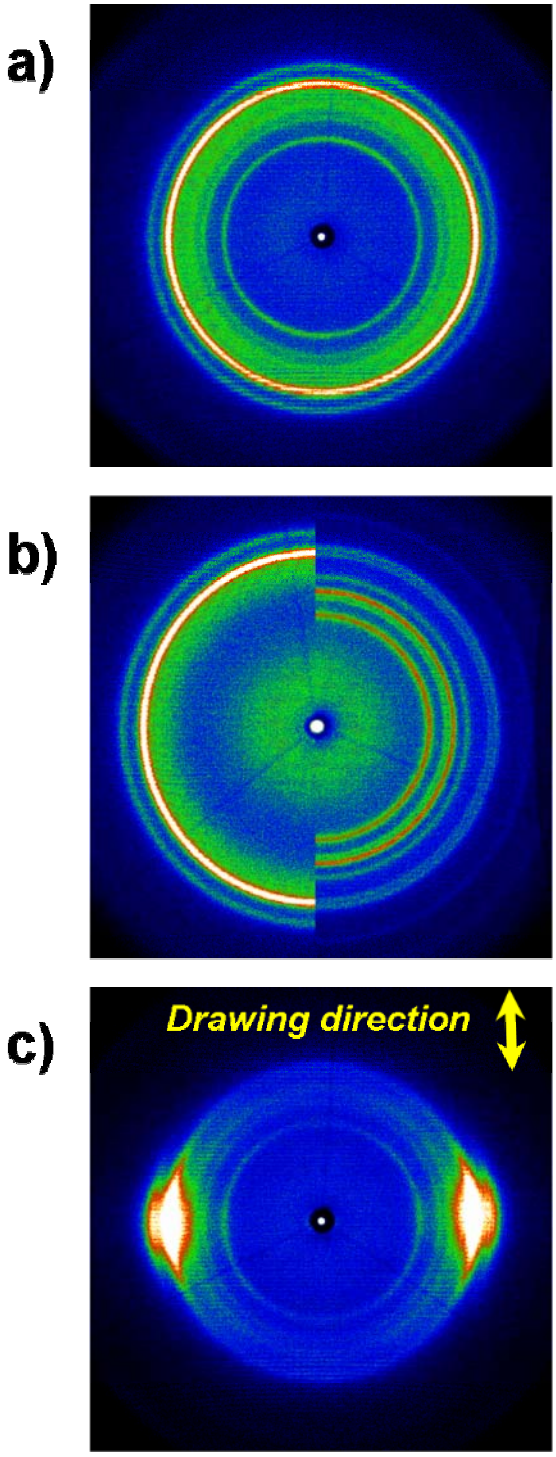

Figure 2.45 - 2D wide angle X-ray scattering patterns recorded at room temperature for a) unstretched LDPE/iPP film, b) unstretched (left panel) LDPE and (right panel) iPP films and c) stretched LDPE/iPP film.

The origin of the macroscopic deformation of LDPE/iPP-based films on the macromolecular size scale was evaluated through wide-angle X-ray scattering

experiments. The measurements were performed on the macroscopically deformed sample after tensile tests. The experimental results for the LDPE/iPP system are well documented by the 2D diffraction patterns shown in **Figure 2.45**. All measurements were performed with the X-ray beam perpendicular to the film surface.

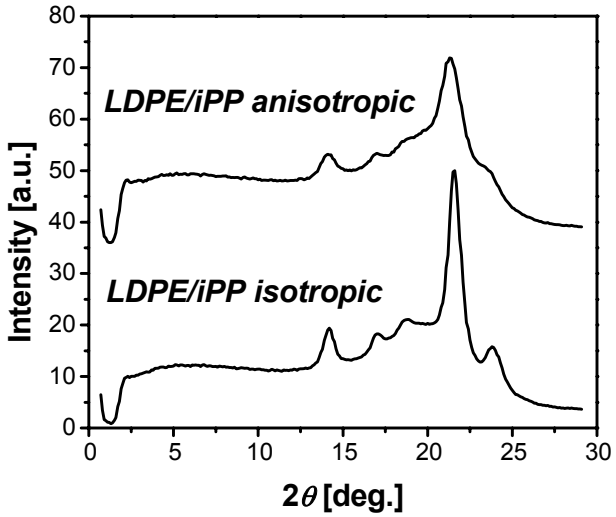

Figure 2.46 - Wide-angle X-ray diffractograms recorded at room temperature for (top) stretched and (bottom) unstretched LDPE/iPP films. The top diffractogram pacorresponds to the azimuthally averaged scattering intensity in the 2D pattern presented in **part c** of **Figure 2.45**.

Similarly to the above discussion about the X-ray diffractograms obtained for the blends with the help of a θ–θ diffractometer the pattern obtained in transmission mode with a 2D detector corresponds to the superposition of reflexions from LDPE and iPP and no differences in the crystal structure was noticed when comparing unstretched to stretched films (**Figure 2.46**). This result demotes a rather uniform crystallization in the bulk and at the surface of the sample. This is also well-displayed by the patterns presented in parts a) and b) of **Figure 2.45**. The top pattern was obtained from an isotropic film of the binary LDPE/iPP blend. A series of five centro-symmetric rings is seen. This indicates an isotropic orientation of the polymer chains within the films. The origin of these rings can be easily identified from the 2D pattern presented in the part b) that presents the 2D patterns characteristic for LDPE and iPP in the left and right hand sides, respectively. The two diffraction rings at wider scattering angles arise from the scattering of the LDPE crystalline structure and the three diffraction rings in the medium angle regime comes from the iPP crystals. The angle positions of the specific reflections remain unchanged in the blend as

compared to the pure homopolymers. This was always the case independently of the nature and amount of the compatibilizer. These observations confirm the absence of co-crystallization.

In part c of **Figure 2.45**, a 2D X-ray pattern typical for the scattering features recorded at any parts of the stretched LDPE/iPP film can be viewed. Orientation was performed by drawing the blend films at a speed rate of 10 $mm.min^{-1}$ at room temperature until ultimate elongation. The first comparison of parts a) and c) of the figure reveals a major difference in the intensity distribution with respect to the azimuthal angle (φ). In contrary to the unstretched case where the scattering intensity distribution is uniform over the φ-angle, in the bottom pattern characteristic for the macromolecular structure of the sample film after extension until break, the scattering pattern reveals a φ-dependent intensity distribution. The changes in the scattering effects indicate that the original structure is transformed upon mechanical deformation toward an oriented structure where the polymer backbones assume a specific orientation nearly parallel to the drawing direction.

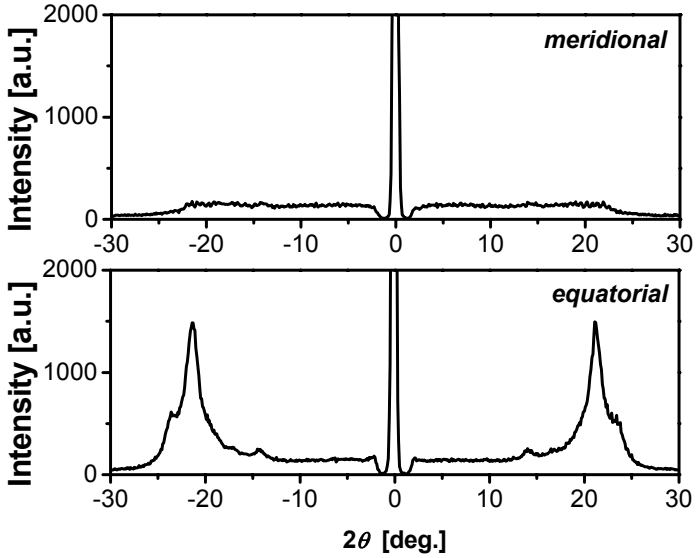

Figure 2.47 - Wide-angle X-ray scattering intensity distributions recorded along (top) the meridional and (bottom) equatorial directions in the 2D pattern presented in **part c** of **Figure 2.45**.

When considering heterogeneous binary systems, there exists a strong relationship between the deformability ability of each component and the degree of interaction, namely the adhesion, between them. It is obvious that if the biphasic morphology is of the type, one phase dispersed in another one, the major component

playing the role of the matrix will respond primarily to the deformation. It is also rather logical to say that when the interaction between the components in the solid state is strong enough, molecular orientation within the dispersed phase domains will also occur. The bottom 2D pattern of **Figure 2.45** gives clear evidence that when 20% of iPP is added to LDPE, tensile stretching experiments lead to highly oriented heterogeneous morphology. The specific location of the five well-distinguishable reflexions along the equatorial direction demonstrates orientation effects for the LDPE matrix and the iPP inclusion. The 2D pattern of the stretched film sample is presented with two intensity distributions recorded along the equatorial and meridional directions (**Figure 2.47**). The intense reflections detected along the equatorial direction (horizontal) together with the nearly zero intensity distribution recorded along the meridional direction (vertical) correspond to the correlation distances between closely packed chains oriented along the drawing direction. Similar scattering were obtained for all the ternary blends (see **Figure 2.48** for the case of LDPE/iPP/Keltan740-15). Thus the evaluation of the changes in the adhesion between the LDPE and iPP was not possible by means of wide-angle X-ray scattering experiments on macroscopically oriented sample films.

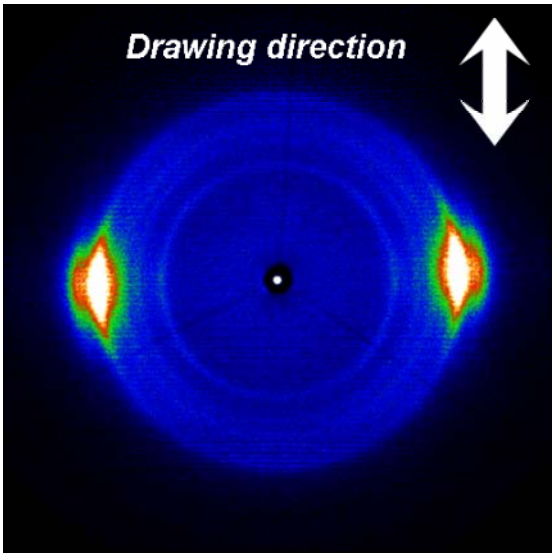

Figure 2.48 - 2D wide angle X-ray scattering pattern recorded at room temperature for a stretched LDPE/iPP/Keltan740-15 film.

Initially, unstrained films show constant diffraction intensity measured at low angle versus the azimuthal angle (**Figure 2.49a**). This indicates an isotropic orientation of the alternating ordered and disordered domains. Then, as films are

tensile stretched until they break the structure as observed on macromolecular size-scale changes and becomes anisotropic.

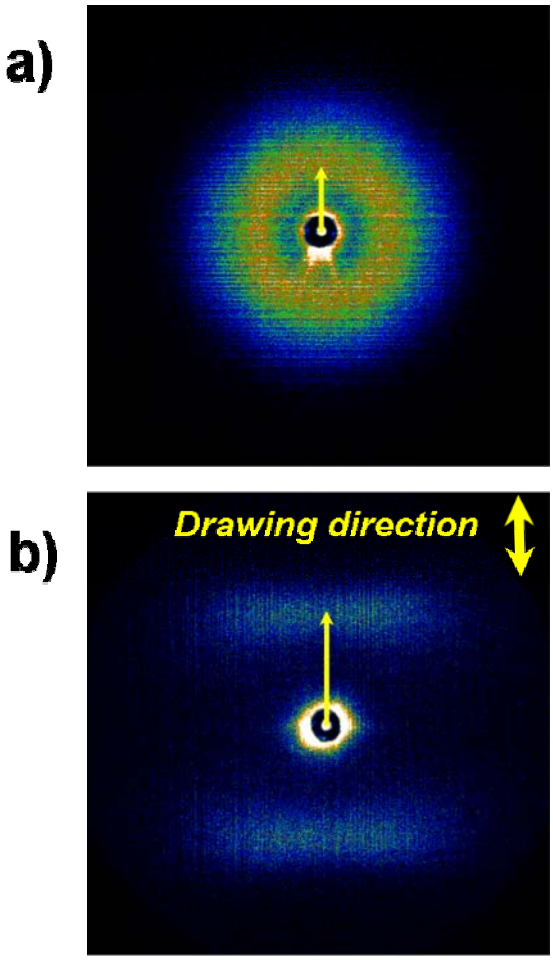

Figure 2.49 - 2D small angle X-ray scattering patterns recorded at room temperature for a) unstretched and b) stretched LDPE/iPP films. The arrows highlight the change in the position of the scattering maximum indicated a decrease of the long period for the stretched film.

Correspondingly, the 2D SAXS pattern indicates a clear ordering along the drawing direction where the bar-shaped scattering intensity maximum seen along the meridional axis gives the long period (**Figure 2.49b**). A more interesting observation is that the position of the scattering maximum is shifted toward larger scattering angle values after tensile stretching of the films. For the case of the LDPE/iPP a decrease of nearly 7 nm of the long period was observed between the non-oriented (~16.5 nm) and oriented (~9.3 nm) films.

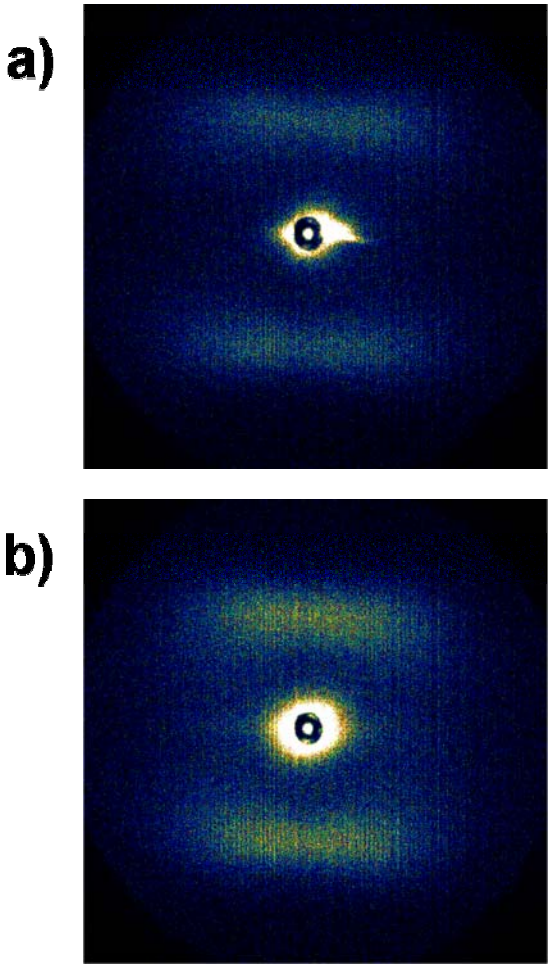

Figure 2.50 - 2D small angle X-ray scattering patterns recorded at room temperature for a) stretched LDPE/iPP/Keltan13-15 and b) stretched LDPE/iPP/Dutral054-15 films.

Similar anisotropic orientation as well as shift of the position of the scattering peak towards larger scattering angle values were observed in all cases after mechanical deformation (**Figure 2.50** and **2.51**). It should be mentioned however that the long period determined for stretched films of a given ternary blend was independent on the EPR content.

All these features clearly demonstrate the change in the morphological elements towards the formation of fibrillar structure.

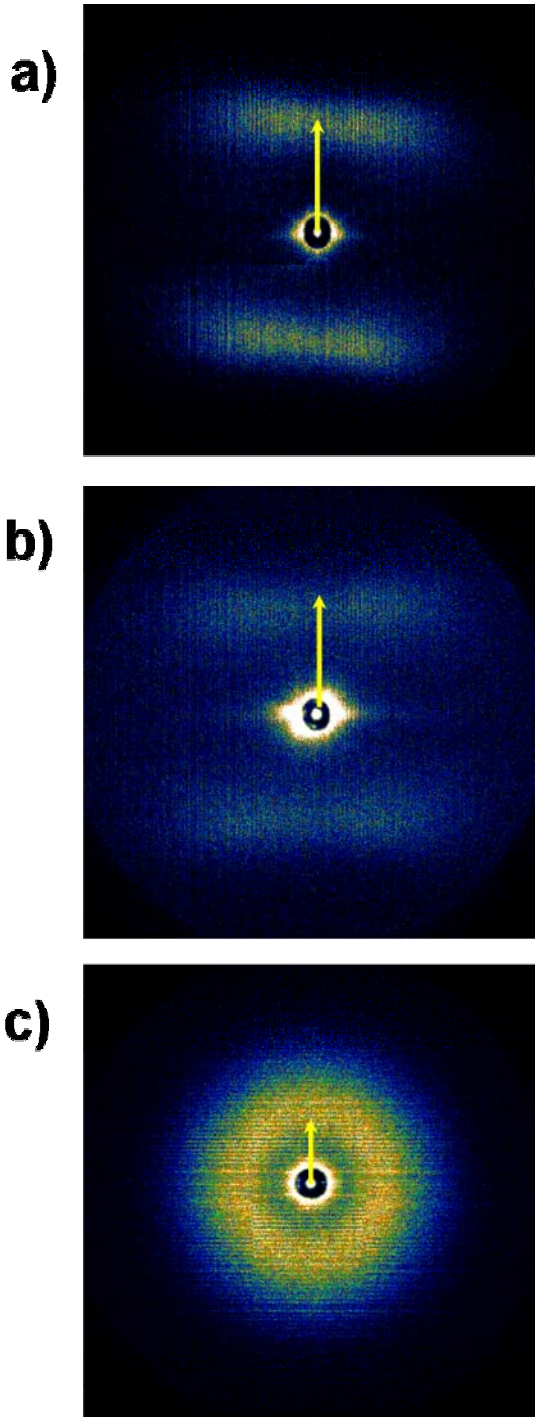

Figure 2.51 - 2D small angle X-ray scattering patterns recorded at room temperature for a) stretched LDPE/iPP/Keltan740-5 film, b) stretched LDPE/iPP/Keltan740-15 film and c) unstretched stretched LDPE/iPP/Keltan740-15. The arrows highlight the change in the position of the scattering maximum indicated a decrease of the long period for the stretched film. The position of the scattering maximum for stretched sample films is independent of the Keltan740 content.

10. Conclusion

In this Chapter, the phase behaviour, morphology and mechanical properties of ternary LDPE/iPP/EPR blends were investigated by means of varied and complementary experimental methods and the results were compared to the behaviour of binary LDPE/iPP blend considered as reference. One of the main concerns of our study was to evaluate the compatibilization ability of the three ethylene-co-propylene copolymers (Keltan13, Dutral054 and Keltan740) and to clearly demonstrate the beneficial effect on the mechanical properties. Depending on the investigation techniques employed, a more or less significant variation of physical properties versus the blend composition was noticed. For example, the DSC results did not evidence major differences in the thermal behaviour of ternary blends as compared to binary one. Similarly, two-dimensional wide angle X-ray scattering performed on film samples after tensile testing did not permit to evidence a difference in orientability of the matrix (LDPE) and dispersed (iPP) phases. In contrast, scanning electron microscopy has revealed to be the most efficient technique to prove the compatibilization effect of EPR. We have shown that EPR may play an important role in reducing the dispersed domains size in semicrystalline/semicrystalline LDPE/iPP 80/20 blends. Chemical composition and molecular weight of the EPR as well as the amount added are the key parameters controlling their ability to compatibilize LDPE/iPP blend. In some cases reduction of the size of the phase separated iPP by a factor two was observed. However, the decrease in the phase segregated domains size does not reflect the enhancement of the miscibility between the LDPE and iPP macromolecules since the DSC data indicate that low density polyethylene and isotactic polypropylene do not cocrystallize although iPP exhibits a considerable depression of crystallization temperature when embedded in a LDPE matrix in comparison to the bulk case. The changes in morphology of ternary blends were corroborated to a large extent by changes in mechanical properties estimated by means of tensile testing. The largest improvement in ductility (elongation at break) was afforded by the high molecular weight and ethylene rich Keltan740 copolymer. From our point of view, Keltan740 provides a better interdiffusion towards the poly(ethylene). Thus in the case of our system where LDPE is used as major component, i.e. constitutes the matrix of the material, Keltan740 exhibits the most efficient compatabilizing effect. In opposite, Dutral054 has a lower ethylene content and is composed of shorter ethylene

segments. So we assume that it exhibits preferential interaction with the propylene. The specific behaviour of Dutral054, for which physical properties such as size of the dispersed iPP domains, elongation at break do not evaluated above 5% of EPR can be interpreted in terms of saturation of the surface covering of the iPP phase separated domains from a content of 5%. Intermediate behaviour was observed for Keltan13-containing blends.

Chapter 3 - Brillouin inelastic light scattering.

Predictions to light scattering from acoustic waves were established by Brillouin[68] and, independently by Mandelstam[69] in the twenties, while a few years later Gross[70] gave the experimental confirmation of these predictions in liquids. The invention of lasers in the sixties gave new impulse to this kind of optical technique, but it was still impossible to detect acoustic as well as spin waves in opaque solids until the advent of new class of spectrometers designed and fabricated for the first time by Sandercock in the seventies[71]. He demonstrated that the sensitivity of a Fabry-Perot interferometer may be dramatically increased by passing the scattered light several times through the same interferometer. Such an improvement led to the observation of light scattering from surface acoustic waves as well as from surface spin waves in both transparent and opaque materials.

1. Introduction.

Brillouin spectroscopy (BS) is based on the scattering of laser by thermal acoustic phonons at hypersonic frequencies (~10MHz-100GHz). From a classical point of view, the compression of medium will changes the index of refraction and therefore lead to some reflection or scattering at any point where the refractive index changes. From a quantum point of view, the process can be considered one of interaction of light photons with acoustical or vibrational quanta (phonons).[72] BS can be used to study directly the dispersion characteristics of sound waves propagating in mesoscopic structures with high accuracy. It has many advantages in comparison with conventional ultrasonic technique or complementary inelastic X-ray scattering since it does not require external generation of acoustic waves and it probes acoustic phonons with wavelengths in the submicron range with moderate absorption. Moreover, BS is a nondestructive and noncontact method which allows to obtain quantitavely the elastic constants of ordered soft matter by monitoring both the momentum transfer and the frequency of the scattered radiation.[73]

Brillouin spectroscopy has become a powerful tool to investigate polymer properties such as molecular orientation, packing state, elastic stiffness coefficients (influenced by polymerization, gelation, and chain length), phase transitions, anisotropy of liquid crystals and interfaces between different materials.[74,75]

A large number of works published by Pietralla and Krüger et al.[76,77] dealt with the study of acoustic properties of amorphous and semicrystalline polymers (PMMA, polyurethane, polycarbonate) under uniaxial tensile-stress using the Brillouin scattering method. The strain dependence of the elastic coefficients was reported. Phase transition in polymers and oligomers and related changes in the order parameters are therefore generally displayed at least by some complex elastic constants involved. The understanding of the complex elastic and anharmonic behavior at the crossover from the fluid state to the glassy (solid) was performed by Patterson.[78]

Recent development in nanotechnology with submicrometer dimensions requires a good knowledge of mechanical properties. Nanostructured photoresistant polymer materials are submitted to several treatments as dissolving, cleaning with deionized water and drying. As a result in of these repeated actions, etched channels between the polymeric walls may collapse. It was shown that structure with higher modulus enhances the resistance to collapse.[79]

For inhomogeneous media, however, with characteristic spacing $d=O(q^{-1})$ additional modes can be observed due to the interaction of light with phonons: particle vibrations and periodic lattice. For example at a given q, lamellar microstructures can display the so-called ″Bragg″-phonons fulfilling the condition $q=k+G$ where G is the reciprocal lattice vector G ($=2\pi/d$).[80] Hence, the phonon dispersion $\omega(q)$ can be a sensitive index of the microphase morphology and the grain orientation in ordered diblock copolymer systems.[81]

Thin films, homogeneous over the length scale O (q^{-1}), have extensively been studied by BS mainly for the determination of the elastic stiffness coefficients; see for example for hard (metal, semiconductor) [82,83] and for soft polymer films.[84,85] In the field of nanotechnology, patterned surfaces are often used in the fabrication of various devices. The elastic excitations in such nanostructured surfaces with a periodic submicrometer grating have been also studied by BS.[86] For Si surfaces patterned with shallow gratings, the dispersion plot $\omega(q||)$ reveals a small gap at the first surface Brillouin zone (π/d) and a hybridization between the surface acoustic modes when the scattering wave vector, $q_{||}$ parallel to the surface is perpendicular to the grating grooves.[87] Besides these transversal and longitudinal surface modes, supported polystyrene films with deep gratings allow for the propagation of additional modes of unknown origin. And very recently, the spatial confinement in thin

poly(methylmethacrylate)/Si_3N_4 double layer membranes with different elastic constants results in thickness dependent longitudinal and transverse standing wave resonances.[88]

Ordered structures are present in simple commodity homopolymers amenable to crystallization e.g. poly(propylene). For spherulites exceeding the probing phonon wavelength, BS should reveal the elastic properties of both crystalline and amorphous regions. In the case of films, the contribution of the surface phonons to the spectrum might provide additional information on the surface rigidity. The use of films rather than bulk samples is compulsory in case of strong multiple light scattering and for thickness much larger than the probing wavelength (~q^{-1}), confinement effects are negligible.

2. Light scattering.

In a normal scattering experiment the monochromatic incident light propagating in a direction given by the wavevector κ_I, this light is scattered in all directions, but in an experiment only one direction of observation given by κ_S is selected, which is described by the modified momentum $\hbar\kappa_S$ (**Figure 3.1**). The change of momentum, which gives information about the interaction of the light with the matter, is defined as $\hbar q = \hbar\kappa_i - \hbar\kappa_S$, q is the scattering vector.[89] For quasi-elastic scattering (i.e the frequencies of the incident and scattered light are approximately equal), as are their wavenumbers $|\kappa_S| \cong |\kappa_i|$) ,the modulus of q follows:

$$q = \frac{4\pi n}{\lambda(\sin\theta/2)} \qquad (3.1)$$

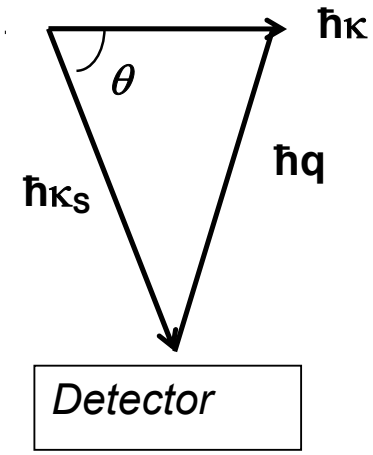

Figure 3.1 - Wavevector conservation of the incident and scattered light.

Static light scattering is recording only an angle-dependent intensity of the scattered light. Dynamic light scattering is considered a frequency (Brillouin spectroscopy) or time resolution of the scattered light. More details will be given in next chapter concerning Brillouin spectroscopy.

3. Inelastic Brillouin scattering

When electromagnetic radiation of optical frequencies travels through matter various spontaneous scattering processes can occur such as Rayleigh scattering, Brillouin scattering and Raman scattering. When light is scattered by acoustic phonons we deal with Brillouin scattering. Acoustic phonons (thermally excited lattice vibration with acoustic modes) produce a periodic modulation of the refractive index.[90] Brillouin scattering occurs when light is diffracted backward on this moving grating, giving rise to frequency shifted Stokes and anti-Stokes waves (**Figure 3.2**). Since the scattered light undergoes a Doppler frequency shift, the Brillouin frequency (frequency difference between pump light and scattered light) v_B depends on the acoustic wave velocity and is given by:

$$\nu_B = \frac{2nV_a}{\lambda_p} \qquad (3.2)$$

where V_a is the acoustic wave velocity within the fiber, n is the refractive index and λ_p is the wavelength of the incident pump light wave. The spectral width $\Delta\nu_B$ is very small and is related to the damping time of acoustic waves or the phonon lifetime T_B. In fact, if the acoustic waves are assumed to decay as exp(-t/T_B), the Brillouin gain has a Lorentzian spectral profile given by:

$$g_B(\nu) = g_B(\nu_B)\frac{(\Delta\nu_B/2)^2}{(\nu-\nu_B)^2+(\Delta\nu_B/2)^2} \qquad (3.3)$$

where ν_B is the full width at half maximum (FWHM). The Brillouin gain spectrum (BGS) peaks at the Brillouin frequency ν_B, and the peak value is given by the Brillouin gain coefficient g_0:

$$g_B(\nu_B) = g_0 = \frac{2\pi n^7 p^2{}_{12}}{c\lambda^2{}_p \rho_0 V_a \Delta\nu_B} \qquad (3.4)$$

where p_{12} is the longitudinal elasto-optic coefficient, ρ_0 is the material density, c is the vacuum velocity of light and λ_p is the pump light wavelength.[91]

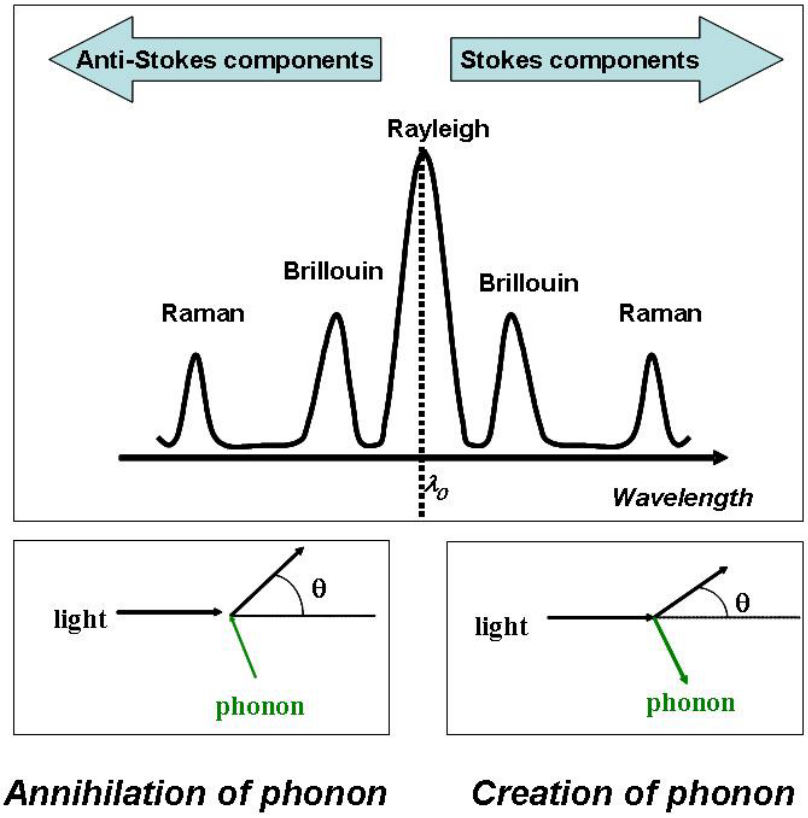

Figure 3.2 - Spectrum of scattered light showing relative powers of Rayleigh, Stokes and anti-Stokes lines.

The kinematics of this light scattering process is governed by energy conservation and momentum:

$$\hbar\varpi_s = \hbar\varpi_i \pm \hbar\Omega \qquad (3.5)$$

$$\hbar k_s = \hbar k_i \pm \hbar q \qquad (3.6)$$

ω_i, ω_s, are the frequencies of the incident laser light, of the scattered light and Ω, of the involved sound wave respectively; k_i and k_s are the wave vectors of the incident laser light and the scattered light with the sample and q is the wave vector of the sound involved. Within the scattering process phonons of energy $\hbar\Omega$ are either created ($\Omega_S=\Omega^-$, Stokes scattering) or annihilated ($\Omega_{AS}=\Omega^+$, Anti-Stokes scattering). A typical BS spectrum is shown in **Figure 3.2**.

The scattering scheme is given in **Figure 3.3**: a laser beam hitting a sound wave with wavelength Λ and frequency Ω under the angleγ. This angle is related to the Bragg condition, $2\Lambda\sin\gamma=\lambda$. Since the sound wave propagates with the velocity ν, the

frequency of the scattered Brillouin light $\nu_B=\omega_s/2\pi$ is shifted according to Doppler effect.

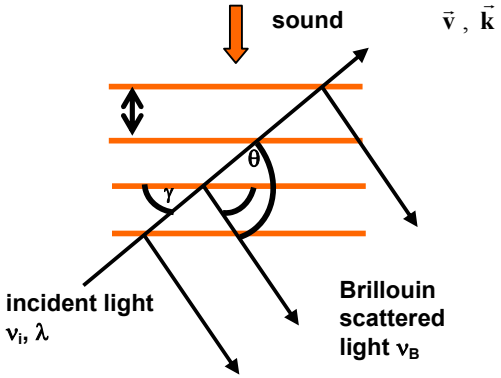

Figure 3.3 - Schematic drawing of Brillouin scattering geometry

$$\nu_B = (1 \pm 2\frac{\vartheta}{c}\sin\gamma)\nu_i$$
$$= (1 \pm 2\frac{\vartheta}{c}\sin\frac{\theta}{2})\nu_i \qquad (3.7)$$

The positive sign in equations (5) and (6) refers to a sound wave counterpropagating to the direction of the incident light (Stokes light), whereas the negative sign describes the sound wave propagating in the same direction (Anti-Stokes light). Inserting in equation (7) the Bragg condition and the relations $\nu/\Lambda=\Omega$ and $c/\lambda=\nu_i$ we obtain a compact condition for the frequency position of the phonon in the Brillouin spectrum:

$$\nu_B = \nu_i \pm \Omega \qquad (3.8)$$

Notice, that besides the elastically scattered Rayleigh light a Brillouin doublet shifted by the frequency of sound appears. The line width of the phonon peak $\Gamma(q)$ defined as the full width at half maximum (FWHM) is inversely proportional to the life time of the phonons involved in the scattering process. Moreover, for moderate sound attenuation (i.e. $\Gamma/\Omega \leq 1$) the frequency of the phonon is proportional to the modulus of the scattering wave vector q:

$$\Omega = \frac{c}{2\pi}\cdot q \qquad (3.9)$$

The proportionality constant *c* is just the sound velocity. Furthermore the elastic stiffness coefficient k is related to the sound velocity *v* and the mass density of the material ρ by:

$$k = \rho \cdot v^2 \qquad (3.10)$$

Brillouin scattering technique is not just a methodological extension of classical ultrasonic techniques to hypersonic frequencies, but also an outstanding spectroscopic method which is especially suitable to investigate the static and dynamic acoustic properties, opto-acoustic and optic properties of soft matter.[90]

4. Scattering geometry.

Figure 3.4 shows schematically the scattering condition for a sample using reflection and transmission scattering geometries. The laser beam hits the sample with wave vector k_i and two possibilities of k_S are displayed by the opposite directions of the scattered wave vector. The reflection case leaves the medium on the same side as the incident laser and in the transmission case leaves the medium on the opposite side. The θ angle can be continuously changed by rotating the sample in case of reflection mode and in case of transmission by rotating laser beam position.

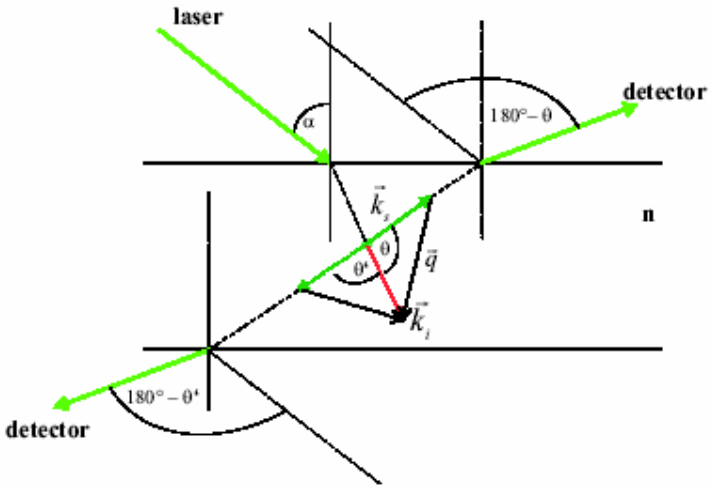

Figure 3.4 - Scattering geometry depicting the reflection and the transmission modes.

5. Experimental set-up.

The set-up used for the measurements consists of a small band Nd:YAG laser (with a wavelength of λ = 532nm and a laser power of *Plaser* = 150mW) which is mounted perpendicularly to the *x*-*y*-plane on the edge of a goniometer (see **Figure 3.5**). A small part of the laser beam is splitted and guided through a fibre into a six-pass tandem Fabry-Perot interferometer (TFPI). This reference beam assures a stabilization of the interferometer without loss of sensitivity. The laser power,

effectively hitting the sample, is reduced to 62mW because of several optical components (prisms, Glan-Thomson polarizer and mirrors) which are necessary to guide the laser beam through the centre of the goniometer. The scattered light is focused through lenses onto the pinhole aperture (∅=200μm) of the TFPI. A synchronized mechanical shutter placed in front of the entrance of the interferometer cuts out the Rayleigh peak. By rotating the arm of the goniometer we can change the scattering angle θ without moving around the complete TFPI set-up. Because of limitations given by the set-up the scattering angle only ranges from θ = 5° to θ = 150°. An avalanche photo diode connected to a multichannel analyzer transfers the collected scattered light to a PC for further signal processing.

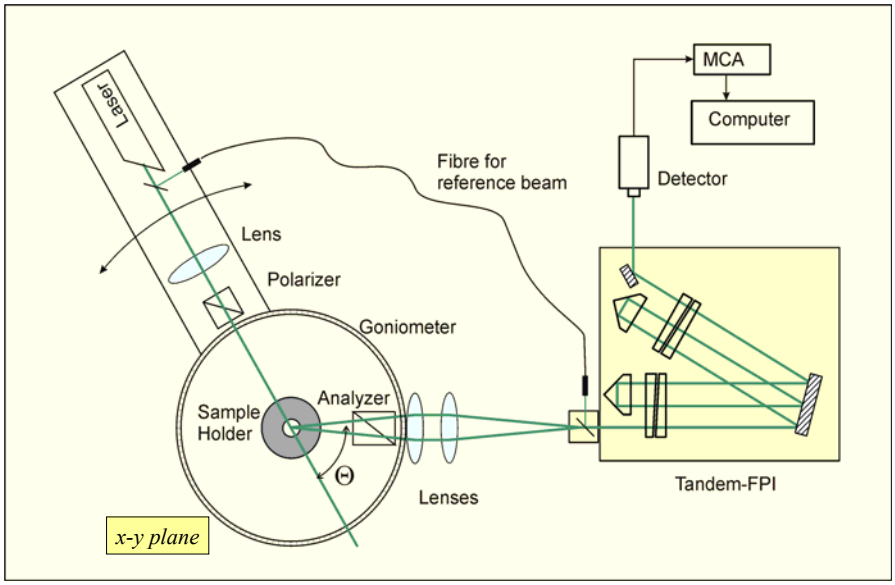

Figure 3.5 - Schematic drawing of the experimental set-up[92].

6. The Tandem Fabry-Perot interferometer.

An important practical application of interference by multiple reflections is the Fabry-Perot interferometer. Its basic construction consists of two flat glass plates, arranged in a mechanical support with spacers between them so that they are parallel to one another. The two inner surfaces are coated so as to have a high reflection coefficient, but to transmit a small amount of light. There are several important qualifications which a Fabry-Perot interferometer should be taking into account: i) the plates must be flat to a very high degree of accuracy (better than λ/50); ii) the inner surfaces (reflective) must be very parallel to one another; iii) the

distance between plates, which can be very large (centimeters) must not change with time, due to temperature or other fluctuations.[93]

For a mathematical description of the interferometer interference of monochromatic light at a plane-parallel plate of thickness *d* with refractive index *n* may be considered. The situation depicted in **Figure 3.6**, light of intensity I_I, with a wavelength λ and a wave vector $\kappa=2\pi/\lambda$ is incident on a plane-parallel plate. The two surfaces affected both by a reflectance *R* and transmittance *T,* defined for the intensities. The absorption of the plate material should be negligible, thus *R*+*T*=1 (energy conservation). To calculate the transmitted and reflected intensities I_t and I_I, we have to sum up the amplitudes of the respective waves, taking into account the phase shifts imposed by the plate. The ratio of transmitted to the incident intensity I_t / I_I is called Airy function

$$\frac{I_t}{I_i} = \frac{1}{1+\frac{4R}{(1-R)^2}\cdot\sin^2(\frac{\varphi}{2})} \qquad (3.11)$$

where φ

$$\varphi = \frac{4\pi\cdot n\cdot l\cdot\cos\alpha}{\lambda} \qquad (3.12)$$

is the phase angle between two neighboring beams. It reduces to $\varphi=4\pi ndcos\alpha/\lambda$ for perpendicular incidence of the light. From equation (11) it is seen that a given spacing *d* the interferometer will transmit only certain wavelengths λ for integral values of *m:*

$d=m^*\lambda/2n$, $m=1,2,3\ldots$ *(13)*

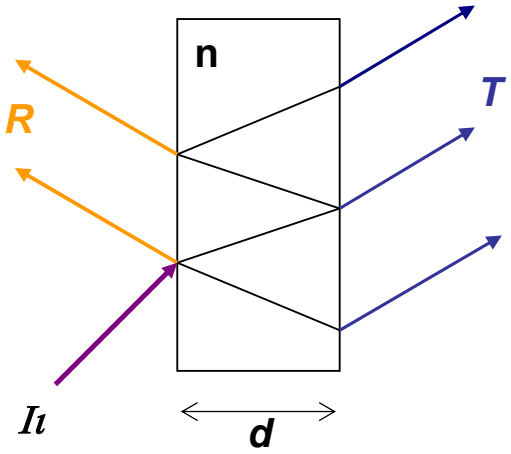

Figure 3.6 - Interference of monochromatic light at a plane-parallel plate of thickness *d*.

The spacing between two minima (or maxima) of the Airy function, i.e. the distance between successive transmitted wavelengths is defined as the free spectral range (FSR) of the FPI. **Figure 3.7** shows the transmitted signal of FPI for several values of the reflectance *R*. With increasing value of R the airy function gets sharper, thus increasing FSP. Furthermore it is customary to define a numerical value which characterizes the width – or sharpness – of the maxima. This number called the *finesse* of an interferometer and is defined as the ratio of the peak distance $\triangle\lambda$ to the full width at half maximum $\delta\lambda$ of the peak.

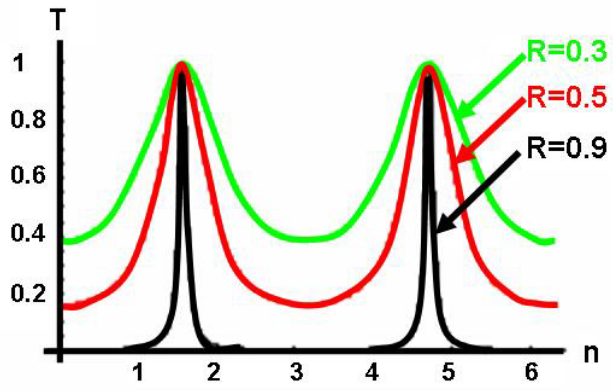

Figure 3.7 - transfer function of a plane-parallel plate for different reflectivities.

The classical FPI setup is used as a spectrometer by varying the spacing *d* in order to scan the light intensity at different wavelengths. Since the measured intensity at a given spacing is the sum of the intensities at all wavelengths satisfying condition (13) an unambiguous assignment of for example two different wavelengths in the spectrum is thus impossible. To overcome this problem one can use two interferometers with different free spectra range in conjunction, one for coarse and one for finer resolution, a so called Tandem-Fabry-Perot interferometer, which was first designed and built by J.R. Sandercock. The two interferometers work in different interference orders N_1 and N_2, respectively. They have to be synchronized such that in the spectral region investigated the interference maxima for all wavelengths coincide:

$$\lambda = \frac{2(l \cdot n)_1}{N_1} = \frac{2(l \cdot n)_2}{N_2} \qquad (3.14)$$

$$\lambda + \Delta\lambda = \frac{2((l \cdot n)_1 + \Delta(l \cdot n)_1)}{N_1} = \frac{2((l \cdot n)_2 + \Delta(l \cdot n)_2}{N_2} \qquad (3.15)$$

this last equation also ensures that neighboring orders are suppressed.

$$\frac{2((l\cdot n)_1+\Delta(l\cdot n)_1)}{N_1}\neq\frac{2((l\cdot n)_2+\Delta(l\cdot n)_2)}{N_2}\quad\text{for}\quad N_1\neq N_2 \qquad (3.16)$$

The synchronization condition necessitates that besides synchronization at λ, the tuning of the two interferometers has to be also synchronized according to:

$$\frac{\Delta(l\cdot n)_1}{\Delta(l\cdot n)_1}=\frac{(l\cdot n)_1}{(l\cdot n)_1} \qquad (3.17)$$

One way to achieve this is to use air spaced interferometers with fixed spacing which are tuned by the air pressure in a common compartment. Equal $\triangle n$ values in both systems obviously fulfill the above condition. A different, very elaborate set-up is used in the interferometers of Sandercock. The principle scheme is sketched in **Figure 3.8**. The two FPI are tilted against each other by an angle θ. The two cavities are adjusted so that the ratio of the two spacing obeys the following condition:

$$\frac{d_2}{d_1}=\cos\theta \qquad (3.18)$$

The movements of the two cavities are coupled using joint mechanics; the direction of scan is indicated in **Figure 3.8**. Through this mechanical set-up it is ensured that $\frac{\Delta d_2}{d_1}=\cos\theta$ which combined with equation (18) directly fullfills the synchronization condition in equation (17).

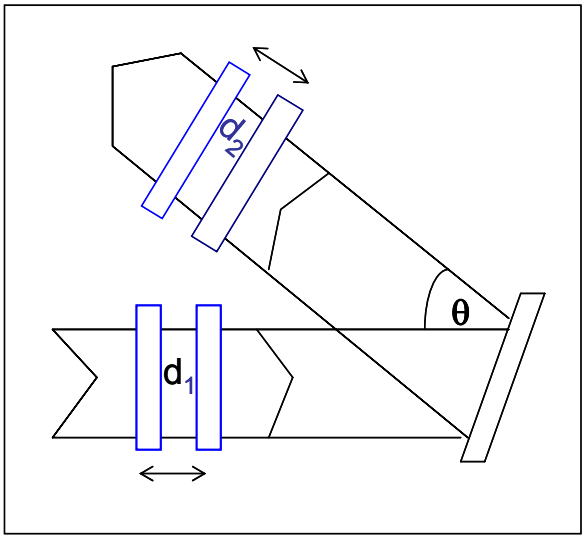

Figure 3.8 - Tandem interferometer with mechanical coupling of the two movable plates. The double arrows indicate the direction of movement.

T-FPI is an optical instrument which uses multiple-beam interference. Advantages are obtained by using a T-FPI: higher contrast (up to 9 optical passes have been realized; larger effective free spectral range. Several hundred cm^{-1} can be obtained. It was demonstrated the improvement of spectra of many amorphous polymers, which generally have only extremely small cross sections for purely transverse polarized acoustic phonons.[94] As a consequence of the strongly increased contrast of the T-FPI, the transverse "phonon lines" of polystyrene could be resolved. For many isotropic amorphous polymers five-pass T-FPI is not sufficient to resolve transverse acoustic phonons.[95]

7. Surface effect by Brillouin spectroscopy

During the last few years a few works were carried in the field of Brillouin scattering from surface excitations, both experimentally and theoretically. On a material boundary where both the optical and acoustic properties undergo a change, the acoustic modes traveling toward the interface have, in general, a displacement component $u_z(q,\Omega)$ perpendicular to the surface. A free surface in thermal equilibrium is therefore rippled by the bulk modes. This dynamic surface roughness acts as a superposition of traveling diffraction gratings when light is incident[96]. In addition to the bulk modes, the thermal acoustic surface modes on a free boundary of an isotropic solid make their contribution to the surface-ripple effect. These so-called Rayleigh waves penetrate into the bulk over a distance comparable to the acoustic wavelength, and hence make also a photoelastic contribution to their scattering light. When two different materials are in close contact along their boundaries, combined acoustic surface excitations are possible which are called Stoneley waves[97].

Several authors have developed the theory of Brillouin scattering from surface phonons in opaque materials[98,99]. These theories take account of the scattering from the surface corrugation induced by the thermally excited phonons (ripple effect) as well as from inhomogeneities induced by the phonons in the dielectric function of the medium (elasto-optic effect).

The light scattering from metallic surfaces was successfully explained in terms of ripple mechanism only. This was done by Loudon for aluminum and by Sandercock for aluminum-coated semiconductors. For opaque semiconductors it has been shown that some features of the spectra are due to the elasto-optic coupling.[100]

8. Investigation of semicrystalline polymers and blends by Brillouin spectroscopy.

In this chapter, we present the first report about the investigation of elastic parameters of semicrystalline polyethylene, polypropylene and its blend by means of the nondestructive Brillouin light scattering (BS) measurement. The mechanical performance of semicrystalline polymeric materials is strongly dependent on the underlying microstructure. The elastic behavior depends on percentage of crystallinity, the initial crystallographic and morphological texture of polymer materials. For spherulites exceeding the probing phonon wavelength, BS should resolve the elastic properties of both crystalline and amorphous regions.

Both low density poly(ethylene) (LDPE) and isotactic poly(propylene) (iPP) are semicrystalline in nature, consequently its blend consists of two amorphous and two crystalline domains, making ore difficult to estimate the influence of elastic properties of iPP on elastic coefficients of LDPE matrix. For this reason, we have studied first the influence of crystal structure and morphology on elastic properties of homopolymers and then we have focused on the study of a LDPE/iPP blend of composition (80/20) (w/w).

8.1 Results and discussion

The three samples used in this work, namely isotactic polypropylene (iPP), low density polyethylene (LDPE) and LDPE/PP blend (80/20), were prepared either by quenching from the melt in water at room temperature (the samples are referred as to q-iPP, q-LDPE, q-LDPE/iPP) or by slowly cooling the films in the press with the cooling rate of 8°C/min (the samples are named a-iPP, a-LDPE, a-LDPE/iPP). In our experiments, laser light is focused onto free standing polymer films, and only a very small amount of the light is scattered from thermally excited waves moving in the material. The thickness of the films was 50-100μm.

Figure 3.9 shows the experimental I (ω) spectra for the quenched iPP film measured at $q=0.034nm^{1}$ (θ=150°) and for two different values of the scattering wave vector component $q_{||}$ parallel to the film surface (θ_r =40° and 50°). The measurement was performed at 20°C. At first glance, the spectra display two Brillouin doublets, only one of which (denoted as mode 2 in the figure) is dependent on $q_{||}$. The shift of the peak position with varying $q_{||}$ is indicated by the dashed vertical lines. The difference

in the behavior of the position of the peaks assigned to mode 1 and 2 with respect to the magnitude of $q_{||}$ allows for distinguishing between bulk (1) and back scattering (2) excitation contributions.

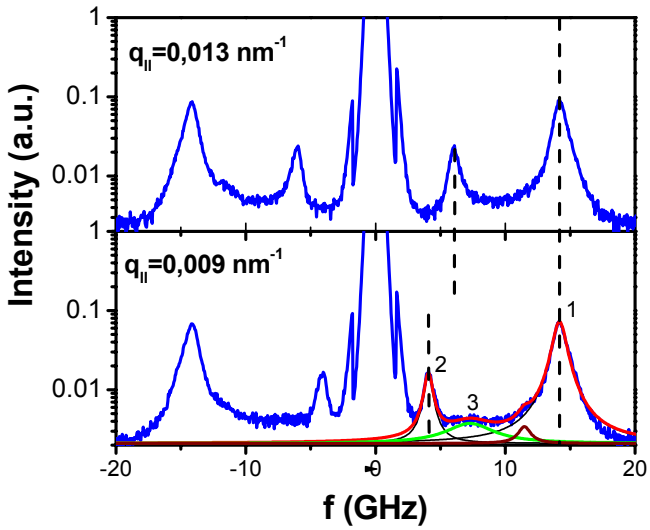

Figure 3.9 - Polarized Brillouin spectra of the free standing quenched polypropylene film at q=0.034nm^{-1} and two values for the photon wave vector q|| parallel to the surface as indicated in the plot. The peak (1) relates to the longitudinal bulk phonon whereas the peak (2) is due to the back scattering effect since its frequency varies with q||. The vertical dashed lines denote the frequencies of the two modes. The weak shoulder at the low frequency side of peaks (1) is due to interferometer ghost lines. The solid line denotes the fit of four lorentzian spectral lineshapes to the experimental spectrum.

For a quantitative analysis, the experimental I(ω) were represented by a sum of three lorentzian lineshapes using the amplitudes (I_i), the peak positions (ω_i) and half width at half height (Γ_i) as free parameters (i=1-3). The third lorentzian is necessary to describe the frequency region between modes (1) and (2) while the small shoulder at the low frequency wing of mode (1) arises from the ghost contribution, i.e the interferometer higher order. The solid line in lower panel of **Figure 3.9** is then the representation of the experimental spectrum considering the four contributions. Next, we consider the two main peaks and postpone the discussion of the intermediate spectral feature (3) to the next section.

The variation of the amplitude I_i and linewidth Γ_i of the modes (1) and (2) are expected to display different q|| dependencies (**Figure 3.9**). The intensity $I_1 \sim kT\beta_s$ is q-independant to local adiabatic density fluctuations controlled by the value of the compressibility β_s and the line width $\Gamma_1 \sim q^2$ is q dependant [101]. In fact, **Figure 3.10** demonstrates the insensitivity of these two quantities for the bulk phonon (1) to $q_{||}$ variation at constant q.

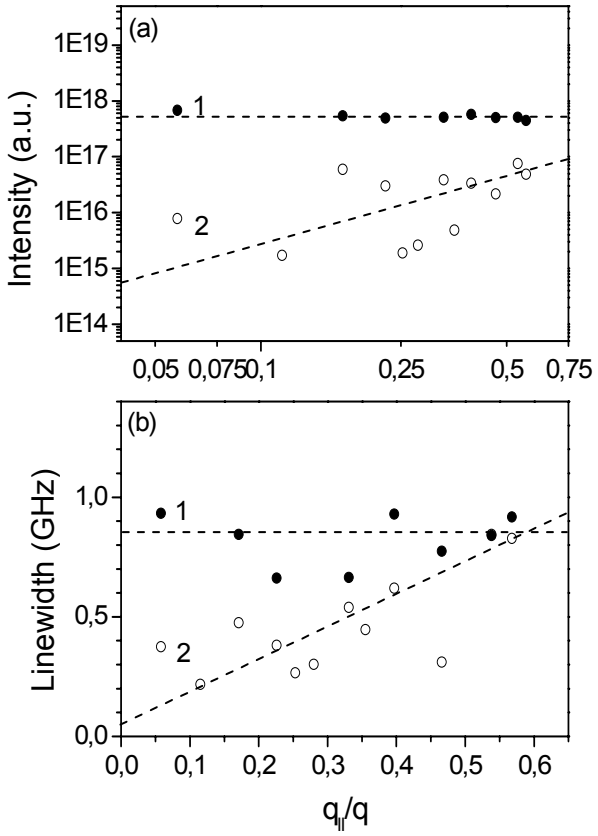

Figure 3.10 - Inelastic scattering amplitude (a) and line width (b) for the back scattering (2) (open circles) and bulk (1) (solid circles) modes of **Figure 1** plotted as a function of q|| in a log-log plot. The dashed lines are to guide the eye.

On the contrary, both I_2 and Γ_2 clearly increase with q|| underlining the surface character of this phonon. Within the experimental error, **Figure 3.10** suggests the scaling $I_2 \sim$ q|| and $\Gamma_2 \sim$ q|| i.e. long wavelength of back scattering mode. Like for the bulk phonons, hydrodynamic viscous fluid behavior would predict a stronger $\Gamma_2 \sim q^2_{||}$ dependence. [102]

The plot in the wave propagation is the dispersion relation of the phonon frequencies $f_i(=\omega_i/2\pi)$ obtained from the experimental I(ω) as a function of q and q||. Based on the latter dispersion shown in **Figure 3.11** at a given q, there is one longitudinal acoustic phonon (open squares) propagating in the bulk of the film with $\omega_1=c_L q$ and one primarily back scattering longitudinal phonon (open circles) with $\omega_2=c\, q_{||}$.

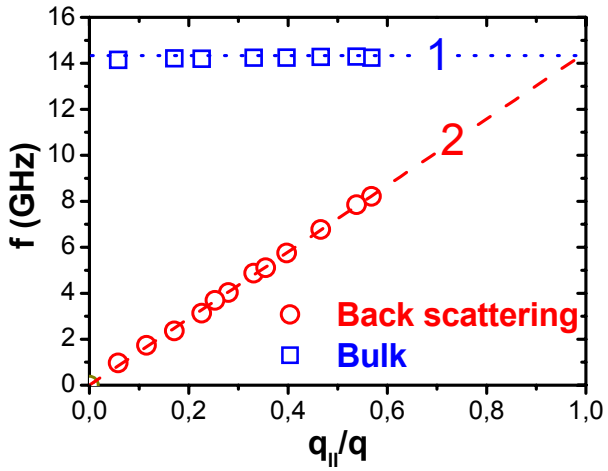

Figure 3.11 - The dispersion relation f(=ω/2π) versus q||/q at constant q=0.034nm^{-1} in q-iPP film obtained from the spectra of **Figure 3.9**. Open squares and circles indicate the longitudinal phonon (1) in the bulk of the q-iPP and the back scattering mode (2), respectively. The frequencies of the two modes coincide at $q_{||}/q=1$.

The phase velocity c_L=2590m/s leads to the modulus M ($=\rho c_L^2$) of about 6 GPa (also known as elastic stiffness constant c_{11}) which is in a good agreement with reported values for PP. [103] Theoretically, the velocity of the usual Rayleigh surface excitation is $0.933c_t$ i.e. localized almost in the transverse bulk threshold for an isotropic solid with Poisson ratio 1/3.[104] Calculations on the relative strength of these matter displacements at soft surfaces are missing. The observation of the longitudinal surface mode is rather unexpected since this mode is polarized parallel to the surface and hence does not ripple it. It was suggested that corrugated (metal) surfaces could rotate the polarization of the longitudinal mode.[105] However, the surface mode of polypropylene and polyethylene films was not observed.

The presence of a single bulk phonon suggests homogeneous **q-PP** film for length scales above about q^{-1} as it is clearly confirmed by the optical micrograph in Figure **3.12a**.

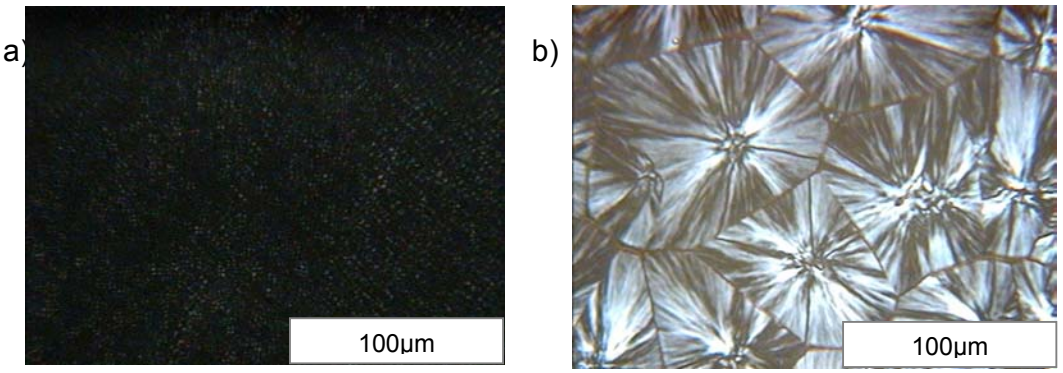

Figure 3.12 - Polarized optical micrographs showing the crystalline morphology of a) quenched and b) annealed iPP films used for the Brillouin scattering experiments.

The absence of sizeable spherulites, however, does not imply a fully amorphous film. In fact, X-ray scattering reveals a low crystallinity (~37%) which apparently does not affect the elasticity of the effective medium.

The Brillouin spectra of q-LDPE and a-LDPE are presented in **Figure 3.13**. The both spectra for annealed and quenched samples exhibited similar picture of two peaks in stoke and anti-stokes frequency range. One peak corresponds to the longitudinal bulk phonon (1) and another to the back scattering effect (2). An analysis of the peaks shows that the longitudinal sound velocity does not vary for a-PE, q-PE and the same value like for q-PP c_L=2590m/s was obtained.

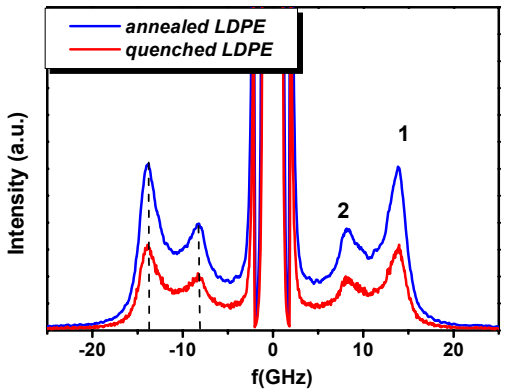

Figure 3.13 - Polarized Brillouin spectra of the free standing quenched and anneled polyethylene films at **q=0.034nm^{-1}** and two values for the photon wave vector $q_{||}$ parallel to the surface as indicated in the plot. The peak (1) relates to the longitudinal bulk phonon whereas the peak (2) is due to the back scattering effect since its frequency varies with $q_{||}$.

In order to see features of submicroscopic structures of these samples were employed X-ray, POM and AFM. The degree crystallinity was integrated from WAXS profile **Figure 3.14** and the results are reported in **Table 3.1**.

A typical orthorhombic crystal structure of polyethylene was obtained for q-LDPE and a-LDPE with the peaks seen in the 2θ range 10-30° corresponding the (110) and (200) reflections. The crystallinity was found to increase from 29% for q-LDPE to 36% for a-LDPE. The size of lamella appears to be almost two times greater for a-LDPE (SAXS not shown).

Table 3.1 - Crystalline characteristics and elastic properties of LDPE and iPP homopolymers melt crystallized under quenched or annealed conditions.

Sample	χ, degree crystallinity %	D, long period, nm	Lc, lamellae thickness, nm	Elastic Constant,GPa	
				c_{11}	C_{44}
a-PP	~60	19.3	11.6	8.2	1.7
q-PP	~37	11.5	4.3	6.8	--
a-PE	~39	4	1.6	6.75	--
q-PE	~26	2	0.6	6.71	--

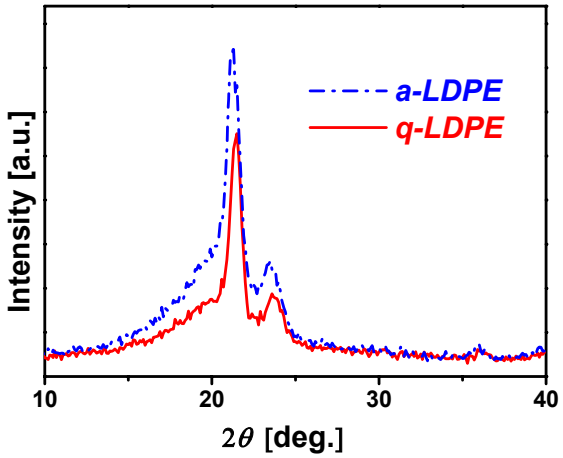

Figure 3.14 - Wide angle X-ray scattering intensity distributions measured at room temperature for (dashed line) annealed LDPE film and (solid line) quenched LDPE film.

It is worth to estimate spherullitic morphology, since q-LDPE and a-LDPE differ in the proportions of crystalline/amorphous phases. The AFM images of films are shown in **Figure 3.15**. In the case of a-LDPE we can see a well-defined nucleus center from which the crystalline lamellae fan out to fill up the volume. The

spherullites are bended to each other, forming compact net with average size 12μm. The spherullitic features of q-LDPE is less obvious and the domains size is about 1,5μm.

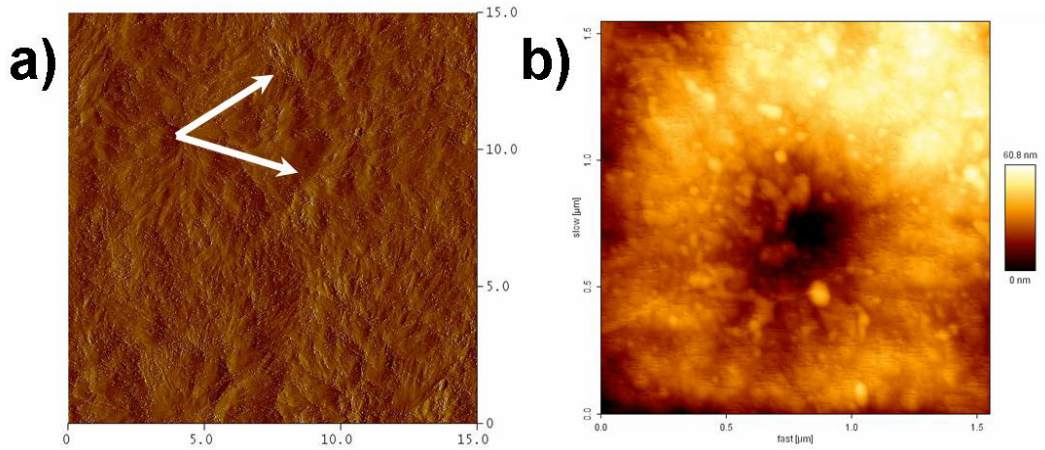

Figure 3.15 - AFM images recorded for a) a-LDPE (phase) and b) q-LDPE (height).

The different thermal treatments affect not just degree crystallinity, but also microstructure, i.e. thicknesses of amorphous and crystalline layers. The crystalline long period, D, which is related to the distance between lamellae, was determined from SAXS measurements. Since sample thickness varied and beam intensity fluctuated during the experiments, ascaled intensity is plotted against the scattering vector q, which is defined as:

$$q = \frac{2\pi}{D} = \frac{4\pi}{\lambda}\sin\theta \qquad (3.19)$$

where D is the lamellar long spacing, λ the X-ray wavelength and θ the scattering angle. The scattering angle can be calculated from the position of the scattered intensity. The peak position of the SAXS profiles is taken to calculate the average lamellar thickness from:

$$Lc = \chi * D \qquad (3.20)$$

Where χ if the degree crystallinity obtained from the WAXS profile and *Lc* the lamellar thickness.

$$\chi = \frac{\int q^2 I_{cr} dq}{\int q^2 I dq} \qquad (3.21)$$

The degree of crystallinity is given by the fraction of the total (I (q)) WAXS scattering due to the crystalline I_{cr} (q) contribution.[106]

The crystallinity χ, lamellar thickness Lc for the samples are shown in **Table 3.1**. As expected, the degree crystallinity was found to be lowest for the quenched samples and higher for the annealed samples for all polymers used. iPP is an attractive polymer to investigate, since the variation of spherullites, ratio crystalline/amorphous is relatively large, range from more amorphous to high crystalline. In order to assess the effect of submicron heterogeneities on the high frequency elasticity, we utilize the slowly annealed a-iPP exhibiting the well developed crystalline morphology with large spherulitic domains shown in **Figure 3.12b**. The Brillouin spectra of the a-PP film in **Figure 3.16** display up to four acoustic excitations depending on the magnitude of q||. The additional peaks in the spectrum present bulk phonons (1′,3′,4) since their frequencies do not depend on q|| at constant q. The experimental I (ω) can be represented by four lorentzians plus the ghost line as it was the case for q-PP, q-PE and a-PE in **Figure 3.9** and **Figure 3.13**, respectively.

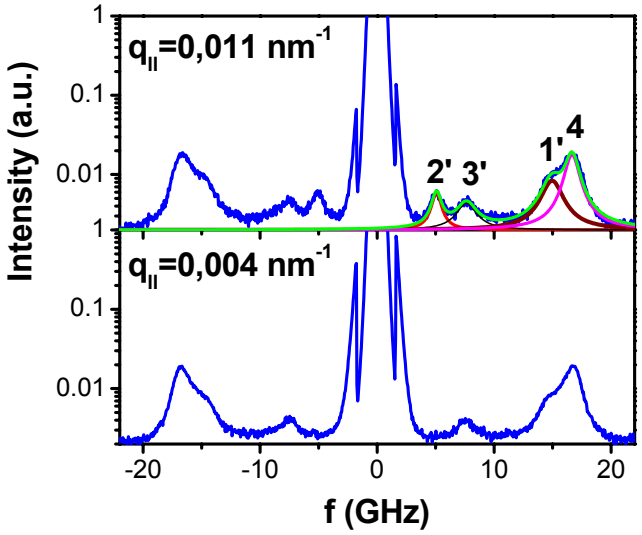

Figure 3.16 - Polarized Brillouin spectra measured at q=0.034nm^{-1} and at two different values of $q_{||}$ for the free standing isotactic polypropylene film obtained by slowly cooling (8°C.min^{-1}, a-iPP) from the molten state to ambient temperature. The a-iPP film shows two additional elastic excitations denoted as (3′) and (4) independent of $q_{||}$ at constant q. The peaks designated by (1′) and (2′) correspond to (1) and (2) of **Figure 3.9** albeit somewhat shifted to higher frequencies. The solid color line denotes the fit of four lorentzian spectral lineshapes to the experimental spectrum.

The frequency f_i (i=1-4) of the four phonons in a-iPP are shown in the dispersion plot presented in the left part of **Figure 3.17** along with the two frequencies of modes (1) and (2) of **Figure 3.11** indicated by dashed lines for the sake of clarity. Based on the displayed relations for the a-iPP film, there are three bulk and one single back scattering phonon. The former present two longitudinal polarizations due to the closeness of the simple acoustic phonon (1) in **q-PP** and a transversal phonon (3′). The bulk origin of these phonons is verified by their dependence on the magnitude of q as shown in right hand side of **Figure 3.17**.

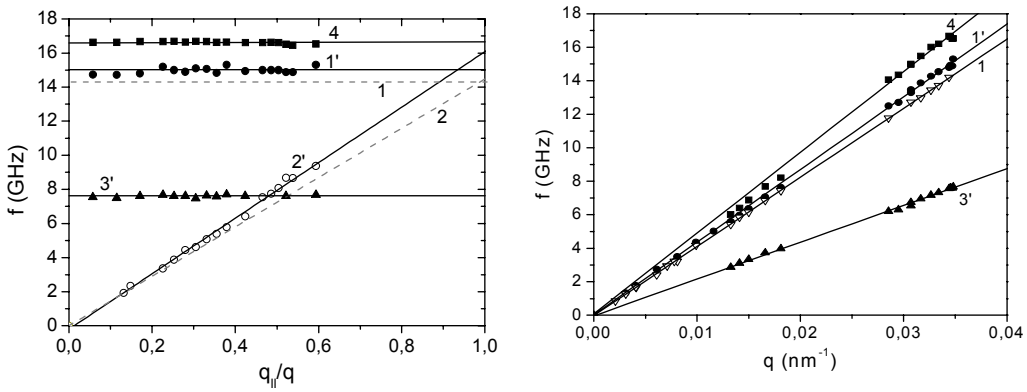

Figure 3.17 - The dispersion relation f(=ω/2π) versus $q_{||}/q$ at constant q(=0.034nm^{-1}) (left panel) and versus q (right panel) obtained from the experimental Brillouin spectra of the a-iPP film. The dispersion relations in **q-PP** is denoted by the two dashed lines Solid symbols indicate the two longitudinal and the transverse phonons in the bulk of the a-PP film whereas the open circles denote the surface mode which reveals longitudinal polarization; the frequency of the back scattering at $q_{||}/q=1$ assumes a value intermediate between the bulk longitudinal phonons.

Note that the frequencies of the bulk phonon (1) and the back scattering excitations (2) in q-PP are systematically lower than the respective (1′) and (2′) in a-PP (Fig.9)**.** The slope of the linear dispersion f~q yields the values c_L=2590m/s for the longitudinal sound velocity in q-PP and c'_L=2730m/s, c_2=3026m/s and c_T=1380m/s for the two longitudinal and shear sound velocity in a-PP. The transversal phonon (mode 3 in **Figure 3.9**) is much stronger in a-PP (mode 3′ in **Figure 3.16**) due to the presence of solid spherulites (**Figure 3.12b**).

The two longitudinal phonons in a-iPP relate to the heterogeneous morphology of the film over length scales larger than the phonon wavelength 2π/q with values in

the range 180-2000nm. In addition, the sufficient elastic constant contrast $(c_2/c_l)^2$ between amorphous and crystalline PP allows the detection of the modes (1′) and (4). Hence, the highest frequency phonon (4) (**Figures 3.16** and **3.17**) is attributed to the sound propagation within the crystalline microphases. The a-PP is then envisaged as an effective medium with c'_L falling between c_L and c_2 of the amorphous and crystalline pure phases, respectively. Since the compressibility β_s $(=1/\rho c'^2_L)$ of the effective medium is a concentration average of the compressibilities of the individual phases, the experimental c'_L can be captured by a crystalline fraction of about 35%. The physical state of the a-PP appears to affect the intensity and the life time of the bulk phonon (1′) and (4) as shown in **Figure 3.18**.

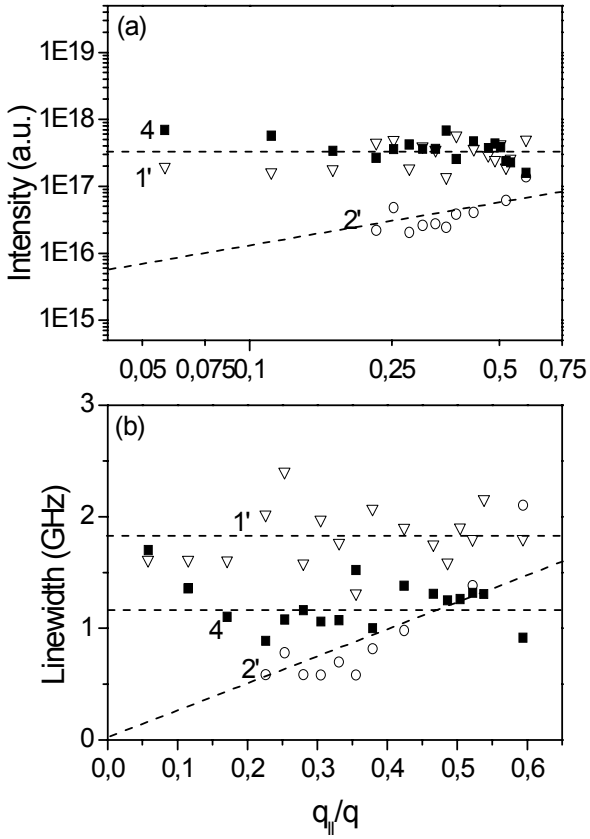

Figure 3.18 - Inelastic scattering amplitude (a) and line width (b) for the surface (2′) (open circles) and bulk modes (1′) (open triangles) and (4) (solid squares) in annealed a-PP film plotted as a function of $q_{||}$ in a log-log plot. The dashed lines are to guide the eye.

While these quantities exhibit the anticipated (**Figure 3.10**) insensitivity to q|| variation, the phonon (1′) decays much faster than (1) in q-iPP due probably to significant phonon scattering by the solid spherulites in a-iPP film.

The lifetime of the phonon (4) in the crystalline regions, albeit longer than for (1′), are still short for solids reflecting phonon scattering due to imperfections. The relative intensities of these two phonons in **Figure 3.18a**, I(1′)/I(4) ~0.5, should depend on the component compressibilities and the fraction Φ of the spherulites of **Figure 12b**. Assuming similar densities, I (1′) should be about 20% higher than I(4) based on the compressibility ratio i.e. $(c_2/c_L)^2$. Hence, the experimental intensity ratio can be approximated by (1-Φ)/ Φ) $(c_2/c_1)^2$ which leads to Φ~0.7. This value however, is twice larger than the estimated fraction from the sound velocity data (see the right panel of **Figure 3.17**).

A rich data of spectroscopy of a-PP could be explained by feature of crystalline domains. The spherulites packed close to each other (more chain of a-PP folded in crystalline part than in q-PP, a-PE, and q-PE.

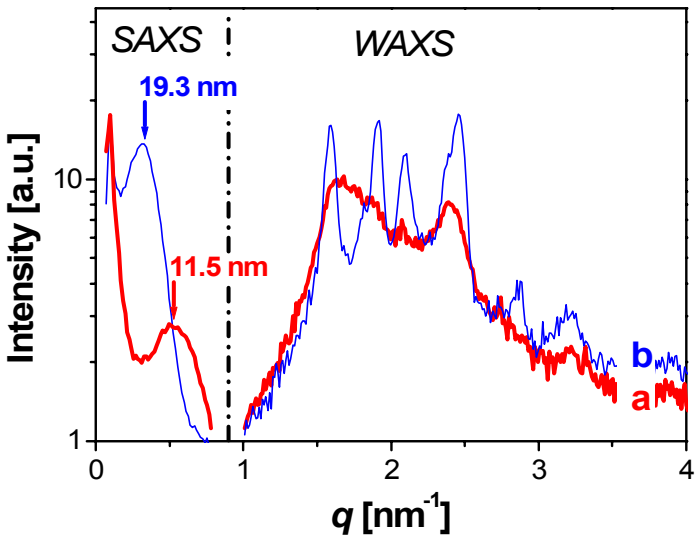

Figure 3.19 - Small (SAXS) and wide (WAXS) angle X-ray scattering profiles for the a-PP ((a) blue line) and q-iPP ((b) red line) films. The arrows indicate the position of the SAXS peaks and the corresponding lamellae long spacing are indicated in the figure as 11.5 and 19.3 nm for q-iPP and a-iPP, respectively.

Figure 3.19 shows combined SAXS and WAXS intensity distributions for the same q-PP and a-PP films used in the Brillouin experiment. Isotactic polypropylene can simultaneously crystallize into three crystalline forms, namely α, γ and β. During

cooling, the crystallization starts from the α-crystals followed soon by the γ-crystals, final amount of α- and γ-phases depends on crystallization temperature. The amount of γ-crystals will decrease with increasing cooling rate and no γ-crystals will be formed if the cooling rate is fast enough. The β phase is formed under high pressure conditions.

A well developed crystalline phase is evident from the WAXS reflections and the strong SAXS peak yielding a distance of 19.3nm in the a-PP film. The reflections a-iPP from WAXS profile demonstrated mixture of α and γ forms. In comparison, the q-PP exhibits much weaker crystalline features, containing mostly α phase. The determined degree of crystallinity was found to be approximately 60% and 37% for a-iPP and q-iPP**,** respectively.

These reliable estimates along with the optical micrographs and the Brillouin spectra (**Figures 3.10** and **3.14**) suggest that the two films are mainly distinguished by the size of spherulites. The crystallites of q-iPP are too small to affect the propagation of phonons with submicron wavelengths.

Brillouin spectroscopy can therefore discriminate the size of spherulites and moreover assess the micromechanics of semicrystalline films.

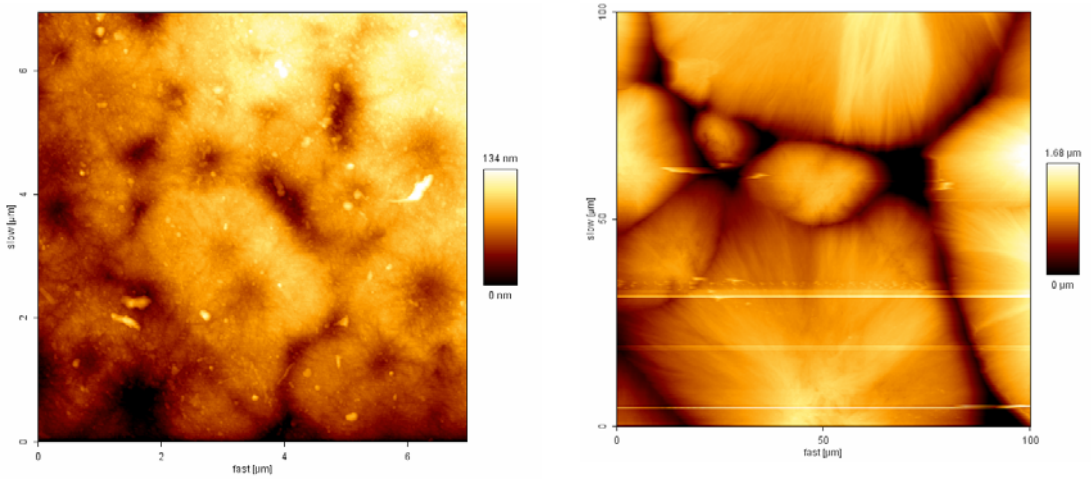

Figure 3.20 - Height AFM mages recorded for (left panel) quenched and (right panel) annealed iPP films.

The propagation of the surface phonon (2) and (2′) in the two free standing films shows some distinct features. Both have longitudinal polarization (**Figure 17 left panel**) but (2′), in contrast to (2), does not propagate with the phase velocity $c'_L$of the effective a-PP medium. Instead, it adopts a speed between c'_L and c_2, the speed of

sound in the two microphases. This intriguing finding might suggest surface modification e.g. a higher density and hence crystallinity than in the bulk and could open a new application of this optical technique. In fact, the height and amplitude AFM images of **Figure 3.20** complement the optical images **Figure 3.12**. Both techniques indicate large spherulites approximately 80μm in the a-PP film located at the surface and in the bulk. The AFM of the a-PP film shows the central part of a spherulite with different sectors, whereas the AFM image of q-PP (**Figure 3.20 left panel**) does not reveal well-define spherulites. Instead, the sample appears to consist entirely of about 2μm (diameter) granules that implies inhibition of spherulite structures. The micrographs show bright and dark regions which relate to harder and softer areas, respectively.

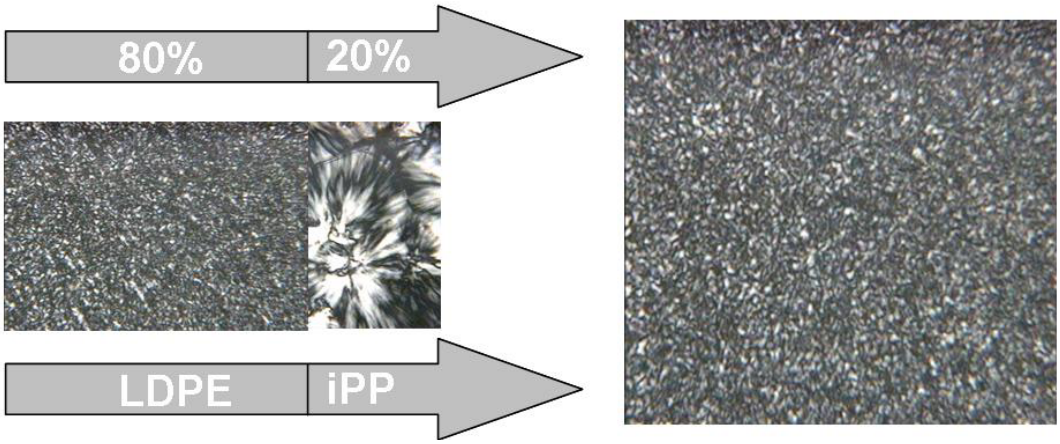

Figure 3.21 - Polarized optical microscopy images showing that the crystalline morphology of LDPE/iPP (80/20) is controlled by the major component.

The morphology of the blend in composition 80% of low density polyethylene and 20% isotactic polypropylene was primarily influenced by a major component as could be seen in **Figure 3.21**. The maximum of spherullite size is in range of 10μm for a-LDPE/iPP, consequently for q-LDPE/iPP is smaller. The Brillouin spectra of q-LDPE/iPP and a-LDPE/iPP reveal two phonon peaks longitudinal bulk and back scattering, with the same frequency shifts as for q-iPP, q-LDPE and a-LDPE (**Figures 3.22**). The elastic coefficient is around 6,8 GPa ($E=\rho c_L^2$) for these samples. They exhibited similar micromechanical properties due to light energy passes from one spherulite to another; such oscillation depends not just from the size of spherulite, and also substructure transition from amorphous to more solid crystalline domains, since ratio of amorphous part is dominant to crystalline for these samples.

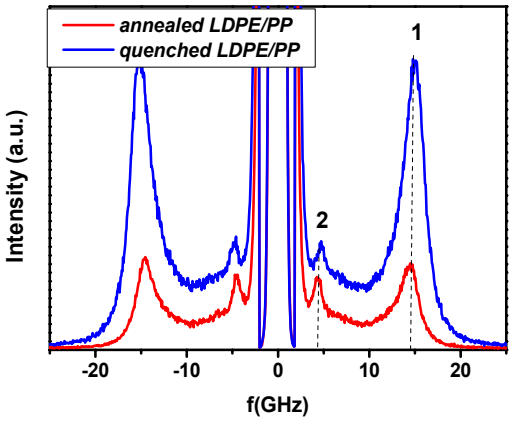

Figure 3.22 - Polarized Brillouin spectra of the free standing quenched and annealed LDPE/PP blend films at q=0.034nm^{-1} and two values for the photon wave vector q|| parallel to the surface as indicated in the plot.

8.2. Conclusions

Inelastic (Brillouin) light scattering from semicrystalline homopolymers can measure the high-frequency elastic constant (c_{11}) of the two microphases if the formed spherulites exceed the size of the wavelength of the probed phonons. In this case, the film is inhomogeneous over the relevant length scales, and there is an access to the transverse phonon in the crystalline phase, yielding the elastic constant c_{44} as well. The degree of crystallinity estimated from c_{11} of the effective medium is expectedly lower than the value from WAXS given the size requirement for revealing crystallinity by the Brillouin scattering. On the other hand, a simple account of the Brillouin line intensities associated with the longitudinal phonon propagating in the two phases leads to a much higher crystallinity value which is close to the WAXS value.

9. Hypersonic velocities of polymer bilayers: PE-PDMS and PE-PI.

Thin film polymer films have received a great deal of attention recently due to their uses in the designing and engineering of electronic components where their physical-mechanical properties are becoming increasingly important. Despite the large number of studies on the bi- and multilayer, very few measurements exist on the effect of interface between layers.

To fully realize the potential of polymer films in technological applications it is necessary to have a detailed understanding of their physical properties. This has led to a recent surge in both experimental and theoretical studies of these systems. Thin

polymer films have properties that may deviate from their bulk values for a number of different reasons. For a thin film supported on a substrate, the properties of the thin film may depend sensitively on the polymer-substrate interaction because of the high surface-to-volume ratio for thin films. In addition, for polymer films with film thickness $h<R_{EE}$ (R_{EE}~2*Rg)* is the average end-to-end distance of the polymer molecules and *Rg* is the radius of gyration, chain confinement effects may affect the physical properties of the film .[107,108]

To probe the effect of confinement on the mechanical properties of polymers, we have used BLS to study the room-temperature mechanical properties of multilayered samples comprised of alternating layers of freely standing polyethylene films covered by a layer of PDMS or polyisoprene (PI). In these experiments, we probed the mechanical properties of the individual layers with thicknesses as small as ~100nm and thick as 10μm.

When two polymers are put into contact at a temperature above their glass transition temperature, two situations can occur. They may either diffuse into each other over long distances as a function of the contact time, if they are fully miscible or they may reach an equilibrium degree of interpenetration when they are immiscible. The adhesion between two polymers is directly related to this interpenetration width, and hence to the degree of miscibility. To understand these adhesion phenomena, we need to know mechanical properties of individual films and its change for bilayers system.

9.1. Description of the Investigated system

Normally, the mechanical properties of elastomeric films are measured floated on water. The elastomers are liquid-like materials, because of this the floating is not stable[109]. Here we investigated properties elastomers films deposited on a polyethylene substrate. Two elastomers were chosen for this work Polydimethylsiloxane (PDMS) and polyisoprene (PI). Molecular weight is not important parameter, since the Mw depends on sound velocity only in oligomeric regime[110]. We studied micromechanical properties of elastomers for 180.000kDa of PDMS and 46.000 kDa of PI.

PDMS is first member of polysiloxanes polymers. The Si-O backbone of this class of polymers endows it with a variety of intriguing properties. For example, the strength of this bond gives the siloxane polymers considerable thermal stability, which is very

important for their use in high-temperature applications properties than any other chain molecule[111]. The nature of the bonding and the chemical characteristics of typical side groups give the chains a very low surface free energy and, therefore, highly unusual and desirable surface properties. For example, polysiloxanes are often used as mold-release agents, waterproof coatings, and biomedical materials[112]. Additional structural information is presented in the sketch of poly(dimethylsiloxane) (PDMS) shown in **Figure 3.23**. First, the Si-O bond length is 1.64 Å, which is significantly longer than that for the C-C bond (1.53 Å). Also, the Si-O-Si bond angle is approximately 143°, which is much larger than the usual tetrahedral value (~110°). In addition, this bond angle is so flexible that it can readily pass through the linear 180° state. Finally, the torsional potential about Si-O bonds is significantly lower than that about C-C bonds. All of these features make the PDMS chain one of the most flexible chains known. This gives PDMS and most other polysiloxanes very low glass transition temperatures.

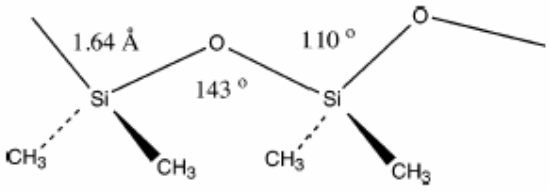

Figure 3.23 - Sketch of a portion of a PDMS chain, showing some structural information relevant to its high flexibility.

The 1,4,-polyisoprene (PI) is an interesting material, not only because of its enormous commercial significance (natural rubber comprises 35% of all commercial elastomers) but also because it exhibits unusual viscoelastic behavior. [113]

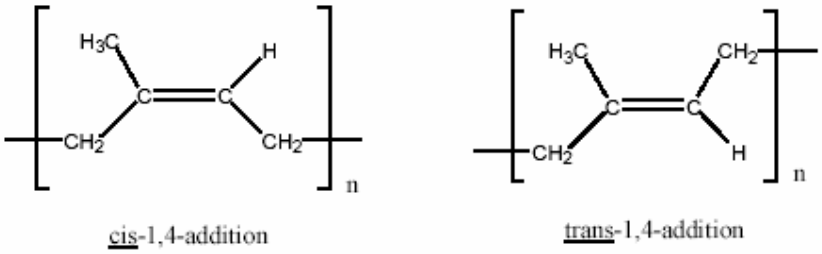

Figure 3.24 - Structure of polyisoprene.

Typical raw polymer and vulcanized properties of polyisoprene are similar to values obtained for natural rubber (**Figure 3.24**). Natural rubber and synthetic polyisoprene

both exhibit good inherent tack, high compounded gum tensile, good hysteretic, and good hot tensile properties. Currently synthetic polyisoprene is being used in a wide variety of industries in applications requiring low water swell, high gum tensile strength, and good resilience, high hot tensile and good tack. Due to different chemical structure and properties of these elastomers we would expect two behaviors of wetting on the surface of polyethylene.

9.2. Results and discussion

In our first experiment we consider films of PI or PDMS disposed on the surface of polyethylene by spin coating (**Figure 3.25**) from 25% toluene solution. Toluene is a good solvent for both polymer components (PDMS, PI). PE is not soluble at room temperature in toluene. The samples were deposited at room temperature and than annealed at 100°C during 10 hours in oven for better contact between laeyrs. Ellipsometry measurements were carried out to verify the thickness of the resulting layers, and were ~ 150nm and ~ 100nm for PDMS and PI, respectively.

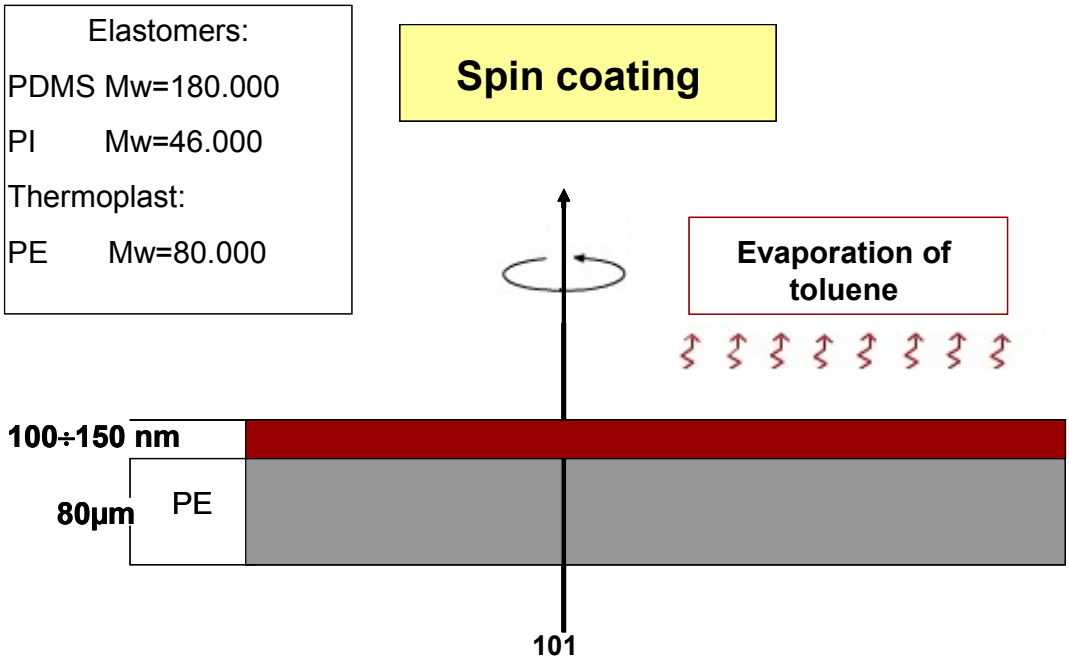

Figure 3.25 - Scheme of obtaining thin films by spin coating technique.

In order to see that all surface of polyethylene covered by layer of PDMS the AFM images are presented in **Figure 3.26**. The surface topology of bilayer LDPE-PDMS demonstrates regular wave shaped cavities of PDMS along the surface of polyethylene.

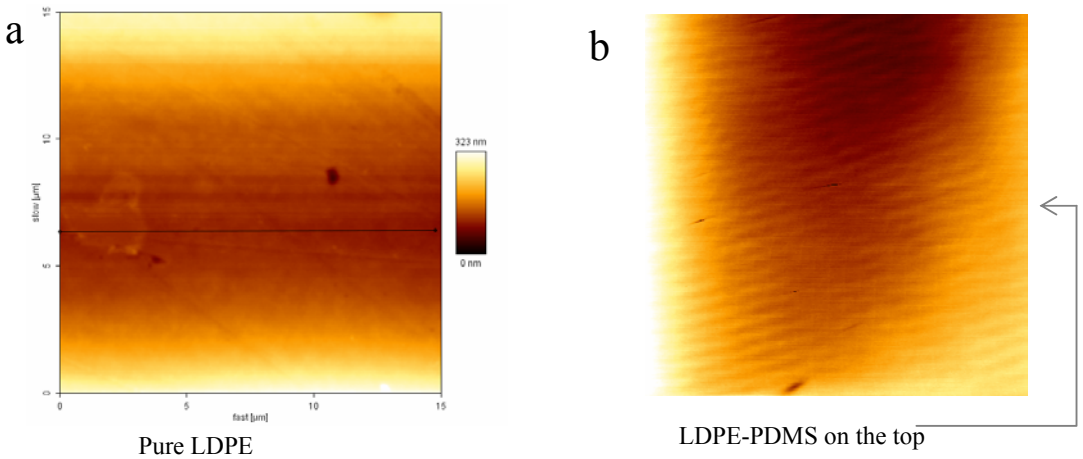

Figure 3.26 - AFM height images of surface polyethylene (a) and (b) polyethylene-PDMS bilayer. (It was not possible to scan image of PI layer due to softness of the material)

The free spectral range of the interferometer was set to 20GHz and the Rayleigh-Brillouin spectrum of PE and bilayers of LDPE-PDMS and LDPE-PI are presented in **Figure 3.27**. The spectrum taken at q=0.034nm^{-1} reveals up to two phonon. These phonons in case of LDPE spectrum correspond to longitudinal and backscattering modes. The spectrum of LDPE was used as reference in order to see influence of thin layer PDMS or PI on polyethylene substrate.

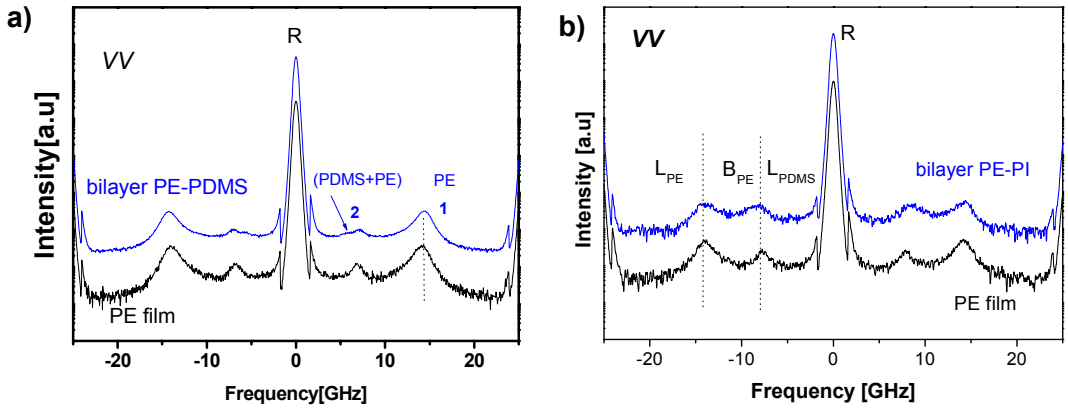

Figure 3.27 - Brillouin light scattering spectra of LDPE is black line and blue line for bilayers (a) PE-PDMS, (b) PE-PI obtained at VV scattering geometry. The FSR was 20GHz.

The spectrum of bilayers have not exhibited additional phonon peak. The peak positions were estimated through the Lorentzians fitting. No change in frequency shift of bulk longitudinal phonon of LDPE was observed in bilayers samples. The location of maximum peak is around 14GHz in all spectra. However, the intensity of backscattering phonon is different for PDMS and PI. The mode (2) of PDMS (**Figure 3.27b**) became less symmetrical; the intensity of backscattering mode of LDPE-PDMS is significantly decreased compare to intensity of backscattering mode of LDPE. In case of PE-PI bilayer the backscattering mode is becoming broader. The layer of PDMS is strongly damping the energy of the back scattering mode in contrast to PI. However, the intensity is not sufficiently high to determine the accurate peak position of layers in nm range.

To increase contrast in spectra between PE and PDMS, PI layers we decide to investigate a thicker layer of PDMS, PI.

The polyethylene film was covered by PDMS, PI on both sides. PDMS and PI were dissolved in toluene. The LDPE film was disposed in solution (**Figure 3.28**) and keep for the time. The speed of disposing, removing and drying was constant for all preparation. The thicknesses were determined by profilometer.

PDMS ~ 10 μm

PI ~ 10 μm

LDPE ~ 80 μm

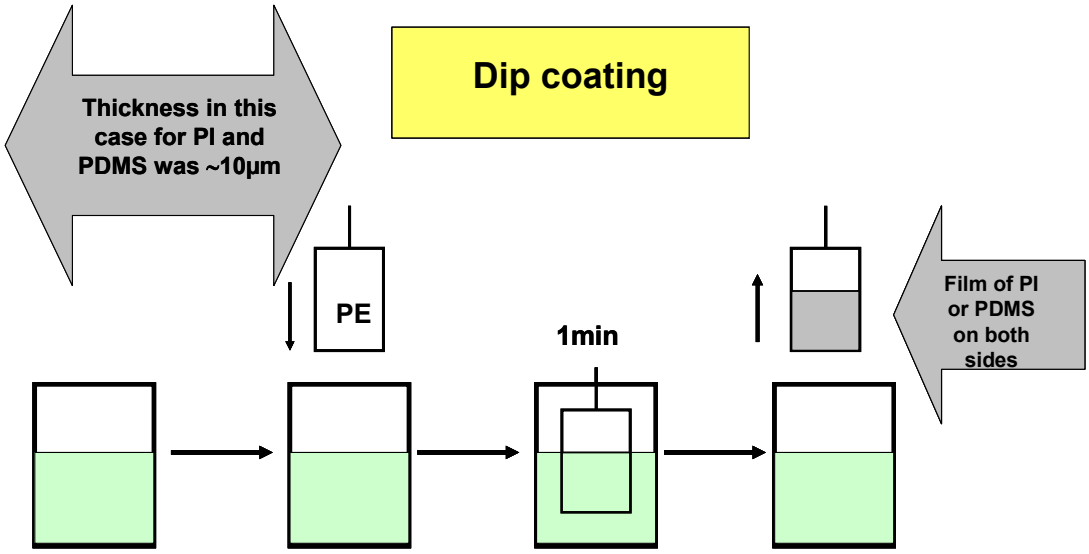

Figure 3.28 - Scheme of covering PE on both side.

The thicker layer of PDMS is exhibited observation of additional phonons in respect to pure LDPE (**Figures 27a** and **29a**). The spectra of LDPE-PDMS reveal up to four phonons. The plot in the wave propagation is the dispersion relation of the phonon frequencies $f_i(=\omega_i/2\pi)$ obtained from the experimental I(ω) as a function of qII based on the dispersion shown in Figure 8.

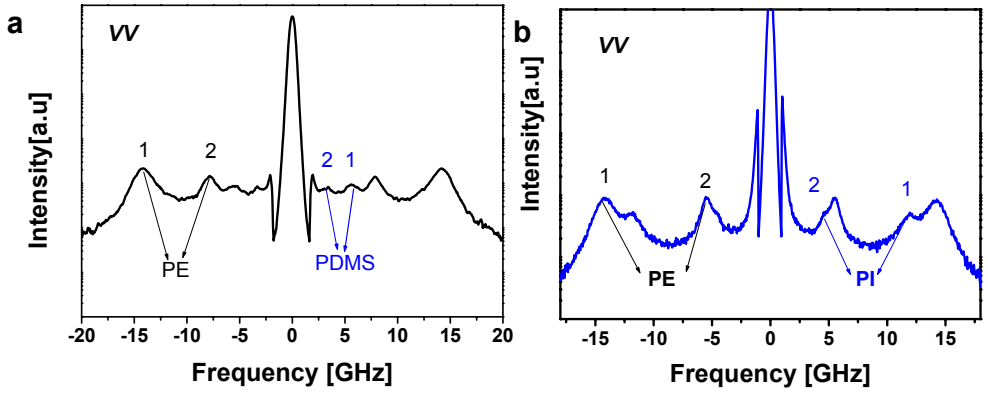

Figure 3.29 - Rayleigh-Brillouin spectra of the (a) LDPE-PDMS and (b) LDPE-PI covered both sides.

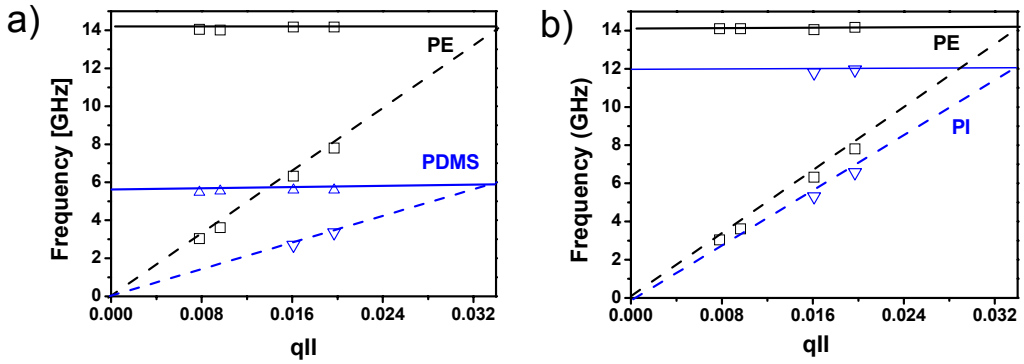

Figure 3.30 - The dispersion curve q|| at constant q(=0.034nm-1) for (a) LDPE-PDMS and (b) LDPE-PI, covered both sides

There are two longitudinal acoustic phonon (straight lines) propagating in the bulk of the film with $\omega_1=c_L q$ and two backscattering (dash lines) –guided primarily longitudinal phonon with $\omega_2=c\ q||$. The longitudinal phase velocity of LDPE is c_L=2590m/s, of PDMS c_L =1000m/s.

The LDPE-PI spectra exhibits a strong doubling effect of acoustic modes, no additional peak is observed as shown in **Figure 29b**. The angular dependence of the sound velocity in LDPE-PI was analyzed and fitted as Lorentzians lines. In dispersion plot the acoustic bulk mode yields the longitudinal phase velocity of sound c_L=2200m/s (**Figure 3.30**). The sound wave propagation of PI and of LDPE are closer in value in contrary to PDMS, this is explained by the appearance of a doublet peak in case of LDPE-PI.

9.3 Conclusions

We have used BLS to investigate the high-frequency mechanical properties of thin as nm and μm size freely standing polyethylene-PI and polyethylene-PDMS films at room temperature. Such measurements are a sensitive, though indirect, probe of the mass density. It was found that the measured velocities of the film-guided phonons for μm size films of PI and PDMS are 2200m/s and 1000m/s, leads to the modulus M (= ρc_L^2) ~4,4 GPa and ~1GPa , respectively.

The fact that the high frequency mechanical properties of PE layer are not changed, confirm the existence of two independent layers and no interfacial adsorption. Measuring the mechanical properties of very thin films supported by substrates is

complicated by the fact that measured properties are strongly influenced by substrate.

Chapter 4 - Structure and properties of polymer nanocomposites

1. Introduction

Reinforcement of polymer materials is usually performed trough addition of fillers. One of the most popular reinforcing materials is fibrous filler in a dispersed state. Glass fibers and carbon fibers have been extensively used. The reinforcing effect of fibrous filler may be theoretically estimated using Cox and Kelly models.[114,115] These theories predict that the degree of reinforcement depends on the characteristics of the filler itself that are the rigidity and aspect ratio, as well as on the adhesive strength between the filler and the polymeric matrix. This latter parameter may be enhanced through chemical modification of the surface of the glass or carbon fibers by organic substances. However the major discrepancy between the characteristic sizes of the organic and inorganic components makes the properties of the resulting materials worse in comparison to the neat polymer. This is usually expressed by a decrease in ductileness, poor moldability and poor surface smoothness in molded items. In contrast to these traditional composite materials for which the reinforcement is in the micrometer (10^{-6} m) size scale, the reinforcement in a polymer nanocomposite occurs at the nanometer (10^{-9} m) level. A more complete definition of a composite material can be found in the work of Hull;[116] a composite material is made of two or more physically distinct and mechanically separable materials mixed in such a way that the dispersion of one material in the other is controlled to achieve optimum properties that are superior to the properties of the individual components. Referring to the IUPAC specification a composite material is a multicomponent material comprising multiple different (nongaseous) phase domains in which at least one type of phase domain is a continuous phase.[117]

A first attempt to minimize the size difference between the filler and the matrix consisted in using a rigid rod-like polymer as reinforcing filler. This type of material initially referred to as “molecular composite” was later considered as a category of nanocomposite.[118] Phase separation related problems appeared as the major limitation to these systems, but the idea led to the design and structure-property relationship investigation of a series of liquid crystalline polymers made of alternating rigid and flexible macromolecular segments. Other ways to reinforce the polymer matrices making the nanocomposites is to add nanofillers such as silica beads[119], precipitated silica[120], silicatitania oxides synthesised by the sol-gel process[121] as well

as zeolites.[122] Interactions between polymer and clay have been studied since the seventies.[123] However, the practical use of polymer-clay nanocomposite has its origin in the more recent studies performed at the Toyota Central Research Laboratories where these two very different materials with organic and inorganic pedigrees were successfully integrated.[124] A nylon-montmorillonite clay nanocomposite was used as timing belt cover on a Toyota Camry automobile. This nanocomposite based material was found to exhibit large increases in tensile strength, modulus and heat distortion temperature without a loss in impact resistance. The composite also showed lower water sensitivity, permeability to gases and thermal coefficient to expansion. Others advanced properties such as enhanced flame retardancy and UV resistance have been obtained. Improvement of these bulk properties was obtained upon low clay content (4 wt.-%). The application of these nanocomposites was stopped because of the high cost caused mainly by the time-intensive preparation process as well as by the high price of nylon. However, since this initial work, many studies have been carried out in both industrial and university laboratories over the past decade leading to the development of many new products. For economical reasons, conventional polymers such as polypropylene have served as a matrix.

In this chapter, we aim to present general features of nanocomposites. We limit ourselves to nanocomposites based on polymers although the term nanocomposite is commonly used in two distinct areas of material science: ceramics and polymers. After a short description of inorganic clay materials, the different classes of nanocomposites as well as preparation methods and properties are discussed. In the last part, emphasis is given to polyolefins-based nanocomposites.

2. Clays and clay modification

Common clays are naturally occurring minerals and are therefore subject to natural variability in their constitution. It is clear that the purity of the clay is an important parameter that may affect the properties of the final nanocomposite. The two most abundant elements of earth's crust, silicon and oxygen, combine to form the basic building blocks for most common minerals, including clays. Generally speaking silicates, i.e. substances that contain silica, are made of "building blocks" of four oxygen atoms packed together around a single, much smaller, silicon atom. The four-sided, pyramidal geometric shape is called a tetrahedron. A single silicon-oxygen

tetrahedron is a complex ion with a formula of SiO_4^{-4}. For the silicon-oxygen tetrahedron to be stable within a crystal structure, it must either be balanced by enough positively charged ions or share oxygen atoms with adjacent tetrahedrons. Therefore there is a wide variety of possible arrangements for silicates ranging from isolated silicate structures (single tetrahedrons), to single and double chain structures, to sheet silicates (to which belong clays) and finally framework silicates such as quartz. Among this large number of inorganic materials with more or less pronounced intercalation ability, layered silicates are one of the most important forms.[125,126]

Most silicate minerals also contain one or more other elements such as aluminium. In addition to tetrahedral sheets, these aluminosilicates may include octahedral sheets as well to form the sheet-like structure. Octahedral sheet structures may occur especially with Al^{3+} in coordination with two oxygen atoms and an OH^- group. In these nanoassemblies, the silica SiO_4 tetrahedrae and alumina AlO_6 octahedrae are held together by only weak interatomic forces between the layers, often hydrogen bonding from water. This bonding can be achieved in various ways.

In kaolinite, one of the most important clay minerals, a single sheet of corner connected silica tetrahedrae is connected by common apex oxygen atoms to a single sheet of edge-connected alumina octahedrae. This nanoassembily is called a 1:1 phyllosilicate. A 2:1 ratio of the tetrahedral to the tetrahedra results in other type of smectite clays, the most common of which is montmorillonite. Montmorillonite consists of three “layers”: an aluminium containing octahedron layer sandwiched between two silicate layers (**Figure 4.1**). The O^{2-} at the apexes of the silica tetrahedral replaces the OH^- groups of the octahedral layer, and are shared between the layers. This three-layer grouping is referred to as a platelet. These clay platelets are truly nanoparticulate. In the context of nanocomposites, it is important to note that the molecular weight of the platelets *(*ca. $1.3x10^8$) is considerably greater than that of typical commercial polymers, a feature which is often misrepresented in schematic diagrams of clay-based nanocomposites. In addition, platelets are not totally stiff, rigid objects as is sometimes assumed. Recent AFM studies on individual silicate platelets have demonstrated that individual silicate layers have a degree of flexibility.[127,128] The clays often have very high surface areas, up to hundreds of m^2 per gram.

The commonly accepted value of 172Gpa reported for a perfect mica crystal is probably unrealistic.[129]

Clays are also classified as expansive or swelling, materials.[130] Upon adding water to the montmorillonite, the water molecules are absorbed into the spaces between the clay platelets, especially if the associated cation is Na^+. This leads to a large increase in volume, sometimes up to several hundred percents. Because variable amounts of water can be held between the layers, the layer spacing can expand and contract depending on the hydration. This causes a great deal of structural damage to buildings sited on soils with high smectite clay content.

There is an unsatisfied negative charge on the face of the clay platelet caused by structural substitutions or vacancies in the octahedral and/or tetrahedral layers. For example Mg^{2+} or another divalent cation may substitute for Al^{3+} in the octahedral layer, or Al^{3+} or Fe^{3+} may replace Si^{4+} in the tetrahedral layer. Cations such as Ca^{2+}, Mg^{2+}, and Na^+ are attracted to the spaces between the platelets due to the net negative charge on the "faces" of the platelets. These cations can be exchanged readily through washing.

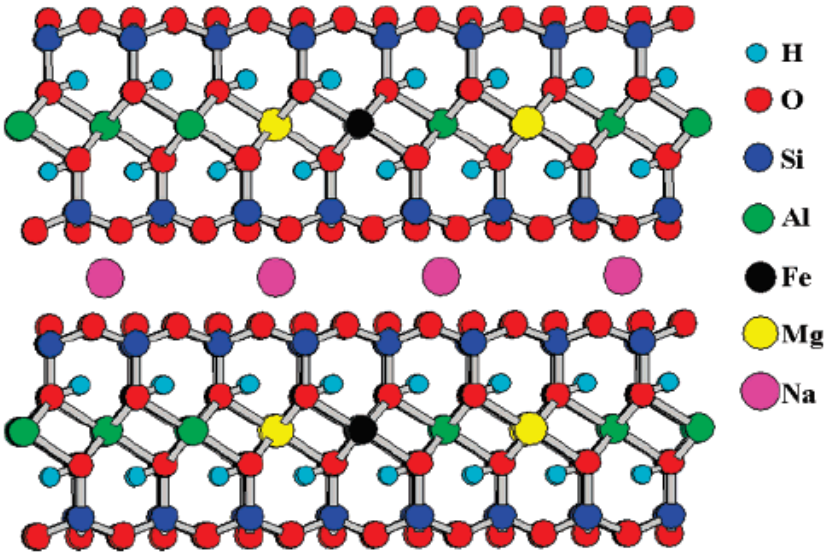

Figure 4.1 - Chemical structure of montmorillonite.

One important consequence of the charged nature of the clays is that they are generally highly hydrophilic species and therefore naturally incompatible with a wide range of polymer types. This lack of affinity between hydrophylic silicate and hydrophobic synthetic polymers leads to agglomeration of the mineral in the polymer matrix. A necessary prerequisite for successful formation of polymer-clay

nanocomposites is therefore alteration of the clay polarity to make the clay 'organophilic'. This can be made in a rather easy way taking advantage of the fact that layered silicates may undergo intercalation with organic molecules.[131] Organophilic clay can be produced from normally hydrophilic clay by ion exchange with an organic cation such as an alkylammonium ion. For example, in montmorillonite, the sodium ions in the clay can be exchanged for an amino acid such as 12-aminododecanoic acid as follows:

$$\text{Clay-Na}^+ + \text{HOOC-R-NH}_3^+\,\text{Cl}^- \longrightarrow \text{Clay-NH}_3^+\text{-R-COOH} + \text{NaCl}$$

Scheme 4.1 - Ion exchange reaction between amphiphilic organic molecule and inorganic clay leading to the synthesis of organophilic clay.

As mentioned above, montmorillonite is one of the most common type of clay used for nanocomposite formation and this is the clay we used in our study; however, other types of clay can also be used depending on the precise properties required from the product. These clays include hectorites (magnesiosilicates), which contain very small platelets, and synthetic clays (e.g. hydrotalcite), which can be produced in a very pure form and can carry a positive charge on the platelets, in contrast to the negative charge found in montmorillonites

3. Classification of polymer-clay nanocomposites

Depending on the strength of the interaction between the polymeric matrix and the inorganic sheets, different morphologies can develop when a given polymer is mixed with layered silicate. The resulting polymer-clay composites can be divided into three general types as schematically presented in **Figure 4.2**.

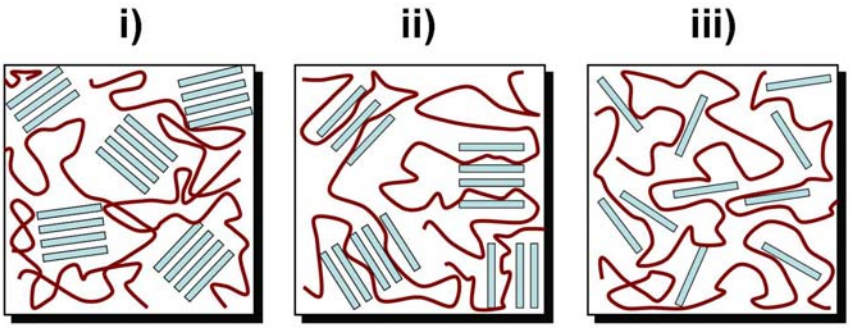

Figure 4.2 - Schematic illustration of three possible structures of polymer-clay composites. i) immiscible nanocomposite, ii) intercalated nanocomposite and iii) delaminated or exfoliated nanocomposites.

i) Immiscible nanocomposite; the macromolecules do not penetrate the ordered structure of the layered silicates so that conventional composite is obtained.

ii) Intercalated nanocomposite: when the polymer exhibits compatibility to the layered silicates and penetrate into the gallery so that the dimension of the nanosheet is increased to a level depending on the degree of penetration. In the intercalation regime, the structure of the inorganic layers remains.

iii) Delaminated or exfoliated nanocomposites : In this case the strong penetration of the macromolecules within the layers hinders the interlayer interactions so that the stack-like self organization of the clay is broken. Ideally, individual silicate layers are dispersed within the polymeric matrix.

The latter type of nanocomposite is of particular interest because the optimized interactions between the polymer chains and the clay that take place on the whole clay surface, should lead to significant changes in mechanical and physical properties. However, intercalation of polymers into inorganic materials with retention of their initial structure is also a very efficient way to design inorganic-polymer nanocomposites.[123 theng]

4. Preparation methods.

There are different ways to prepare polymer nanocomposites; from solution, from the melt and by in-situ polymerization. The two latter being the main pathways of producing useful layered inorganic-polymer systems.

4.1. Intercalation from solution.

In **Figure 4.3** the different steps of the synthesis of intercalated polymer-clay nanocomposites through the “solution” method are presented. This method has been applied for the preparation of high-density polyethylene-[132], polyimide-[133], and nematic liquid crystal polymers-based[134] nanocomposites. First, the organoclay is dispersed in a polar solvent such as toluene or N, N- dimethylformamide. In polar organic solvents, alkylammonium treated clays may swell considerably leading to the formation of gel structures. At this stage, the polymer that is dissolved in the solvent,

is added to the solution and intercalates between the clay layers. The last step aims at removing the solvent by evaporation usually under vacuum.

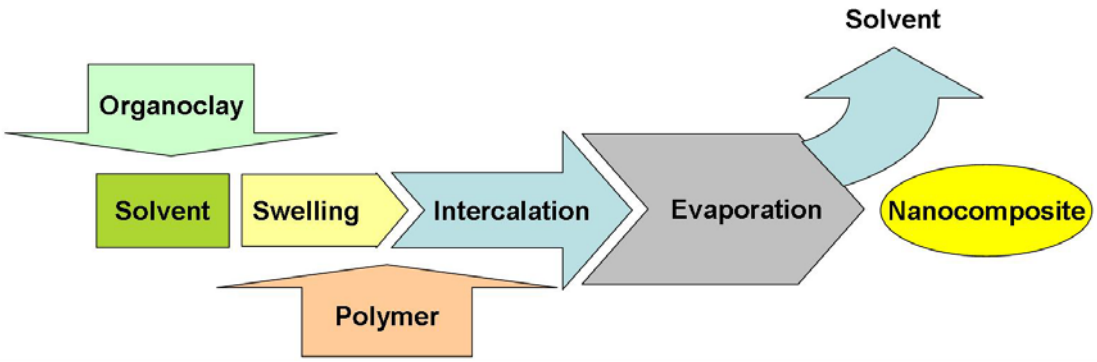

Figure 4.3 - The different steps for the synthesis of intercalated polymer-clay nanocomposites through the "solution" approach.

Untreated clays have also been used in combination with deionized water as the polar solvent. In this particular case, the polymer must be either dispersed in water (poly(ethylene)oxide[135]) or synthesised by emulsion polymerisation (polymethylmethacrylate[136] and epoxy[137]). When considering solution process, the driving force for the intercalation of the macromolecules is the entropy gain caused by desorption of solvent molecules, which compensates for the decrease in conformational entropy of the intercalated polymer chains.[138] Thus it is needed that a large number of solvent molecules are desorbed from the clay to accommodate the incoming polymer chains. By this method, a broad range of intercalated nanocomposites based on low or even no polar polymers is possible. However, this solution approach remains difficult for industrial application due to problems related to the use of large quantities of solvent.

4.2. Intercalation from the melt.

In some cases the polymer may be directly intercalated. This approach was developed by Giannelis et al.[139,140] As presented in **Figure 4.4** it relies on the blending of a molten thermoplastic with an organoclay in order to enhance the interactions between the polymer and clay. An annealing step, performed in a temperature range above the glass transition temperature of the polymer leads to the formation of the nanocomposite.

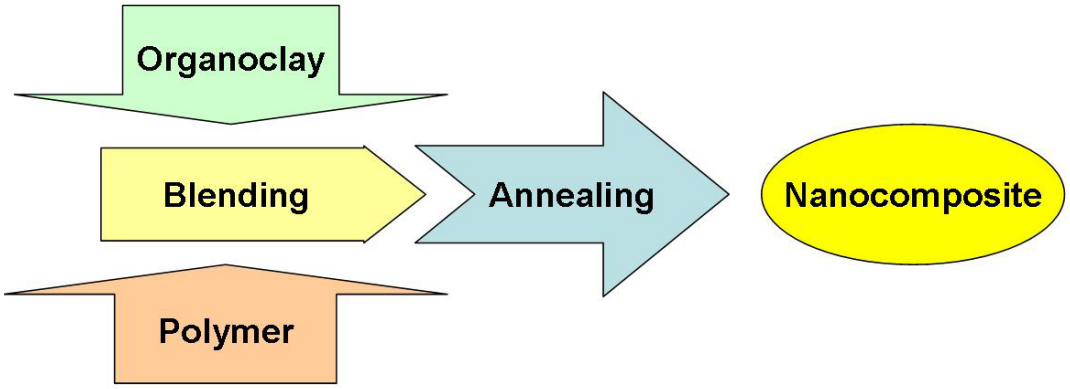

Figure 4.4 - The different steps for the synthesis of intercalated polymer-clay nanocomposites through the "melt intercalation" approach.

Through the intercalation process, the change in the polymer chains conformation is expressed by a significant loss of conformational entropy. This effect may be counterbalanced by the large enthalpic contribution of the interactions between the polymer and the organoclay during the subsequent blending and annealing steps.
In contrast to the solution intercalation process described above, the melt method has become of great importance for industrial application. Many examples can be found where thermoplastics were used to prepare polymer-clay nanocomposites from the molten state.[141,142] Polyolefins which represent the biggest volume of polymers produced have also been utilized, see reference[143] as an example for the case of polypropylene. Direct polymer melt intercalation is the most attractive technique because of its low cost, high productivity and compatibility with current processing techniques.

4.3. *In-Situ* Polymerization

The strategy is nearly similar to the one used in the "from solution" approach. The first report on the synthesis of polymer-clay by *in-situ* polymerization dates from 1990.[144] The corresponding synthetic pathway is presented in **Figure 4.5** After the organoclay being swollen in the monomer, the polymerization is started through addition of species allowing for initiating the reaction. By a precise control over the interaction between the monomer, the surfactant, and the clay surface, nylon-6-[145], poly(ε-caprolactone)[146] and epoxy-[147,148] containing nanocomposites with exofoliated structure were successfully synthesized via ring-opening polymerization. The in-situ polymerization method was also extended to the cases of vinyl monomers.[149,150] Intercalated PMMA and PS nanocomposites have been prepared by

either emulsion [151] or bulk polymerization.[152,153] The systematic investigation of the interaction between the monomer, the initiator, and the modified clay surface is often a prerequisite to predict the structure of the polymer-clay hybrid.[154] To favour the formation of exfoliated structure, efforts have also been made to anchor either a living free radical polymerization initiator or a more conventional initiator in the interlayer region to improve the intralayer polymerization rate. In these two studies, exfoliation of clay was achieved in PS[155] and PMMA[156] matrices, respectively.

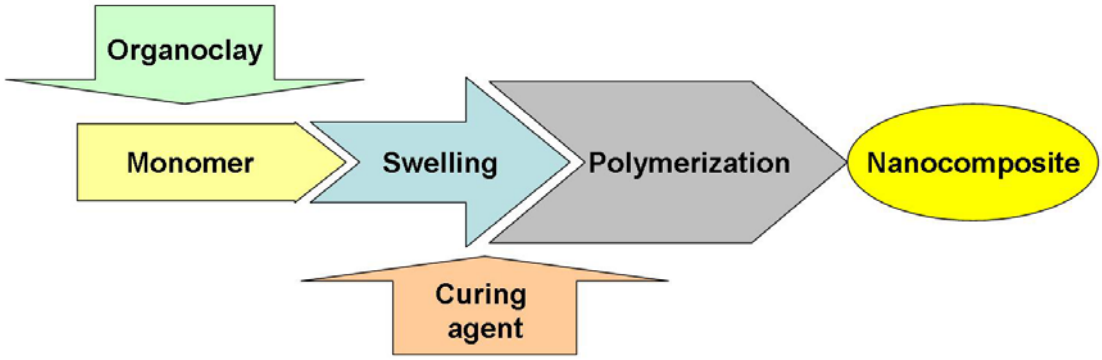

Figure 4.5 - The different steps for the synthesis of intercalated polymer-clay nanocomposites through the "in situ polymerization" approach.

5. Polyolefin-clay nanocomposites.

Polyolefins represent one of the most widely used type of thermoplastics in both packaging and engineering applications notably because of their good balance of physical and chemical properties, low-cost, light weight, favourable processing and recycling characteristics. Like all plastics, polyolefins exhibit some shortcomings in their performance. In packaging, they are poor gas barrier. Both thermal and dimensional stabilities constitute a limit to their application in automotive industry. As mentioned in the first chapter of this work, gas barrier properties of polyolefins may be improved by adding higher barrier plastics *via* a multilayer structure. Dimensional and thermal stability may be improved by adding mineral or glass fillers with loading in the range between 15 to 25%. However, these approaches carry major drawbacks. They increase the production cost of the materials, make more stringent the processing conditions and high loading results in end products with much larger weight. Considering these different aspects, polymer-nanocomposite are unique materials that address the shortcomings of conventional polyolefin-based products in low-cost, easy processing and light weight ways.

To date, polypropylene remains one of the fastest growing turnover polymers,[157] and the preparation of polypropylene-based nanocomposites has been discussed in

depth.[158] One of the major concerns when dealing with polypropylene-nanocomposite is to produce materials with enhanced mechanical properties in comparison to the neat polymer. Improvement in elastic modulus and impact resistance has been obtained at low filling ratios.[159] However, the dispersion of the clay at the nanometer level into polypropylene matrix is very challenging because of their unlike nature; hydrophilic for the clay and hydrophobic for the polymer.[160] The weak adhesion between the polar filler and non-polar matrix results in poor boundary strength between the two components.[161] This problem can be overcome by tailoring the affinity between the organic polymer and inorganic clay.[162,163] As mentioned above, the clays can be easily hydrophobized through a simple exchange reaction. Clays are usually modified by cationic surfactants like organic ammonium or alkyl phosphonium salts.[164] The resulting chemically modified clays also referred to as organoclays, exhibit more organophilic surface.

Theoretical models suggest that an increase in the length of the organic molecules linked onto the clays allows for a better dispersion of clay sheets in a polymer matrix.[165] On this basis, a wide variety of polymer-bearing clay has been synthesized.[166],[167] Moreover, the specific positioning of functional groups along the polymer chains allows for a control of the hybrid structure. The studies of Krishnamoorti demonstrated that chain end functionalized polypropylene adopts a unique molecular structure atop of the clay surfaces leading in an exfoliated montmorillonite structure.[168] The terminal group that is hydrophilic (NH_3^+) anchors the PP chains through an ion exchange reaction onto the inorganic surfaces, while the hydrophobic and semicrystalline PP “tail” effectively exfoliates the clay platelets. In contrast, Wang et al. have shown that sidechain-functionalized or block copolymer PPs form multiple contacts with each of the clay surfaces. This multi anchorage event results in aligning the polymer chains parallel to the clay surfaces and can bridge consecutive clay platelets promoting intercalated structures.[169]

With the continuous aim to improve the dispersion of the nanoparticles, polypropylene modified by polar groups were also applied in an attempt to overcome the difference in polarity between the clay surface and bulk polypropylene.[170, 171] In reference 52, the authors investigated three hybrid systems prepared by mixing polypropylene with i) Na–montmorillonite, ii) organophylic-montmorillonite obtained by a cation-exchange reaction between Na–montmorillonite and the distearyldimethylammonium ion and iii) polypropylene-montmorillonite obtained by

mixing the organophylic-montmorillonite with a polyolefin oligomer with telechelic OH groups. When the nanocomposite material was prepared using the montmorillonite containing the polyolefin diol, the silicate layers were exfoliated and dispersed uniformly in the polypropylene matrix at the nano level. In contrast, in the case of the organophylic-montmorillonite the silicate layers were laminated and aggregated in the polypropylene matrix. Dispersion at the micron level was observed when using Na–montmorillonite. Unfortunately, the range of available functional polypropylene is limited due to synthetic chemical difficulties and in most of cases the commercially available, maleic anhydride grafted polypropylene (PP-*g*-MA) is used. Maleic anhydride-g-polypropylene exhibits a complex molecular structure due to many side reactions including chain degradation during the free radical grafting process as well as many impurities.[172,173] Maleic anhydride-g-polypropylene has proven to be an effective compatibilizer in various complex systems such as polypropylene/polyamide-6 blends.[174] In this case, the highly electrophilic maleic anhydride groups react with the nucleophilic amine moieties at the chain end of the polyamide to form amic acid, followed by ring closure to form thermally stable imide. The use of maleic anhydride-g-polypropylene, in the oligomeric regime, was largely extended to the preparation of clay-nanocomposite.[175] The intercalation ability of the polypropylene oligomers within the layer structure of the clay as well as the miscibility of maleic anhydride modified polypropylene oligomers with the polypropylene making the organic matrix and the are two key parameters governing the dispersibility of the clay and consequently the mechanical properties of the hybrids.[176] The level of dispersion of silicate layers was found to be directly related to the content in polypropylene oligomers bearing maleic anhydride groups.[177] Dispersion at the nanometer level, i. e. exfoliation, was obtained by adding rather large amount of maleic anhydride containing polypropylene oligomer (~22% by weight). The correlation between the dispersibility of the clays and the reinforcement effect by the clays was clearly demonstrated.

The effect of the nature of the inorganic nanoparticles on structure and properties of polypropylene-based nanocomposites was also clearly demonstrated.[178] In their study, the authors kept constant the particle content (4.5%) but compared colloidal versus powder silica nanoparticules. The samples were prepared without modifiers, i.e the filler does not have a direct chemical interaction with the polymer matrix. No significant improvement in the mechanical properties was noticed when

powder silica was employed while the presence of silica-sol nanoparticles resulted in an increase of both Young modulus (from 1.2 to 1.6 GPa) and impact strength (from 3.4 to 5.7 $KJ.m^{-2}$). This major difference was attributed to the state of filler dispersion in the matrix, varying from unaggregated particles (colloidal silica) to aggregates of various shapes (powder silica) though the primary filler particles were in the same diameter range (less than 30 nm). The addition of inorganic component also affected the thermal behaviour of the semi-crystalline matrix. Regardless of the kind of inorganic filler, the melting temperature of the polypropylene was observed to decrease upon addition of silica. This suggests a decrease in the lamellar thickness. Correspondingly, the crystallization temperature increased of about 2-4°C for the filled samples. It is well-established that the presence of inorganic fillers affects the crystallization features of the polymer when the particles act as nucleation agents. This effect is more pronounced when the surface of the filler is chemically modified.[179]

It should be also noted that a large number of studies has been focused on the preparation and investigation of structure-property relationship of polymer-layered silicate nanocomposites from polyamides,[180],[181] polymethacrylates,[182] polystyrenes,[183, 184] epoxies,[185] elastomers.[186] Moreover, beyond the control of mechanical behaviour, improvement of heat distortion temperature,[187, 188] barrier properties,[189, 190, 191] reduced flammability,[192] resistance to UV degradation,[193] resistance to atomic oxygen,[194] and improved ablative performance[195] were also reported. Thermoplastic nanocomposites based on blends of two or more polymeric materials, i.e. binary or ternary blends, have also proved to exhibit advanced properties. [196]

6. Structure and properties of isotactic poly(propylene)/montmorillonite nanocomposites.

The phase behaviour and corresponding temperature dependent morphology formation were analyzed using complementary experimental methods giving information on various size scale as well as in both real and reciprocal space. The properties of isotactic poly(propylene)-based nanocomposites with clay loading of 2, 5 and 7 wt.-% were examined and the corresponding samples are referred as iPP/iPPMA-2, iPP/iPPMA-5 and iPP/iPPMA-7, respectively. Along this text, the iPP/iPPMA sample (without clay) was used as reference material. It is a blend of isotactic poly(propylene) (iPP) and isotactic poly(propylene)-*graft*-maleic anhydride (iPPMA). iPPMA having a grafting content in maleic anhydride moiety of 1% was added at a weight ration of 4% to neat iPP. iPPMA serves as compatibilizer between the unlike organic matrix (hydrophobic) and inorganic filler (hydrophillic). The montmorillonite we employed in this study was chemically modified through ion exchange reaction to make it more hydrophobic. According to several literature reports, effective silicate modification is obtained when surfactant with alkyl substituents larger than hexyl are used.[197,198]

6.1. Differential Scanning Calorimetry and polarized optical microscopy in non-isothermal mode

We will start the discussion on the basis of data obtained by means of differential scanning calorimetry. Two types of experiments were performed allowing for the monitoring of the ordering/disordering of polypropylene blend and related nanocomposites from the melt under non-isothermal as well as isothermal conditions. The crystallinity of the polyolenific matrix in all materials was calculated from the expression:

$$\chi = \frac{\Delta H_m}{f_p \Delta H^0_m} \times 100 \qquad (4.1)$$

where ΔH_m (J/g) is the enthalpy of melting of the polymer matrix, f_p is the iPP/iPPMA weight fraction in the sample and ΔH^0_m is the enthalpy of melting of pure crystalline iPP (207.1 J/g ref [199]).

For all the experimental data presented below, each sample was measured at least three times and the results were found to be reproducible.

The DSC traces displayed by the solid lines in the top and bottom parts of **Figure 4.6** show the thermograms for iPP/iPPMA recorded during cooling and heating runs, respectively. Intense endothermic (*Tm*) and exothermic (*Tc*) transitions are seen but no glass transition temperature were noticeable for iPP/iPPMA even when cooling down to a temperature of about -150°C.

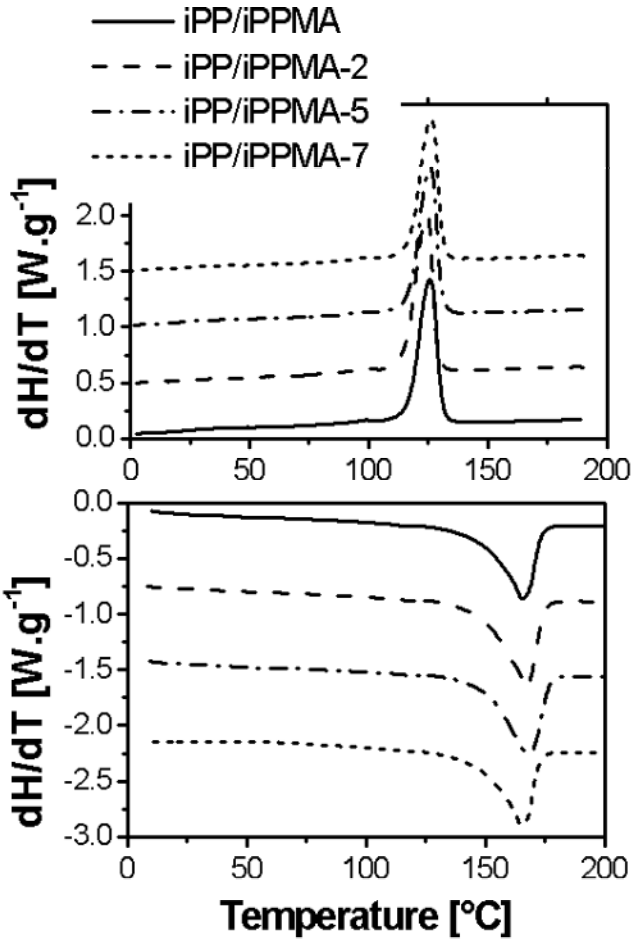

Figure 4.6 - DSC thermograms recorded with the temperature rate of 10°C.min^{-1} upon (top) first cooling and (bottom) second heating cycles. The DSC traces correspond to the iPP/iPPMA and iPP/iPPMA-clay samples assigned as (solid line) iPP/iPPMA, (dash line) iPP/iPPMA-2, (dash dot line) iPP/iPPMA-5 and (short dash line) iPP/iPPMA-7.

The crystallization/melting behavior of the polymer-nanocomposite is comparable to that of the pure iPP/iPPMA blend matrix. The following remarks can be made from the DSC scans presented in **Figure 4.6**; i) all samples display a melting endotherm extending from about 120 to 180°C. The shape of the

endothermic transition peaks is asymmetric and broadened on the low temperature side. The area under the peaks is rather constant so that the degree of crystallinity was calculated to vary gradually from 51% for iPP/iPPMA to 44% for iPP/iPPMA-7 whereby the melting temperature is nearly constant; ii) for all samples the crystallization process was recorded at rather similar undercooling with respect to the melting point i.e. at a temperature of 125°C. Accordingly, the observed crystallization behaviour may be attributed to heterogeneous nucleation of iPP. The main transitions, namely crystallization and melting processes, were also observed using polarized optical microscopy.

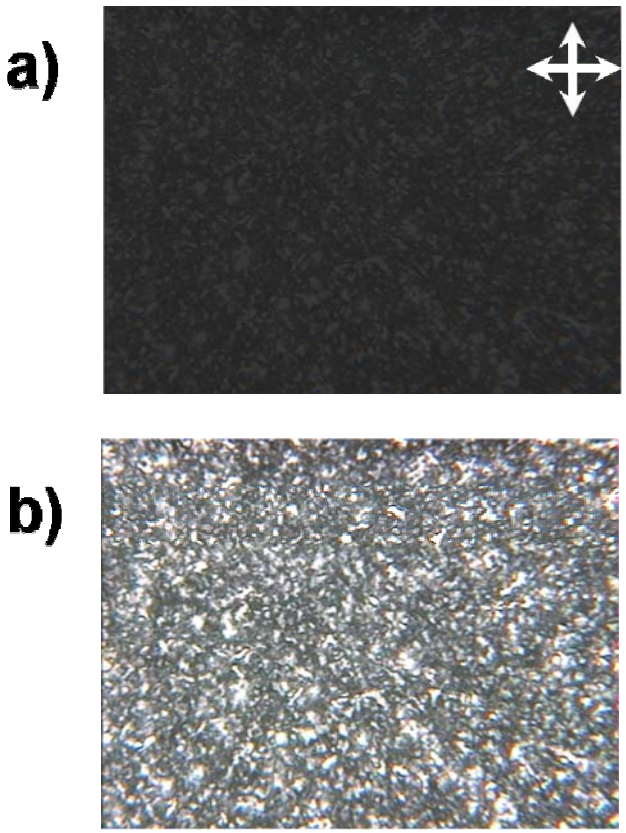

Figure 4.7 - Polarized optical microscope images showing a) the optically isotropic state as observed at a temperature of 180°C and b) the room temperature melt crystallized morphology for iPP/iPPMA sample. The sample was placed between two glass slides. Both images were taken under cross polarization conditions.

Upon cooling from the optically isotropic state, see the black pattern observed under cross polarization conditions at a temperature of 180°C for iPP/iPPMA in the **part a** of **Figure 4.7**, the development of anisotropic superstructures throughout the polymeric samples was detected from a temperature range corresponding well to the

by DSC detected exothermic peak. Examples of melt crystallized morphologies observed for thin sample films submitted to non-isothermal thermal treatment (10^{o}C/min) are shown for iPP/iPPMA in **part b** of **Figure 4.7** and for iPP/iPPMA-2, iPP/iPPMA-5 and iPP/iPPMA-7 in **Figure 4.8**.

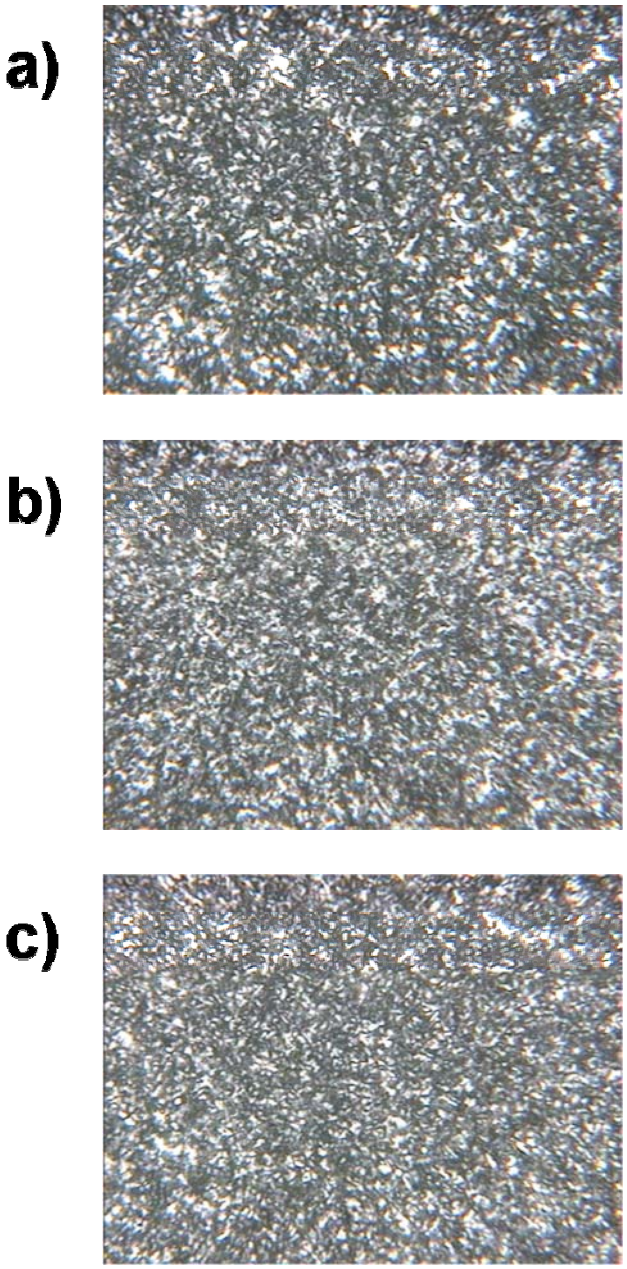

Figure 4.8 - Polarized optical microscope images showing the melt crystallized morphologies as observed at room temperature for a) iPP/iPPMA-2, b) iPP/iPPMA-5 and c) iPP/iPPMA-7 samples. The samples were placed between two glass slides. Both images were taken under cross polarization conditions.

Birefringent domains are clearly seen in the four optical micrographs recorded at room temperature and the size of the domains can be estimated to a few

micrometers. Although no clear structural features could be distinguished using polarized optical microscopy technique because of the limited size of the domains, qualitative optical microscopic observations have given the impression that domains nucleate at random position within the bulk material and grow with subsequent cooling. These findings indicate that the structure formation from the polymer melt goes by nucleation and growth, which usually can be strongly influenced by cooling rates or temperature of an isothermal process.

This effect is demonstrated to a large extend in the **Figures 4.9-12** where the thermograms recorded for all materials during cooling (with varied temperature rates of 1, 5 and 10°C/min) and heating (with a fixed temperature rate of 10°C/min) are presented.

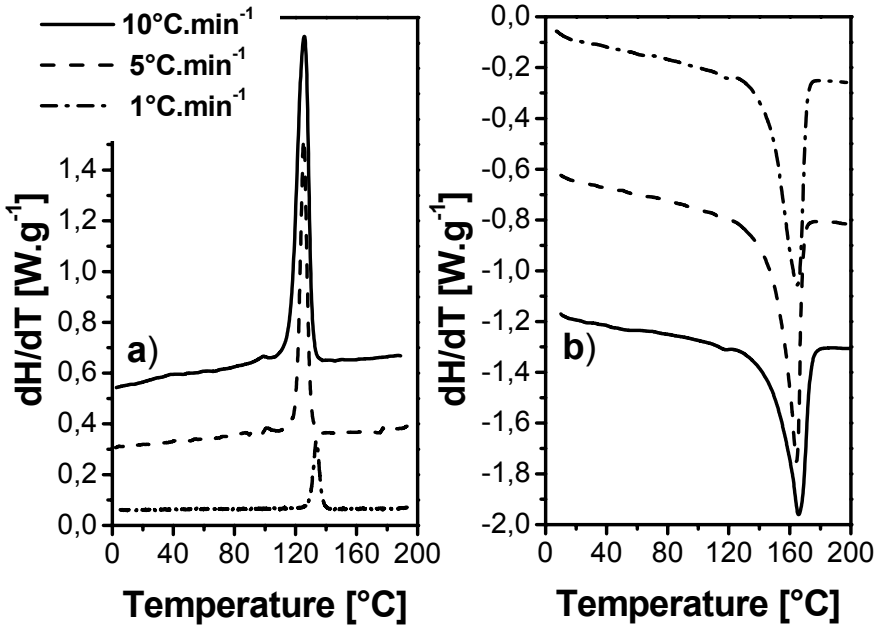

Figure 4.9 - DSC thermograms recorded during (a) cooling and (b) heating scans for the bulk iPP/iPPMA. The crystallization processes were measured with various temperature rates (10, 5 and 1°C/min). The melting processes were recorded with a fixed temperature rate of 10°C/min).

In brief, the same remarks as mentioned before are still valid, that is an exothermic peak is detected on cooling with the corresponding endothermic peak on subsequent heating.

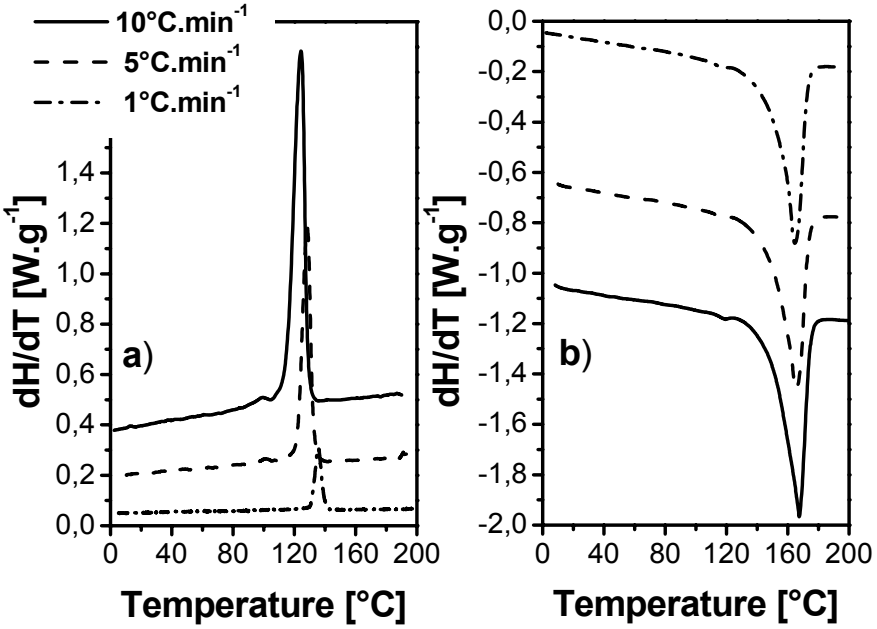

Figure 4.10 - DSC thermograms recorded during (a) cooling and (b) heating scans for the bulk nanocomposite iPP/iPPMA-2. The crystallization processes were measured with various temperature rates (10, 5 and 1°C/min). The melting processes were recorded with a fixed temperature rate of 10°C/min).

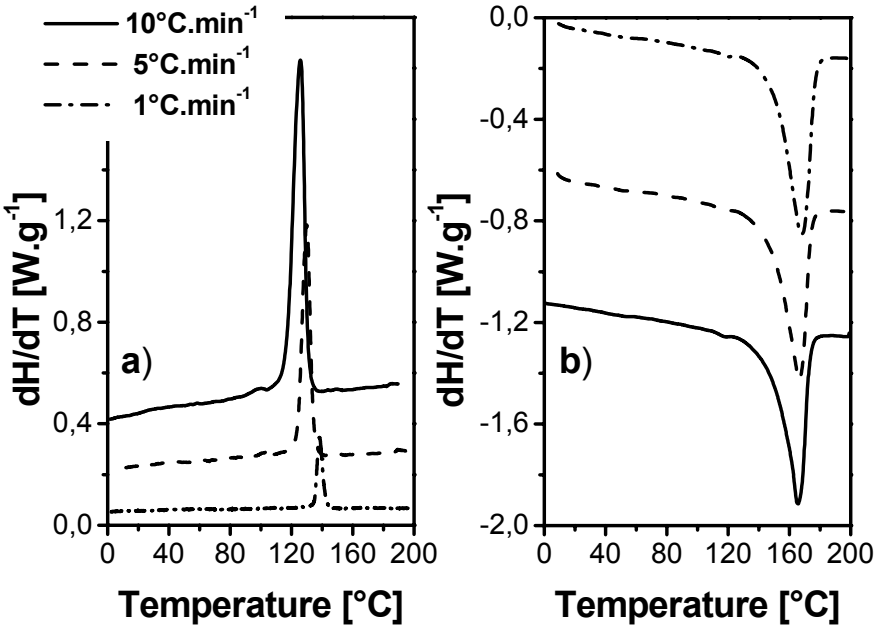

Figure 4.11 - DSC thermograms recorded during (a) cooling and (b) heating scans for the bulk nanocomposite iPP/iPPMA-5. The crystallization processes were measured with various temperature rates (10, 5 and 1°C/min). The melting processes were recorded with a fixed temperature rate of 10°C/min.

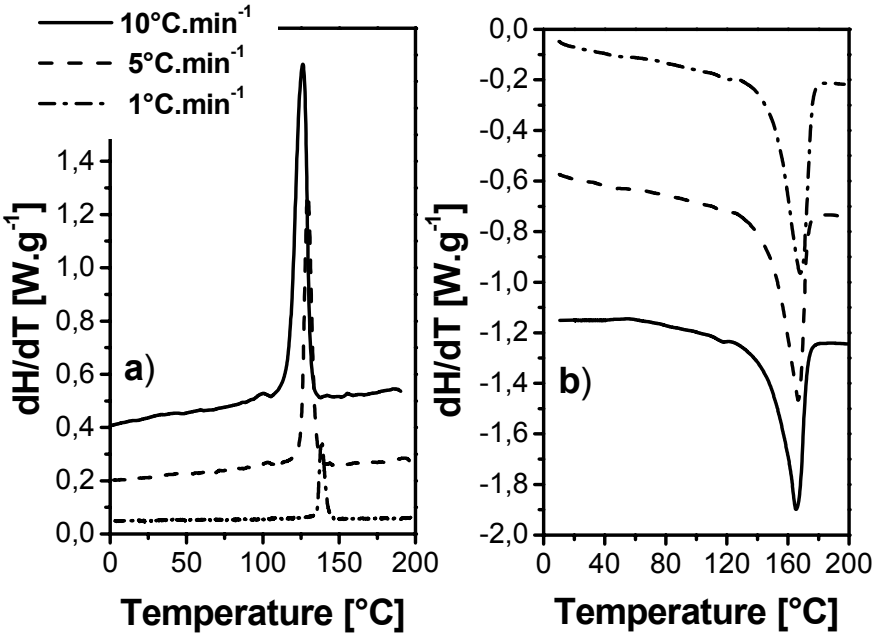

Figure 4.12 - DSC thermograms recorded during (a) cooling and (b) heating scans for the bulk nanocomposite iPP/iPPMA-7. The crystallization processes were measured with various temperature rates (10, 5 and 1°C/min). The melting processes were recorded with a fixed temperature rate of 10°C/min).

In addition, it should be mentioned that independent of the clay content, the melting temperature defined as the maximum of the endothermic peak is found to decrease when the cooling rate is increased. The observed change when going from a cooling rate of 10 to 1°C/min was more significant for the polymer nanocomposite with high clay content. A shift of 3°C was measured for iPP/iPPMA-7. Less ordered and or smaller crystals melt at lower temperature. Moreover, the figures clearly demonstrate that the crystallization temperatures are strongly dependent on the thermal history. Under rather fast cooling (10°C/min) the peak maximum is observed at lower temperature as can be viewed in **Figure 4.13**. This effect is assumed to arise from the discrepancy between the kinetics of cooling and crystallization. Here also, the dependence of the temperature of transition (T_c) versus the cooling temperature rate is more pronounced for the 7wt.-%-clay containing nanocomposite showing a decrease of 12°C when the cooling rate is changed from 1 to 10°C/min to be compared with the decrease of 9°C observed for the pure iPP/PPMA blend. When regarding solely the effect of the cooling rate on the variation of T_C observed from iPP/iPPMA through iPP/iPPMA-clay with increasing content of inorganic filler, we see that variation is directly proportional to the cooling rate. The strongest

variation is obtained for the lower cooling rate upon which an increase of 5°C was recorded. The increase of T_C observed from iPP/iPPMA through iPP/iPPMA-clay with increasing content of inorganic filler, is more pronounced for the lower cooling rate upon which an increase of 5°C was recorded.

Another interesting observation that can be made in **Figures 4.9-12** is that when the cooling is performed at 5 or 10°C/min additional exothermic peak is observed in the temperature range below the main crystallization transition. The corresponding transition temperature is increased from 99 to 102°C when the temperature rate is decreased from 10 to 5 °C/min. This is evidence that the system is not at equilibrium. However, the cooling rate does not have a significant effect on the degree of crystallinity as expressed by the heat flow recorded upon heating.

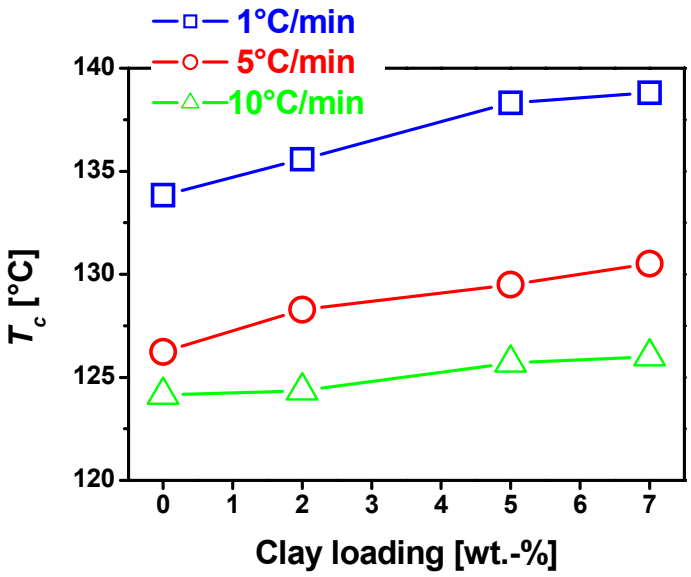

Figure 4.13 - Dependence of the crystallization temperature (T_c) as a function of the clay loading determined from the peak maximum in the DSC cooling measured with the temperature rates of 1, 5 and 10°C/min.

To summarize this preliminary characterization, it appears that crystallization of the semicrystalline organic component occurs with very little morphological restriction within the organic-inorganic materials.

6.2. Dynamic Mechanical Analysis

The transitions observed in the non-isothermal DSC experiments discussed above for pure iPP/IPPMA blend and iPP/IPPMA-based nanocomposites may also be investigated by dynamic mechanical analysis. The measurements were performed to evaluate the influence of the presence of clay on the properties under shear deformation in a broad temperature range. In a first run of mechanical testing, small shear amplitudes were used and the temperature sweep experiment was carried out over the temperature range from room temperature to 250°C. Herein only the cooling behaviour is reported. The dynamic storage and loss moduli together with the DSC thermogram as measured for the IPP/iPPMA blend matrix upon cooling from the melt are shown in **Figure 4.14** to illustrate the effects of the thermal transitions on the rheological behaviour.

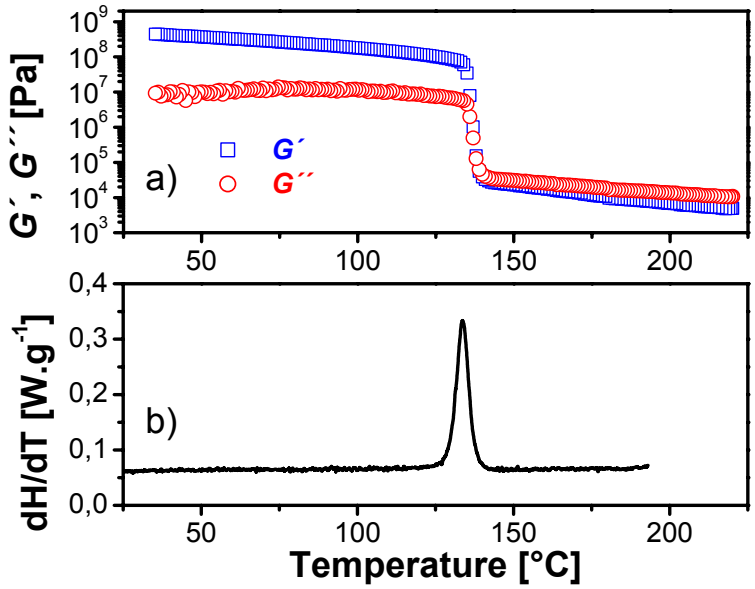

Figure 4.14 - a) Temperature dependencies of the storage (*G´*) and loss (*G´´*) shear moduli as measured for the iPP/iPPMA blend matrix upon cooling from the melt with the temperature rate of 2°C/min b) DSC thermograms recorded during cooling scan measured with the temperature rate of 1°C/min for the bulk iPP/iPPMA. A good agreement is obtained for the transition temperature by the two techniques despite the differences in the temperature rate.

A first inspection reveals a good agreement between the temperatures of transition obtained from the two techniques and the small discrepancy can be assigned to the different thermal treatment involved for the two types of measurement. The mechanical measurement was performer upon cooling with a temperature rate of 2°C/min to be compared with the 1°C/min temperature rate used

for DSC analysis. As was shown above, effect of temperature rate on bulk properties is more important when low variation rates are involved.

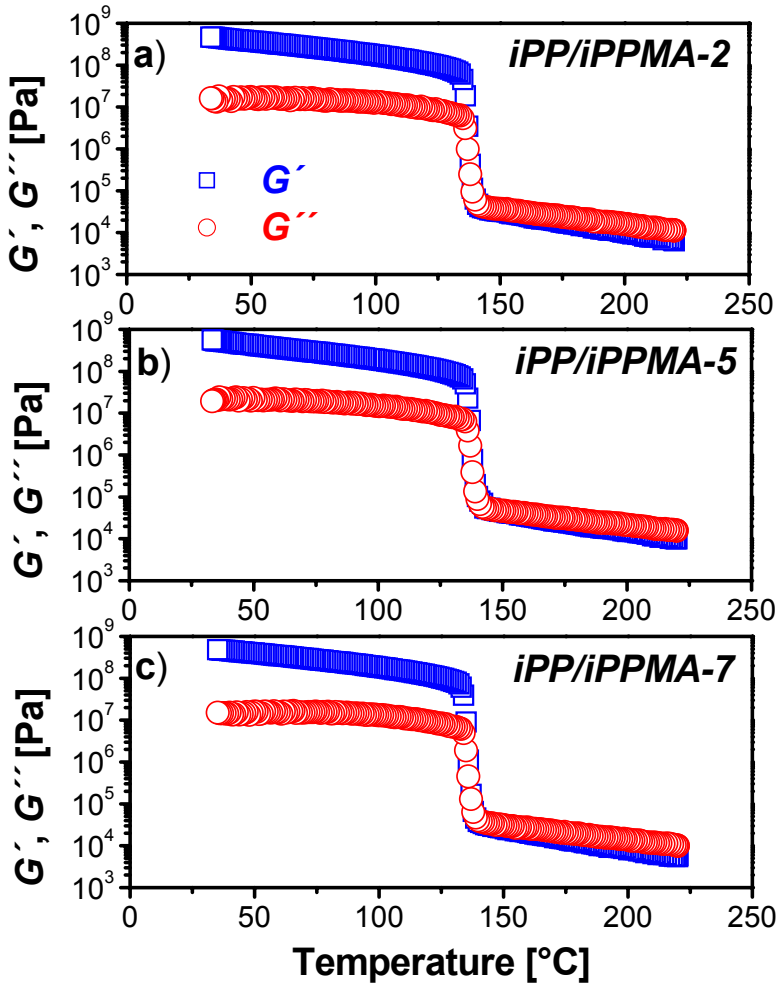

Figure 4.15 - Temperature dependencies of the storage (*G´*, square) and loss (*G´´*, circle) shear moduli as measured for a) iPP/iPPMA-2, b) iPP/iPPMA-5 and c) iPP/iPPMA-7 polymer nanocomposites upon cooling from the melt with the temperature rate of 2°C/min.

In the temperature range corresponding to the by DSC detected exothermic transition, common rheological feature related to such a transition, namely abrupt change in the storage and loss moduli, was observed. The increase in the *G'* and *G''* curves is located between two plateau regions characteristic of hard and soft materials in the low and high temperature ranges, respectively. The storage modulus assumes values of the order of 10^4 and 10^8 Pa in the two regimes. In the high

temperature range, the variation of the mechanical characteristics indicates that the materials are rather viscous.

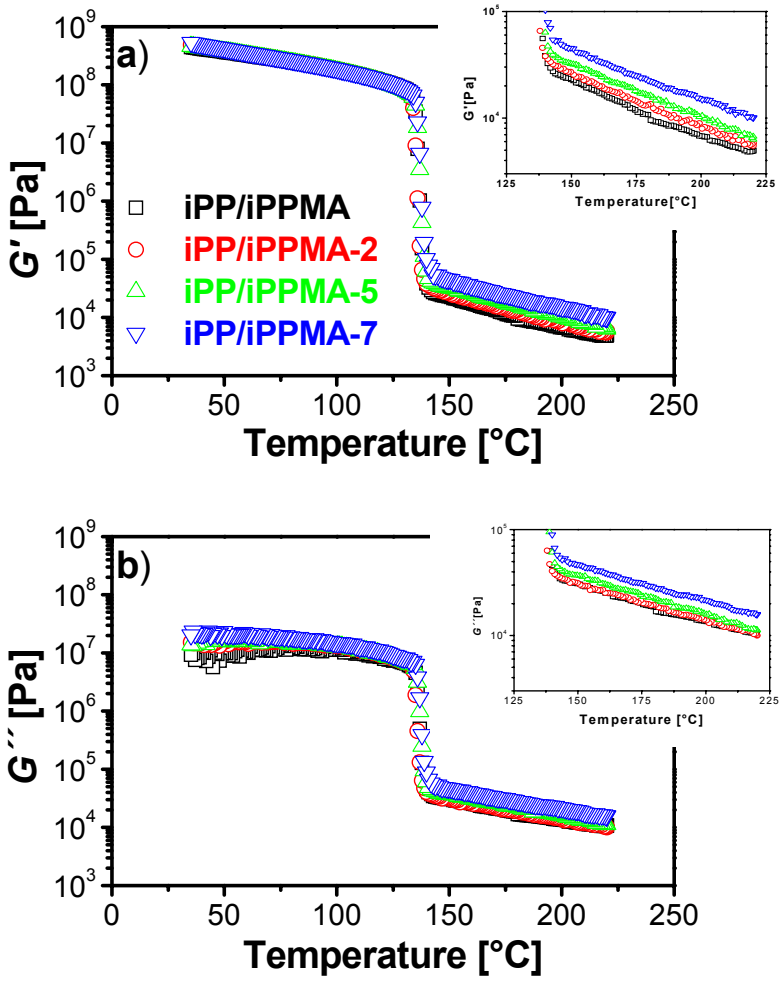

Figure 4.16 - Superposition of the temperature dependencies of a) the storage (*G´*) and b) loss (*G´´*) shear moduli as measured for iPP/iPPMA, iPP/iPPMA-2, iPP/iPPMA-5 and iPP/iPPMA-7 polymer nanocomposites upon cooling from the melt with the temperature rate of 2°C/min. The insets in parts a and b of the figure clearly show the increase in the plateau values of *G'* and *G''* in the molten state from iPP/iPPMA through iPP/iPPMA-2 and iPP/iPPMA-5 to iPP/iPPMA-7.

The nanocomposites displayed similar features in the temperature dependence of their rheological characteristics (**Figure 4.15**). Comparing the behaviour of iPP/iPPMA blend to the iPP/iPPMA-clay with various content of clay, the major difference is the values of modulus in the plateau regime (**Figure 4.16**). The increase of both the storage and loss moduli from the iPP-based matrix to the polymer nanocomposite with larger clay loading may be attributed to the high

stiffness of the nanosheets as well as to their large aspect ratio. The fact that the observed variation is more significant in the flowing state rather than in the solid state is rationalzed by an enhanced reinforcement effect from further alignment of the layered silicate filler in the molten state. The last information that can be extracted from this DMA concerns the change in the crystallization temperature when the clay content is varied. In full agreement with the DSC results, we also see that the crystallization is delayed from iPP/iPPMA-7 to iPP/iPPMA.

6.3. Differential Scanning Calorimetry in isothermal mode

In a second step, DSC experiments were performed in the isothermal mode. The samples were initially brought to the molten state and then quickly cooled down to the selected temperatures of 134, 138, 142 and 146°C at which the crystallization was recorded. Similarly to the non-isothermal measurements, the experiments were conducted under flow of nitrogen to avoid materials degradation. Here, we show the static crystallization DSC traces results only for the iPP/iPPMA nanocomposite containing 2% of clay (**Figure 4-17**). However the results are discussed with respect to the behaviour of pure iPP/iPPMA matrix and they are presented as the variation of the half-time of crystallization versus the crystallization temperature for all the materials in **Figure 4-18**.

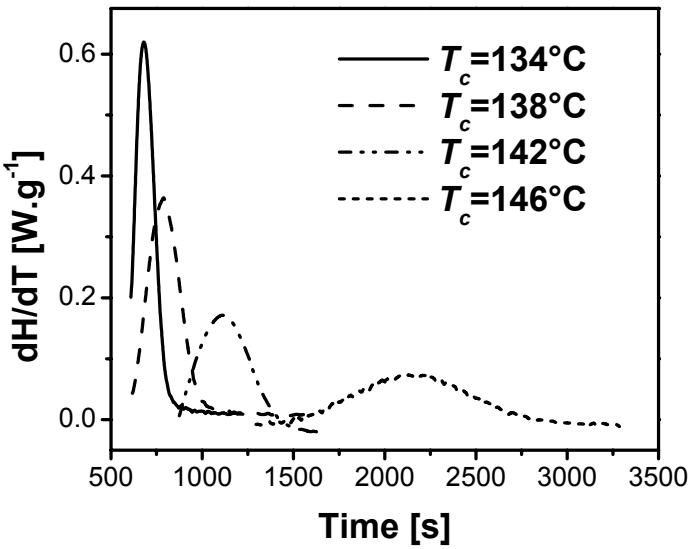

Figure 4.17 - DSC exothermic peaks recorded during isothermal crystallization at temperatures of (solid line) 134, (dash line) 138, (dash dot line) 142 and (short dash line) 146°C for the polymeric nanocomposite iPP/iPPMA-5.

When looking at all the samples separately, the crystallization process is slowed down when the crystallization temperature chosen for the isothermal process is changed from 134 through 138 and 142 to 148°C. This can be easily recognized from the shift of the maximum in the DSC profiles to higher time values along the *x* axis while decreasing the temperature (**Figure 4.17**). This is the expected behaviour for crystallizable polymeric systems for which structure formation goes by nucleation and growth. The extent of supercooling determines the nucleation efficiency and growth rate. For a crystallization temperature of 138°C or less, the clay-containing composites crystallize at a rate comparable to that of iPP/iPPMA while a dramatic difference is observed for higher crystallization temperatures. The crystallization process recorded at 142 and 148°C is accelerated upon addition of the montmorillonite clay as expressed in **Figure 4.18** by a decrease in the DSC isothermal crystallization half-time. The strongest effect is observed for a temperature of 146°C. This acceleration effect is more pronounced when increasing the clay content up to 5%. Effectively, iPP/iPPMA-5 and iPP/iPPMA-7 exhibits very similar behaviour indicating that above 5% further addition of clay does not affect the crystallization process. The observed acceleration of crystallization which is usually accompanied by a decrease in the spherulite size may be assigned to enhancement of spherulite nucleation by the montmorillonite particles.

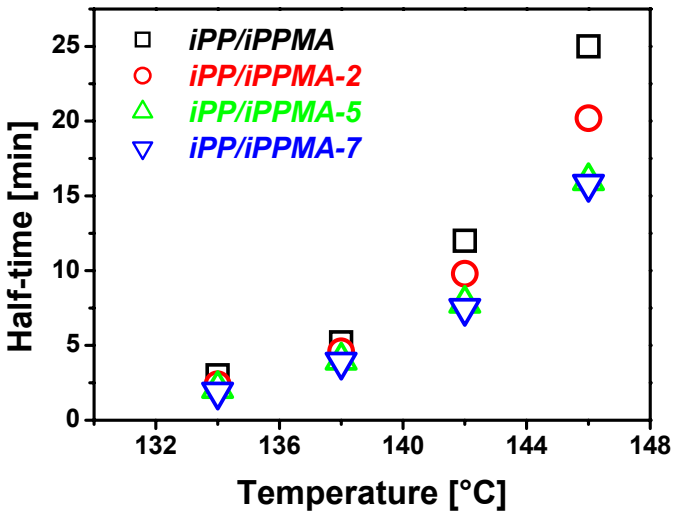

Figure 4.18 - Dependences of the half-time of crystallization versus the crystallization temperature as determined from the DSC experiments performed in isothermal mode for iPP/iPPMA, iPP/iPPMA-2, iPP/iPPMA-5 and iPP/iPPMA-7.

It should be mentioned that 2D small angle light scattering experiments were performed to estimate the average size of the spherulites in iPP/iPPMA and clay-containing iPP/iPPMA. The number of investigated sample was limited and the obtained results did not allow to establish a clear tendency (broad scattering maxima obtained in the 2D pattern indicated a very large distribution of the size of the scattering elements). However, the size of the spherulites determined for iPP/iPPMA-2, iPP/iPPMA-5 and iPP/iPPMA-7 was found to be equal or slightly lower than the one determined for iPP/iPPMA. It is rather difficult to judge whether the difference in crystallization behaviour observed for iPP/iPPMA-2 and iPP/iPPMA-5,7 should be attributed to a simple composition effect or if it should be related to the structure of the clay within the considered systems; exfoliated for iPP/iPPMA-2 and intercalated for iPP/iPPMA-5 and iPP/iPPMA-7 since in our sample both morphologies. Considering that a given number montmorillonite particles (about hundreds of montmorillonite particles according to Nowacki et al.[200]) are required to induce the nucleation of one iPP spherulite in quiescent conditions, it is obvious that in the exofialated configuration the number of potentially effective nucleation sites is higher as compared to the intercalated one. This consideration is in contradiction with our experimental results. Since the montmorillonite we used has mineral impurities, one cannot exclude the fact that the impurities play a role in the nucleation activity.

6.4 Atomic force microscopy

Many reports can be found in the literature about the application of atomic force microscopy to the investigation of polymer surfaces. [201,202] AFM has been extensively used to study the morphology of polyolefinic films in both undrawn and drawn states. Among all these studies, one should mention the extensive work of Magonov and co-workers on the investigation of the development of fibrillar structure from lamellae for gel-drawn films with various draw ratios.[203] Herein only isotropic films, i.e. before tensile test, have been examined. Because for AFM measurements in the contact regime the interaction between the tip and the sample surface may be strong enough to damage soft materials of polymeric nature, height and phase imaging were performed simultaneously in tapping mode at the fundamental frequency of the –Si cantilever with typical scan rate of 0.5-1.0 line.s^{-1}. The AFM analysis of 5µm thick films prepared from the pure polypropylene homopolymer (iPP) and anhydride maleic grafted copolymer (iPPMA) are displayed in **Figure 4.19** and

4.20, respectively. AFM images of film made of the blend of the two types of propylene polymers (iPP/iPPMA) are presented in the **Figure 4.21**. In all cases, the Figures present the morphologies as obtained after cooling from the melt down to room temperature and the semicrystalline character of the homopolymers and iPP blend can be easily identified. In both cases, regions with low topography are seen in the border regions of spherulitic-like elements. The AFM measurements of the iPPMA sample crystallized nonisothermally shows more bundle-like entities as compared to the non-modified iPP but the center of the spherulites, from where nucleate the crystallization is clearly seen.

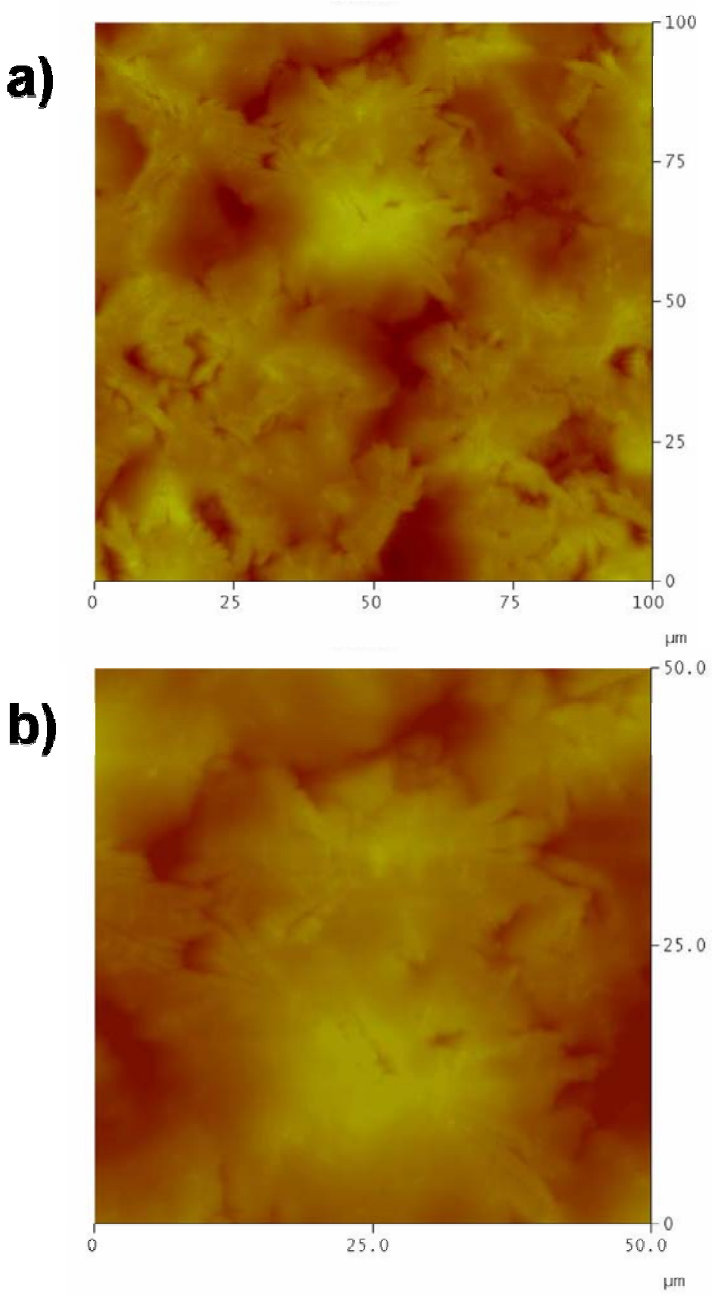

Figure 4.19 - Semicrystalline morphology of iPP sample film of 5μm thickness crystallized nonisothermally. The a is the height image with scan size of 100 μm the b is the phase image with scan size of 50 μm.

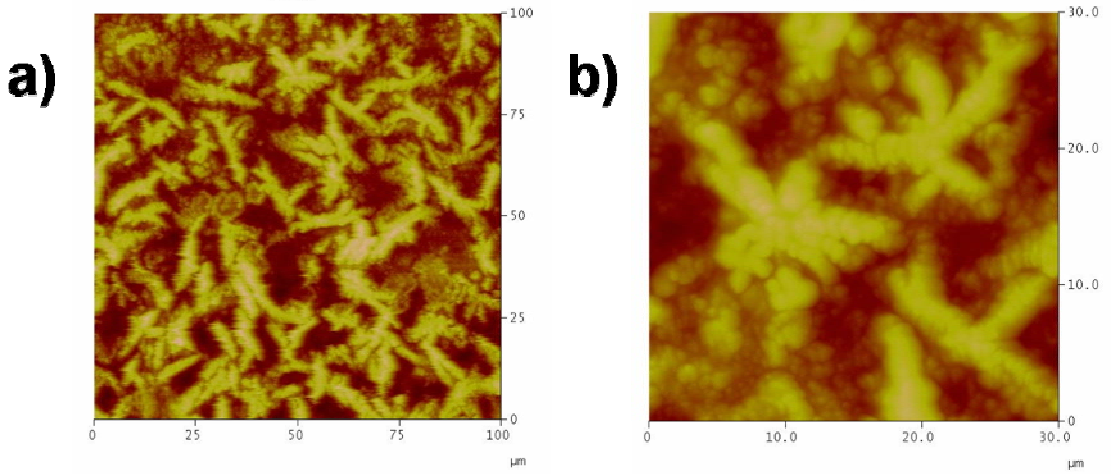

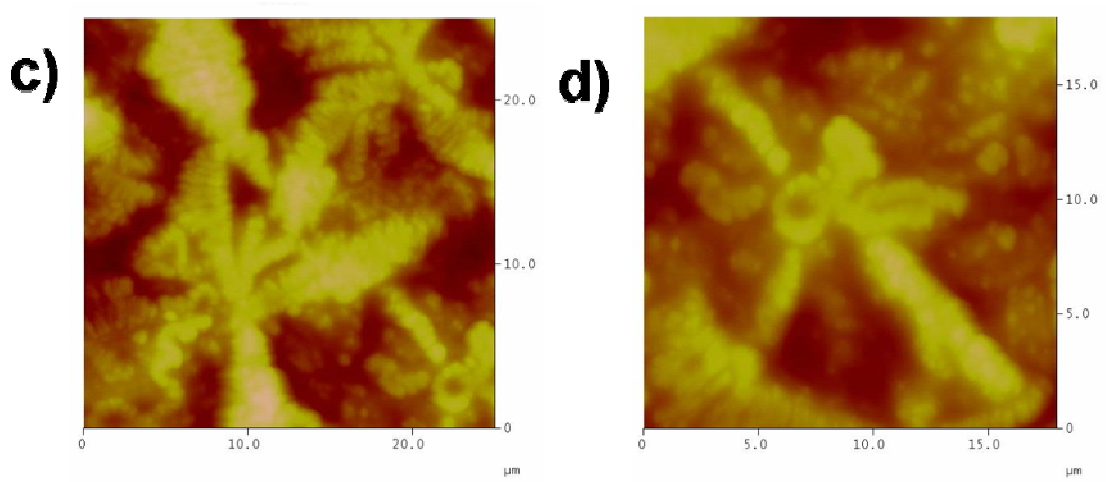

Figure 4.20 - Semicrystalline morphology of iPPMA sample film of 5μm thickness crystallized nonisothermally as observed by AFM phase images with scan size of a) 100 b) 30, c) 25 and d) 20 μm, respectively.

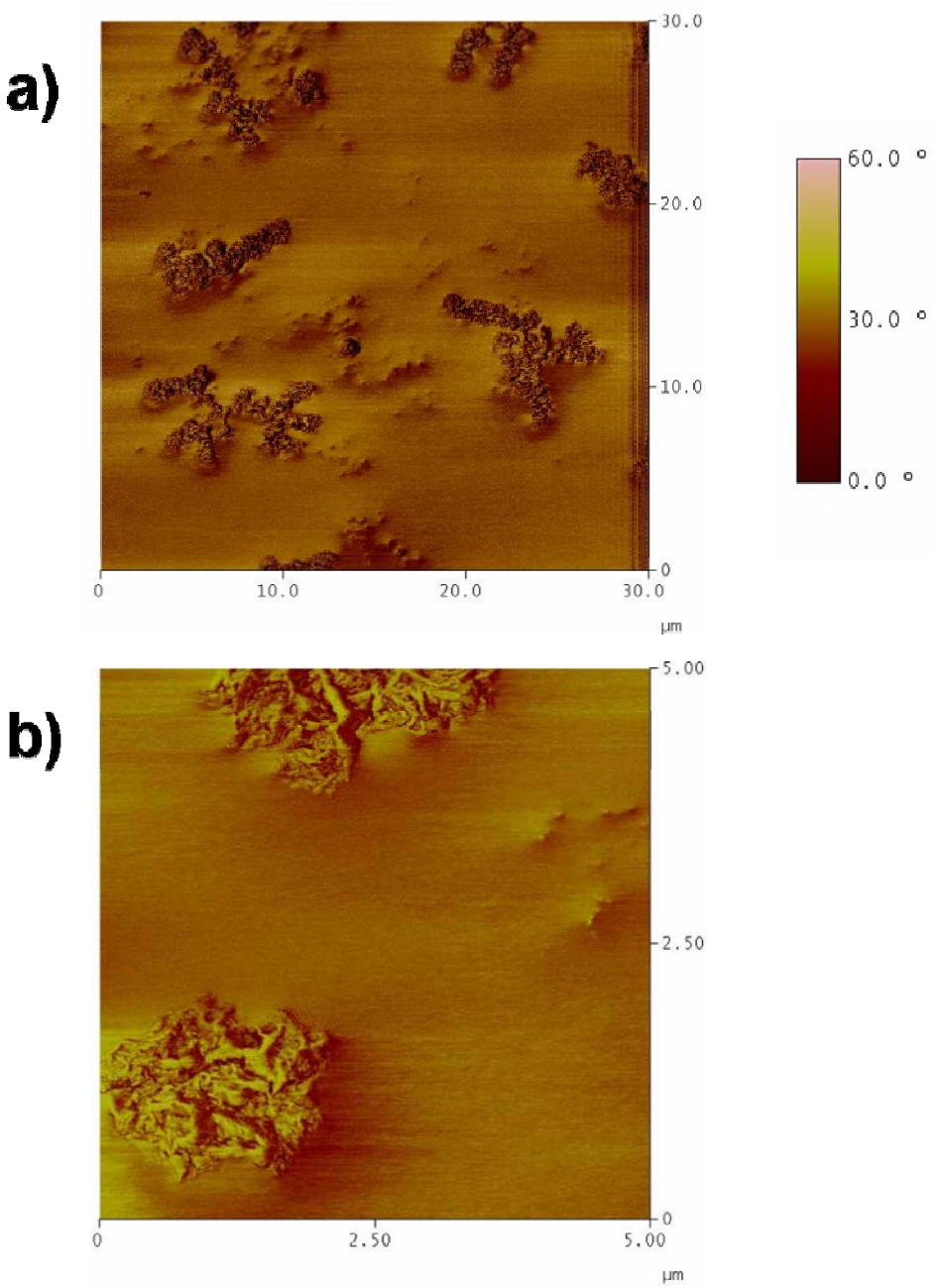

Figure 4.21 - Semicrystalline morphology of iPP/iPPMA sample film of 5µm thickness crystallized nonisothermally. Images were recorded in phase modde with scan size of a) 30 and b) 5 µm, respectively.

AFM is a well-suited method to illustrate the spatial distribution of components making composite materials, as for example the distribution of the crystalline and amorphous phases. With respect to these considerations, nanocomposite polymer substances made from a semi-crystalline polymer may be considered as a three phase system, namely the amorphous and crystalline parts of the organic matrix and

the inorganic inclusion can theoretically be distinguished. In the context of our study, the main motivation of using AFM technique was to detect the presence and to estimate the surface density of clay particles in our nanocomposites systems.

Surface images of polypropylene nanocomposites having the lower and higher clay contents are shown in **Figures 4.22** and **4.23**. They demonstrate the presence of domains with a rather random distribution over the whole field of view. Such image indicates selectivity of the scanning probe towards the polymeric matrix and the inorganic fillers. On the basis of a qualitative analysis of the AFM images recorded for iPP/iPPMA-2, iPP/iPPMA-5 and iPP/iPPMA-7 we concluded that the AFM surface analysis results were in good agreement with nominal volume fractions of clay in the samples; the number of “dark“ inorganic inclusions increase with the clay content.

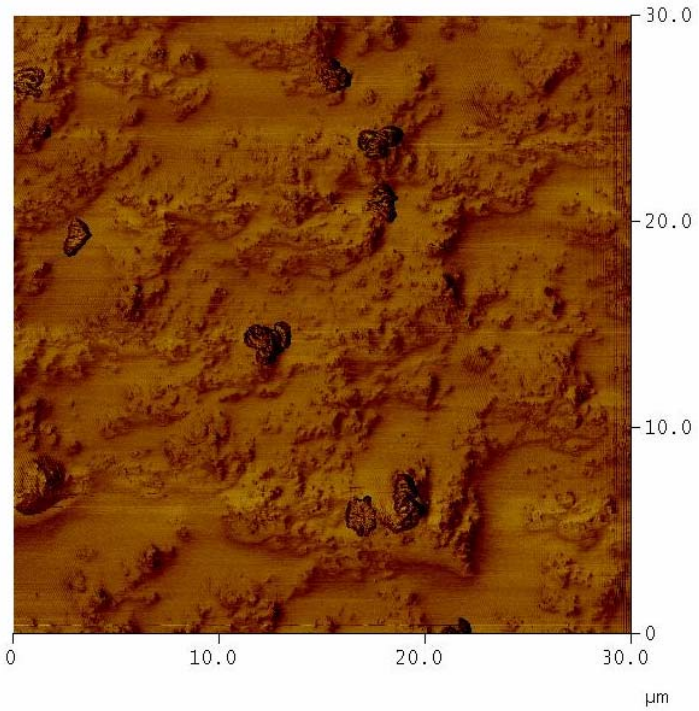

Figure 4.22 - Phase AFM image recorded for melt crystallized sample of iPP/iPPMA-2.

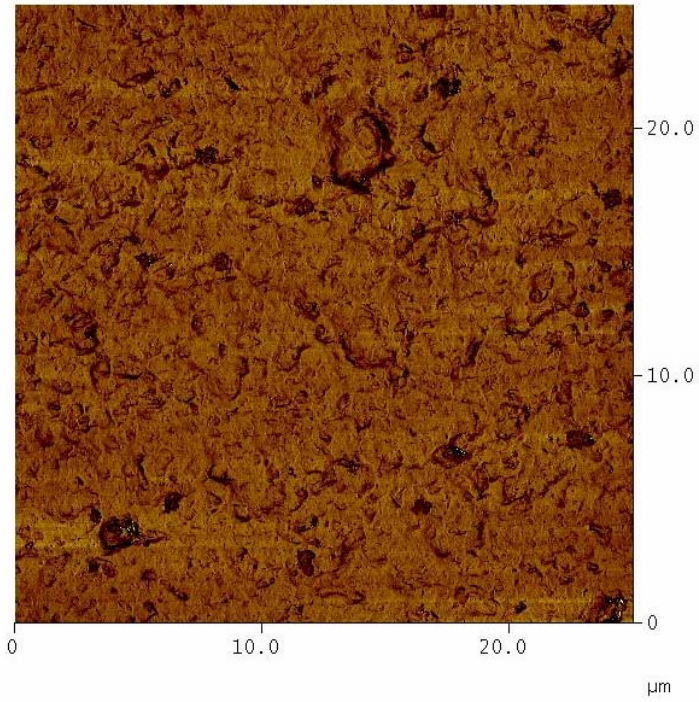

Figure 4.23 - Phase AFM image recorded for melt crystallized sample of iPP/iPPMA-7

6.5. Scanning electron microscopy

The presence of the montmorillonite clay within the bulk nanocomposites was also ascertained by scanning electron microscopy. In contrast to the AFM data providing information about the surface morphology, SEM performed on fracture samples gives insight in the bulk morphology of samples. **Figure 4.24** shows the typical SEM photograph of the cross section of iPP/iPPMA film.

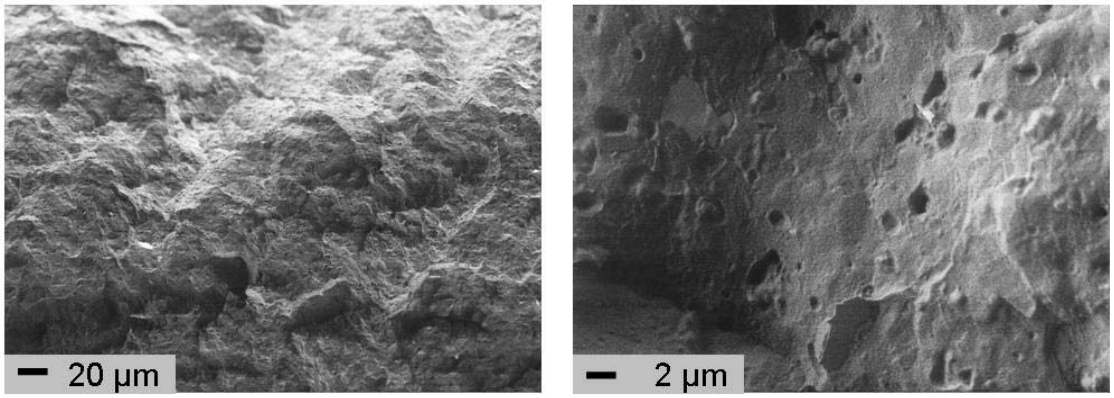

Figure 4.24 - Scanning electron micrographs of fractured sample showing the bulk morphology of iPP/iPPMA.

A series of six SEM micrographs of iPP/iPPMA involving dispersed montmorillonite hybrid particles with weight fractions of 2, 5 and 7 are shown in **Figure 4.25**. The

images were taken with different magnification as indicated in the scale bars of the micrographs.

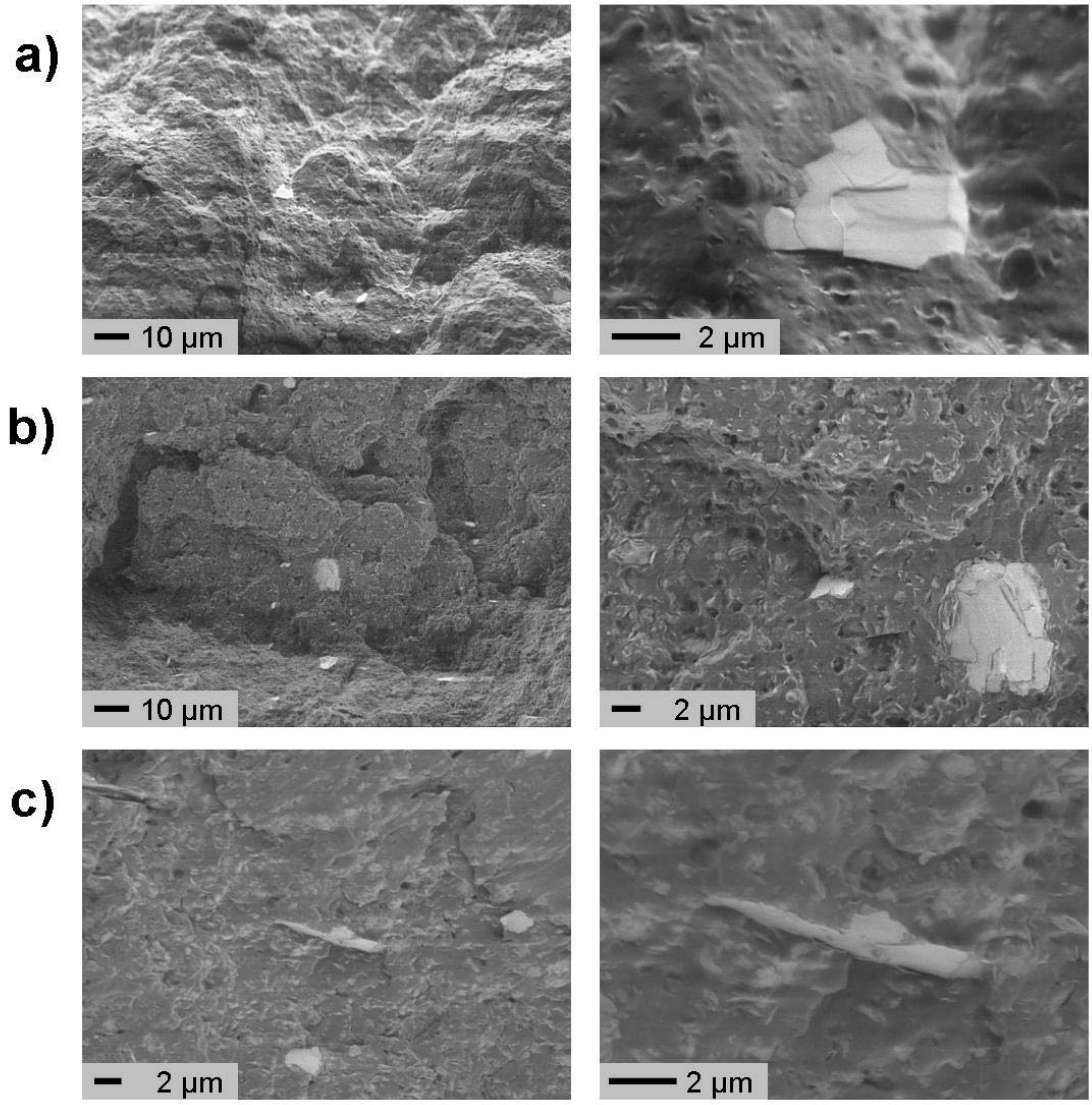

Figure 4.25 - Scanning electron micrographs of fractured samples showing the bulk morphology of a) iPP/iPPMA-2, b) iPP/iPPMA-5 and c) iPP/iPPMA-7.

It can be seen that the organic-clay hybrid particles, with a lighter appearance in the micrographs, are dispersed as platelets of around 1-4 *µ*m length in the iPP/iPPMA matrix. The particles assume a random distribution over the whole field of view with no specific orientation. While the clay content is increased it is seen that the inter-hybrid particle distance is significantly reduced. Imaging techniques provide only information on the morphological elements in the real space but quantitative

evaluation of the structural details remains difficult. To go further in our investigation we characterized our system using X-ray diffraction technique.

6.6. Wide angle X-ray diffraction

Wide-angle X-ray investigation was first performed in reflection mode for isotropic samples to gain insight in the crystalline morphology. The wide-angle X-ray diffractogram presented in **Figure 4.26** for the iPP/iPPMA confirms the DSC results displayed in **Figure 4.6**. The WAXS spectrum shows exclusively the diffraction peaks characteristic of the monoclinic α-phase; *a* = 6.66 Å, *b* = 10.78 Å, c = 6.495 Å, and β = 99.62°. The α-phase is known to be the most stable crystalline phase of PP.[204] Crystalline diffraction pattern typical for the PP α-phase was also obtained for the three clay containing PP-based materials when the measurement was performed at ambient temperature. **Figure 4.27** displays the scattered intensity as a function of scattering angle for iPP/iPPMA-5 as a representative example. X-ray data was also collected at a temperature of 200°C.

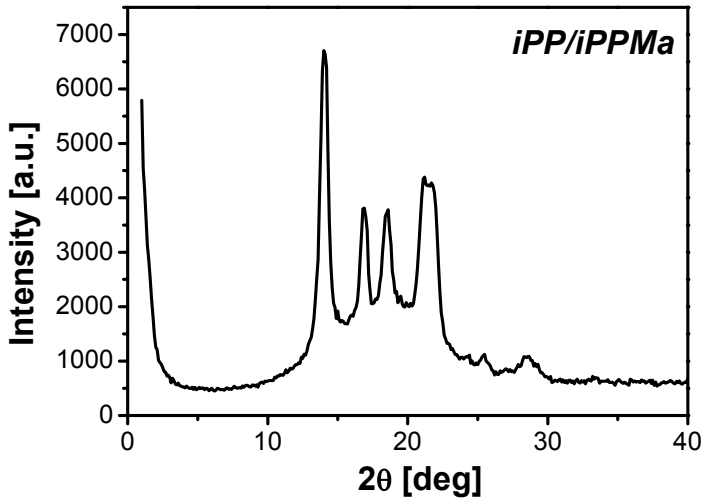

Figure 4.26 - Wide-angle X-ray scattering intensity distributions recorded at room temperature for the iPP/iPPMA matrix.

The increase of measurement temperature to 200°C caused melting of crystalline PP, which became amorphous. The scattering diffuse halo corresponds to a broad distribution of inter-atomic distances of about ~0.6 nm related to the liquid-like organization of the polypropylene matrix in the melt. Scattering effects

reminiscent of the α–crystalline phase were observed to appear upon further cooling in a temperature range correlating well to the by DSC detected crystallization peak.

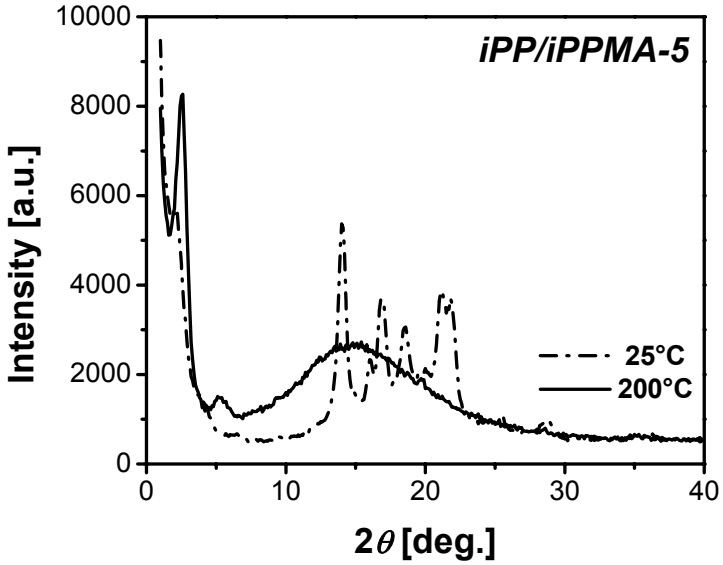

Figure 4.27 - Wide-angle X-ray scattering intensity distributions recorded for iPP/iPPMA-5 in (dash line) the crystalline and (solid line) molten states.

In both crystalline and melt scattering data shown in **Figure 4.27**, broad diffraction peaks can be seen in the range of 2θ value below 10°. These peaks originate from the presence of the montmorillonite clay.The level of intercalation in the polymer nanocomposites can be evaluated from a comparison of the clay interlayer spacing (d_{001}) for the polymeric composites and for the neat clay. The interlayer spacing can be calculated from the 2θ position of the clay diffraction peak using Bragg's law. The organo-modified montmorillonite used in this study shows maximum in the diffraction intensity profile at a 2θ value of 2.68° (X-ray diffractogram not shown), which corresponds to an interlayer spacing of 3.34 nm. Such relatively large inter-layer spacing (in comparison to the typical value obtained for natural clay, 1.1-1.3 nm) confirms the presence of the intercalant between the clay platelets. The profile of the intensity distribution, i.e. broad Bragg peak with no clear higher order reflections, indicated a broad distribution of the interlayer spacing corresponding to a short range order. For clarity purpose, **Figure 4.28** shows again the diffraction spectra for iPP/iPPMA, iPP/iPPMA-2, iPP/iPPMA-5 and iPP/iPPMA-7 recorded at room temperature in the low angle regime. For the iPP/iPPMA system (bottom diffractogram), no diffraction peak is observed in contrast to the case of iPP/iPPMA-7

(top diffractogram), where a broad scattering maximum is seen at a 2θ value of about 2.4°. The low angle peak of iPP/iPPMA-7 is shifted towards lower 2θ value as compared to the position of the peak of the neat clay (indicated by the vertical dashed line in the **Figure**). Correspondingly the low angle peak (2θ = 2.4°) gives an interlayer distance of 3.68nm for iPP/iPPMA-7 that is slightly larger (~0.3nm) than the distance of the clay without polymer. An increase in the clay interlayer spacing expresses the incorporation of polymer within the inorganic layer structure.

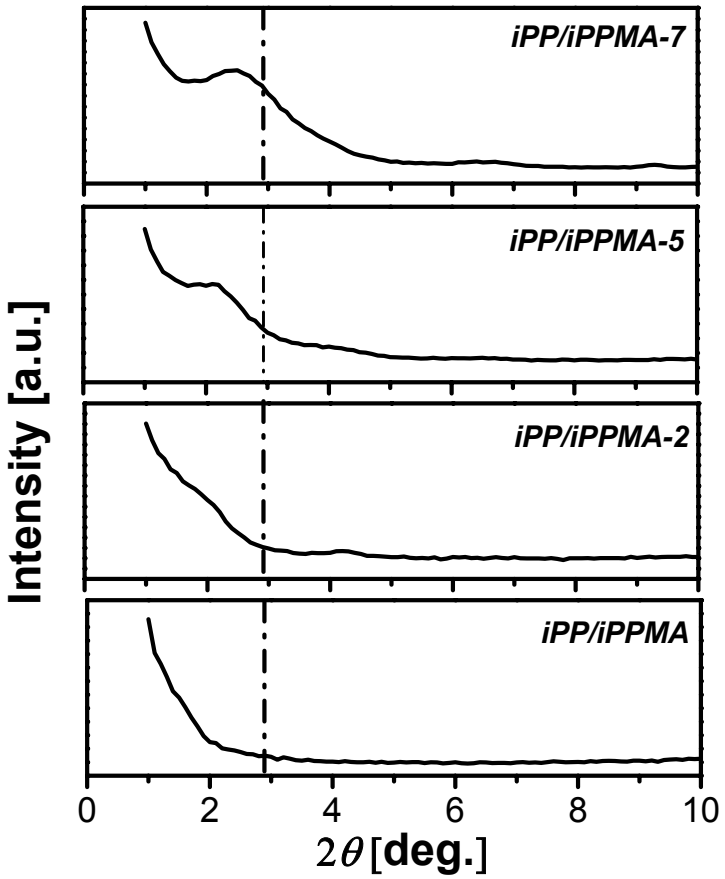

Figure 4.28 - Wide-angle X-ray scattering intensity distributions recorded for iPP/iPPMA, iPP/iPPMA-2, iPP/iPPMA-5 and iPP/iPPMA-7. Only the low-angle regime is presented to clearly highlight the scattering features due to the presence of the clay. The vertical dashed lines shown in the four diffractograms correspond to the 2θ position of the bragg peak assigned to the interlayer spacing for the neat clay.

The extent of incorporation should be directly related to the measured increase. It is obvious that the silicate interlayer distance increase with decreasing the clay content in the polymer nanocomposites. This effect is more clearly seen in

the case of iPP/iPPMA-2 for which it is difficult to determine unambiguously the position of the bragg peak since it is superimposed to the scattering signal arising from the beam stop. And that the interlayer separation is more efficient at low clay loading. The change in the low-angle diffraction features observed from iPP/iPPMA-7 to iPP/iPPMA-2 is considered as an indication of change in the superstructures based on a complex self-organization of iPP/iPPMA and montmorillonite. At this level, we may presume that for iPP/iPPMA-7 and iPP/iPPMA-5 exfoliation is not complete but incorporation of the hydrophobic polypopylene chains within the silicate layer occurs. This suggests an improvement of interfacial adhesion between iPP and fillers due to the compatibilizing effect of iPPMA.[205] Whereas for iPP/iPPMA-2 the almost disappearance of low angle diffraction peak accounts most likely for exfoliation of the silicate during processing. In the next parts of this chapter, transmission electron microscopy and mechanical data collected for iPP/iPPMA and the three iPP nanocomposites will be presented in order first to document the proposed structural changes and second to evaluate the effect of exfoliation on the macroscopic characteristics such as stiffness, ductility…

Returning to **Figure 4.27** it should be mentioned that when the X-ray measurements were performed at a temperature of 200°C, at which the polymer matrix is in the molten state, the basal spacing peak is narrower, exhibits higher intensity and is slightly shifted to lower 2θ values as compared to the room temperature measurement. These changes were observed for all the clay compositions. These findings are assumed to result from the thermal expansion of the polymer matrix at high temperature.

6.7. Transmission electron microscopy.

By using transmission electron microscopy, direct evidence of the local structure of the polymer layered silicate nanocomposites was obtained in real space in complement to the reciprocal space based scattering technique. The dispersion features of the montmorillonite clay within the iPP matrix as determined by wide angle X-ray diffraction were largely confirmed by TEM images shown in **Figure 4.29**. The part a of the Figure, displaying the nanoscale morphology of iPP/iPPMA, can serve as reference for comparison with iPP/iPPMA-2, iPP/iPPMA-5 and iPP/iPPMA-7. Morphological examination at this size scale does not allow identifying clear features in the TEM image of iPP/iPPMA and the major difference observed in

the images of the clay-containing materials (**parts b-c**) is the presence of dark lines distributed over the whole field of view of the figure. This finding indicates that for all three nanocomposition the clay particles embedded in the semicrystalline polymer matrix. However, variation in the state of dispersion of the inorganic phase can be noticed.

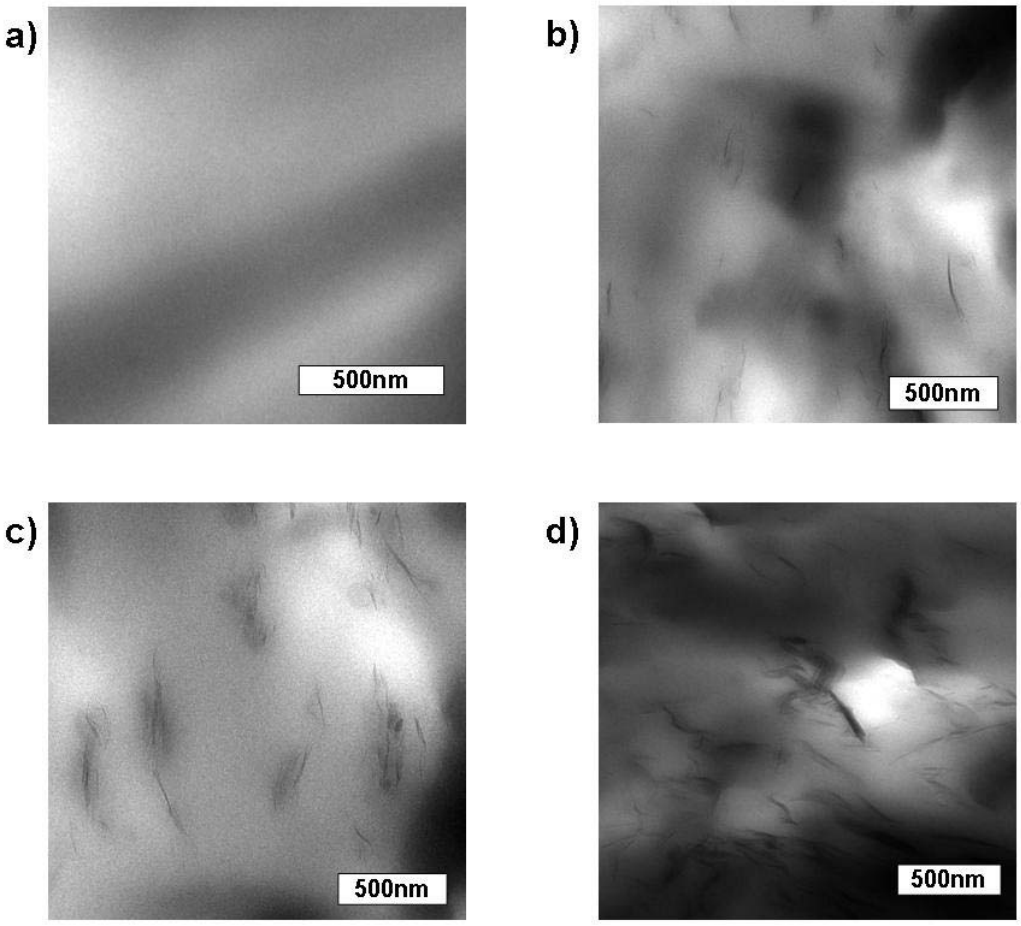

Figure 4.29 - Transmission electron micrographs showing the nanoscale morphology for a) iPP/iPPMA, b) iPP/iPPMA-2, c) iPP/iPPMA-5 and d) iPP/iPPMA-7.

These dark lines correspond to the silicate sheets and exhibit cross section of nearly 2-4nm in thickness. Most of the clay particles (edges of the silicate layer) display perpendicular alignment with respect to the surface of the film. With increasing the concentration of clay, it is seen that the distance between clays is decreased. High density of stacked silicate layers are clearly observed for the iPP/iPPMA-7 sample (**Figure 4.29-d**). On the other hand, single clay platelets (indicating exfoliation) are observed in image taken for the specimen containing the lower clay content (**Figure 4.29 - b** for iPP/iPPMA-2). These two extreme cases are

indicative of the different morphologies possible for polymer nanocomposites described in the introduction part of this chapter; exfoliation for iPP/iPPMA-2 and intercalation for iPP/iPPMA-7. Intermediate situation is obtained for the iPP/iPPMA-5 sample where both stacked as well as single clay platelets are seen. Together with the X-ray data, this suggests that the penetration of the PP chains within the clay system occurred leading to the production of intercalated morphology but transformation into an exfoliated-dispersion state was not possible during the time of the melt process. These TEM data confirm that iPPMA acts efficiently as an interfacial compatibilizer.

6.8. Mechanical properties.

In our study, the composition of the iPP/iPPMA matrix was kept constant so that the change in the mechanical behaviour can be directly related to the clay content or more precisely to the relative amount of clay with respect to iPPMA. Tensile stress–strain curves (not shown here) were recorded for at least five independent film samples of neat polypropylene and the filled hybrid materials. A a clear effect of the presence of nanoparticles was observed and the results are shown in **Figure 4.30** as dependences of the tensile strength, tensile modulus, elongation at yield and elongation at break versus clay content. It is seen that the combined introduction of maleic anhydride-g-polypropylene and montmorillonite results in a general increase in the tensile strength. The effect is more pronounced in the lower loading region. For a clay content of 2% by weight, the tensile strength value is nearly twice (~24MPa) as compared to pure polypropylene (~12MPa). When the particle fraction if of 5wt.-% or more, the tensile strength is seen to slightly decrease down to a value of about 15 MPa but it remains larger than for polypropylene. Similar clay loading dependence can be observed for the elongation at yield that assumes a maximum value for iPP/iPPMA-2. The decrease in both tensile strength and elongation at yield above 2wt.-% corresponds to the change in the dispersion level of the montmorillonite. High filler loading is detrimental to the uniform dispersion of clay in the polymer matrix and consequently deterioration of some mechanical properties is obtained due to the inevitable clay aggregation.[206] Young's moduli of the nanocomposites exhibit a simple relationship to the clay content. A direct proportionality, nearly linear, is obtained in the composition range studied and the value of the modulus is increased by factor 3 increasing from 0.35GPa for

polypropylene to 1.3GPa for PP-PPMA-7. The increase in stiffness is obviously a result of the high modulus of the particulate fillers ($modulus_{silica}$ ~ 70GPa). Part d of **Figure 4.30** reveals that addition of montmorillonite above a threshold value of 2% leads to a linear decrease of the elongation at break so that no improvement in ductility is obtained.

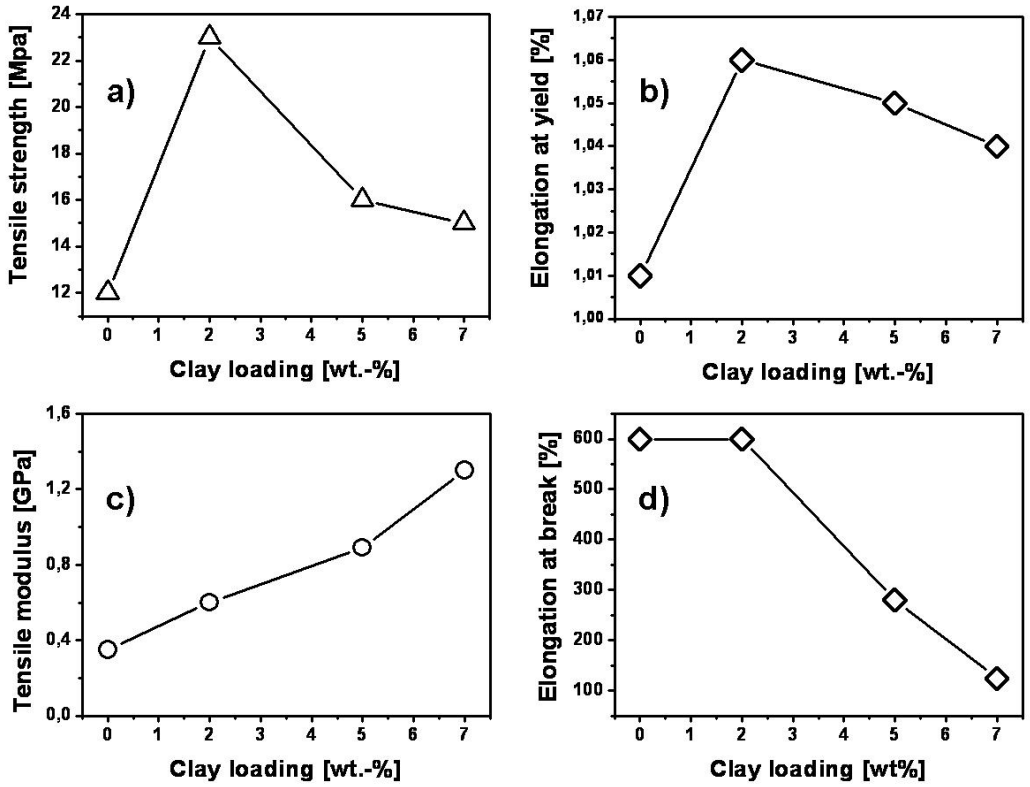

Figure 4.30 - Dependence of the mechanical characteristics versus the clay content for iPP/iPPMA nanocomposites. a) tensile strength, b) elongation at yield, c) tensile modulus and d) elongation at break.

The mechanical results presented above corroborate well the structure and morphology data obtained by WAXS and TEM, i.e., for small amount of the modified clay leads probably to better dispersion within the time of mixing.

6.9. Two-dimensional wide angle X-ray scattering

The degree of molecular orientation in stretched films is dependent of a number of parameters, including the extent of elongation, deformation rate, temperature of deformation, molecular weight of the macromolecules. Morphology of deformed films of polypropylene investigated by means of a broad range of method has been published as early as 1965 by Samuels.[207] The organization on a submicroscopic size scale can be examined by means of infrared dichroism, birefringence, small-angle light scattering, electron microscopy and X-ray diffraction. In our study on polymer nanocomposites we mainly focused on the application of the last two techniques. [208]

Semicrystalline polymer films are made of ordered domains, namely the crystallites consisting of aggregates of lamellae and of disordered domains, namely the amorphous phase. In the isotropic state, these domains assume random orientation within the bulk material. Elongation of such films leads to a gradual transformation of the structure which thus assumes specific orientation with respect to the orientation axis. Upon uniaxial deformation as is the case during tensile testing, the main chains are assumed to orient along the drawing direction. The deformation of semicrystalline polymer samples is non selective towards the biphasic structure-making domains so that it results in an orientation of both crystalline and amorphous regions. In the course of mechanical deformation, the crystallites are transformed into fibrils. The ability of polymer materials to deform and consequently to orient under external stress is due to the intrinsic properties of macromolecules. In the case of multiphasic systems, as for example polymer nanocomposites, other parameters play an important role. Among them, one may cite the state of dispersion of the minor phase (inorganic filler) that is strongly related to the interaction strength between components. All these aspects were confirmed to a large extend by our wide angle X-ray data collected in transmission mode with the help of a 2D position sensitive detector. From an experimental aspect, the orientation of macromolecular chains making part of crystallized domains can be easily probed from 2D WAXS patterns by integrating the scattering features along specific directions. The diffraction peaks detected along the direction parallel to the drawing direction gives information about periodicities along the polymer chains. Interchain correlations are extracted from the diffraction peak detected along the direction perpendicular to the stretching direction.

The manner by which the crystal axes are oriented through deformation is illustrated in **Figure 4.31** for iPP/iPPMA as a comparison of the WAXS 2D patterns obtained before and after tensile testing.

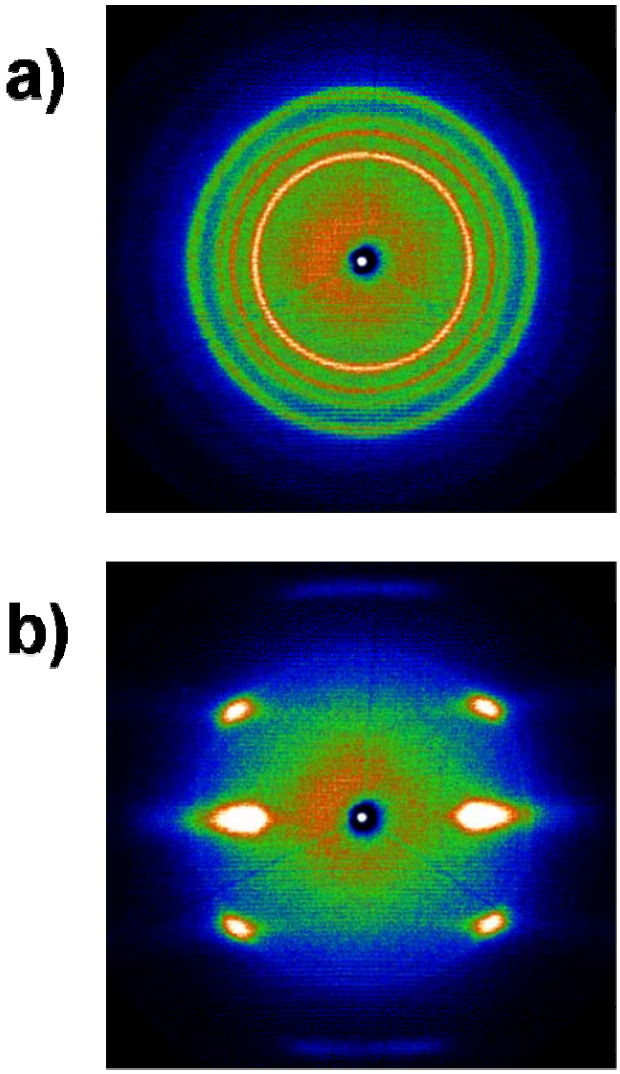

Figure 4.31 - Two-dimensional wide angle scattering patterns recorded for iPP/iPPMA films a) before and b) after tensile test measurement performed until break. The scattering pattern was recorded with the iPP/iPPMA film with perpendicular orientation with respect to the X-ray beam direction. The deformation direction is along the vertical of the 2D pattern.

In the two presented diagrams, the same number of intense diffraction is detected but the major difference is the azimuthal independent scattering intensity distribution for unstretched films to be opposed to the azimuthal dependent scattering intensity distribution for stretched films. This evidences the macromolecular origin of

the deformability of the materials. This type of orientation, *c*-axis orientation, is typical for cold-drawn sample. It should also be mentioned that the position of the diffractions are in good concordance with the wide angle X-ray diffactograms shown in **Figure 4.26**, where the position of the diffraction peaks indicate that iPP in its crystalline form adopt the classical α–phase. Reinforcing the mechanical data presented above, 2D WAXS experiments have revealed a dependence of the orientation ability of the clay modified polypropylene matrix on the content of clay.

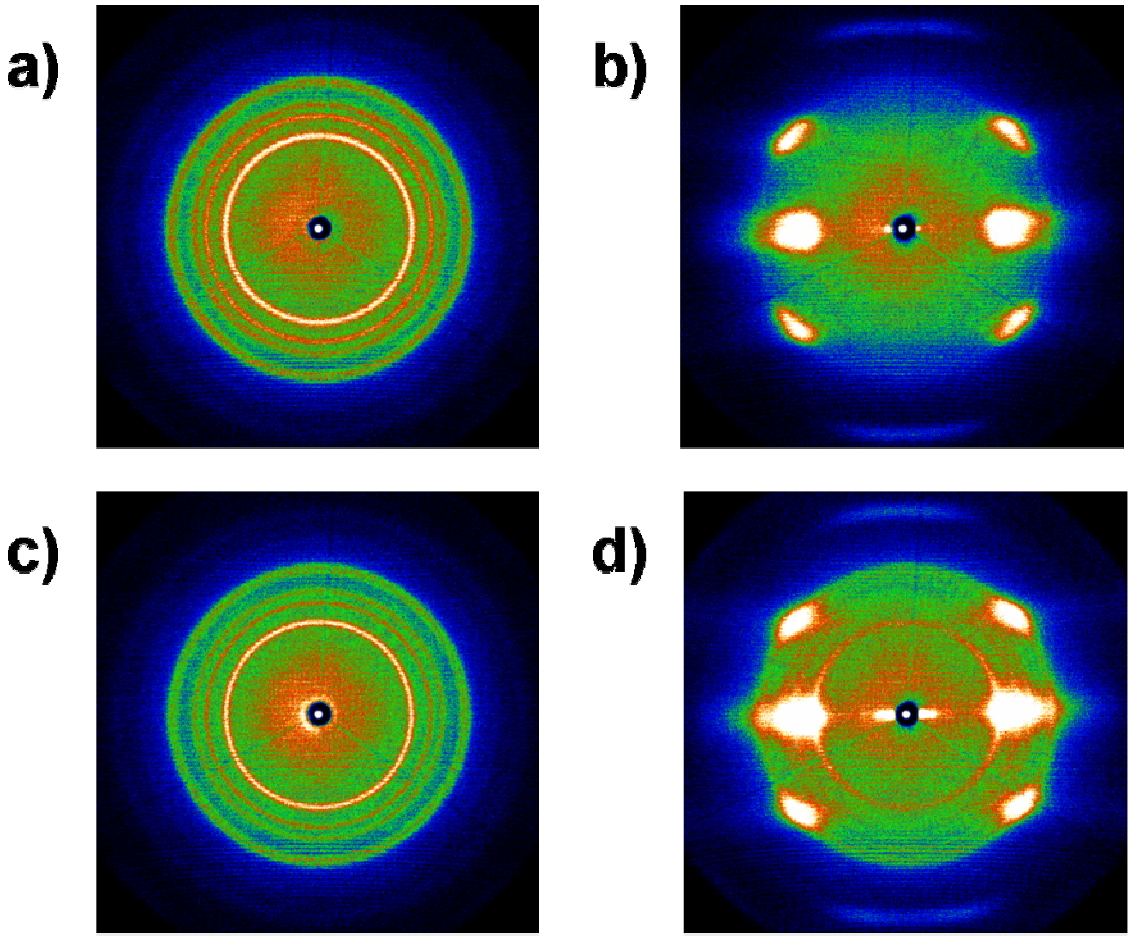

Figure 4.32 - Two-dimensional wide angle scattering patterns recorded for (top) iPP/iPPMA-2 and (bottom) iPP/iPPMA-d films (left) before and (right) after tensile test measurement performed until break. The patterns were recorded in the same configuration as indicated in **Figure 4.31**.

2D WAXS experiments performed on film samples after breaking appeared to be also a sensitive method for the examination of the orientability of clay-loaded polymeric samples. This is shown by the **Figure 4.32**, where both unstretched and stretched films of iPP/iPPMA-2 and iPP/iPPMA-5 have been investigated. Though

the variation in the scattered intensity may be mainly attributed to the difference in the thickness of the sample films, a closer inspection of the 2D patterns recorded for stretched specimens indicates that in iPP/iPPMA-5 specimen, polymer chains exhibit a lower degree of orientation as compared to iPP/iPPMA-2. This can be recognized by the specific shape of the c-axis reflections oriented along the equatorial direction. For iPP/iPPMA-5, these reflections assume arc-like shape while for iPP/iPPMA-2 spot-shaped diffractions are seen. From a clay content of 7%, a totally different behaviour can be observed where scattering recorded from both unstretched and stretched films reveal similar effects. In the patterns presented in the **Figure 4.33** scattering rings, i.e. with uniform intensity over the azimuthal angle, are seen. These findings clearly corroborate the mechanical results presented above (**Figure 4.30)**. Above a threshold content value comprised between 5 and 7 wt.-%, the presence of montmonitrille inorganic modifier bring to a high level the rigidity of the films so that the polymer chains do not orient upon external force and breaking of the sample is obtained at low stress. These data also indicate that the interaction between the polymer matrix and the layered silicate decreases from iPP/iPPMA-2 to iPP/iPPMA-7.

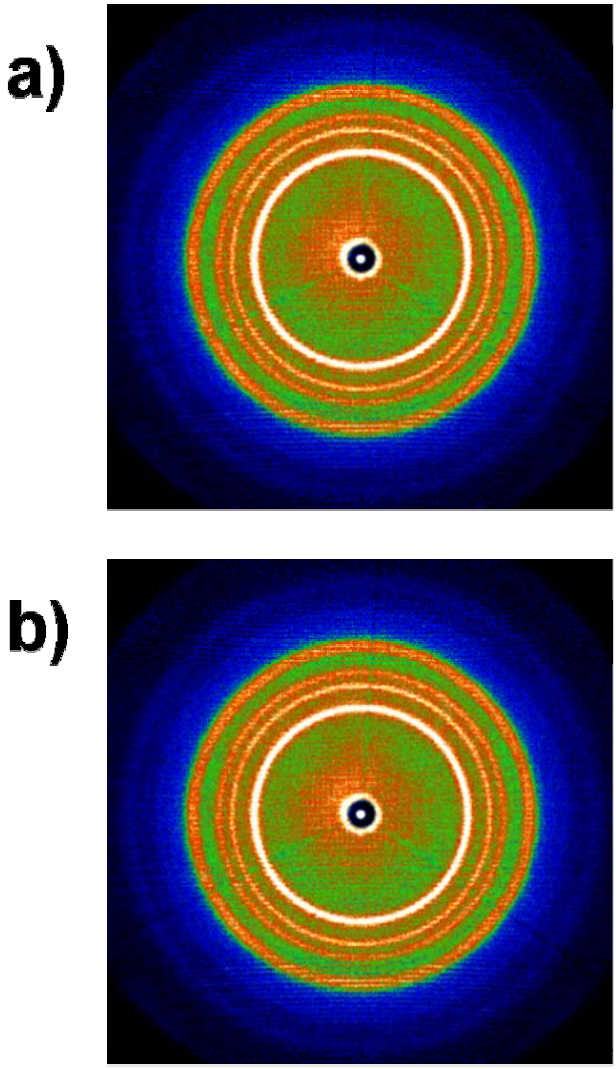

Figure 4.33 - Two-dimensional wide angle scattering patterns recorded for iPP/iPPMA-7 films a) before and b) after tensile test measurement performed until break. The patterns were recorded in the same configuration as indicated in **Figure 4.31**.

Another very interesting effect to be discussed is the scattering maximum observed in the patterns of the three clay containing nanocomposites in the very low angle region (in the close vicinity of the beam stop). Such scattering effect, with white appearance indicating high scattering intensity, is not seen in the 2D patterns presented for iPP/iPPMA (**Figure 4.31**). This feature is better illustrated in **Figure 4.34** where the equatorial intensity distributions recorded from the iPP/iPPMA, iPP/iPPMA-2 and iPP/iPPMA-5 are presented. The low angle scattering peak is more clearly seen in the 2D patterns of the nanocomposite having the higher clay content in comparison to the nanocomposite having the lower clay content. This is

also expressed in the 2D patterns. This suggests that the position of the diffraction is function of the clay content; it is sifted toward lower scattering angle when the clay loading is decreased.

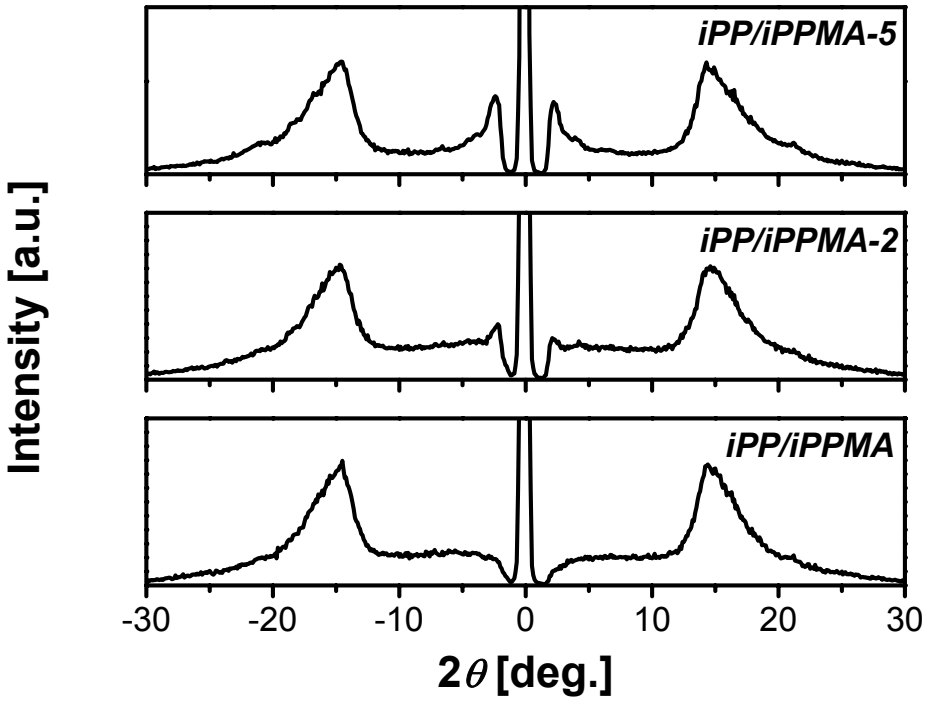

Figure 4.34 - Scattering intensity distributions recorded along a) the equatorial (horizontal) and b) meridional (vertical) directions in the WAXS 2D patterns recorded for iPP/iPPMA, iPP/iPPMA-2 and iPP/iPPMA-5 after tensile measurements.

Such behaviour was presented in the descriptive part of **Figure 4.28** where the shift of the low angle diffraction peak was attributed to the incorporation of the polypropylene chains within the layered clay structure; the incorporation being more efficient when the clay content was lower. The unambiguous assignment of the low angle diffractions observed for films specimens to the basal spacing (d_{001}) of the clay is ascertained by the **Figure 4.35** where powder wide angle X-ray diffractogram is shown together with the azimuthally averaged scattering intensity obtained from iPP/iPPMA-7. There is a perfect agreement in the position of the low angle peak along the 2θ axis. For iPP/iPPMA-2 and iPP/iPPMA-5, the equatorial position of these diffractions in the drawn samples indicates that due to a strong interaction between the iPP chains and the clay, in the course of the tensile test the iPP macromolecules orient along with the clays. Thus similarly to the iPP chains the clays

are oriented with their long axis parallel to the drawing direction. Orientation of both polypropylene chains and dispersion of clay under shearing has been reported.[209]

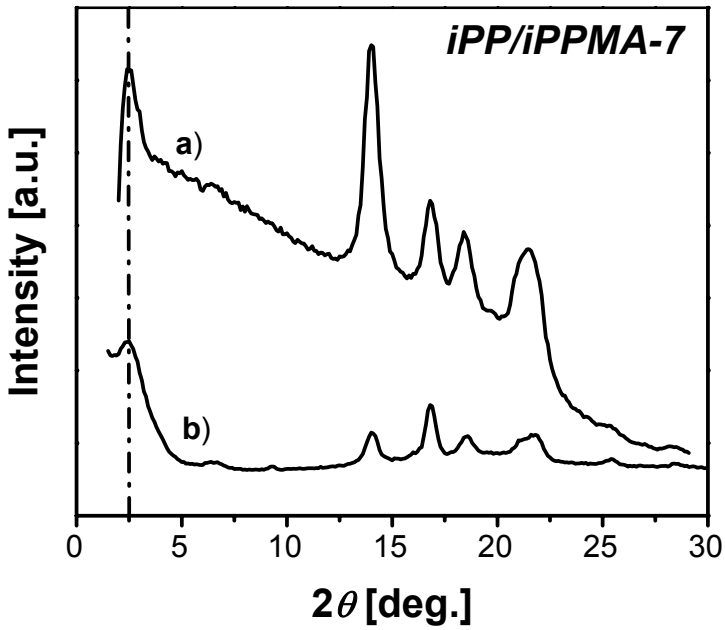

Figure 4.35 - Scattering intensity distributions versus the scattering angle recorded at room temperature for iPP/iPPMA-7; a) is the azimuthally averaged intensity distribution of the 2D WAXS pattern presented in part a of **Figure 4.33**; b) is the WAXS profile measured in reflection geometry.

6.10. Brillouin scattering

Physical properties of polymer composites including macro-micromechanical behavior are strongly influenced by the size, structure, of the nanoparticules; composition, viscosity ratio, elasticity and interfacial tension of combined components, as well as process conditions. [210,211] Brillouin scattering measurement was employed to study micromechanical characteristics through inelastic light scattering from acoustic phonons at hypersonic frequencies. Brillouin scattering experiments as previously reported is a sensitive technique for studying the degree of alignment of polymer chains. [212,213] Elastic constants of poly(methylmethacrylate) grafted onto two dimensional silicate layers were investigated in solution.[214] However, to our knowledge the change of phonon velocity within poly(propylene) nanocomposite in solid state, i.e. where chain mobility is limited in comparison to solution, has not been studied.

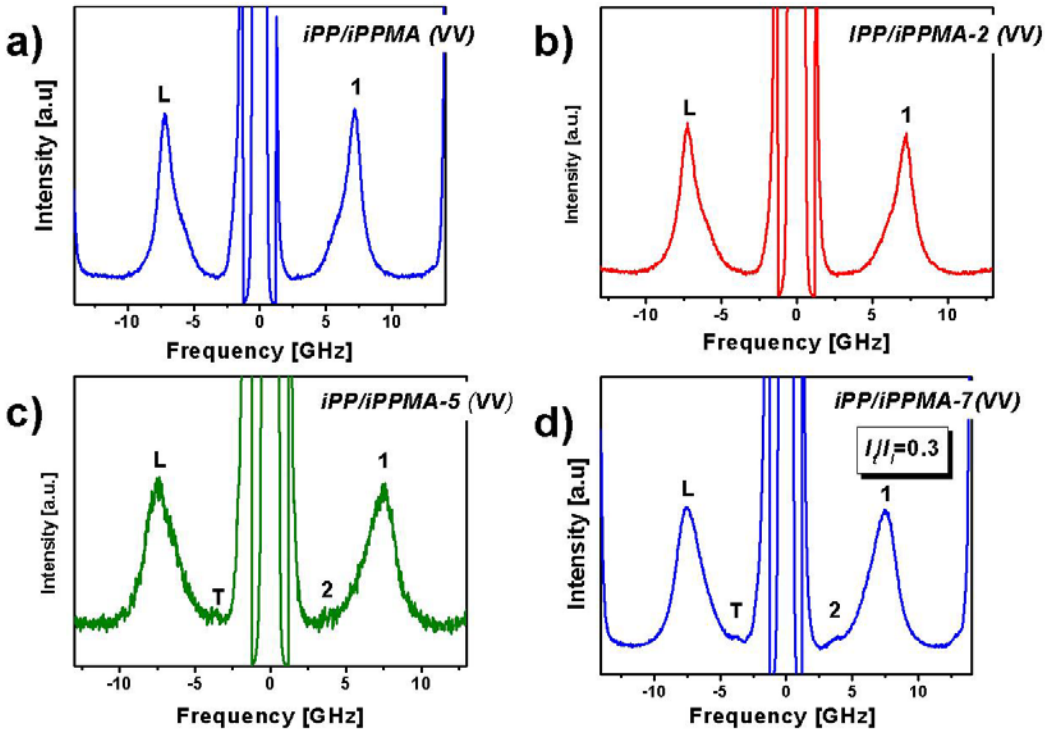

Figure 4.36 - Brillouin scattering spectra measured at q=0.016nm^{-1} for a) iPP/iPPMA, b) iPP/iPPMA-2, c) iPP/iPPMA-5 and d) iPP/iPPMA-7 with a 90° geometry and under *VV* polarization conditions. The longitudinal (L) and transverse (T) modes are referred as mode (1) and (2), respectively.

By employing several scattering angles, we measured the sound velocity as a function of frequency at room temperature. The range of scattering angles corresponds to a frequency range of approximately 3-7.5 GHz. The main phonon is of acoustic nature and it is due to the presence of longitudinal acoustic waves within the bulk polypropylene. **Figure 4.36** presents Brillouin spectra for pure iPP/iPPMA and polypropylene nanocomposites iPP/iPPMA-2, iPP/iPPMA-5 and iPP/iPPMA-7 measured at q=0.016nm^{-1}. It exhibits one strong acoustic (ω~q) longitudinal phonon at $f=\omega/2\pi$=7.2GHz for iPP/iPPMA. The corresponding peak is observed at 7.5GHz for iPP/iPPMA-7 indicating a small frequency shift towards higher frequency in the presence of rather high clay loading. The positions of the Brillouin peaks as a function of q are plotted in **Figure 4.37**. The phonon speed was calculated from the slope of the disperse curve. In general, the sound velocity of a longitudinal phonon within a given material is proportional to the square root of the longitudinal modulus and inversely proportional to the square root of the density. The speed of the phonon

is increasing proportionally to the amount of clay added to the system as it is shown in **Table 4.1**.

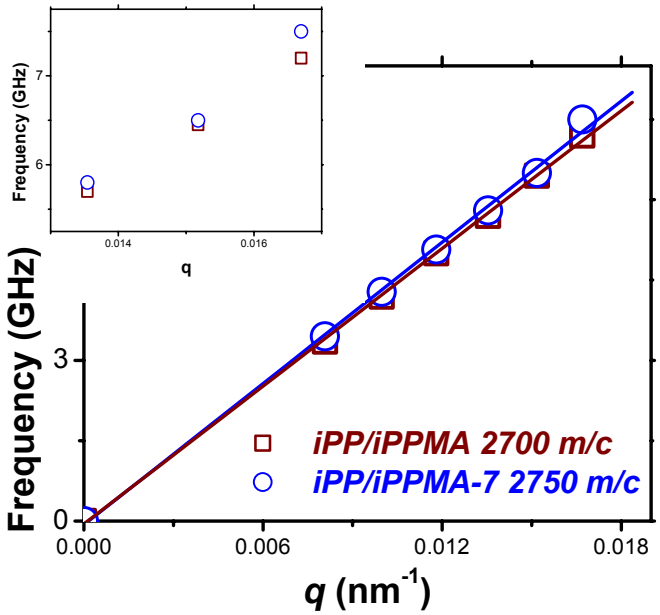

Figure 4.37 - Dispersion relationship between frequency (f=ω/2π) versus the scattering vector (q=4π$\sin\theta/\lambda$) for iPP/iPPMA and iPP/iPPMA-7 samples.

Table 4.1 - Elastic properties of nanocomposite materials

Sample	V_l (m/c)	C_{11}*	V_t	C_{44}*	I_t/I_l VV	I_t/I_l VH
iPP/iPPMA	2690	6.37	—	—	—	—
iPP/iPPMA-2	2700	6.41	—	—	—	—
iPP/iPPMA-5	2710	6.46	1500	1.98	0.3	0.32
iPP/iPPMA-7	2750	6.66	1540	2.07	0.3	0.58

* where $C_{11}=\rho v_l^2$ and $C_{44}=\rho v_t^2$

However, only little changes are noticed for the 2 and 5% clay-containing hybrid systems for which the values of the phonon speed are about 2700 m/s and 2710 m/s to be compared to the value of 2690 m/s for iPP/iPPMA. A much larger increase of the phonon speed was obtained for the composition of 7% of clay (2750 m/s). Contribution of a second peak, indicated as mode (2) in **Figure 4.36**, was observed for the iPP/iPPMA-7 and iPP/iPPMA-5 samples. However, the intensity of

the peaks was observed to be dependent on the clay loading, since iPP/iPPMA-7 gives a more intense signal.

The relative polarization of the scattered light has to be determined in order to establish the character of the scattering excitation of the second mode. With incident light polarized normal to the scattering plane (*V*) longitudinal waves will scatter fully polarized light (*VV*), while shear wave scattering will be polarized in the scattering (*VH*). The dependence of the Brillouin shifts on scattering angle was used to verify the acoustic nature of the excitation. **Figure 4.38** shows depolarized (*VH*) spectra for iPP/iPPMA and iPP/iPPMA-7. The *VH* spectra were taken under identical conditions as for the *VV* shown in **Figure 4.36**. In the case of iPP/iPPMA-7, the intensity of the transverse peak is increased at depolarized condition. In contrast, the reference iPP/iPPMA sample does not show any features of transverse phonon at *VH* scattering regime.

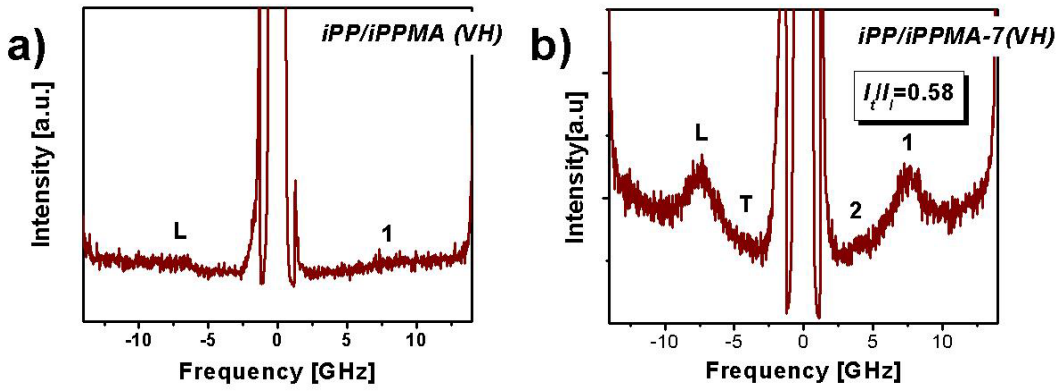

Figure 4.38 - Brillouin scattering spectra measured for a) iPP/iPPMA and b) iPP/iPPMA-7 with a 90° geometry and under *VH* polarization conditions. The longitudinal (L) and transverse (T) modes are referred as mode (1) and (2), respectively.

The Brillouin peaks were analyzed to quantify the ratio I_t/I_l and the results are presented in **Table 4.1**. The transverse peak was observed for only two compostion; iPP/iPPMA-5 and iPP/iPPMA-7. However, from a comparison of the I_t/I_l ratio for the investigated compositions we may notice that only in the case of iPP/iPPMA-7 the value of I_t/I_l at *VH* scattering geometry is increasing. This confirms the existence of shear wave phonon. Though the change in the speed phonon remains rather limited with increasing the silicate content within the polymer matrix, the frequency range of the longitudinal mode becomes broader with larger amount of nanofillers. The line-

width, i.e. the half-width at half-maximum, measures the temporal attenuation of the acoustic modes. All Brillouin peaks were fitted to a Lorentzian to extract the line-width values. The line-width values are dependent on *q* as shown in **Figure 4.39**. This can be explained in terms of elastic longitudinal modulus *M*, which has contributions from the bulk modulus and a shear modulus contribution, *G*. At these high frequencies, the sound wave propagation of a polymer depends primarily on the local intermolecular potential which is a function of the free volume. The sound wave interacts with local motions of a few segments dissipating the phonon mode energy. The polypropylene chains are linked with silicate layers to form the hybrid structure, the free volume goes down. This can lead to an increase of the local longitudinal viscosity resulting in an increase in the line-width (Γ)

$$\Gamma = 2/3k^2 \eta/\rho \qquad (4.2)$$

Where η is the longitudinal viscosity, *k* is the wave vector and Γ is the measured line-width in Hertz.

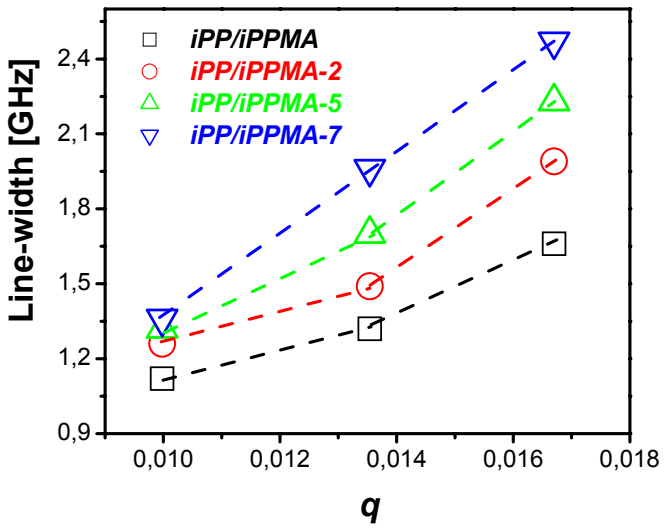

Figure 4.39 - Dependences of the line width of the longitudinal mode versus the scattering vector for iPP/iPPMA, iPP/iPPMA-2, iPP/iPPMA-5 and iPP/iPPMA-7.

The elastic constants of the unfilled polymer and nanocomposites were calculated using the longitudinal and the transverse sonic waves multiplied by the density (denoted as C_{11} and C_{44}, respectively in **Table 4.1**).

Finally, were able to establish a correlation between the mechanical data determined for poly(propylene)/montmorillonite by means of Brillouin spectroscopy and tensile testing. This is well-documented by **Figure 4.40** showing the

dependence of the elastic modulus versus the tensile modulus. It is seen that upon addition of clay, both micro- and macro-mechanical data reveal that polypropylene become stiffer. The exponential growth relationship is indicative of the change in the structure of the nanocomposites varying from exfoliated for iPP/iPPMA-2 to intercalated for iPP/iPPMA-7. Linear dependence is expected for systems in the composition range where the level of dispersion of the layered silicate remains constant. This is the case when considering the three nanocomposites iPP/iPPMA, iPP/iPPMA-2 and iPP/iPPMA-5 as indicated by the dashed line in the figure. Exfoliation was found to occur in both iPP/iPPMA-2 and iPP/iPPMA-5 with the concomitant presence of intercalation for the latter.

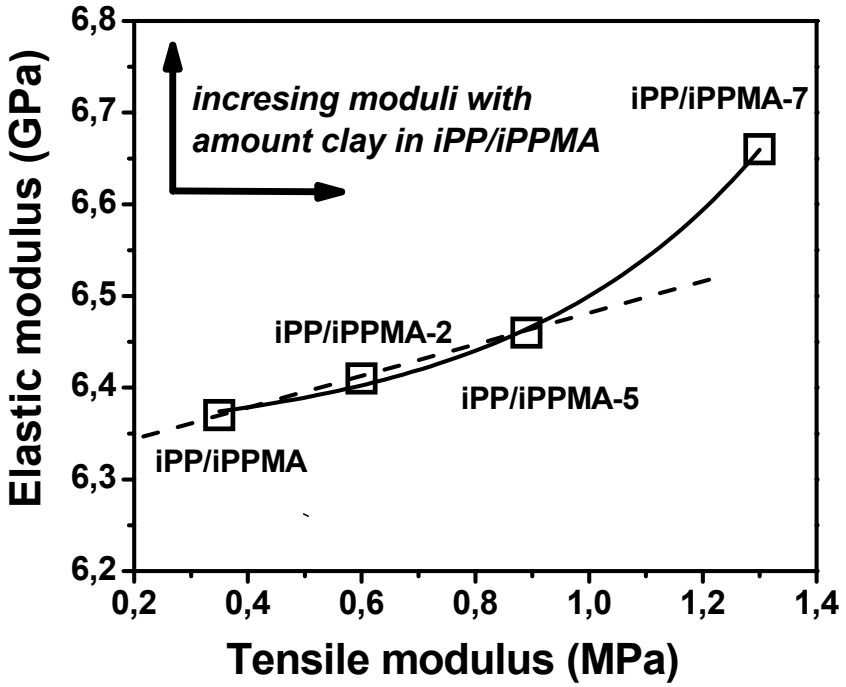

Figure 4.40 - Dependence of the elastic modulus versus the tensile modulus for the iPP/iPPMA-clay systems. The solid line indicates the exponentional growth fit

6.11. Conclusions

All experimental results indicated a strong dependence of the physical properties of iPP/iPPMA-Clay materials with respect to the clay content. Recall that the content of polypropylene-maleic-g-anhydride was kept constant implying that iPP/iPPMA-2 has the largest relative amount of iPPMA with respect to the clay. The overall solid state behaviour observed for iPP/iPPMA-clay indicates that the characteristics of the polymer layered silicate interaction fundamentally affect the i)

crystallization process (DSC, POM, DMA), ii) state of dispersion of clay (WAXS, TEM), iii) mechanical properties (tensile test) and iv) orientability of the hybrid systems (2D WAXS), v) micromechanical properties (BS).

As noted previously; i) the crystalline form (α-type) and crystalline morphology (spherulitic) in iPP/iPPMA-clay remain as observed for the iPP/iPPMA matrix but the half-crystallization time data derived from DSC experiments performed in isothermal mode indicate variation in the nucleation and growth controlled regime. In the presence of clay the crystallization is much faster with a less pronounced effect for the 2% clay-containing iPP/iPPMA in comparison to iPP/iPPMMA-5 and iPP/iPPMA-7 which behave similarly. A possible explanation for this is that the tethering of iPPMA chains at the layered silicate-polymer matrix interface provides favourable conditions for greater growth rate probably because the fraction of chains located at the interface has restricted mobility and specific orientation with respect to the silicate platelet surface (nearly parallel) enhancing the crystallite growth at interface. A differentiation in the behaviour of iPP/iPPMA-2 on one hand, and both iPP/iPPMA-5 and iPP/iPPMA-7 on the other hand, was also possible on the basis of our further experimental investigation. ii) On the basis of a qualitative and quantitative analysis of TEM and WAXS results, different structure can be assigned, exfoliated for iPP/iPPMA-2 and intercalated for iPP/iPPMA-5 and iPP/iPPMA-7 with a lower incorporation of polymer chains in the latter case. Referring to the composition of the nanocomposites, the weight ratio of iPPMA/montmorillonite is the variable that appears to govern the ultimate level of dispersion reachable. iPPMA plays the role of compatibilizer between the hydrophobized clay and the hydrophopic polypropylene. To achieve an efficient effect, it is obvious that a big enough amount of iPPMA is required to provide an effective “interfacial layer” ensuring a stable interaction between the dispersed particles and the matrix. iii) iPP/iPPMA-2 shows the best mechanical properties with improvement in tensile strength, tensile modulus in comparison to iPP/iPPMA-5 and iPP/iPPMA-7 and similar elongation at break as compared to iPP. iv) In systems with high clay content (7%) the macromolecules cannot be macroscopically oriented under uniaxial deformation and a breaking behaviour is observed. This indicates weak adhesion between the clay and the matrix. In contrast, systems with low clay content (5 and 2%) give a good response under loading where both polymer chains and dispersed clay particles orient parallel to the drawing direction. v) The sound velocity in nanocomposite materials as

investigated at GHz frequencies using Brillouin spectroscopy depends on the level of dispersion of the layered silicate within the polymer matrix. When the morphology is mainly of the exfoliated type as for iPP/iPPMA-2, no significant change is observed in the spectra as compared to the iPP/iPPMA matrix. Higher clay concentration leading to change in the morphology from exfoliation to intercalation is accompanied by an increase in the longitudinal viscosity. The increase of line-width with the amount of clay is due to a change in local motions of material and more efficient dissipation of energy within the hybrid layers as compared to unfilled polypropylene. The *VV* scattering provides a direct description of the morphology of the polymer-silicate hybrid layered structure and rationalizes the results from the anisotropic *VH* scattering as well. The modulus of the layered silicate dispersed within bulk poly(propylene) is of the order of 6 GPa as determined by Brillouin scattering.

From our point of view, the characterization results summarized above indicate that iPP/iPPMA-2 behave as a one-phase system explaining its greater mechanical properties. More generally speaking, macroscopic and microscopic properties of our systems are determined by the structural hierarchy of the morphological elements extending over various size scales, from microscopic level for the spherulites to nanoscopic level for the single clay platelets. In this study we have clearly demonstrated the crucial importance of the control of structure on the nanometer size scale that is in the case polymer filled with silicate layers, the achievement of single clay platelet dispersion. Moreover a clear correlation has been established between micro- and macro-mechanical properties determined by means of Brillouin scattering and tensile measurements, respectively.

For further Improvement in physical properties a particular should be paid to the processing conditions including variation of the hybrid materials composition in terms notably of content in iPPMA as compatibilizer.

Chapter 5 - Experimental Section.

5.1 Materials

5.1.1 Blending

The commercially available low density polyethylene (LDPE, Kaplen MPZ Moscow, brand 158-03 020) with a weight average molecular mass M_w=200.000g/mol and isotactic polypropylene (iPP, Moscow MPZ, brand Kaplen 01025, MFI 2,5g $[10min]^{-1}$) with a weight average molecular mass M_w=400.000g/mol, were used in this study. Three ethylene-propylene random copolymers (EPR) with different monomer compositions were used as compatibilizater of the LDPE/iPP blend: Keltan-740 and Keltan-13 were provided by DSM and Dutral-054 was obtained from Du Pont. Blends were prepared by mixing the appropriate amounts of binary (LDPE/iPP) or ternary (LDPE/iPP/EPR) mixtures of the pelletized samples through melt blending in a Brabender mill for 10 min, at a temperature of 190°C . All the blends were made with a LDPE/iPP weight ratio (wt.-%) of 80/20 and the compatibilizater content was adjusted to 5, 10 and 15 wt.-% with respect to the total weight of the blend. The resulting blends were compression molded at a temperature of 190°C to produce films of nearly similar thickness.

5.1.2 Brillouin spectroscopy

The semicrystalline polymers used in this study were low density polyethylene and isotactic polypropylene with M_w=200.000g/mol and M_w=400.000g/mol, respectively. The polymer pellets were melted for 10 min at 200°C in a press consisting of two heated plates .The films were then either quenched in water at room temperature or slowly cooled in the press at 8K/min.

5.1.3 Nano-clay composites

The matrix used was isotactic polypropylene (iPP) with Mw=250.000 g/mol and was provided by Basel. Isotactic polypropylene-*graft*-maleic anhydride (iPPMA) was chosen as compatibilizater with 1% grafting content and Mw=330.000g/mol (Crompton Co). Commercially available montmorillonite was used as clay reinforcements (intercalant: quaternary ammonium salt) as received from Southern clay products.

Blends of iPP and iPPMA without clay and with 2, 5 and 7 % were compounded in twinscrew extruder (*L/D*=34mm) at a temperature of 200°C. For characterization

pellets of nanocomposites and polymer blend samples were molded by compression in press at 200°C. The thickness of the samples was 50-100μm.

5.2 Characterization

5.2.1 Infra-red spectroscopy

The microstructure of chains was studied by recording the InfraRed spectra at room temperature using a Specord M-80 spectrometer. Polymer films of ~40μm thickness were prepared by solvent-casting from 10 wt.-% polymer solutions in tetrachloromethylene solutions; liquid samples were slowly dried within 12 hours at room temperature. The optical densities of the bands characteristic for the both ethylene (815, 752, 735 and 722 cm^{-1}) and propylene (936, 973 and 1155 cm^{-1}) components were measured and normalized with respect to the band located at 1470 cm^{-1} to preclude any effects from films thickness.

5.2.2 Differential scanning calorimetry (DSC)

DSC measurements were performed on a Mettler DSC 30 apparatus with a cell purged with nitrogen at a temperature variation rate of 10°C.min^{-1} for both heating and cooling runs. The instrument was calibrated using indium as a standard. About 8mg from each sample were placed in sealed aluminium cells and were initially heated up to a temperature of 200°C to erase all previous thermal history. The subsequent cooling and heating cycles were considered as reflecting the properties of the compact bulk material and the reported transition temperatures and melting enthalpies were taken from the second heating runs.

5.2.3 Polarized optical microscopy (POM)

Polarized optical microscopy (POM) observations were performed using a Zeiss microscope (D-7082) equipped with a temperature controlled stage (Linkam TMS91/THM600) and a color digital camera (Hitachi KPD50). The samples were placed between a glass slide and a glass cover for observation and similar temperature variation rate as for the DSC measurements (10°C.min^{-1}) was applied to produce the crystalline morphologies from the polymer melt.

5.2.4 Small-angle light scattering (SALS)

SALS measurements were conducted with a He-Ne laser (λ=633nm) beam and a CCD camera (Hamamatsu C-4880) recording the 2D scattering patterns under cross (H_V) polarization conditions for polymer samples as obtained after POM observations. In order to determine the spherulite sizes the scattered intensity distributions vs. scattering angle were analyzed at 45° with respect to polarization directions for at least 4 independent polymer films having a thickness of few microns.

5.2.5 Large deformation tensile tests

Measurements of the mechanical properties of the blends were performed using a mechanical testing machine INSTRON (Model 6022). The sample specimens having a thickness of about 80 μm were cut with a dumbbell shape in which the gauge length was 25 mm. The stress-strain curves were measured at a constant cross-head speed of 10 mm.min^{-1}. Young modulus (E) and the coordinates of the yield point as well as of the elongation at break have been determined as averages of at least 7 independents drawing experiments performed in the same conditions. Only the room temperature behaviour is reported.

5.2.6 Dynamic mechanical analysis (DMA)

The variations of storage moduli (G'), loss moduli (G'') and loss factor ($\tan\delta = G''/G'$) as a function of temperature were assessed by dynamical mechanical thermal analysis using Rheometrics RMS 800 mechanical spectrometer. Plate-plate geometry was used with plate diameters of 6 mm. The gap between the plates (sample thickness) was about 1 mm. The measurements were performed at a

constant deformation frequency of 10 rad/s^{-1} and with a 2.0°C /min heating rate in a broad temperature range between -100 and 250°C).

A Rheometric Scientific Instrument (ARES) was used for rheological measurements. A stress sweep was performed to define the region of linear viscoelasticity. All measurements were conducted under a dry nitrogen atmosphere to preclude oxidative degradation of the samples.

5.2.7 Scanning electron microscopy (SEM)

SEM images were obtained using a LEO EM 1530 Gemini scanning electron microscope. In order to observe the bulk features of the blends, compression moulded films having a thickness of about 400 μm were fracture in liquid nitrogen and the fractured surfaces were examined.

5.2.8 Transmission electron microscopy (TEM)

TEM characterization of the nanocomposites was done on cryo-ultramicrotomed sections using a electron microscope Philips CM12 operated at 300 kV.

5.2.9 X-ray diffraction

Small angle (SAXS) and wide angle (WAXS) X-ray scattering techniques have been used to characterize the structure of bulk polymers. WAXS measurements have been performed using a Siemens θ-θ difractometer (D500T) as well as a 2D position sensitive detector with a pin-hole collimation of the incident beam. *Cu Kα* radiation (λ=0.154nm) was used. In the SAXS experiment, a 18kW rotating anode X-ray source (Rigaku, RA.Micro7) with a pin-hole collimation and a 2D position sensitive detector were used to obtain the scattering intensity profile for angles between 0.1°-1.1° in steps of 0.02° with a 1.8m sample to detector distance .The duration of a SAXS measurement was about 1h.

5.2.10 Brillouin spectroscopy

Inelastic light scattering spectra I(ω) were recorded as a function of both the scattering wave vector q (=(4πn/λ)sin(θ/2) with n being the refractive index, θ the scattering angle and λ=532nm the laser wavelength) and $q_{||}$ at a fixed θ=150° by a six-pass Fabry-Perot interferometer using the set-up described elsewhere[17].The variation of the component of q parallel to the film surface (q||) proceeds through the

rotation of film about the optical axis of the goniometry i.e. changing the angle of incidence θ_r. The polarization of the incident laser beam was perpendicular to the plane of incidence whereas the polarization of the scattered light was chosen by means of a high extension Glan-Tompson analyzer.

Chapter 6 - Summary

Blending a polymer with other components of macromolecular nature or not, provides a versatile and effective method for the preparation of new materials, namely composites, with advanced properties. In general, the goal of blending polymers is to develop materials with characteristics of both components through improvement of the properties of the substance chosen as matrix. Unfortunately, this is not often the case because of the immiscible character of the primary products making the composite. For example, when two polymers phase separate, the size of the dispersed domains is coarse, irregular, and unstable, moreover the interface is sharp and weak. The poor stress transfer across interface may induce preferential fracture path. Thus, the process of modification of interfacial properties of a multiphase system leading to the creation of a new blend, which is called compatibilization plays an important role in the development of new materials. Additive with specific chemical composition can be used as compatibilizer to control the level of dispersion of the minor component within the major one. Initial studies on polymer composites were based on blending two polymers where the dispersion occurs at the micrometer level. More recently, academic and industrial interests have focused on incorporation of organoclays in polymer matrices. In most favourable cases, nanometer dispersion of single clay layer is obtained. In nearly all cases, achievement of ultimate properties requires a compatibilization step. However it is obvious that the resulting ternary systems may be very complex especially when dealing ordered materials since in the case of semicrystalline materials, complexity starts with simple homopolymers that can be regarded as two-phase systems where crystalline and amorphous layers are stacked alternately. Thorough investigation of such systems may become very difficult and requires the application of a broad range of experimental techniques giving information about the various elements of the hierarchical structure.

On the basis of the various aspects discussed above, establishment of correlation between the morphological structure and properties of the studied systems is the leading theme through this thesis.

In Chapter 2 the beneficial influence of adding ethylene-co-propylene polymer of amorphous nature, to low density poly(ethylene)/isotactic poly(propylene) (80/20)

blend is demonstrated. This effect is expressed by the major improvement of mechanical properties of ternary blends as examined at a macroscopic size scale by means of tensile measurements. The structure investigation also reveals a clear dependence of the morphology on adding ethylene-co-propylene polymer. Both the nature and the content of ethylene-co-propylene polymer affect structure and properties. It is further demonstrated that the extent of improvement in mechanical properties is to be related to the molecular details the compatibilizer. Combination of high molecular weight and high ethylene content is appropriate for the studied system where the poly(ethylene) plays the role of matrix.

In Chapter 4 structure and properties of isotactic poly(propylene) matrix modified by inorganic layered silicate, montmorillonite, are discussed with respect to the clay content. Isotactic poly(propylene)-*graft*-maleic anhydride was used as compatibilizer. It is clearly demonstrated that the property enhancement is largely due to the ability of layered silicate to exfoliate. The intimate dispersion of the nanometer-thick silicate result from a delicate balance of the content ratio between the isotactic poly(propylene)-*graft*-maleic anhydride compatibilizer and the inorganic clay. With the assumption that poly(propylene)-*graft*-maleic anhydride acts at the interface between the montmorillonite clay and the polypropylene matrix, it is obvious that an optimum amount of polymer compatibilizer is required to provide an efficient covering effect. In our case, the nanocomposite composition consisting of 2% of montmorillonite is favourable to the exfoliation morphology. It results a large improvement in mechanical properties.

In Chapter 3 we present a new way to characterize semicrystalline systems by means of Brillouin spectroscopy. By this method based on inelastic light scattering, we were able to measure the high frequency elastic constant (c_{11}) of the two microphases in the case where the spherulites exhibit size larger than the size of the probing phonon wavelength. In this considered case, the sample film is inhomogeneous over the relevant length scales and there is an access to the transverse phonon in the crystalline phase yielding the elastic constant c_{44} as well. Isotactic poly(propylene) is well suited for this type of investigation since its morphology can be tailored through different thermal treatment from the melt. Two distinctly different types of films were used; quenched (low crystallinity) and annealed

(high crystallinity). The Brillouin scattering data are discussed with respect to the spherulites size, lamellae thickness, long period and crystallinity degree and are well documented by AFM images.

References

[1] Sinha Ray, S., Okamoto, M. *Prog. Polym. Sci.* **2003**, 28, 1539.

[2] Fukushima, Y. Okada, A. Kawasumi, M., Kurauchi, T., Kamigaito, O. *Clay. Miner*. **1988**, 23, 27.

[3] Bucknall, C. B., Gilbert, C. H. *Polymer* **1989**, 30, 213.

[4] Mackinnon, A. J., Jenkins, S. D., McGrail, P. T., Pethrick, R. A., *Macromolecules* **1992**, 25, 3492.

[5] a) Buchert, M., Jenseit, W., Wollny, V. *Kunstoffe* **1993**, 83, 451. b) Bertin, S., Robin, J-J. *Eur. Polym. J.* **2002**, 38, 2255.

[6] a) Barlow, J. W., Paul, D. R. Polym. Eng. Sci. 1989, 24, 525. b)Fortelny, I., Navratilova, E., Kovar, J. *Angew. Macromol. Chem*. **1991**, 188, 195.

[7] a) Kawasumi, M., Hasegawa, N., Kato, M., Usuki, A., Okada, A. *Macromolecules* **1997**, 30, 6333. b) Kato, M., Usuki, A., Okada, A. *J. Appl. Polym. Sci*. **1997**, 66, 1781. c) Hasegawa, N., Kawasumi, M., Kato, M., Usiki, A., Okada, A. *J. Appl. Polym. Sci.* **1998**, 67, 87.

[8] Reichert, P. Nitz, H., Klinke, S., Brandsch, R., Thomann, R., Mulhaupt., R. *Macromol. Mater. Eng*. **2000**, 275, 8.

[9] Priadilova, O., Cheng, W., Tommaseo, G., Steffen, W., Gutmann, J. S.; Fytas, G. *Macromolecules* **2005**; 38, 2321.

[10] Flory PJ. *Principles of polymer chemistry*. Ithaca, NY: Cornell University Press; **1953**.

[11] Hildebrand, J. H., Scott, R. L. *The solubility of non electrolytes*. Reinhold, New York ed. 3, **1950**.

[12] Lipatov, Yu. S., Shumsky, V. F., Gorbatenko, A. N. Panov, Yu. N., Bolotnikova, L. S. *J. Appl. Polym. Sci.* **1981**, 26, 499.

[13] Hunter, R.J., Foundation of Colloid Science, Volumes I et II, Oxford Science Publishers, Oxford, **1989**.

[14] Paul, D. R. Interfacial agents (“compatibilizers”) for polymer blends, Chap 12 in Paul, D. R., Newman, S. (eds.) Polymer Blends, Vol 2, Academic Press, New-York **1978**.

[15] Favis, B.D. Factors affecting the morphology of immiscible blends in melt processing, Chapter 16 in Paul, D.R., Bucknall, C.B. (eds.), *Polymer Blends: Formulation and Performance*, John Wiley, New York, **2000**.

[16] Brown, H.R. Strengthening polymer-polymer interfaces, Chapter 23 in Paul, D. R., Bucknall, C. B. (eds.), *Polymer Blends: Formulation and Performance*, John Wiley, New York, **2000**.

[17] a) Ide, F, Hasegawa, A. *J. Appl. Polym. Sci*. **1974**, 18, 963. b) Xanthos, M. *Polym. Eng. Sci.,* **1988**, 28, 1392. c) Dharmarajan, N, Datta, S., G. Ver Strate and L. Ban, *Polymer*, **1995**, 36, 3849. d) Tricca, V. J., Ziaee, S. Barlow, J. W., Keskkula H., Paul, D. R. *Polymer*, **1991**, 32, 1401.

[18] Lu, M., Keskkula, H. Paul, D.R. *Polym. Eng. Sci*. **1994**, 34, 33.

[19] a) Keskkula, H. Paul, D.R. Toughening agents for engineering polymers, Chapter 5 in Collyer, A. A. (ed.), *Rubber Toughened Engineering Plastics*, Chapman and Hall, London, **1994**. b) Mzrechal, P., Coppens, G., Legras, R., Dekoninck, J.M. *J. Polym. Chem. Part A Polym. Chem*. **1995**, 33, 757.

[20] Oshinski, A.J., Keskkula, H., Paul, D.R. *J. Appl.Polym. Sci.,* **1996***,* 61, 623.

[21] Gan, P.P. and Paul, D.R. *Polymer* **1994**, 35, 3513.

[22] a) Turska, E., Utracki, L. J. Appl. Polym. Sci. **1959**, 4, 46. b) Turska, E., Utracki, L. J. Appl. Polym. Sci. **1962**, 22, 393. c) Turska, E., Utracki, L. J. Appl. Polym. Sci. **1962**, 22, 399.

[23] McMaster, L. P. Macromolecules, **1973**, 6, 760.

[24] a) Snyder, H. L., Meakin, P., Reich, S. Macromolecules, **1983**, 16, 757. b) Snyder, H. L., Meakin, P., Reich, S. J. Chem. Phys., **1983**, 78, 3334. c) Snyder, H. L., Meakin, P. J. Chem. Phys., **1983**, 79, 5588.

[25] a) Russel, T. P., Stein, R. S., J. Polym. Sci., Polym. Phys., **1982**, 20, 1593. b) Russel, T. P., Stein, R. S., J. Polym. Sci., Polym. Phys., **1983**, 21, 999. c) Schwahn, D., Mortensen, K., Yee-Madeira, H. Phys. Rev. Lett. **1987**, 58, 1544.

[26] a) Nishi, T., Wang, T. T. Macromolecules, **1975**, 8, 909. b) Wang, T. T., Nishi, T. Macromolecules, **1977**, 10, 421.

[27] a) Penning, J. P., Manley, R. St. J. *Macromolecules* **1996,** *29,* 77. b) Kuo, S. W., Chang, F. C., *Macromolecules* **2001,** *34,* 4089. c) Lake, W.B., Kalakkunnath, S., Kalika, D. S. J. Appl. Polym. Sci. **2004**, 94, 1245.

[28] a) Maier, R-D., Kressler, J., Rudolf, B., Reichert, P., Koopmann, F., Frey, H., Mülhaupt, R., Macromolecules **1996,** *29,* 1490. b) Privalko, V.P., Lipatov, Yu. S., Besklubenko, Yu. D. Yarema, G. Ye. Vysokomol. Soyed. **1985**, A27, 1021.

[29] Fox, T. G. *Bull. Am. Phys. Soc.* **1956**, 1**,** 123.

[30] Shibata, M., Fang, Z., Yosomiya, R. J. Appl. Polym. Sci. **2001**, 80, 769.

[31] Shultz, A. R., Young, A. L. Macromolecules, **1980**, 13, 663.

[32] a) Ting, S.-P., Pearce, E. M., Kwei, T. K. J. Polym. Sci., Polym. Lett. Ed. **1980**, 18, 201. b) Moskala, E. J. Varnell, D. F., Coleman, M. M. Polymer, **1985**, 2, 228. c) Coleman, M. M., Skrovanek, D. J., Hu, J. Painter, P. C. Macromolecules, **1988**, 21, 59.

[33] Douglass, D. C., McBrierty, V. J. Macromolecules, **1978**, 11, 766.

[34] a) Kargin, V. *Vysokomol. Soedin*. **1971**, A13, 231. b) Lebedev, E., Lipatov, Y., Privalko, V. *Vysokomol. Soedin*. 1975, A17, 148. c) Sogolova, T., Akutin, M. S., Zankin, D. J. *Vysokomol. Soedin*. **1975**, A17, 2505.

[35] a) Karger-Kocsis, J., Kalló, A., Kuleznev, V. N. *Polymer* **1984**, 25, 279. b) Copolla, F. Greco, R., Martuscelli, E., Krammer, H. W. *Polymer* **1987**, 28, 47. c) Tam, W., Cheung, T., Li, R., K. Y. *Polym. Test*. **1996**, 15, 452. d) Van der Wal, A. Mulder, J. J. Oderkerk, J., Gaymans, R. J. *Polymer*, **1998**, 39, 6781. e) Yokoma, Y., Ricco, T. *J. Appl. Polym. Sci*. **1997**, 6, 1007.

[36] a) Hayashi, T., Inoue, Y., Chujo, R. *Macromolecules* **1988**, 21, 3139. b) Feng, Y., Hay, J. N. *Polymer* **1998**, 39, 6589. c) Saga, K., Shiono, T., Doi, Y. *Macromolecules Chemistry* **1988**, 189, 1531.

[37] Wang, D., Gao, J. G., Li, S. R., Wang, H. *China Plastics* **2003**, 17, 19.

[38] a) Karger-Kocsis, J., Kalló, A., Szafner, A., Boder, G., Sényer, Z. *Polymer* **1979**, 30, 37. b) Martuscelli, E., Silvestre, C., Abate, G. *Polymer* **1982**, 23, 229. c) Karger-Kocsis, J., Kiss, L., Kuleznev, V. N. *Polym. Commun*. **1984**, 25, 122. d) Barkczak, Z., Galeski, A., Martuscelli, E. *Polym. Eng. Sci*. **1984**, 24, 1155.

[39] Greco, R., Mancarella, C., Martuscelli, E., RagostaYin Jinghua, G. *polymer* **1987**, 28, 1922.

[40] Greco, R., Mancarella, C., Martuscelli, E., RagostaYin Jinghua, G. *polymer* **1987**, 28, 1929.

[41] a) Song, H.H., Stein, R. S., Wu, D-Q., Ree, M., Philips, J. C., Legrand, A., Chu, B., *Macromolecules* **1988**, 21, 1180. b) Tashiro, K., Stein, R.S., Hsu, S. L. *Macromolecules* **1992**, 25, 1801. c) Tashiro, K., Izuchi, M., Kobayashi, M., Stein, R. S. *Macromolecules* **1994**, 27, 1221. d) Tashiro, K., Izuchi, M., Kobayashi, M., Stein, R. S. *Macromolecules* **1994**, 27, 1228. e) Tashiro, K., Izuchi, M., Kobayashi, M., Stein, R. S. *Macromolecules* **1994**, 27, 1234. f) Tashiro, K., Izuchi, M., Kaneuchi, F., Jin, C., Kobayashi, M., Stein, R. S. *Macromolecules* **1994**, 27, 1240. g) Tashiro, K., Imanishi, K., Izumi, Y., Kobayashi, M., Kobayashi, K., Satoh, M., Stein, R. S.

Macromolecules **1995**, 28, 8477. h) Wignall, G. D., Londono, J. D., Lin, J. S., Alamo, R. G., Galante, M. J., Mandelkern L. *Macromolecules* **1995**, 28, 3156.

[42] a) Blackadder, D. A., Richardson, M. J., Savill, N. G., *Macromol. Chem.* **1981**, 182, 271. b) Noel, III. O. F., Carley, J. F. *Polym. Eng. Sci.* **1984**, 24, 488. c) Wignall, G. D., Child, H. R. Samuels, R. J. *Polymer* **1982**, 23, 957. d) Lohse, D. J. *Polym. Eng. Sci.* **1986**, 26, 1500. e) Montes, P., Rafiq, Y. A., Hill, M. J. *Polymer* **1998**, 39, 6669.

[43] Blom, H. P. Teh, J. W., Bremmer, T., Rudin, A. *Polymer* **1998**, 39, 4011.

[44] Li, J., Shanks, R. A., Long, L. *J. Appl. Polym. Sci*. **2000**, 76, 1151.

[45] Nolley, E., Barlow, J. W. Paul, D. R. *Polym. Eng. Sci*. **1980**, 20, 364.

[46] a) Stein, R.S., Khambatta, F.B., Warner, F.P., Russell, T., Escala, A., Balizer, E. *J. Polym. Sci., Polym. Symp.* **1978**, 63, 313. b) Avramova, N. *Polymer* **1995**, 36, 801.

[47] Liu, A.S., Liau, W.B., Chiu, W.Y. *Macromolecules* **1998**, 31, 6593.

[48] a) Penning, J.P., Manley, R. StJ. *Macromolecules* **1996**, 29, 77. b) Penning, J.P., Manley, R. StJ. *Macromolecules* **1996**, 29, 84. c) Fujita, K., Kyu, T., Manley, R. StJ. *Macromolecules* **1996**, 29, 91. e) Liu, L-Z., Chu, B., Penning, J.P., Manley, R. StJ. *Macromolecules* **1997**, 30, 4398.

[49] a) Avella, M., Martuscelli, E. *Polymer* **1988**, 29, 1731. b) Avella, M., Martuscelli, E., Greco, P. *Polymer* **1991**, 32, 1647. c) Avella, M., Martuscelli, E., Raimo, M. *Polymer* **1993**, 34, 3234.

[50] Shin, Y-W., Uozumi, T., Terano, M., Nitta, K. *Polymer*, **2001**, 42, 9611.

[51] a) Fan, W., Waymouth, R. M. *Macromolecules*, **2001**, 34, 8619. b) Pietikäinen, P., Seppälä, J. V. *Macromolecules*, **1994**, 27, 1325. c) Ver Strate, G., Cozewith, C., Ju, S. *Macromolecules*, **1988**, 21, 3360.

[52] a) Kissin, Yu.V., Tcvetkova, B.I., Chirkov. N.M. *Reports of Academy of Science, USSR*, **1963,** 152, 1162. [b)] Yu.V. Kissin. *Rubber materials .USSR*. **1965,** 12, 87. [c)] Dechant, I., Danz, R., Kimmer, W., Schmolke. R., *Ultrarotspektroskopische untersuchungen an polymeren*, Berlin: Academie, **1972.**

[53] a) Drushel, H. V., Iddings, F.A. *Anal. Chem.* **1963**, 35, 29. [b)]. Veerkamp, Th. A , Veermans, A., *Makromol. Chemie,* **1961**, 50, 147.

[54] Wei, P. E. *Anal. Chem.* **1961**, 33, 215.

[55] Corish, P. J., Small, R. M. B. *Anal. Chem.* **1961**, *33*, 1799.

[56] Yamaauchi J, Kemoto K.J., Yamaoka A, Peroxy radicals produced in polypropylene through oxidation with ozone. *Macromol. Chem*., **1977**; 178 (8):2483-5

[57] Kulik E.A., Cahalan L, Verhoeven M., Cahalan P. Ozone activation of polyolefins for subsequent surface modification. Surf. Modif. Techn. X Proc. Int. Conf. 10th, 1997. p.451-63

[58] Shinn-Gwo Hong, Chien-Mao Liao, *Polymer Degradation and Stability* **1995**, 49, 437.

[59] a) Flory, P. J. *J. Chem. Phys.* **1947**, 13, 684. b) Flory, P. J. *J. Chem. Phys*. **1949**, 17, 223.

[60] Strobl, G. *The Physics of Polymers: Concept for Understanding Their Structure and Behaviour, 2nd Edition*; Springer-Verlag Berlin Heidelberg, Germany **1997**.

[61] a) Schultz, J. M. *Polym. Eng. Sci.* **1984**, 24, 770. b) Mucha, M., Kryszewski, M. *Colloid Polym. Sci.* **1980**, 258, 743. c) Galeski, A., Koenczoel, L., Piorkowska, E., Baer, E. *Nature* **1987**, 325, 40.

[62] a) Howard, P. R., Crist, B., *J. Polym. Sci. Part B: Polym. Phys.* **1989**, 27, 2269. b) Weimann, P. A., Hajduk, D. A., Chu, C., Chaffin, K. A., Brodil, J. C., Bates, F. S., *J. Polym. Sci. Part B: Polym. Phys.* **1999**, 37, 2053.

[63] Flory, P. J. *Trans. Faraday Soc.* **1955**, 51, 848.

[64] Wunderlich, B. *J. Chem. Phys*. **1958**, 29, 1395.

[65] a) Turner-Jones, A., Aizlewood, J. M., Beckett, D. R., *Makromol. Chem.* **1964**, 75, 134. b) Moore, E. P. *Polypropylene Handbook*, Cincinnati: Hanser; **1996**.

[66] Marigo, A., Marega, C., Causin, V., Ferrari, P. *J. Appl. Polym. Sci.* **2004**, 91, 1008.

[67] Nielsen, L.E. *Mechanical properties of polymers,* Van Nostrand reinhold, New York,**1962**

[68] Brillouin, L. *Ann. Phys.(Paris)* **1922**, 17, 88.

[69] Mandelstam, L. I., *Zh. Russ. Fiz-Khim. Ova*. **1926**, 58, 381

[70] Gross, E.F. *Nature* **1930**, 126, 201.

[71] J.R. Sandercock *Optics Commun*. **1970**. 2, 73

[72] Dil, J.G. *Rep. Prog. Phys.,* **1982**, 45.

[73] Srivastava, G. P. *The Physics of Phonons*, Adam Hilger, Bristol, **1990.**

[74] Jakson , D. A., Pentecost, H. T. A., Powles, J.G. *Mol. Phys*. **1972**, 23,425.

[75] Lin, Y. H., Wang, C. H. *J. Chem. Phys.* **1979**, 70, 681.

[76] Krüger, J. K., Pietralla, M. *Colloid. Polymer Sci.,* **1983**, 261,409.

[77] Krüger, J. K., Peetz, L., Wildner, W., Pietralla, M. *Polymer* **1980**, 21, 620.

[78] Patterson, G.D., Latham, J.P. *J. Polym. Sci., Macromol. Rev.,* **1980**, 15, 1.

[79] Tanaka, T.; Morigami, M.; Atoda, N. *Jpn. J Appl. Phys.* **1993**, 32, 6059.

[80] Urbas, A., Thomas, E. L., Kriegs, H., Fytas, G., Penciu, R. S., Economou, E. N. *Phys.Rev.Lett*. **2003**, 90, 108302.

[81] Tommaseo, G., Penciu, R. S., Fytas, G., Economou, E. N., Hashimoto, T. *Macromolecules*. *2004*, 37, 5006.

[82] Bortolani, V., Nizzoli, F., Santoro, G., Malvin, A., Sandercock, J. R. *Phys. Rev. Lett.* **1979**, 43, 224.

[83] a) Grimsditch, M., Bhadra, R., Schuller, I.K. *Phys. Rev.Lett.* **1987**, 58, 1216. b) Hillebrands,B., Lee, S., Stegeman, G. I., Cheng, H., Potts, J. E., Nizzolli, F. *Phys. Rev. Lett.* **1988**, 60, 832.

[84] Nizzolli, F.; Hillebrands, B.; Lee, S.; Stegemann, G. I.; Duda, G.; Wegner, G.; Knoll, W. **Phys.Rev. 1989**, 40, 3323.

[85] a) Sun, L.; Dutcher, J. R.; Giovannini, L.; Nizzoli, F.; Stevens, J. R.; Ord, J. L. *Appl.Phys.* **1994**, 75, 7482. b) Forrest, J.A.; Rowat, A.C.;DAlnocki-Veres, K.; Stevens, J.R.; Dutcher, J.R. *J. Polym. Sci. Part B: Polym.Phys.* **1996**, 34, 3009.

[86] Roberston, W. M., Grimsditch, M., Moretti, A .L., Kaufman, R. G., Hulse, G. R., Fullerton, E., Schuller, I. K. *Phys. Rev .B* **1990**, 41, 4986.

[87] a) Dutcher, J. R., Lee, S., Hillebrands, B., McLaughlin, G. J., Nickel, B.G.., Stegeman, G. I. Phys. Rev. Lett. **1992**, *68*, 2464. b) Giovannini, L., Nizzoli, F., Malvin, A. M. *Phys. Rev. Lett.***1992**, 69, 1572.

[88] Bandhu, R. S., Zhang, X., Sooryakumar, R., Bussmann, K. *Phs .Rev. B* **2004**, 70, 075409.

[89] Kaiser W., M. Maier M, "*Stimuilated Rayleigh, Brillouin and Raman Sectroscopy,*" in *Laser Handbook*, F.T. Arecchi and E. O. Schulz-Dubois, eds. (North-Holland,), **2**, 1077-1150, **1972.**

[90] Cho S. B, Lee J. J., Kwon B., *Optic Express* **2004**, 12, 4340.

[91] Agrawal G. P, *Nonlinear Fiber Optics*, Academic Press, Boston, chap. 9, **1989.**

[92] Tommaseo G., "Towards polymer based phononic crystals- a characterization with high resolution Brillouin scattering", *private report*, **2004.**

[93] Yariv A., *Quantum electronics*, Wiley &Sons, New York, **1967**. resolution Brillouin scattering", *private report*,**2004.**

[94] Cavanaugh D. B., Wang C. H, J*. Polym. Sci.: Polym. Phys. Ed*. 1981, 19, 583.

[95] Lindsay S. M., Anderson M. W., Sandercock J. R. *Rev. Sci. Instruments* **1981**, 52, 1478.

[96] Mishra A.M., Bray R., *Phys. Rev. Lett*. **1977**, 39, 222

[97] Marvin A.M., Toigo F., Celli V., *Phys. Rev. B*, **1975**, 11, 2777

[98] Loudon R., Phys. Rev. Lett., **1978**, 40, 581; Loudon R., *J. Phys. C,* 1978,11, 2623

[99] Rowell N.L., Stegeman G.I., *Phys.Rev. B,* **1978**, 18, 4181; Marvin A., Bortolani F., Nizzoli F., Santoro G., *J. Phys. C*, **1980**, 13, 1607

[100] Marvin A., Bortolani F., Nizzoli F., Santoro G., *J. Phys. C*, **1980**, 13, 1607

[101] Berne, B., Pecora, R. Dynamic Light Scattering Wiley NY **1976.**

[102] Harden, J.L., Pleiner, H., Pincus, P.A. *J.Chem.Phys.***1991**, 94, 5208

[103] Kumar, S.R.; Renusch, D.P.; Grimsditch, M. *Macromolecules* 33, 1819, **2000**

[104] Landau, L.D.; Lifshitz E.M. Theory of Elasticity; Pergamon Oxford **1970.**

[105] Giovannini,L.;Nizzoli,F.;Malvin,A.M. *Phys.Rev.Lett*.**1992**,69,1572

[106] Roe, R.J. Methods of X-ray and Neutron Scattering in Polymer Science, New York Oxford, **2000.**

[107] a)Bruder F.,Brenn R., *Phys.Rev.Lett*.,**1992**, 69, 624;b) Puri S., Binder K., *Phys. Rev. Lett.,E*, **1994**, 49, 5359;c) Geoghegan M., Jones R.A.L., Clough A.S., *J. Chem. Phys.*, **1995**, 103, 2719; d) Frish H.L., Niebala P., Binder K., *Phys. Rev. E*, **1995**, 52, 2848

[108] a)Keblinski P., Kumar S.K., Maritan, A., Koplik J., Banavar J.R., *Phys. Rev. Lett*, **1996**,76, 1106; b)Tanaka H*., Phys. Rev. Lett*.,**1996**, 76, 787; c)Rogers T.M., Desai R.C., *Phys. Rev. B*., **1989**, 39, 11956

[109] Forrest J. A.,.Dalnoki-Veress K., Dutcher J.R., *Physic. Rev.E*., **1998**, 58, 6109

[110] Krvebeck H., Krüger J.K., Pietralla M., *Journ. of Polymer Science, Part B,* **1993**,31,1477

[111] Mark, J. E. Some Unusual Elastomers and Experiments on Rubberlike Elasticity. *Prog. Polym. Sci*. **2003**, 28, 1205-1221.

112 Mark, J. E.; Allcock, H. R.; West, R. *Inorganic Polymers, 2nd ed*.; Oxford University Press: New York, **2004.**

[113] Reisch, M. S. *Chem. Eng.* News**, 1997**, *75*, 5(36), 18.

[114] Cox, H. L. Br. *J. Appl. Phys.* **1952**, 3, 72.

[115] Kelly A., Tyson, W. R. *High Strength Materials*, John Wiley & Sons, **1965**, 578.

[116] Hull, D. *An Introduction to Composite Materials*; Cambridge University Press: Cambridge, **1981**; p 3.

[117] Work, W. J.; Horie, K.; Hess, M.; Stepto, R. F. T. *Pure. Appl. Chem.* **2004**, *76*, 1985.

[118] Ziolo, R. F., Giannelis, E. P., Weinstein, B. A., O´Horo, M. P., Ganguly, B. N., Mehrotra, V., Russell, M. W., Huffman, D. R. *Science*, **1992**, 257, 219.

[119] Pu, Z. Mark, J. E. Jethmalani, J. M. Ford, W.T., *Polymer Bulletin*, 1996, **37**, 545.

[120] Motomatsu, M. Takahashi, T. Nie, H.-Y. Mizutani W. H. Tokumoto, H. *Polymer*, **1997**, 38, 177.

[121] Wen J. Mark J. E., *Rubber Chem. & Tech*., 1994, **67**, 806.

[122] Frisch H. L., Mark, E. J. *Chem. Mater.,* **1996**, **8**, 1735.

[123] Theng, B. K. G. Formation and properties of clay-polymer complexes, Elsevier, New-York, **1979**.

[124] a) Fukushima, Y., Okada, A., Kawasumi, M., Kurauchi, T., Kamigaito, O. *Clay. Miner*. **1988**, 23, 27. b) Usuki, A., Kojima, Y., Kawasumi, M., Okada, A., Fukushima, Y., Kurauchi, T., Kamigaito, O. *J. Mater. Res.* **1993**, 8, 1179.

[125] Okada, A., Usuki, A., Mater. Sci. Eng. 1995, C 3, 109.

[126] Ogawa, M., Kuroda, K., Bull. Chem. Soc. Jpn. 1997, 70, 2593.

[127] Prasad, M.; Kopycinska, M.; Rabe, U.; Arnold, W. *Geophys. Res. Lett.* **2002**, *29*, 13.

[128] Piner, R. D.; Xu, T. T.; Fisher, F. T.; Qiao, Y.; Ruoff, R. S. *Langmuir* **2003**, *19*, 7995.

[129] Shell, H. R.; Ivey, K. H. *Fluorine Micas*; Bureau of Mines, U.S. Department of the Interior: Washington, DC, **1969**; Vol. 647.

[130] Katti, K. S.; Katti, D. R. *Langmuir* **2006**; *22,* 532.

[131] Jordan, J.M. J. Phys. Colloid Chem., **1950**, 53, 245.

[132] Jeon, H. G., Jung, H.-T., Hudson, S. D. *Polymer Bulletin* **1998***,* 41, 107.

[133] Yano, K., Usuki, A., Okada, A., Kurauchi, T., Kamigaito, O. *J. Polym. Sci. Part A,* **1993***,* 31, 2493.

[134] Kawasumi, M., Hasegawa, N., Usuki, A., Akane, O. *Mater. Eng. Sci.* **1998***, C* **6**, 135.

[135] Vaia, R. A., Sauer, B. B., Tse, O. K., Giannelis, E. P., *J. Polym. Sci.: Part B*, **1997**, 35, 59.

[136] Lee, D.C., Jang, L. W., *J. Appl. Polym. Sci*., **1996**, 61, 1117.

[137] Lee D. C. Jang, L. W. *J. Appl. Polym. Sci*., **1998**, 68, 1997.

[138] Theng, B. K. G. *Formation and properties of clay-polymer complexes*, Elsevier, Amsterdam, **1979**, p 133.

[139] a) Vaia, R. A., Ishii, H., Giannelis, E. P., *Chem. Mater*. **1995**, 5, 1694. b) Messersmith, P. B., Giannelis, E. P. *Chem. Mater*. **1994**, 6, 1719.

[140] Giannelis, E. P. *Adv. Mater.* **1996**, 8, 29.

[141] Liu, L. Qi, Z. Zhu, X. *J.Appl. Polym. Sci.,***1999***,* 71, 1133.

[142] Vaia, R. A. Jandt, K. D. Kramer, E. J., and Giannelis, E. P. *Chem. Mater*., **1996**, 8, 2628.

[143] Kawasumi, M. Hasegawa, N. Kato, M. Usuki, A. Okada, A., *Macromolecules*, **1997**, 30, 6333.

[144] Okada, A. Kawasumi, M. Usuki, A. Kojima, Y. Kurauchi, T.and Kamigaito, O., *Mater. Res. Soc. Proc*., **1990**, 171, 45.

[145] Usuki, A., Kojima, Y., Kawasumi, M., Okada, A., Fukushima, Y., Kurauchi, T., Kamigaito, O. *J. Mater. Res.* **1993**, *8*, 1180.

[146] Messersmith, P. B., Giannelis, E. P. *J. Polym. Sci., Part A: Polym. Chem.* **1995**, *33*, 1047.

[147] Messersmith, P., Giannelis, E. P. *Chem. Mater.* **1994**, *6*, 1719.

[148] Lan, T.; Kaviratna, P. D.; Pinnavaia, T. J. *Chem. Mater.* **1995**, *7*, 2144. b) Brown, J. M.; Curliss, D.; Vaia, R. A. *Chem. Mater.* **2000**, *12*, 3370. c) Wang, M. S.; Pinnavaia, T. J. *Chem. Mater.* **1994**, *6*, 468.

[149] Zeng, C., Lee, L. J., *Macromolecules* **2001,** *34,* 4098.

[150] Fan, X., Xia, C., Advincula, R. C. *Langmuir* **2003,** *19,* 4381.

[151] Noh, M. W.; Lee, D. C. *Polym. Bull*. **1999**, *42*, 619. (29) Lee, D. C.; Jang, L. W. *J. Appl. Polym. Sci.* **1996**, *61*, 1117

[152] Okamoto, M.; Moritaa, S.; Taguchi, H.; Kim, Y. H.; Kataka, T.; Tateyama, H. *Polymer* **2000**, *41*, 3887.

[153] Biasci, L.; Alietto, M.; Ruggeri, G.; Ciardelli, F. *Polymer* **1994**,
35, 3296.

[154] Doh, J. G.; Cho, I. *Polym. Bull.* **1998**, *41*, 511.

[155] Weimer, M. W.; Chen, H.; Giannelis, E. P.; Sogah, D. Y. *J. Am. Chem. Soc.* **1999**, *121*, 1615.

[156] Huang, X.; Brittain, W. J. Polym. Prepr. (Am. Chem. Soc., Div. Polym. Chem.) **2000**, 41, 521.

[157] Zhu, M. F., Yan, W. D., Lu, Y., Chen, Y. M., Adier, H. J. P., Potschke, P., Pionteck, J., Macromol. Symp. 2001, **164**, 369.

[158] a) Hasegawa, N., Okamoto, H., Kato, M., Tsukigase, A., Usuki, A. *Macromol Mater Eng* **2000**;76, 280. b) Hasegawa, N., Okamoto, H., Kato, M., Usuki, A. *J Appl Polym Sci* **2000**, 78, 1981. c) Nam, P.H., Maiti, P., Okamoto, M., Kotaka, T., Hasegawa, N., Usuki, A. *Polymer* **2001**, 42, 9633. d) Okamoto, M., Nam, P. H., Maiti,

P., Kotaka, T., Hasegawa, N., Usuki, A. *Nano Let.t* **2001**, 1, 295. e) Maiti, P., Nam, P. H., Okamoto, M., Kotaka, T., Hasegawa, N., Usuki, A. *Polym Eng Sci* **2002**, 42, 1864. f) Okamoto, M., Nam, P. H., Maiti, P., Kotaka, T., Nakayama, T., Takada, M., et al. *Nano Lett* **2001**, 1, 503.

[159] a) Rong, M. Z., Zhang, M. Q., Zheng, Y. X., Zeng, H. M., Walter, R., Friedrich, K. *Polymer* **2001**, 42, 167. b) Rong, M. Z., Zhang, M. Q., Zheng, Y. X., Zeng, H. M., Friedrich, K. *Polymer Com.* **2001**, 42, 3301.

[160] Vaia, R. A.; Giannelis, E. P. *Macromolecules* **1997**, *30*, 7990.

[161] Gahleitner, M., Bernreitner, K., Neissl, M., J. Appl. Polym. Sci., **1994**, 53, 283.

[162] Lee, S. Y., Lee, J. D., Yang, S. M. *J. Mater. Sci*. **1999**, 34, 1233.

[163] Khan, M. A., Hinrichsen, G., Drzal, L. T. *J. Mater. Sci. Lett*. **2001**, 20, 1711.

[164] Alexandre, M., Dubois, P. *Mater. Sci. Eng*. **2000**, 28, 1.

[165] a) Balazs, A. C.; Singh, C.; Zhulina, E. *Macromolecules* **1998**, *31*, 8370. b) Kuznetsov, D. V.; Balazs, A. C. *J. Chem. Phys.* **2000**, *113*, 2479.

[166] Beyer, F. L.; Tan, N. C. B.; Dasgupta, A.; Galvin, M. E. *Chem. Mater.* **2002**, *14*, 2983.

[167] Huang, X. Y.; Brittain, W. J. *Macromolecules* **2000**, *34*, 3255.

[168] a) Krishnamoorti, R.; Giannelis, E. P. *Langmuir* **2001**, *17*, 1448. b) Krishnamoorti, R.; Ren, J. X.; Silva, A. S. *J. Chem. Phys.* **2001**, *114*, 4968. c) Ren, J. X.; Casanueva, B. F.; Mitchell, C. A.; Krishnamoorti, R. *Macromolecules* **2003**, *36*, 4188.

[169] Wang, Z. M., Nakajima, H., Manias, E., Chung, T. C. *Macromolecules* **2003**, *36,* 8919.

[170] Kurokawa, Y., Yasuda, H., Oya, A., *J. Mater. Sci. Lett.* **1996**, 15, 1481–1483.

[171] Usuki, A., Kato, M., Okada, A., Kurauchi, T., *J. Appl. Polym. Sci*. **1997**, 63, 137.

[172] Heinen, W.; Rosenmöller, C. H.; Wenzel, C. B.; de Groot, H. J. M.; Lugtenburg, J.; van Duin, M. *Macromolecules* **1996**, *29*, 1151.

[173] a) Lu, B.; Chung, T. C. *Macromolecules* **1998**, *31*, 5943. b) Lu, B.; Chung, T. C. *Macromolecules* **1999**, *32*, 2525.

[174] Tseng, F. P., Lin, J-J., Tseng, C-R., Chang, F-C., Polymer 2001, 42, 713.

[175] Chow, W. S., Mohd Ishak, Z. A., Karger-Kocsis, J., Apostolov, A. A., Ishiaku, U. S., *Polymer* **2003**, 44, 7427.

[176] Kawasumi,M., Hasegawa, N., Kato, M., Usuki, A., Okada, A. *Macromolecules* **1997**, *30,* 6333.

[177] Hasegawa, N., Kawasumi, M., Kato, M., Usuki, A., Okada, A., *J. Appl. Polym. Sci.*, **1998**, 67, 87.

[178] Garcia, M., Vliet, G. van, Jain, S., Schrauwen, B. A. G., Sarkissov, A., Zyl, W. E. van, Boukamp, B., Rev. Adv. Mater. Sci., **2004**, 6, 169.

[179] Janigová, I., Chodák, I., *J. Therm. Anal. Calorim.* **2000**, 60, 401.

[180] Fong, H.; Vaia, R. A.; Sanders, J. H.; Lincoln, D. M.; John, P. J.; Vreugdenhil, A. J.; Bultman, J.; Cerbus, C. A.; Jeon, H. G. *Chem. Mater.* **2001***, 13*, 4123.

[181] Yang, F.; Ou, Y.; Yu, Z. *J. Appl. Polym. Sci.* **1998**, *69*, 355.

[182] Bandyopadhyay, S.; Hsieh, A. J.; Giannellis, E. P. *ACS Symp. Ser.* **2002**, *804*, 15.

[183] Akelah, A.; Moet, A. *J. Mater. Sci.* **1996**, *31*, 3589.

[184] Sikka, M.; Cerini, L. N.; Ghosh, S. S.; Winey, K. I. *J. Polym. Sci., Part B: Polym. Phys.* **1996**, *34*, 1443.

[185] Lan, T.; Pinnavaia, T. J. *Chem. Mater.* **1994**, *6*, 2216.

[186] Song, M.; Hourston, D. J.; Yao, K. J.; Tay, J. K. H.; Ansarifar, M. A. *J. Appl. Polym. Sci.* **2003**, *90*, 3239.

[187] Kojima, Y.; Usuki, A.; Kawasumi, M.; Okada, O.; Fukushima, Y.; Kurachi, T.; Kamigaito, O. *J. Mater. Res.* **1993**, *8*, 1185.

[188] Ke, Y.; Long, C.; Qi, Z. *J. Appl. Polym. Sci.* **1999**, *71*, 1139.

[189] Kojima, Y.; Usuki, A.; Kawasumi, M.; Okada, A.; Kurachi, T.; Kamigaito, O. *J. Appl. Polym. Sci.* **1993**, *49*, 1259.

[190] Messersmith, P. B.; Giannelis, E. P. *J. Polym. Sci., Part A: Polym. Chem.* **1995**, *33*, 1047.

[191] Akelah, A.; Moet, A. *J. Mater. Sci.* **1996**, *31*, 3589.

[192] Gilman, J. W.; Kashiwagi, T.; Lichtenhan, J. D. *SAMPE J.* **1997**, *33*, 40.

[193] Lincoln, D. M.; Vaia, R. A.; Benson Tolle, T. H.; Brown, J. M. *IEEE Aerospace Conf. Proc.*; Conf. Proc. of 2000 Meeting. IEEE Aerospace Conf. Big Sky, MT, March 18-25, 2000.

[194] Fong, H.; Vaia, R. A.; Sanders, J. H.; Lincoln, D. M.; John, P. J.; Vreugdenhil, A. J.; Bultman, J.; Cerbus, C. A.; Jeon, H. G. *Chem. Mater.* **2001***, 13*, 4123.

[195] Vaia, R. A.; Price, G.; Ruth, P. N.; Nguyen, H. T.; Lichtenhan, *J. Appl. Clay Sci.* **1999**, *15*, 67.

[196] Chow, W. S., Mohd. Ishak, Z. A., Ishiaku, U. S., Karger-Kocsis, J., Apostolov, A. A. *J. Appl. Polym. Sci.*, **2004**, 91, 175.

[197] a) Hofmann, U., Angew. Chem., **1956**, 68, 53. b) Weiss, A., *Angew. Chem*., **1963**, 75, 113.

[198] Reichert, P., Nitz, H., Klinke, S., Brandsch, R., Thomann, R., Mülhaupt, R., *Macromol. Mater. Eng*. **2000**, 275, 8.

[199] Bu, H.S., Cheng, S.Z.D., Wunderlich, B., *Makromol. Chem. Rapid Commun*. **1988**, 9, 75.

[200] Nowacki, R., Monasse, B., Piorkowska, E., Galeski, A., Haudin, J. M., *Polymer* **2004**, 45, 4877.

[201] Magonov, S. N ., Reneker, D. H. *Annu. Rev. Mater. Sci.* **1997**, 27, 175.

[202] Goh, M. C. In Advances in Chemical physics; Progogine, I., Rice, S. A., Eds; Wiley-Interscience: New-York, 1995, Vol XCI, 1.

[203] Magonov, S. N ., Sheiko, S. S., Deblieck, R. A. C., Möller, M. *Macromolecules* **1993**, 26, 1380.

[204] Turner-Jones, A., Aizlewood, J. M., Beckett, D. R., *Makromol. Chem*. **1964**, 75, 134.

[205] Kawasumi, M., Hasegawa, N., Kato, M., Usuki, A., Okada, A. *Macromolecules* **1997**, 30, 6333.

[206] Liu, X., Wu, Q., *Polymer* **2001**, 42, 10013.

[207] Samuels, R. J., *J. Polym. Sci., Part A* **1965**, 3, 1741.

[208] Stein, R. S. in Newer Methods of Polymer Characterization, Ke, B., Interscience, New-York, 1964, Chap. 4.

[209] Wang, K., Liang, S., Du, R., Zhang, Q., Fu, Q., *Polymer* **2004**, 45, 7953.

[210] Favis, B.D., Factors influencing the morphology of immiscible polymer blends in melt processing, Vol.1 John Wiley, New Yourk, 1999

[211] Lipatov, Y.S.; Nesterov, A.E., Ignatova, T.D., Nesterov D.A., *Polymer*, 2002,43, 875

[212] Academic R. J., Wang, C. H. *Macromolecules* **1984**, 17, 2018.

[213] a) Wang, C. H., Liu, Q. L., Li, B. Y. *J. Polym. Sci., Polym. Phys. Ed.* **1987**, 25, 485. b) Krbecek H. H., Pietralla, M. *Int. J. Polym. Mater.* **1993**, 22, 177.

[214] Shah, D., Fytas, G., Vlassopoulos, D., Di, J., Sogah, D., Giannelis, E. P. *Langmuir* **2005**, 21, 19.